New insights on the nature of blazars from a decade of multi-wavelength observations : Discovery of a very large shift of the synchrotron peak frequency, long-term optical-gamma-ray flux correlations, and rising flux trend in the BL Lac 1ES 1215+303

Janeth Veronica Valverde Quispe

HAL Id: tel-02972820

https://tel.archives-ouvertes.fr/tel-02972820

Submitted on 20 Oct 2020

NNT : 2020IPPAX013

INSTITUT POLYTECHNIQUE DE PARIS

ÉCOLE POLYTECHNIQUE

IP PARIS

Thèse de doctorat

New insights on the nature of blazars from a decade of multi-wavelength observations:
Discovery of a very large shift of the synchrotron peak frequency, long-term optical-γ-ray flux correlations, and rising flux trend in the BL Lac 1ES 1215+303

Thèse de doctorat de l'Institut Polytechnique de Paris
préparée au Laboratoire Leprince-Ringuet - École Polytechnique

École doctorale n°626 Dénomination (EDIPP)
Spécialité de doctorat : Astrophysique

Thèse présentée et soutenue à Palaiseau, le 24 février 2020, par

JANETH VALVERDE

Composition du Jury :

Pascal Paganini
Directeur détudes, École Polytechnique (Laboratoire
Leprince-Ringuet)   Président

John Quinn
Associate Professor, University College Dublin (School of Physics)   Rapporteur

Jean-Philippe Lenain
Chargé de Recherche, Sorbonne Université (Laboratoire de
Physique Nucléaire et de Hautes Energies)   Rapporteur

Reshmi Mukherjee
Professeur, Columbia University (Barnard College), New York,
United States   Examinateur

Jonathan Biteau
Maître de conférences, Université Paris-Saclay (Laboratoire de
physique des 2 infinis Irène Joliot-Curie)   Examinateur

Deirdre Horan
Chargée de Recherche, École Polytechnique (Laboratoire
Leprince-Ringuet)   Directrice de thèse

Dedicated to:

Dona, prof. Valqui,

Deirdre and Denis.

Abstract

Blazars are known for their variability on a wide range of timescales at all wavelengths; and their classification (into flat spectrum radio quasars, low-, intermediate- or high-frequency-peaked BL Lac; FSRQ[1], LBL, IBL, HBL) is based on broadband spectral characteristics that do not consider the source being at, possibly, different states of activity. Recently, it was proposed that blazars could be classified according to the kinematics of their radio features. Most studies of TeV γ-ray blazars focus on short timescales, especially during flares, due to the scarcity of observational campaigns or due to the relatively young existence of specialized, sensitive enough detectors.

With a decade of observations from the *Fermi*-LAT and VERITAS, I present an extensive study of the long-term multi-wavelength variability of the blazar 1ES 1215+303 from γ-rays to radio. This unprecedented data set reveals multiple strong γ-ray flares and a long-term increase in the γ-ray and optical flux baseline of the source over the ten-year period, which results in a linear correlation between these two energy bands over a decade. Typical HBL behaviors are identified in the radio morphology of the source. However, analyses of the broadband spectral energy distribution at different flux states of the source, unveil an extreme shift in energy of the synchrotron peak frequency from IR to soft X-rays; indicating that the source exhibits IBL characteristics during quiescent states and HBL behavior during high states. A two-component synchrotron self-Compton model is used to describe this dramatic change.

---

[1]For the comfort of the reader, a list of abbreviations has been compiled in page vii.

A detailed framework of the analysis of the data from the *Fermi*-LAT instrument is provided, and could serve as a guideline for researchers interested in this field. I present the thorough efforts that were employed in validating the methods used and the sanity checks that were performed on the results obtained. A description of the higher-level analyses are provided, including the flare-selection algorithms, the search for harder-when-brighter behavior in the *Fermi*-LAT data, the multi-wavelength cross-correlation and variability analysis, the search for trends, log-normality and variability, the characterization of flares and of the spectral energy distributions, and the search for simultaneous *Fermi*-LAT - VERITAS observations. These are the heart of this PhD work.

The different methods applied and presented in this work provide a complete and detailed panorama of the intricate nature of this blazar, and possibly even challenge our current classification scheme. Moreover, this work provides an illustration of the type of long-term analyses that future imaging atmospheric instruments, such as the Cherenkov Telescope Array, will not only allow but potentially improve.

Contents

List of Abbreviations

2MASS	2 Micron All-Sky Survey
ACD	Anticoincidence Detector
ACT	Atmospheric Cherenkov Telescopes
ADAF	Advective Dominated Accretion Flow
AGN	Active Galactic Nucleus
ALFOSC	Alhambra Faint Object Spectrograph and Camera
ApJ	Astrophysical Journal
ARR	Automatic Re-point Requests
ASM	All-Sky Monitor
ATel	Astronomer's Telegram
BAT	(*Swift*) Burst Alert Telescope
BCU	Blazar Candidates of Uncertain type
BDT	Boosted Decision Tree
BH	Black Hole
BLF	Broken Linear Function
BLR	Broad Line Region
CL	Confidence Limits
COBE	COsmic Background Explorer
CTA	Cherenkov Telescope Array
DAQ	Data Acquisition System
DCF	Discrete cross-Correlation Function
DCNs	Deep Convolutional Neural Networks
d.o.f.	degrees of freedom
DQM	Data-Quality Monitoring
EBL	Extragalactic Background Light
EHBL	Extreme HBL
FA	Flare Advocate
FGL	*Fermi* Gamma-ray LAT
FITS	Flexible Image Transport System
FLWO	Fred Lawrence Whipple Observatory
FoV	Field of view
FR	Fanaroff-Riley
FSRQ	Flat Spectrum Radio Quasar
FSSC	*Fermi* Science Support Center
FWHM	Full Width at Half Maximum
GBM	Gamma-ray Burst Monitor
GRB	Gamma-ray Bust
GST	Gamma-ray Space Telescope
GTI	Good Time Interval
HBL	High-frequency-peaked BL Lac object
HDU	Header Data Units
HE	High Energy

H.E.S.S.	High Energy Stereoscopic System
HR	Hardness Ratio
HSP	High-Synchrotron-Peaked BL Lac object
IACT	Imaging Atmospheric Cherenkov Telescopes
IBL	Intermediate-frequency-peaked BL Lac object
IC	Inverse Compton
IGRB	Isotropic Diffuse Gamma-ray Background
IR	Infrared
IRF	Instrument Response Functions
ISM	Interstellar Medium
ISP	Intermediate-Synchrotron-Peaked BL Lac object
KVA	Kungliga Vetenskapsakademien telescope
LAC	LAT AGN Catalog
LAT	Large Area Telescope
LBL	Low-frequency-peaked BL Lac object
LP	Log-Parabola
LSP	Low-Synchrotron-Peaked BL Lac object
LSP	Lomb-Scargle periodograms (only in Section 5.7)
MAGIC	Major Atmospheric Gamma Imaging Cherenkov Telescopes
mas	milliarcsecond
MET	Mission Elapsed Time
MIP	Minimum Ionizing Particles
MJD	Modified Julian Date
ML	Maximum Likelihood
MOJAVE	Monitoring Of Jets in Active galactic nuclei with VLBA Experiments
MRO	Metsähovi Radio Observatory
MWL	Multiwavelength
NA	Not Applicable
NASA	National Aeronautics and Space Administration
NH	Null Hypothesis
NOT	Nordic Optical Telescope
NRL	Narrow Line Region
NSB	Night Sky Background
OVRO	Owens Valley Radio Observatory
P.A.	Position Angle
PC	Photon Counting
PDF	Probability Density Function
PL	Power-Law
plSECO	Power-law Sub Exponential Cutoff
PMT	Photomultiplier Tube
PSD	Power Spectral Density
PSF	Point Spread Function
QPO	Quasi-Periodic Oscillations
QSO	Quasi-Stellar Object

RF	Random Forest
ROI	Region Of Interest
SAA	South Atlantic Anomaly
SED	Spectral Energy Distribution
SMBH	Super Massive Black Hole
SN	Supernova
SR	Source Region
SSC	Synchrotron Self-Compton
SSD	Silicon-Strip tracking Detectors
TDE	Tidal Disruption Events
ToO	Targets of opportunity
TS	Test Statistic
UV	Ultraviolet
UVOT	(*Swift*) UV/Optical Telescope
VERITAS	Very Energetic Radiation Imaging Telescope Array System
VHE	Very High Energy
VIP	Very Important Project
VLBA	Very Long Baseline Array
VLBI	Very Long Baseline Interferometry
WT	Window Timing
WWZ	Weighted Wavelet Z-transform
XML	eXtensible Markup Language
XRT	(*Swift*) X-Ray Telescope
ZDCF	z-transformed Discrete cross-Correlation Function

Preface

During the last three years, I have had the extraordinary opportunity to participate in the performance of different tasks, the main one being the subject of this manuscript, the detailed study of certain active galactic nuclei (AGNs), 1ES 1215+303 and three FSRQs, with a focus on their γ-ray emission. In this endeavor I learned how to use the *Fermi*-LAT analysis tools, I analyzed a large amount of data on γ-ray AGNs, and developed scripts that speed up the obtention of light curve data, a complex analysis chain, by working dynamically with my group at LLR and as part of the *Fermi*-LAT Collaboration.

I worked closely with a few members of the VERITAS collaboration, namely Prof. Reshmi Mukherjee and her group at Columbia University NY, in the thorough multi-wavelength (MWL) variability, inter-band correlation and time-resolved broadband spectral analysis of the extragalactic BL Lac object 1ES 1215+303. In this project, we found a 10-year long global correlation between the optical and γ-ray bands and a radio morphology and polarization typical of TeV high-synchrotron-peaked BL Lac objects. More interestingly, we found an extreme shift of the synchrotron peak between different flux states of the source, which locate this source in different places of the current classification scheme of blazars at different times, therefore challenging it. We probed a blob-in-jet model that describes the broadband electromagnetic emission in terms of synchrotron and synchrotron-self-Compton mechanisms, from which we inferred that the system is well described by a matter-dominated blob.

I presented these results, in the different stages of the project, at a number of venues such as the *Fermi*-LAT Collaboration meetings (Valverde et al. 2017a, 2018a), Summer School (Valverde et al. 2017b), the 7th and 8th International *Fermi* Symposium (Valverde et al. 2017e, 2018c), ISCRA School 2018 (Valverde et al. 2018b), Blazar analysis teleconference (Valverde et al. 2017c), at the XIV Meeting of Physics (Valverde et al. 2017d), at the TeV Particle Astrophysics 2019; and at the 30th Texas Symposium on Relativistic Astrophysics 2019, where our work was recognized when I was awarded the best student presentation prize in the γ-ray parallel session. A first version of the publication on this project was drafted and underwent a thorough scrutiny within the *Fermi*-LAT and VERITAS collaborations and among the multi-wavelength co-authors. Finally, I submitted a comprehensive, robust manuscript to the Astrophysical Journal (ApJ).

While this paper was undergoing internal review, I started working on the analysis of γ-ray data from other sources, triggered by the invitation of Prof. Mukherjee to collaborate on a new project based on the γ-ray study of the extremely bright flat spectrum radio quasar (FSRQ) 3C 279, and the FSRQ PKS 1222+216, recently detected at very high energies by VERITAS. These sources will be the subject of a second publication in which we will probe absorption models by the broad line region. Finally, there is the possibility of a study of the FSRQ Ton 0599, also detected at TeV energies by VERITAS and for which there is no detailed publication. We already have lightcurves and a SEDs available for this source, and are at the moment of writing looking for possible partnerships to be able to fully explore the potential of this source, as we have done for 1ES 1215+303.

As a member of the *Fermi*-LAT Collaboration, I took part in a number of activities. I undertook data-quality-monitoring and sky-watch shifts (known as DQM and (Deputy) Flare Advocate shifts, respectively), which enabled me to learn more about the analysis pipeline, the sources that we observe and the technicalities of the spacecraft itself as well as to work closely with members of the blazar group and instrument team. In particular, the Flare Advocate effort resulted in a number of Astronomer's Telegrams (ATels). The first of this list of ATels reported the first γ-ray detection of the radio source PMN J1747-5236 (Ojha et al. 2017a), followed by reports on enhanced γ-ray emission of the FSRQs PKS 0035-252 (Valverde & Ojha 2017b; Angioni et al. 2018), PKS 1004-217 (Valverde & Ojha 2017a), PKS 0131-522 (Ojha et al. 2017b), and of the Crab Nebula (Valverde et al. 2018d); and finally, the report on the *Fermi*-LAT detection of γ-ray activity and a hard spectrum of the BL Lacertae object TXS 0506+056, located inside the IceCube-170922A error region (Ojha & Valverde 2018). I also participated in the AGN working group effort in the making of the fourth catalog of AGNs detected by the *Fermi*-LAT (The *Fermi*-LAT collaboration 2019). Furthermore, I had the opportunity to contribute to the *Fermi*-LAT AGN group by serving as the internal referee for the paper on *A Fast Very High Energy γ-ray Flare from BL Lacertae during a Period of Multiwavelength activity in June 2015* (MAGIC Collaboration et al. 2019), which was published in the ApJ.

On December 2018, I was given the extraordinary news that I was chosen as one of the grantees of the Alliance Doctoral Mobility for the project *"Characterization of blazars at GeV-TeV energies in a MWL context"* [2]. I departed from Paris in March 2019, with destination Nevis Labs, Columbia University, NY. I spent a few weeks as an exchange student of Columbia University in NY, working closely with professor Reshmi Mukherjee's group. Then, as my research project involved performing astronomical observations with VERITAS at the Fred Lawrence Whipple Observatory (FLWO), I travelled to Arizona for an observing shift that lasted for three weeks. While in New York, I became an active member of the Gamma-ray Astronomy group at Columbia University. I attended the Astroparticle seminars, and I participated in the weekly group meetings together with other graduate students, postdocs and professors, where we discussed our work and results. While at NY or AZ, we had constant meetings and discussions regarding our ongoing projects. Our then advanced project was the publication on 1ES 1215+303. The visit greatly contributed to boost our discussions and address the input involved in the internal review process within our collaborations, before the submission of the paper. We were as well able to discuss, draw a plan and consolidate collaborations for our younger project on the FSRQs, 3C 279 and PKS 1222+2016, as mentioned above. I was given the opportunity to help two Barnard undergraduate students to get started on a number of *Fermi*-LAT γ-ray data analyses.

At the VERITAS base camp, a typical day would start around 5pm, when we would decide the potential objects to observe, then discuss the communications received, if any, from the day crew or other VERITAS members regarding the observations. During the

---

[2]https://alliance.columbia.edu/people/janeth-valverde-quispe

next two hours before startup, we inspected the telescopes and trailers, where the digital equipment of each telescope is, turned on the different devices and launched the software that remotely controls and monitors the telescopes sub-systems and data, including the program that tracks the stellar objects. We benefited from favorable weather during most of this shift, allowing us to cover ∼20% of the total goal of observation time for that season. Among the targets observed were 1ES 1215+303, 3C 279 and PKS 1222+216, subjects of our projects mentioned above. Other interesting sources observed were M 87, that provided for the first time the picture of a black hole (in the radio band) in a press release during this shift, observations triggered by a gamma-ray burst alert and by a gravitational-wave alert. I would like to express my thankfulness to the Alliance program for the opportunity. It not only boosted the progress of our research projects and future publications, therefore greatly benefiting my thesis; but also enabled me to expand enormously my γ-ray expertise whilst strengthening the ties within our Ecole Polytechnique - Columbia University Gamma Astronomy group.

In this manuscript, as a PhD candidate, I am expected to draw the reader's attention to the work I have done. However, I would like to point out - probably against the wishes of my supervisors - that even when I might have carried out certain tasks, it was most of the time, if not always, triggered by a strong interaction with the members of my group, and the brilliant and most kind feedback I received from them. Lastly, I would like to say that none of the wonderful experiences I had these last years would have been possible without the extraordinary support of my supervisors, Deirdre and Denis, the Astro-Gamma group, my team, the LLR-École Polytechnique, the _Fermi_-LAT Collaboration, the amazing support of Reshmi and her group, and the VERITAS Collaboration. To all of them, I am deeply grateful.

I acted as the coordinator the multi-wavelength research project of the BL Lac object 1ES 1215+303. Each data extraction was done separately in each Collaboration; I performed the analysis for the _Fermi_-LAT data.

For the science analyses, the tasks were distributed as follows:

- J. Valverde;

  - LAT flare selection and search for trends,

  - harder-when-brighter searches for the LAT data,

  - LAT high energy photons analysis,

  - the multi-wavelength cross-correlation and variability analysis,

  - searches for log-normality and variability,

  - characterized the flares and the LAT SEDs,

  - long-term LAT SED analysis with three different spectral models,

- – searches for simultaneous LAT-VERITAS observations.

- O. Hervet was in charge of the SED modeling.

- Q. Feng performed the ZDCF, PSD analysis and scalograms.

- S. Fegan performed the search for quasi-periodicities.

1. INTRODUCTION

Fig. 1.1.— **Composite of visible and IR observations of M 87, from the Hubble Heritage Team (STScl/AURA) and NASA. A jet of subatomic relativistic particles is powered by a BH located at its center.**

In many ways, the Universe can be considered as a laboratory of fundamental and particle physics. In the present day, astronomy is principally concerned with the study of objects that cover the electromagnetic spectrum from radio waves to very-high energy (VHE; $\gtrsim$100 GeV) γ-rays. Theories predict that γ-rays are produced in particle acceleration and radiative mechanisms. These processes undergo extensive research nowadays in order to study the structure and evolution of astronomical objects, black hole (BH) formation and growth, gravitational waves, dark matter, violation of Lorentz invariance, etc. Other processes could affect the propagation of γ-rays at cosmological distances, and the transparency of the Universe to γ-rays, i.e. they can produce a modulation in the measured spectra. For instance, the extragalactic background light, that encloses the history of the entire star light emitted through the history of the universe, has a more significant impact on the absorption of VHE photons at higher redshifts (Franceschini & Rodighiero 2017; Biteau & Williams 2015; Biteau 2013).

An active galactic nucleus (AGN) is a galaxy that has an extremely luminous core, which is powered by a BH with a mass ranging from millions to billions of times the mass of the Sun. The hot diffuse material of the accretion disk spirals down towards the BH, and then part of that material is ejected out to the Universe, sometimes through the formation of jets (like the one exhibited by M 87 in Figure 1.1, which can be detected across the entire electromagnetic spectrum. Blazars are a type of AGN whose jets point almost directly towards the Earth (Beckmann & Shrader 2012), and that are particularly variable at all wavelengths on time scales from less than an hour to years. The study

of this variability at different wavelengths is crucial for testing models attempting to
identify the nature of the particles in the jet. Measurements across the spectrum are
challenging, thus the communication between the multi-wavelength facilities who can
simultaneously observe these blazars is of crucial importance; in particular, coordinated
campaigns between space-based, for observations at high energies (HE; 100 MeV $< E <$
100 GeV), and ground-based γ-ray telescopes, for observations at VHE, that enable the
exploration of the sky in the entire γ-ray spectrum. The study of the variability of blazars
allows us to put constraints on the size and location of the emitting region, while at the
same time enabling us to probe the particle acceleration mechanisms in the blazar jets.
Spectral studies across the entire γ-ray range can also allow us to study the extragalactic
background light (EBL; Hauser & Dwek 2001). This is because the γ-ray photons pair
produce e^+e^- with the IR–UV photons that comprise the EBL. This absorption signature
can be measured in the γ-ray spectra of blazars (e.g. Ackermann et al. 2012b).

BL Lac objects are a subclass of blazars that usually do not have significant emission
or absorption features in their optical spectra (Dermer & Giebels 2016). Flat spectrum
radio quasars (FSRQs) are the other subclass of blazars, which are characterized by
strong emission lines and, most of them, by a more powerful second broadband spectral
peak; however, due to their soft spectra at VHEs, they are often not detected at these
energies. The largest population of sources detected by the current generation of space-
based and ground-based γ-ray telescopes are blazars and they comprise more than 50%
of the associated sources in the Third *Fermi* Catalog (3FGL, based on data from the first
four years of the *Fermi* mission; Acero et al. 2015), more than 70% of the Third Catalog of
Hard *Fermi*-LAT Sources (Ajello et al. 2017), and more than 30% of the objects detected
at TeV energies[1]. As of writing, there have been 72 blazars detected at TeV energies, of
which 7 are FSRQs.

The past two years have borne witness to extraordinary astrophysical events, all of
which involved γ-ray emission. The first observed gravitational event with an electromag-
netic counterpart, GW170817, took place on August 2017 and triggered observations by
dozens of instruments, including the *Fermi*-GBM. The GBM γ-ray detection was com-
pletely unexpected, however it is now believed to have had its origin in the after-glow
of a merger (van Putten & Della Valle 2019). A month later there was a high-energy
astrophysical neutrino alert, IceCube-170922A, in the region of the BL Lacertae object
TXS 0506+056, which had been detected in an increasingly higher activity state during
the previous months by the *Fermi*-LAT. The possibility of this neutrino event having
been originated in this BL Lac object is still undergoing extensive studies by the commu-
nity, since it would make TXS 0506+056 the first source of HE astrophysical neutrinos
(IceCube Collaboration et al. 2018b). These two events have in common that they are
possibly associated to the formation or presence of a central black hole and the emission
of plasma jets. On January 2019, the first reported Gamma-ray Burst (GRB) detec-
tion by a TeV instrument, was announced by the MAGIC Collaboration (GRB 190114C;

---

[1]`tevcat.in2p3.fr`

Mirzoyan 2019). This was followed by the report of the first VHE GRB ever detected (GRB 180720B; Abdalla et al. 2019), on May 2019; and of GRB 190829A (de Naurois 2019) by the H.E.S.S. Collaboration. These observations open a window for new possible observational campaigns and science for imaging atmospheric Cherenkov telescopes (IACT), such as the future Cherenkov Telescope Array (CTA). The emission of GRBs has been modeled with similar particle acceleration mechanisms as for AGNs (Abdo et al. 2009; Ajello et al. 2020). All of these multi-messenger detections have made this field of study only even more exciting!

In this work, I apply a number of existing methods and tools for the variability and spectral analysis of the electromagnetic emission of AGNs, to the characterization of 1ES 1215+303 with a focus on its γ-ray emission. The knowledge on AGNs to the present day with current detectors (*Fermi*-LAT, VERITAS, etc.) is reported. Most of these analyses have been a joint effort with the VERITAS (VHE ground-based telescopes) Collaboration and with other multi-wavelength partners; therefore, in order to be able to give a consistent description of the results, I will be doing my best to describe their work as well. In Chapter 2; I briefly present the state of the art of our knowledge of AGNs. Chapter 3 describes the main characteristics of the detectors whose data have been used. Subsequently, a detailed description of the *Fermi*-LAT data and of the analyses that I have performed is presented in Chapter 4; then I proceed to the detailed description of the physical characteristics that we were able to draw for 1ES 1215+303 with all of the information collected in Chapter 5.

With a decade of observations from the *Fermi*-LAT and VERITAS, Chapter 5 presents an extensive complete study of the long-term multi-wavelength variability of the blazar 1ES 1215+303. Blazars' classification (into flat spectrum radio quasars, low-, intermediate- or high-frequency-peaked BL Lac; FSRQ, LBL, IBL, HBL) is based on broadband spectral characteristics that do not consider the source being at, possibly, different states of activity (The *Fermi*-LAT collaboration 2019). Recently, it was proposed that blazars could be classified according to the kinematics of their radio features (Hervet et al. 2016). Most studies of TeV gamma-ray blazars focus on short timescales, especially during flares, due to the scarcity of observational campaigns or due to the relatively young existence of specialized, sensitive enough detectors. The unprecedented data set presented in this work reveals multiple strong γ-ray flares and a long-term increase in the γ-ray and optical flux baseline of the source over the ten-year period, which results in a linear correlation between these two energy bands over a decade. Typical HBL behaviors were identified in the radio morphology of the source. However, the multi-wavelength data reveal that the source underwent an extreme shift in energy of the synchrotron peak frequency from the IR to soft X-rays; indicating that the source exhibits IBL characteristics during quiescent states and HBL behavior during high states. A two-component synchrotron self-Compton model was used to describe the different flux states of the source. The different methods applied and presented in this manuscript provide a complete and detailed panorama of the intricate nature of blazars, and possibly even challenge our current classification scheme. Moreover, this work provides an illustration of the type of long-term analyses that future

imaging atmospheric instruments, such as the CTA, will allow.

Finally, the appendices provide a brief view of the studies being performed that will be the subject of future publications. The analysis on FSRQs 3C 279 and PKS 1222+216 is mainly focused on their γ-ray emission, to look for a possible imprint of the broad line region in their γ-ray spectra.

2. ACTIVE GALACTIC NUCLEI

"Exceedingly bright; the sharp nucleus shows well in 5^{m} exposure. The brighter central portion is about $0'.5$ in diameter, and the total diameter about $2'$; nearly round. No spiral structure is discernible. A curious straight ray lies in a gap in the nebulosity in p.a. $20°$, apparently connected with the nucleus by a thin line of matter. The ray is brightest at its inner end, which is $11''$ from the nucleus."
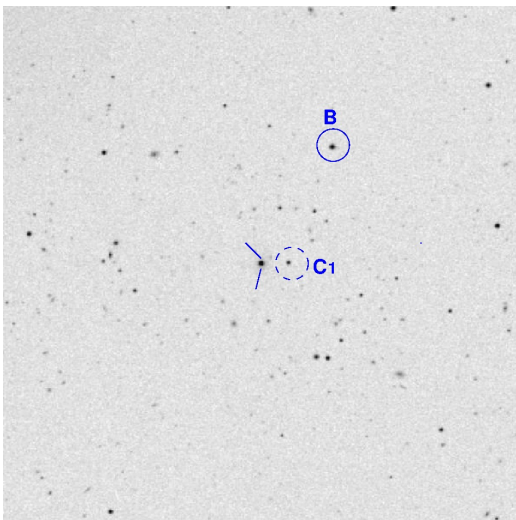
— Curtis (1918), *on M 87*

Fig. 2.1.— Tuorla R-band finding chart in $12'$ FoV (Nilsson et al. 2018) with lines pointing to "quasi-stellar" radio object 1ES 1215+303 at the center. B and C_1 are comparison and control stars respectively.

The term Active Galactic Nucleus (AGN) refers to the existence of energetic phenomena in the central region, or nucleus, of galaxies that cannot be attributed to stars. These kinds of nuclear sources can be brighter than the surrounding forefront stars by a factor of 100 or more. At very large distances, only the nuclear source of these objects is seen, and the light from the host galaxy, because of its small angular size and relative faintness, is outshone by the nucleus.

This chapter provides an overview of the physical properties of AGNs. First, a brief review is provided covering the main scientific contributions from the first reported observation of an AGN, to the main ideas that have shaped our current conventionally accepted concept of AGNs. I then elaborate on the physical mechanisms related to the emission of AGNs before proceeding to describe the different classes and properties of these objects. Since this work focuses on their γ-ray emission, I also dedicate some lines to two of the main γ-ray catalogs of AGNs, The Fourth Catalog of Active Galactic Nuclei detected by the *Fermi* Large Area Telescope (4LAC; The *Fermi*-LAT col-

laboration 2019), and TeVCat [1]. Since the main subject of this manuscript is the radio quasar 1ES 1215+303 ($z = 0.131$), I show a biased selection of sky maps from the literature towards this source, to illustrate the properties mentioned above. For instance, Figures 2.1 and 2.2 show optical and radio maps of this object; where its compactness and radio jet can be visualised at a subarcsecond scale.

2.1.   A Brief History of AGNs

Although not yet known as such at the time, AGNs have been observed since the early twentieth century. Two of the first studies reported the spectroscopic detection of emission lines from the nuclei of spiral galaxies Messier 81 and NGC 1068 by Fath (1909), and the very first observation of the presence of a jet in an astronomical object, Messier 87 (M 87; Curtis 1918). Up until 1943, extensive spectroscopic investigations had revealed the detection of unusual emission lines coming from some galactic nuclei. 1943 saw the publication of Carl Seyfert's pioneering work (Seyfert 1943) on the observation of close-by bright galactic nuclei with unusually broad emission lines. These sources were thereafter known as Seyfert galaxies.

The advent of remarkable developments in radio astronomy (1930 -) played a major role in the understanding of AGNs. Particularly, the third Cambridge Catalogue of Radio Sources (3C, at 159 and 178 MHz; Bennett 1962) listed > 300 radio sources. Most of their sizes ranged between 5 arcsec and a few arcminutes, however, around 10 of them were less than 1 arcsec in size, nearly point-like, resembling very much stars at visible wavelengths. One of these objects was 3C 48, with strong emission lines and variable brightness.

The intriguing emission lines remained a mystery until 1963, when, thanks to the sufficient accuracy in the determination of the position of the compact source 3C 273 (Hazard et al. 1963), an optical counterpart was identified for this source whose spectrum showed the presence of four characteristic emission lines at wavelengths that were displaced from their known locations; indicating that the source had a redshift of $z = 0.158$ (Schmidt 1963). 3C 273 was therefore not one of the billions of stars in our galaxy, but an extremely bright, distant and compact extragalactic object. Brightness fluctuations and a $\approx 20''$-long optical jet had also been observed in this source, an indication of a much more violent environment than what is expected from a star. Later on, a second look at the spectrum of 3C 48 would provide an explanation for its apparent peculiarity, it showed an even larger redshift than originally derived of $z = 0.37$ (Greenstein 1963). At a time when the largest redshifts of galaxies measured was $z \approx 0.2$, this was a major discovery. These objects therefore drew so much attention that this year saw the birth of the 'Texas Symposia', where theoreticians and observers would convene to discuss the implications of these discoveries. Henceforth, these sources were known as "quasi-stellar"

---

[1] `tevcat.in2p3.fr`

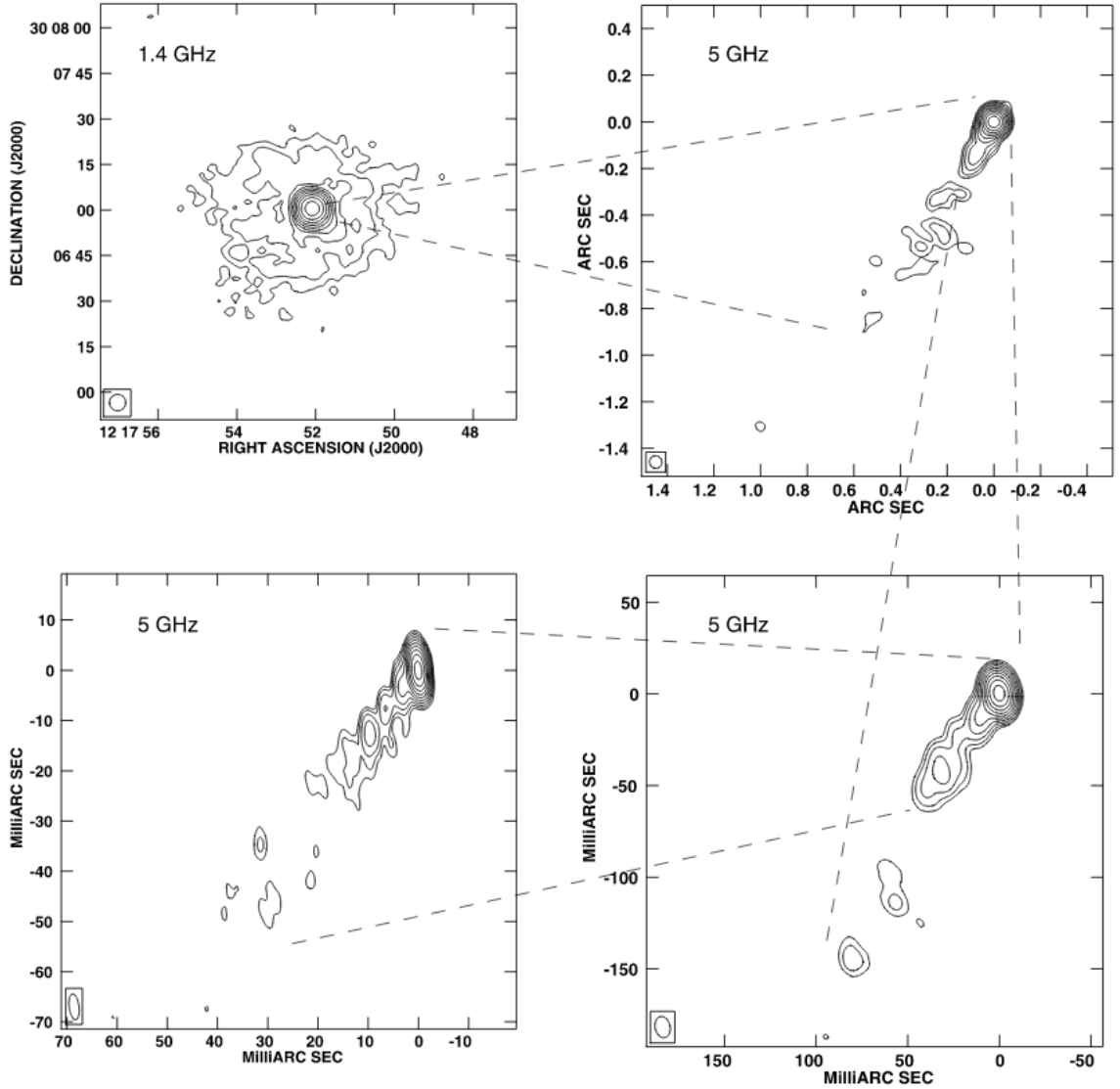objects (QSO) or quasars, regardless of their radio luminosity.

Fig.   2.2.—— Radio images of 1ES 1215+303 taken from Giroletti et al. (2006).   The contours indicate flux density levels of -1, 1, 2, 4, ... times the noise levels. The noise level and restoring beam, clockwise from top left, are 0.45 mJy beam^{-1}, 0.35 mJy beam^{-1} and 55 × 52 mas^2 in position angle (P.A.) 29°, 11.7 × 8.2 mas^2 in P.A. 12°; and 5.2 × 1.9 mas^2 in P.A. 7°.

Two years later, Schmidt (1965) reported on five more radio quasars, including 3C 9 which was found to be at redshift of $z = 2.01$ on the basis of [C IV], and the first detection of the Lyα line, i.e. the Lyman-α line that results from the ultraviolet emission of the electronic transition from level $n = 2$ to $n = 1$ within a hydrogen atom.   The high redshift detections had an important cosmological impact, allowing the amount of neutral hydrogen in the intergalactic space to be tightly constrained (Gunn & Peterson 1965).

By this time, an emitting region of narrow lines had already been well identified, exhibiting an electron density of $N_e = 10^4$ cm^{-3}, a temperature of $\approx 20,000$ K and a

diameter of the order 100 pc from studies of Seyfert galaxies (e.g. Woltjer 1959). The same author postulated a separate region of fast moving and possibly gravitationally bounded gas responsible for the presence of the broad Balmer line wings in these objects. Furthermore, Souffrin (1969) and Williams & Weymann (1968) rejected the hypothesis of ionization and heating produced by fast protons that resulted from collisions of clouds at high velocities, under the argument of thermal equilibrium, which provided the right temperatures, and that ionization by means of thermal collision was inconsistent with the observed temperatures. This led them to the conclusion that the ultraviolet emission was non-thermal and was the only relevant source of ionization, which was later confirmed by detailed computer calculations applied to AGNs and other sources (e.g. Davidson 1972). Later on, Kristian (1973) showed evidence that the QSO phenomenon may occur in galactic nuclei. By 1974, the possible existence of a dense and small region of fast-moving clouds responsible for the emission of broad lines, the so-called *broad line region* (BLR), and a less dense and larger region of slower moving clouds responsible for the emission of narrow lines, i.e. the *narrow line region* (NLR) was strengthened by the photoionization models of Shields (1974). Further constraints on the BLR were achieved thanks to the availability of the reverberation mapping tool, or echo mapping, which makes use of the time delays between the *continuum* (spectrum) and the variations of the lines that may be caused when light travels across the BLR (Blandford & McKee 1982). It was thus shown that the BLR was even denser and smaller than what had been indicated by photoionization models.

In spite of their success, photoionization models faced challenges in the coming years since they could not explain well the observed hydrogen spectral lines ratios (e.g. Wills et al. 1985). During this epoch, Collin-Souffrin et al. (1980) suggested the existence of another high-density ($N_e \sim 10^{11}$ cm^{-3}), Fe II-emitting region not heated by photoionization; possibly the outer part of an extended accretion disk. By this time, the community had already been assuming the presence of a black hole (BH) at the center of QSOs whose masses could be derived with sufficient precision. Early attempts to explain the AGN system included shock waves caused by a supernova that would trigger the explosion of neighboring stars (Burbidge 1961), among others. Hoyle & Fowler (1963a,b) proposed the presence of a supermassive star ($10^5\,M_\odot$ to $10^8\,M_\odot$), allowing the production of large amounts of energy, the acceleration of particles to relativistic energies and the ejection of gas clouds at velocities compatible with the broad emission line wings mentioned above. The same authors claimed the possible presence of a toroidal magnetic field, between the central star and a surrounding disk, storing an energy of $\sim GM^2/R$, whose potential occasional explosion could cause lances or jets such as the one of M 87. Shortly after, the idea of accretion onto a supermassive BH producing the energy observed in QSOs was proposed; e.g., in the model of Salpeter (1964), a turbulent transport of angular momentum would allow matter closer to the hole, causing its mass to grow during the accretion progress. It was Lynden-Bell (1969) who brought to the attention of the community the idea that BHs could be present in galactic nuclei, due to their energy output and prevalence in the early times of the Universe; and that different values of BH mass and accretion rate could provide an explanation for high-energy phenomena ongoing in

these objects, or even the production of cosmic rays.

Lastly, Hoyle et al. (1966) pointed out that relativistic electrons, which emit synchrotron radiation in the IR and optical bands, would also Compton scatter ambient photons thus boosting their energy factors, yielding to a divergence known as the "inverse Compton catastrophe". The authors argued that the rapid loss of energy the electrons would suffer under this conditions supported the idea of a non-cosmological redshift. Later that year, Woltjer (1966) argued that inverse Compton does not contradict the cosmological interpretation of redshifts in QSOs if the electrons were not moving isotropically but in a narrow cone around the magnetic field lines of a radial field. In such a case, electrons would be streaming out of the QSO, and the possibility of relating QSOs to extended radio sources would arise.

2.2.   Radiating phenomena in AGNs

The emission from AGNs can cover the entire electromagnetic spectrum, from radio to γ-rays. AGN emission can be produced by a number of processes. Synchrotron and bremsstrahlung radiation can be modified by scattering, absorption and re-emission. Before continuing with the topic of AGNs, some mechanisms related to the emission of these objects are briefly reviewed in a fairly simplified manner since a thorough development of the complex underlying mechanisms currently considered for AGN modelization is beyond the scope of this manuscript.

2.2.1.   Synchrotron emission

This form of radiation is emitted when charged particles (e.g. relativistic electrons) are accelerated by a magnetic field. According to the Lorentz force, we have:

$$\frac{d}{dt}(\gamma m \mathbf{v}) = \frac{e}{c}(\mathbf{v} \times \mathbf{B}),$$

where $\mathbf{B}$ is the magnetic field, e, m and $\mathbf{v}$ are the charge, rest mass and velocity, respectively, of the particle, in this case the electron; and $\gamma = (1 - \beta^2)^{-1/2}$ its Lorentz factor, where v is the magnitude of $\mathbf{v}$ and $\beta = v/c$. As the acceleration is normal to $\mathbf{v}$ and $\mathbf{B}$, v, γ, $\mathbf{v}_\perp$ and $\mathbf{v}_\parallel$ are thus constant, where the parallel and perpendicular symbols are with respect to $\mathbf{B}$. For isotropically distributed particle velocities, the emitted power, averaged over the pitch, angle is given by

$$P = \frac{4}{3}\,\sigma_T\,c\beta^2\gamma^2 U_B = \frac{4}{3}\,\sigma_T\,\beta^2\frac{E^2}{m^2c^3}U_B, \tag{2.1}$$

where σ_T is the Thomson scattering cross-section[2], $U_B = \frac{B^2}{8\pi}$ is the magnetic field energy

---

[2]This is a special case of Compton scattering (see Section 2.2.2), that occurs when the energy of the

density, and $E = \gamma m c^2$ is the particle energy. The spectrum produced by an electron with energy E peaks at the critical frequency ν_c (e.g. Rybicki & Lightman 1986):

$$\nu_c = \frac{3eB_\perp}{4\pi mc}\left(\frac{E}{mc^2}\right)^2,$$ (2.2)

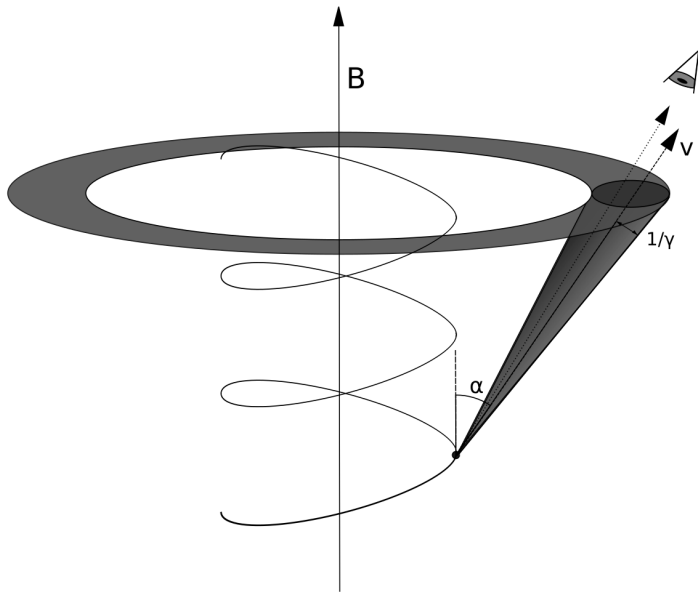where $B_\perp = B\sin(\alpha)$.

Fig. 2.3.— **Helical trajectory of a charged particle in a magnetic field B. If relativistic, the synchrotron radiation is emitted within a narrow cone with opening angle $1/\gamma$, and whose axis is the instantaneous velocity v. The angle between v and B, α, is known as the pitch angle.**

The power in Equation (2.1) is mainly emitted in a narrow cone, as shown in Figure 2.3, within a half opening angle of $\theta \approx 1/\gamma$ (Rybicki & Lightman 1986). Since the emitted power is proportional to $1/m^2$, the synchrotron radiation from electrons (or positrons) from an electrically neutral plasma should therefore be dominant over that from protons or heavier particles at the same energy as the electrons.

Synchrotron loss time (cooling)

A radiating electron cools down, that is, loses energy at the rate $dE/dt = -P$. The time scale for the particle to lose half its energy, in a constant magnetic field, is thus given by

$$t_{1/2} = \frac{3m^2c^3}{4\sigma_T U_B \beta^2 E_i},$$ (2.3)

incident photon is considerably smaller than the rest-mass energy of the electron. In such a case, the total cross-section is given by $\sigma_T = \frac{8\pi r_0^2}{3}$, where $r_0 = \frac{e^2}{mc^2}$.

where E_i is the particle initial energy. For instance, an electron with $\gamma_i = 10^3$ in a magnetic field $B = 10^{-2}$ G, would take $\approx 10^2$ years to lose half its energy.

Synchrotron emission from an ensemble of electrons

The power emitted by an ensemble of electrons with energies in the range (E_i, E_f) as a function of the frequency of the emitted radiation is given by

$$P(\nu) = \int_{E_i}^{E_f} P(E, \nu) n(E) dE,$$

where $n(E)dE$ is the number density of particles with energies in $(E, E + dE)$. Often, spectra from emission regions which are transparent to the radiation are of the power-law form $P(\nu) \propto \nu^{-\alpha}$, where α is known as the photon index. This shape is naturally produced if the radiating particles have a power-law distribution of energy (e.g. Rybicki & Lightman 1986), i.e.

$$n(E)dE = CE^{-p}dE, \tag{2.4}$$

where p is the particle index and C is a constant; in which case the emitted spectrum has power-law form

$$P(\nu) \propto B^{(p+1)/2}\nu^{-(p-1)/2} \qquad \text{or} \qquad P(\nu) \propto \nu^{-\Gamma}, \text{ with } \quad \Gamma = \frac{p-1}{2}. \tag{2.5}$$

It should be pointed out that the power-law approximation is valid for values of ν in the range (ν_i, ν_f) and far from the boundaries within this range, where ν_i and ν_f are the critical frequencies corresponding to E_i and E_f respectively. Furthermore, the energy density u_e and pressure p_e due to the electrons is given by

$$u_e = \int_{E_i}^{E_f} n(E)E dE = \frac{C}{2-p}\left(E_f^{2-p} - E_i^{2-p}\right), \quad p_e = \frac{u_e}{3}, \quad \text{for } p \neq 2 \tag{2.6}$$

This integral reduces to $\log(E_f/E_i)$ for $p = 2$.

Polarization of the synchrotron emission

The synchrotron emission from a single electron is elliptically polarized (Westfold 1959). The observed elliptical polarization depends on the angle between $\mathbf{v}$ and the line of sight, let us call this angle ψ. From Figure 2.3, this polarization would be linear for $\psi = 0$. For other values of ψ, the radiation is only partially linearly polarized. For an electron energy distribution as in Equation (2.4), the degree of polarization is given by

$$\Pi(\nu) = \frac{3p+3}{3p+7}. \tag{2.7}$$

It therefore does not depend on the frequency but only on the particle index. See Kembhavi & Narlikar (1999) for a more elaborated description.

Absorption of synchrotron radiation

A spectral shape such as the one in Equation (2.5) is observed only if there is no absorption of photons by the emitting region or by background radiation field or by the galaxy hosting the AGN, or by some other form of intervening galaxy, like other galaxies such as the Milky Way. The spectra from optically thin emission regions can sometimes show low-frequency absorption features due to thermal absorption by the galactic interstellar medium (ISM). For instance, in the presence of a magnetic field, electrons can absorb photons and get excited to higher energy states ; and absorbed photons, on the other hand, can stimulate the emission of photons with the same energies as the incident ones. This process is called synchrotron self-absorption.

Another possible process occurs when an electron absorbs a photon, causing it to accelerate in the field of an ion through bremsstrahlung. This process is called thermal bremsstrahlung absorption when the charged particles involved have a thermal distribution (e.g. Rybicki & Lightman 1986).
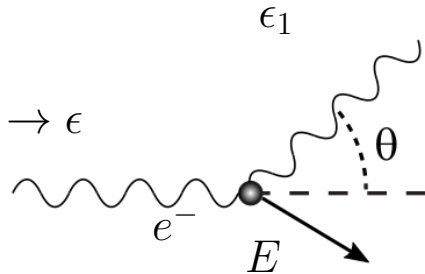
2.2.2. Compton scattering

Fig. 2.4.— **An incident photon with energy ϵ is scattered by an electron at its rest-mass frame. The scattered photon has an energy of ϵ_1, while the electron obtains an energy E.**

This term refers to the scattering of photons by electrons. More specifically, the exact term refers to the case in which the electron that scatters the photon gains energy from the event to satisfy momentum conservation, there is thus a decrease in the photon energy, i.e. $\epsilon_1 < \epsilon$ in Figure 2.4, where ϵ and ϵ_1 are the energies of the incident and scattered photons respectively. From four-momentum conservation it can be demonstrated that

$$\epsilon_1 = \frac{\epsilon}{1 + \frac{\epsilon}{mc^2}(1 - \cos\theta)}, \qquad (2.8)$$

where θ is the angle between the directions of the incident photon and that of the scattered one, see Figure 2.4.

The total cross-section for Compton scattering of unpolarized radiation is given by

$$\sigma_{\mathrm{KN}} = \frac{3\sigma_T}{4} \left\{ \frac{1+x}{x^3} \left[\frac{2x(1+x)}{1+2x} - \ln(1+2x) \right] + \frac{\ln(1+2x)}{2x} - \frac{1+3x}{(1+2x)^2} \right\}, \text{ with } x = \frac{\epsilon}{mc^2}, \tag{2.9}$$

where KN stands for Klein-Nishina, in honor to the scientists who first obtained it. The special case with $x \ll 1$ is known as the Thomson scattering, where $\epsilon = \epsilon_1$ is obtained, thus the Klein-Nishina cross-section converges to the Thomson cross-section.

Inverse Compton scattering

The particular case in which the scattered photon gains energy, $\epsilon_1 > \epsilon$ in Figure 2.4, is known as inverse Compton scattering (ICS or IC). Let us discuss the cases of the two energy limits taking place in the ICS, for a detailed description of this process see Rybicki & Lightman (1986). Let S be the laboratory frame where the electron moves with a Lorentz factor γ, and S' the electron rest-mass frame. Thus, the energy of the incident photon, ϵ', in S' is given by

$$\epsilon' = \gamma\epsilon(1 - \beta \cos(\theta)). \qquad (2.10)$$

If $\epsilon' \ll mc^2$, i.e. Thomson scattering would be taking place in S', then $\epsilon'_1 = \epsilon'$. Transforming back to S, using Equation (2.10), we obtain $\epsilon_1 \approx \gamma^2\epsilon$, where γ can be large for a highly relativistic electron. Needless to say, the energy gained by the scattered photon cannot be greater than γmc^2 due to energy conservation. In the case when $\epsilon' = \gamma\epsilon \gg mc^2$, known as the extreme Klein-Nishina limit, from Equation (2.8), it follows that $\epsilon'_1 \approx mc^2$, i.e. is comparable with the electron energy.

Thus, in the case of Thomson scattering, the region in which the interaction takes place becomes a source of high-energy emission. Let us focus now on the emission from an optically thin region, which means that the photons undergo a single scattering before emerging from this region. Again, in the case of Thomson scattering of photons with number density $n(\epsilon)$ in S, the number of photons in the range $(\epsilon', \epsilon' + d\epsilon')$' in S', per unit time scattered by the electron is $c\sigma_T n'(\epsilon')d\epsilon'$; and the power carried by them would be

$$P'_{\text{scat}}(\epsilon'_1) = c\sigma_T \int \epsilon'_1 n'(\epsilon')d\epsilon' \Rightarrow P_{\text{scat}}(\epsilon) = c\sigma_T\gamma^2 \int (1 - \beta \cos(\theta))^2 \epsilon n(\epsilon)d\epsilon,$$

since both $n'(\epsilon')d\epsilon'/\epsilon'$ and the power are relativistically invariant (e.g. Rybicki & Lightman 1986), $\epsilon'_1 \approx \epsilon'$ and Equation (2.10) was used. Assuming an isotropic distribution of incident photons of the form $p(\theta)d\theta = \frac{1}{2}\sin(\theta)d\theta$ with $\theta \in [0, \pi]$, and integrating over θ we obtain $P_{\text{scat}}(\epsilon) = \left(1 + \frac{4}{3}\gamma^2\beta^2\right)c\sigma_T U_{\text{ph}}$, with $U_{\text{ph}} = \int \epsilon n(\epsilon)d\epsilon$. Since the incident energy per unit time on the electron is $c\sigma_T U_{\text{ph}}$, the Compton power, the rate of the net energy output is given by

$$P_{\text{Comp}} = \frac{4}{3}\sigma_T c\beta^2\gamma^2 U_{\text{ph}}. \qquad (2.11)$$

For a general calculation of the power, outside the Compton approximation, see Blumenthal & Gould (1970). The Compton power in Equation (2.11) is similar to the synchrotron power, Equation (2.1), since the synchrotron process can be equivalently taken to come from the scattering of virtual photons of the magnetic field by an electron. The ratio of the powers of electrons emitting in both synchrotron and Compton is

$$\frac{P_{\text{Comp}}}{P_{\text{sync}}} = \frac{U_{\text{ph}}}{U_B}. \qquad (2.12)$$

Blumenthal & Gould (1970) also derive the spectra of the Compton emission from an electron with a power-law energy distribution to be $P_{\text{Comp}}(\epsilon_1) \propto \epsilon_1^{-(p-1)/2}$ in the Thomson

approximation, similar to the spectrum obtained for the synchrotron case since in both processes the scattered photon energy is proportional to γ^2. Outside the Thomson limit though the spectrum has the shape $P_{\text{Comp}}(\epsilon_1) \propto \epsilon_1^{-(p+2)}$, significantly steeper than that obtained in the Thomson approximation.

Synchrotron self-Compton emission

Synchrotron photons emitted by relativistic electrons can undergo inverse Compton scattering from the same set of electrons. During this process, as seen before, the energy of the scattered photon can be incremented by a factor of γ^2, where γ is the electron Lorentz factor. This process is known as the synchrotron self-Compton (SSC) emission, and is important when the emission region is compact. For instance, depending on the value of γ, radio to IR photons could be scattered to X-ray or γ-ray energies, which could explain the high-energy emission observed in AGNs. Therefore, a relationship between the self-absorbed radio emission and IC emission should be expected, however, this relationship depends on the geometry of the emission regions, the physical parameters and the relativistic bulk motion. A model that makes use of this kind of process is discussed and applied in Chapter 5.

2.2.3.   Electron spectrum

Relativistic electrons moving in a magnetic field may lose their energy by all of the mechanisms discussed above, for instance, synchrotron emission, inverse Compton scattering of the synchrotron photons (i.e. SSC). In some cases, the Thomson limit is applicable in the electron rest-mass frame, as seen in Section 2.2.2, where only a small fraction of the electron energy is lost in the emission of a single photon. In cases like this, the time evolution of the electron density can be derived by defining small energy bins $(E, E+dE)$ and counting the density of electrons gained or lost in a small interval of time. Electrons can be lost and gained from this interval in the process of radiation, or exclusively gained from external injections or by re-accelerations caused by perturbations in the magnetic field. These possible changes are expressed in the following partial differential equation

$$\frac{\partial n(E,t)}{\partial t} = -\frac{\partial}{\partial E}\left[\frac{dE}{dt}n(E,t)\right] + q(E,t), \tag{2.13}$$

where $q(E,t)$ is the electron injection rate per unit volume. If the number density of electrons is not constant across the volume of the source, electrons will be lost and gained from a volume element due to diffusion. To account for this effect, the term $D\nabla^2 n$, where D is the diffusion coefficient, needs to be added to the right-hand side of Equation (2.13). The expression in the Klein-Nishina limit or bremsstrahlung emission are more complex and require an integro-differential equation. See Blumenthal & Gould (1970) for a detailed description.

In order to consider a few simple solutions of Equation (2.13), let us first briefly

discuss the term dE/dt. From Equations (2.1) and (2.11), it can be noted that electrons spiralling in a magnetic field lose their energy at a rate $dE/dt \propto E^2$, by either synchrotron emission or IC scattering of synchrotron photons (i.e. SSC) and other ambient radiation. In the case of bremsstrahlung or adiabatic expansion of the source, the electron energy decreases at a rate $dE/dt \propto E$. Another process causing energy loss is the ionization of atoms and molecules in the plasma. In this case, dE/dt depends logarithmically on the energy and can be approximated to a constant. Therefore, the net energy loss rate would be given by:

$$\frac{dE}{dt} = a_0 + b_0 E + c_0 E^2, \qquad \text{where } a_0,\ b_0,\ c_0 \text{ are constants.} \qquad (2.14)$$

Hence, if we consider electrons with an initial power-law spectrum, the more energetic electrons will lose their energy more rapidly and the spectrum is thus distorted from its initial power law.

Let us now go back to Equation (2.13) and consider the case of a continuous injection of electrons at a constant rate $q(E)$. If an equilibrium between the injection and energy loss is reached, then $\partial n/\partial t = 0$ and:

$$n(E) = \left(\frac{1}{a_0 + b_0 E + c_0 E^2} \right) \int_E^{\inf} q(E')dE'.$$

From this equation, in the case when the energy loss is restricted to synchrotron or IC processes only (i.e. $a_0 = b_0 = 0$) and the injection is at a single energy E_0:

$$q(E) = \delta(E - E_0) \Rightarrow n(E) \propto E^{-2}, \qquad E \leq E_0,$$
$$n(E) \propto 0, \qquad E > E_0.$$

On the other hand, if $q(E) \propto E^{-p_0} \Rightarrow n(E) \propto E^{-(p_0+1)}$, for $p_0 > 1$. From Equation (2.5), this means that the spectral index of the synchrotron radiation is steepened by $1/2$. For $p_0 < 0$ the integration needs to be cut off at a $E_{\max} \gg E$, resulting again in a number density of $n(E) \propto E^{-2}$.

2.2.4. Hadronic Emission

Synchrotron radiation can also be produced by cosmic-ray protons or ions in the blazar jet, something that requires highly magnetized jets (Mücke et al. 2003; Aharonian 2002). The radiation is then produced in the GeV-TeV energy range, at much higher energy than for leptons. In the case of a varying source, no correlation is expected with the variations at lower energies such as in the optical band of the source (Dermer & Giebels 2016).

Hadronic interaction can also generate γ-ray through the production of π^0 mesons that later decay into two photons or photo-lepton cascades, for the charged pions.

Some examples of hadronic models include the recent work of Cerruti et al. (2015). By using a lepto-hadronic model that includes lepton and hadron synchrotron and photo-hadronic processes, the authors explained the weakly very high energy (VHE) variability of a few high-synchrotron-peaked BL Lac objects as due to the long timescale needed for hadronic cooling processes. The connection of the production of PeV neutrinos with the spectral properties of ultra-high-energy cosmic ray blazar candidates was also made by Petropoulou et al. (2015).

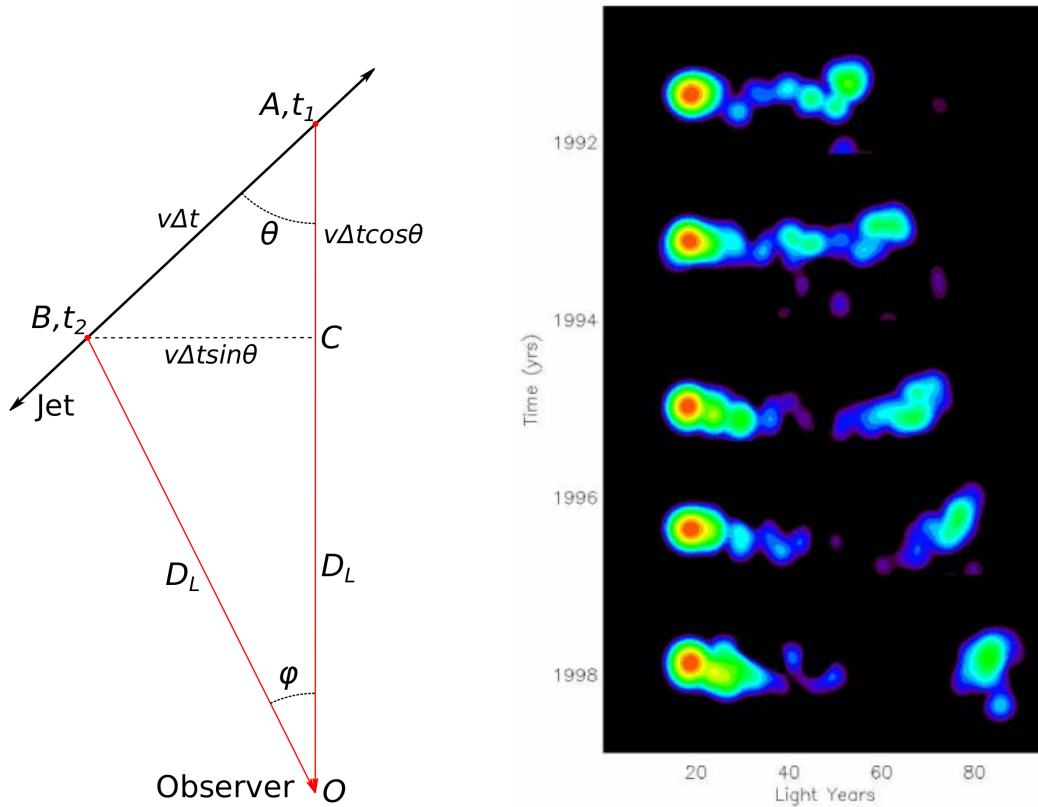## 2.2.5.   Relativistic bulk motion

Superluminal motion

Fig. 2.5.— *Left:* **A bulk of matter consisting of radiating particles moves with speed v, from points A to B. Light rays are emitted from A and B towards the observer at O.** *Right:* **Apparently superluminal motion of the radio features in the flat spectrum radio quasar 3C 279. The left-hand-side component represents the fixed radio core, while the right-hand-side bright feature appears to have moved 25 light years on the plane of the sky from 1991 to 1998 (image credit to the NRAO's Charlottesville, Virginia).**

The advent of the very large baseline interferometry (VLBI) radio campaign in the late 1960s made possible the observation of radio structures in AGNs at the milliarcsecond (mas) angular scale. These structures, referred to as *radio components*, were sometimes seen to move at speeds seeming to exceed that of light in vacuum (Rees 1966). In the

case of AGNs, these components are often located within the plasma jet.

To elucidate this effect, we consider a bulk of matter moving from point $A(t = t_1)$ to $B(t = t_2 = t_1 + \Delta t)$ on the left-hand-side of Figure 2.5, where it also emits light rays that reach the observer O at times t'_1 and t'_2 respectively. For small angles ϕ, the distances labeled as D_L are approximately equal. Then, working out the distances:

$$ct'_1 = ct_1 + D_L + v\Delta t \,\cos(\theta)$$
$$ct'_2 = ct_2 + D_L$$
$$\Rightarrow \Delta t' = (1 - \beta \,\cos(\theta))\,\Delta t.$$

It should be pointed out that the observer is able to see only the component of the motion normal to the line of sight, i.e. $\overline{BC}$ on the left-hand-side of Figure 2.5. Thus

$$\beta_\perp = \frac{\overline{BC}}{c\Delta t'} = \frac{\beta \,\sin(\theta)}{1 - \beta \,\cos(\theta)}. \tag{2.15}$$

The maximum value of $\beta_\perp$ is $\beta_{\perp\,\mathrm{max}} = \beta\gamma$ and is reached for values of θ such that $\sin(\theta_{\mathrm{max}}) = 1/\gamma$. Then, for small values of θ, $\sin(\theta_{\mathrm{max}}) \approx \theta_{\mathrm{max}} = 1/\gamma$. Thus, for sufficiently large values of γ, apparent superluminal motion can be reached.

Flux amplification and variability

From Rybicki & Lightman (1986), the photon flux observed from a bulk of radiating particles moving at relativistic speed can be significantly higher when the source is moving towards the observer, and considerably smaller when the source moves away from the observer. By this process, features that would be otherwise symmetric, such as a two-sided jet, can appear to be one-sided. For a source of radiation moving towards the observer, with ν and ν' as the frequencies seen by the observer and at the rest frame respectively, z the redshift, and δ as the Doppler boosting,

$$\delta = \frac{1}{\gamma(1 - \beta \,\cos(\theta))}, \tag{2.16}$$

the following transformations apply for the frequency, intensity and flux respectively,

$$\nu = \frac{\delta\nu'}{1 + z}, \tag{2.17}$$

$$F(\nu) = \left(\frac{\delta}{1 + z}\right)^{3+\Gamma} F'(\nu), \quad \text{with } F(\nu) \propto I(\nu) \text{ and } F(\nu) \propto \nu^{-\Gamma}. \tag{2.18}$$

The intrinsic luminosity can be calculated from the observed flux using the following expression

$$L'(\nu') = \left(\frac{\delta}{1 + z}\right)^{-(3+\Gamma)} \frac{4\pi D_L^2}{1 + z} F(\nu), \tag{2.19}$$

where D_L is the luminosity distance of the source.

Now let us consider a source in which the flux density changes over a time $\approx \Delta t_{\mathrm{var}}$. The usual argument is to relate the variability time to the emission region size by $\approx c\Delta t_{\mathrm{var}}$. Since in the rest frame $\Delta t'_{\mathrm{var}} = \frac{\delta}{1+z}\Delta t_{\mathrm{var}}$, then the size of the emission region R is

$$R \leq \frac{c\delta}{1+z}\Delta t_{\mathrm{var}}. \tag{2.20}$$

2.2.6.   Particle acceleration mechanisms

The production of γ-ray photons in the universe is believed to require the presence of relativistic charged particles, i.e. cosmic rays, of high energies (electrons, positrons, hadrons as discussed above), which have been so far measured up to 10^{21} eV. These particles are thought to exist in the form of magnetized plasma within extreme astrophysical environments. Blandford & Znajek (1977) showed that an electric potential difference is induced when a rotating black hole is threaded by magnetic field lines supported by external currents flowing in a surrounding disc. For sufficiently large field strength, the vacuum experiences instabilities to cascade production of e^-e^+ pairs, thus establishing a surrounding force-free magnetosphere. They argued that this model applied to AGNs allows the acceleration of relativistic electrons at large distances from the hole without incurring serious losses. A few years later, Blandford & Payne (1982) demonstrated that a magnetically focused jet outflow can be established through a mechanism they proposed for the evolution of accretion disks around the massive BH in AGNs. They showed that, if the poloidal component of the magnetic field makes an angle smaller than $60°$ with the disk surface, the formation of a centrifugally driven outflow of matter from the accretion disk is possible. The toroidal component of the magnetic field, on the other hand, becomes important at large distances, collimating the outflow into a pair of anti-parallel jets perpendicular to the disk; whereas while the disk the flow could be driven by gas pressure in a hot magnetically dominated corona. The jet solutions they proposed have in common that most of their power is concentrated within a central core, whereas most of the angular momentum and magnetic flux is carried close to the jet walls. Event though this mechanism is of crucial importance for BH, and therefore AGNs, it can also be applied, for instance, to stellar mass objects such as those with central neutron stars, or it might cause jet precession.

Another acceleration mechanism is the one known as shock acceleration, in which physical properties such as pressure, velocity and temperature are nearly discontinuous from one side to the other of the shock front that separates the shocked and unshocked material. This process is usually considered to take place in a low density medium (i.e. Coulomb collisions of particles are negligible). Instead, particles gain through collisions with massive magnetic clouds when they cross the front shock. This mechanism is known as first-order Fermi acceleration (Fermi I; Fermi 1949). The particle distribution in this diffusive shock acceleration process satisfies the Vlasov equation, which is the simplified

version of the Fokker-Planck equation without collision, and includes terms describing diffusion, compression, advection, energy loss, injection and escape. A particle gains energy by a factor of the Lorentz factor of the shock to the power of 2 in the first shock crossing in average; and by a factor of ≈ 2 in the subsequent ones (Gallant & Achterberg 1999). The acceleration timescale in the comoving frame, assuming the mean free path of the particle is equal to it gyroradius, is given by:

$$t_{\text{Fermi I}} = 3.4 \left(\frac{\gamma}{10^4} \right) \left(\frac{B}{1\text{G}} \right)^{-1} \beta_s^{-2} \text{ ms},$$

where β_s is the speed of the shock (Tammi & Duffy 2009). Another type of shock acceleration is the second-order Fermi acceleration (Fermi II), particles are stochastically scattered by random magnetic fields (Tammi & Duffy 2009), which becomes important when the shock speed is almost as low as the Alfvén speed, so diffusion in momentum space dominates. The timescale in this case depends on the particle number density and the strength of the magnetic field; and it is much faster to accelerate particles via Fermi II than via Fermi I. For instance, The acceleration may be fast for AGN jets where there is low density plasma and strong magnetic fields.

A third form of acceleration mechanism is known as magnetic reconnection (Yamada et al. 2010). It is an abrupt change from a high magnetic energy field structure to a lower magnetic energy one. It is believed to occur in, e.g., AGNs, GRBs, star formation, during solar flares or coronal mass ejection. Magnetic fields are attached to the plasma in highly conductive environments where the assumption of ideal magnetohydrodynamics is valid. Magnetic reconnection occurs when particles get unattached in a small region due to the convection of magnetic field lines that have opposite directions and a particle inflow. Then, localized magnetic islands are formed and the magnetic energy is converted into plasma kinetic energy (Drake et al. 2006), e.g. through Fermi I where particles bounce within and between magnetic islands.

2.3. Active Galactic Nuclei Classification

AGNs are galaxies with extremely luminous ($L_{\text{bol}} \approx 10^{43}$–$10^{48}$ erg s^{-1}) cores powered by accretion onto super massive black holes (SMBHs, $\sim 10^9 \, M_\odot$). Possibly, nearly 1% of all galaxies can be categorized as having an active nucleus[3] (Padovani 1998), exhibiting a very characteristic spectral energy distribution (SED, see Figure 2.7). AGNs can be visible at redshifts as high as $z = 7.1$ (Mortlock et al. 2011), which would mean that the SMBH was formed within 1 Gyr of cosmic time. In some cases, AGNs release energy in the form of relativistic plasma jets, which can be detected with current detectors across

---

[3]It is believed that all galaxies went through a period of intense activity at the time of formation of the core and BH. Indeed, at distant redshifts the percentage of galaxies that are classified as being active increases.

the entire electromagnetic spectrum. *It is not yet known how these jets form, of what particles they are composed of or how they accelerate particles*, even though models trying to explain the mechanism have been around almost since the AGN class was established (e.g. Blandford & Znajek 1977).
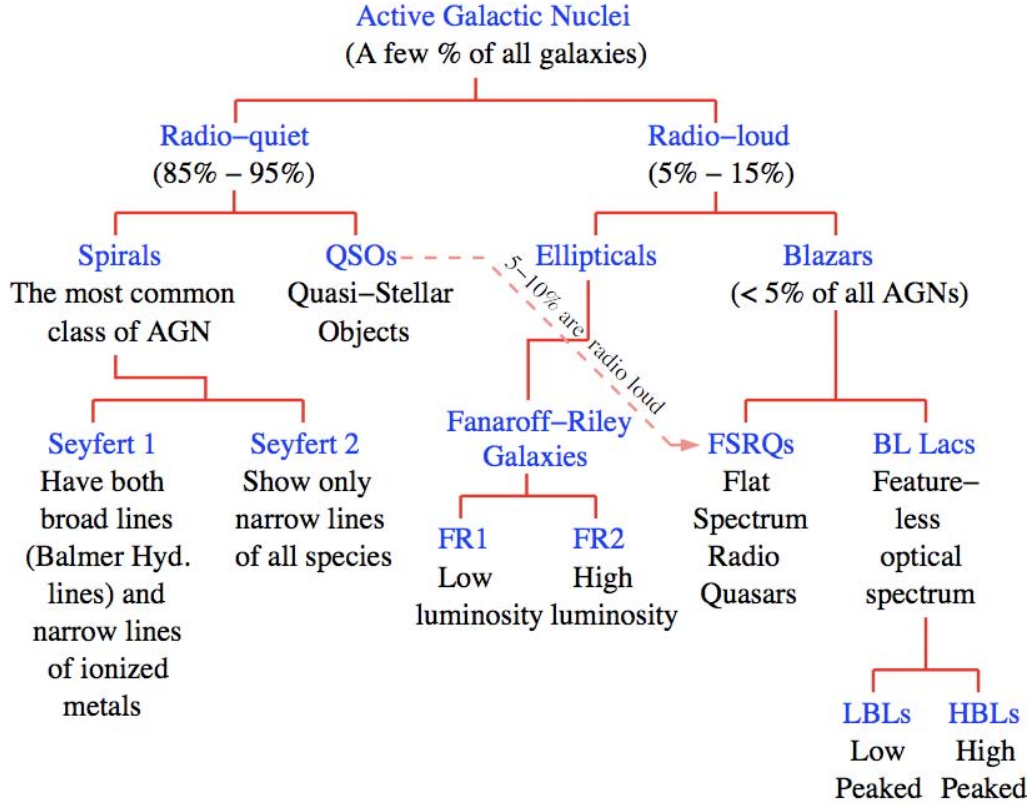

Fig. 2.6.— **Classification chart of active galactic nuclei. Courtesy of D. Horan.**

AGNs are classified in terms of their orientation, accretion rate, the presence of plasma jets and even according to their host galaxy. The subclassification of AGN according to their so-called radio loudness has been one of the most utilised classifications to this day. Padovani et al. (2017) emphasize that the distinction should be made in that most of the energy emitted by radio loud AGNs is of non-thermal origin and is related to the presence of relativistic jets; whereas the radio quiet AGNs emission is mainly of thermal origin and is in relation to the accretion disk. The difference between radio-loud and radio-quiet depends on the presence or absence of radio-emitting jets powered by the central nucleus, which in turn may be induced by the rotation of the black hole. We observe that at high accretion rates and large luminosities, both types of AGNs have dusty tori, broad-line regions, narrow-line regions, and big strong blue/UV bump emissions. Broad-line region clouds illuminated by the accretion-disk are obscured in Seyfert2 AGN when viewing through the dusty torus, thus only narrow lines from high altitude far from the BH are seen. Figures 2.6 and 2.7 provide a panorama of the current AGN classification scheme.
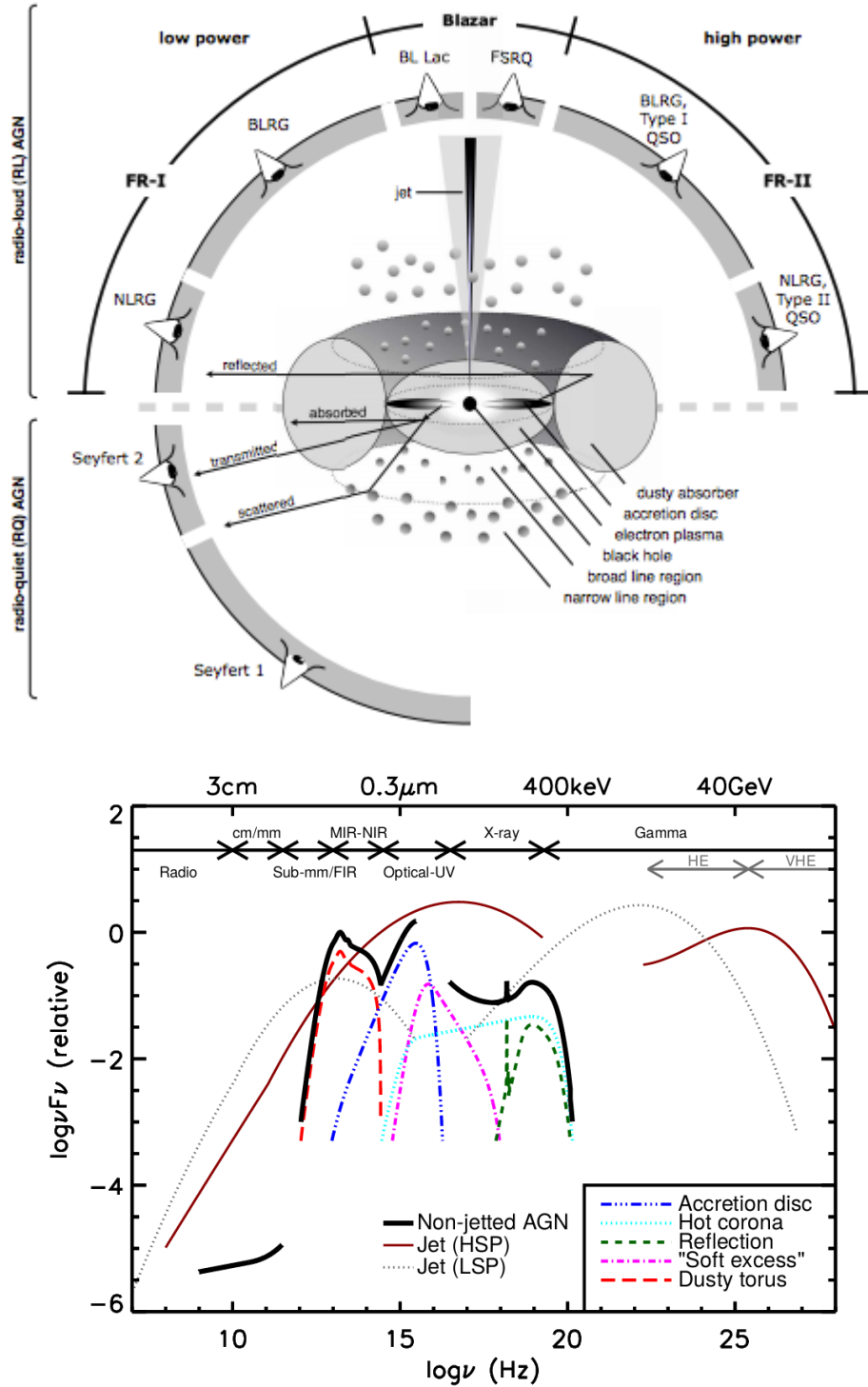
Fig. 2.7.— *Top:* Schematic diagram showing that the classification of AGNs depends critically on the orientation of the accretion disk axis with respect to our direction of view from Earth. AGN structure according to Beckmann & Shrader (2012). *Bottom:* Typical SED shapes of different types of AGNs. The addition of the AGN components (in colored dashed lines, accretion disk, dusty torus, hot corona) is shown in solid black. In the Padovani et al. (2017) nomenclature, "jetted" refers to radio loud AGNs and "non-jetted" to radio quiet AGNs. LSP and HSP refer to Low- and High-synchrotron-peaked blazars, the dominant γ-ray population of the sky (see text). The "double hump" structure is characteristic of the blazar class, the low energy corresponding to synchrotron emission, and the high-energy one currently interpreted as having leptonic or hadronic origins. From Padovani et al. (2017).
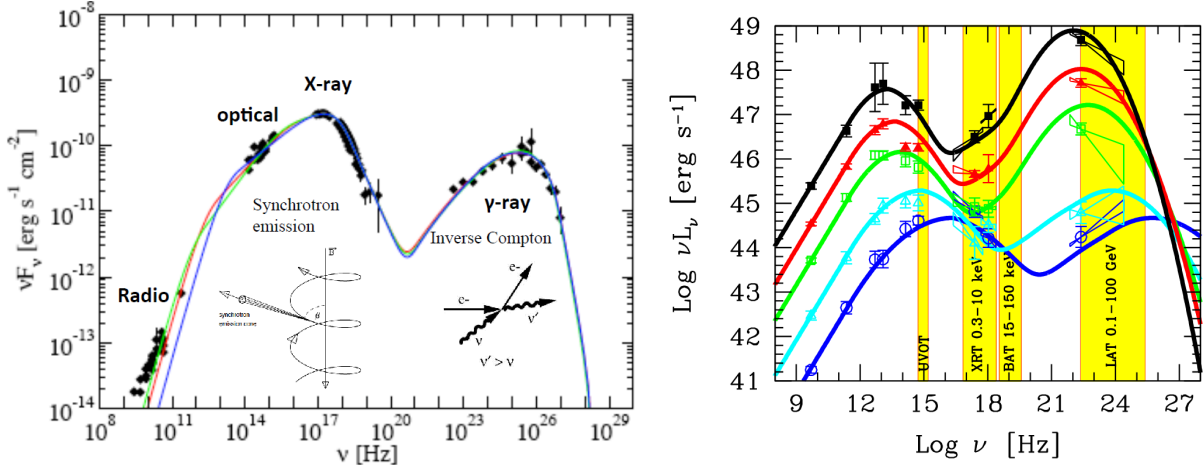
2.3.1. Blazars

Fig. 2.8.— *Left:* **Broadband SED of the blazar Mrk 421. The first hump is modeled with synchrotron emission, whereas the second one is modeled with synchrotron self-Compton processes. From Abdo et al. (2011a).** *Right:* **Blazar sequence, from (Ghisellini 2015).**

Blazars are AGNs with flat radio spectra (i.e. with photon indices $\alpha < 0.5$, as in $S_\nu \propto \nu^{-\alpha}$), whose jets happen to be oriented closely to our line of sight ($\lesssim 20°$); and that are possibly hosted by giant elliptical galaxies (Falomo et al. 2000). In spite of being very rare objects, orders of magnitude less abundant than non-jetted AGN of the same optical magnitude, the blazar population dominates the bright radio (e.g. Padovani 2016; Kuehr et al. 1981) and γ-ray wavelengths; *exhibiting highly-variable behavior that is not necessarily correlated at all wavelengths, which challenges current theoretical models.* Their intense non-thermal emission and remarkably special geometrical conditions make blazars the perfect candidates to reach the most extreme parts of the electromagnetic spectrum, where particles are accelerated to the highest energies.

The SED of blazars ($\nu f(\nu)$ vs. ν) is characterized by two broad, non-thermal radiation components, or a "double hump" shape. The first component is generally agreed to be due to synchrotron emission, which is corroborated by variable polarization data (Lister et al. 2018; Blinov et al. 2016).

The origin of the high-energy component, however, remains to this day a matter of debate. A number of models exist to explain the origin of this second hump. They can be broadly divided into two categories depending on the nature of the accelerated particles, namely, leptonic (dominated by electrons, positrons) or hadronic (dominated by ultrarelativistic protons). In leptonic scenarios the emission is conventionally interpreted as inverse Compton scattering by electrons with their own synchrotron emission (henceforth synchrotron self-Compton, SSC), with the jet emission or with an external source of photons (external inverse Compton, EIC) coming from the accretion disk, broad line region (BLR) or the dusty torus, (see the AGN structure on the right-hand side of Figure 2.7). Hadronic scenarios are based on protons losing energy through synchrotron emission

or through photo-pion production, followed by pion decay into high-energy photons and pairs; it is also possible that neutrinos could be emitted from the decay of charged pions. Recently, IceCube reported the *detection of high-energy astrophysical neutrinos possibly coming from a blazar* while it was undergoing a relatively high state in γ-rays (IceCube Collaboration et al. 2018a,b). Of the two types of models, hadronic scenarios predict a significantly higher degree of polarization (Zhang et al. 2016).
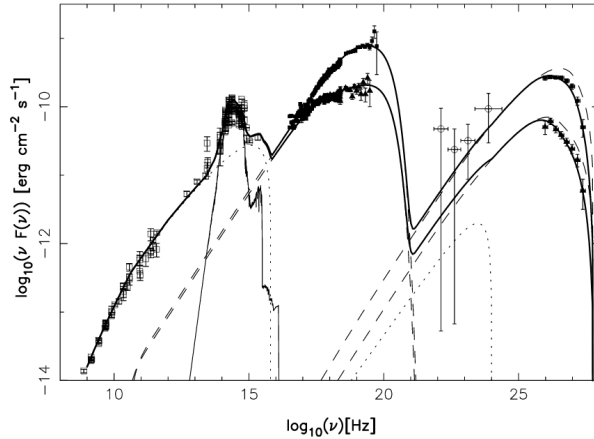

Fig. 2.9.—— Broadband distribution of Mrk 501 exhibiting a high activity during 1997 April 7 (triangles) and 16 (squares). Notice the harder VHE spectrum during the brighter state of April 16. The thick solid lines represent multi-wavelength modeling of the emission from the source for the two different states of activity. The dashed lines indicate SSC emission, while the dotted lines represent the contribution from the conical jet. The thin solid lines indicate the emission from the host galaxy. From Katarzyński et al. (2001a).

Blazars are further divided into two sub-classes, the flat spectrum radio quasars (FSRQ) characterized by strong broad emission lines ($> 5\,\text{Å}$), and BL Lacertae objects (or BL Lacs) which show weak emission or absorption lines or exhibit no such spectral features at all, making it difficult to spectroscopically establish their redshift. Another type of subclassification consists in splitting the blazar class according to the position of the synchrotron peak frequency (ν_{sy}), that is, the frequency of the peak emission of the first SED hump. Blazars with $\nu_{\text{sy}} \leqslant 10^{14}$ Hz are referred to as low-synchrotron-peaked (LSP), and they include FSRQs and low-frequency- peaked BL Lac objects[4] (LBLs). Intermediate-synchrotron-peaked (ISP), with 10^{14} Hz $\leqslant \nu_{\text{sy}} \leqslant 10^{15}$ Hz, include LBLs and intermediate-frequency-peaked BL Lac objects (IBLs). High-synchrotron-peaked BL Lac (HSP) objects have their 10^{15} Hz$\leqslant \nu_{\text{sy}}$ and are almost all high-frequency-peaked BL Lac objects (HBLs). Low-luminosity Fanaroff-Riley 1 (FR1) radio galaxies are the possible parent population of BL Lac objects (Dermer & Giebels 2016). They do not show significant emission from accretion disk, broad lines or dusty torus. Flat Spectrum Radio Quasars (FSRQ), with radio spectral index ~ 0 at a few GHz, correspond to jets of higher luminosity Fanaroff-Riley 2 (FR2) radio galaxies (Padovani et al. 2017). The presence of accretion-disk radiation and dense BLR material is an indication of a FSRQ also having strong broad optical lines.

The SEDs of blazars are seen to be inversely correlated with their luminosity. For instance, the synchrotron and Compton humps of BL Lacs peak at higher frequencies than

---

[4]As defined on an earlier classification scheme by Padovani & Giommi (1995) based on the ratio of the flux at 5 GHz to that at 1 keV.
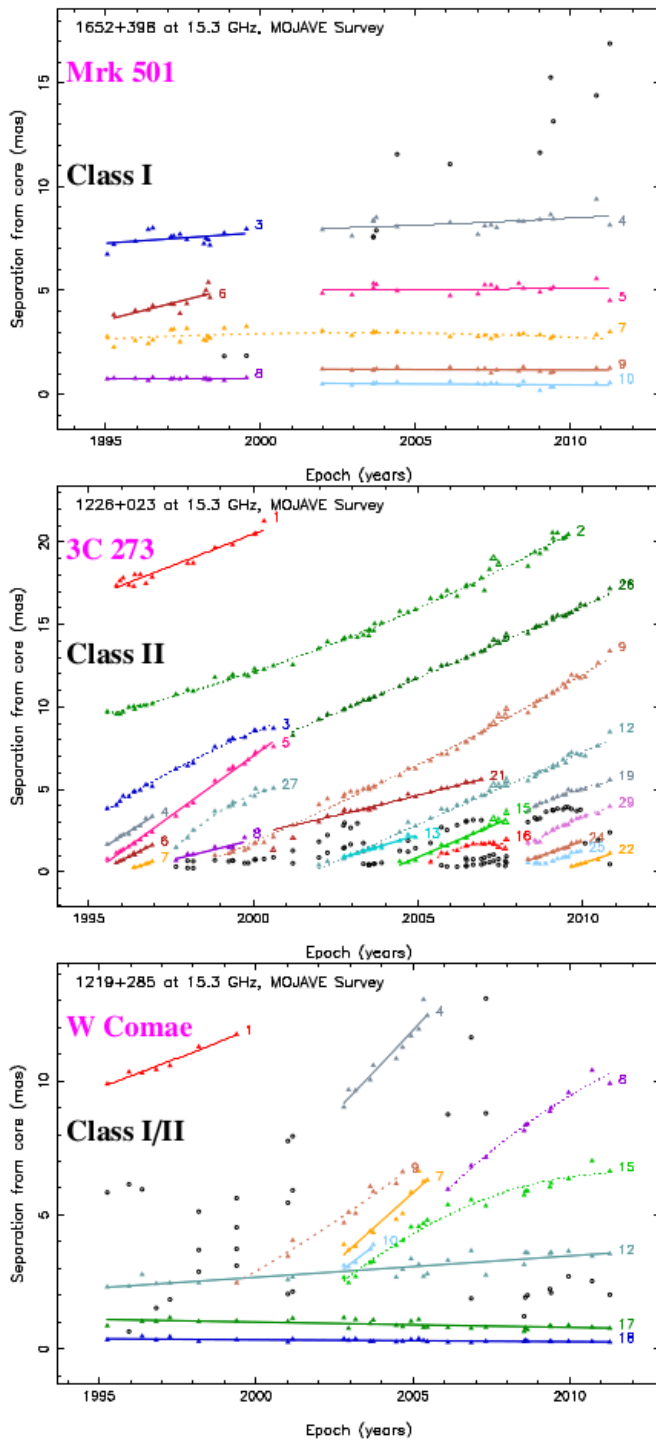
Fig. 2.10.— **Hervet et al. (2016)'s blazar classification according to the temporal evolution of knot-core distances.**

those of the FSRQs. For the latter, on the other hand, the Compton hump is significantly brighter than for BL Lacs. Therefore, the brighter the source, the softer it is at hard X-rays or γ-rays. This kind of behavior, shown on the right hand side of Figure 2.8, is known as the "blazar sequence", and has been attributed to the idea that electrons in more powerful sources lose energy more quickly. Ghisellini et al. (1998) hypothesized that in powerful blazars with strong lines (such as FSRQs), the more radiatively efficient accretion disks are able to ionize the clouds of the BLR and its luminosity would reach the torus, which would subsequently re-emit in the IR. These photons would be a source of external radiation to the jet and would lead to the production of an enormous quantity of HE photons via IC. The Compton hump in these objects tend to peak at MeV energies with a higher luminosity than that of the synchrotron hump peak. The same authors claimed that the disks of BL Lacs would be radiatively less efficient, therefore less external seed photons are produced so less emitting electrons are scattered, allowing the population of these particles to reach higher energies; hence the greater the Compton peak energy. Additionally, it has often been observed that individual blazars tend to become brighter and harder during a high state, flare (Katarzyński et al. 2001a; Ghisellini 2015), see Figure 2.9, that is, their IC peak tend to increase, not decrease.

All of the classification types are subject to bias due to wavelength and source-state selection. For instance, the fraction of radio-loud AGNs would be $\approx 10 - 20\%$ if the AGNs were optically selected, but would possibly be $< 1\%$ based on the integration of

the radio luminosity functions of AGNs (Padovani 2011). A standard assumption about the different states, quiescent and flaring (high flux during a clearly bounded period of time), is that they correspond to intrinsically different physical properties. However, in the determination of ν_{sy}, all of the published data available are generally used (The *Fermi*-LAT collaboration 2019), which can be highly biased by the dominant state in which the source was during the time that it was observed. For instance, observations of variable sources are often triggered by flare alerts resulting from information-sharing agreements between observatories operating at different wavelengths.

A recent proposed classification by Hervet et al. (2016) is based on the kinematic features of the radio jets as seen by VLBI (see Figure 2.10). In this method of classification, Class I corresponds to blazars with quasi-stationary knots, and include HBLs. Class II corresponds to blazars with knots in relativistic motion from the jet base, and includes FSRQs. Finally Class I/II would be the blazars with quasi-stationary knots close to the jet base and in relativistic motion downstream, which would include IBLs and LBLs.

2.4.   Current state of γ-ray astronomy

Three major imaging atmospheric Cherenkov telescopes (IACTs) are in operation today, VERITAS, MAGIC and H.E.S.S.. A description of their functioning is provided in the next chapter. As of December 2019, 225 sources have been reported to be detected at VHEs[5], 78 of these are AGNs. All of these sources have also been detected at high energies (HE). The blazar class consists of 72 sources, and contains 52 HBLs, 7 IBLs, 2 LBLs, and 7 FSRQs. A subclass of HBLs is emerging,

Table 2.1: Evolution of catalogs from space experiments in HE γ-ray astronomy.

Satellite or experiment	Catalog	Year of the catalog	Number of sources
COS-B	2CG	1981	25
EGRET	3EG	1999	271
Fermi-LAT	2FGL	2012	1873
	3FGL	2015	3033
	4FGL	2019	5065

called the extreme high-frequency-peaked BL Lac objects (EHBL), with $\nu_{sy} > 10^{17}$. Only a handful of such sources have been detected at TeV energies (Costamante et al. 2018; Foffano et al. 2019), and two more have shown EHBL behavior during flaring states (e.g. Mrk 501; Pian et al. 1998). At the time of writing, 55 of the known TeV sources have been detected by VERITAS, (the telescope whose VHE data is used in this manuscript), 36 of which are AGNs.

The last 40 years have witnessed remarkable progress in the area of HE astrophysics. The advent of the *Fermi* Large Area Telescope (*Fermi*-LAT) has played a key role in our knowledge of γ-ray sky. After eight years of sky monitoring, *Fermi*-LAT has detected
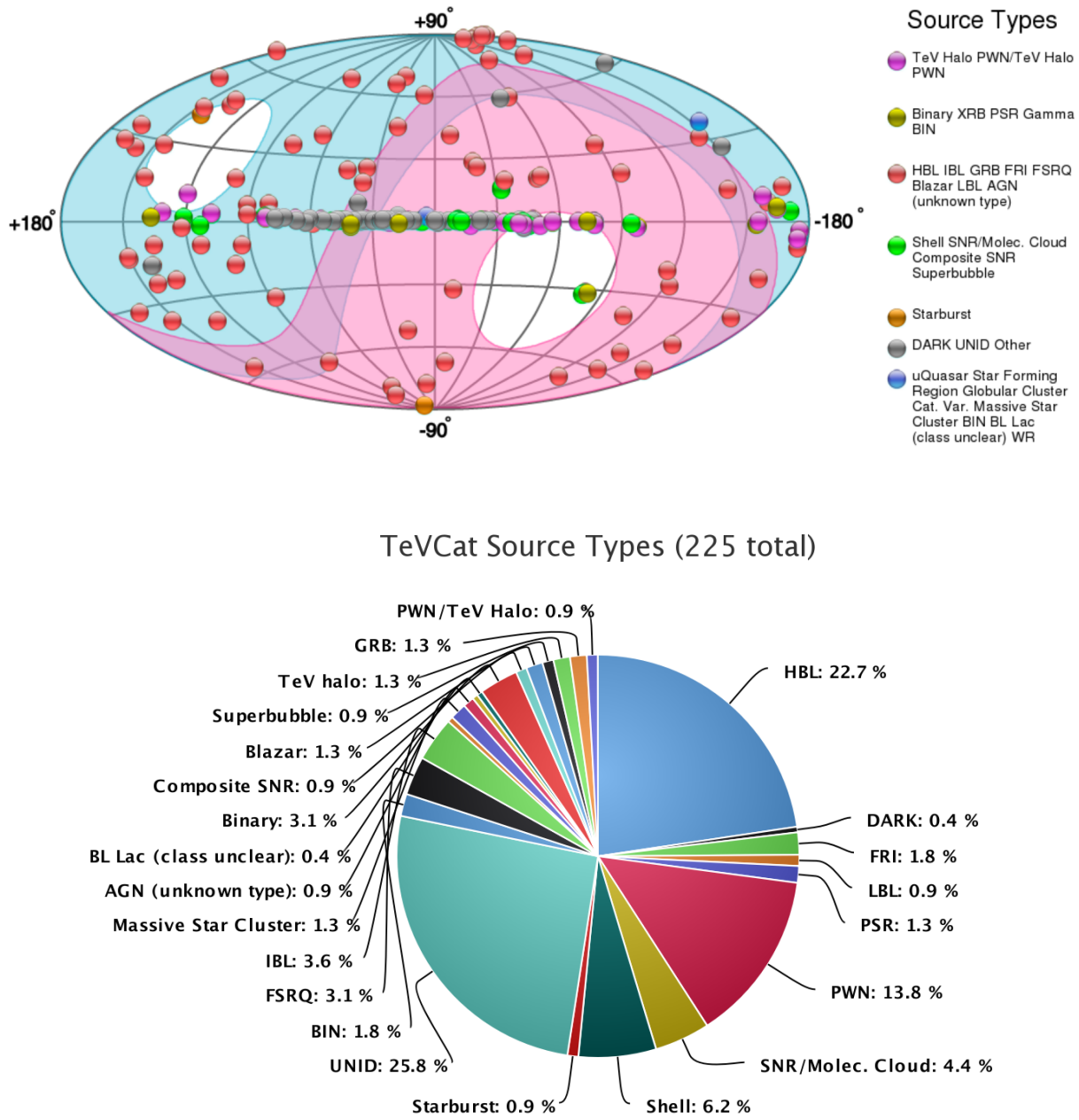
---

[5]`tevcat.in2p3.fr`

Fig. 2.11.— *Top*: Skymap of the 225 VHE gamma-ray sources detected up to December 2019 in galactic coordinates. The approximate region of the sky seen by VERITAS and MAGIC (at small zenith angles), located in the north hemisphere, is shown in light blue; the approximate region of the sky seen by H.E.S.S., located in the southern hemisphere is shown in pink. *Bottom*: Pie chart showing the population of TeV sources detected per class. From TeVCat.

95% of the HE γ-ray astrophysical objects known today, or a total of 5065 sources with a significance above 4 standard deviations ($> 4\sigma$), which is a considerable number with respect to its predecessor EGRET (decommissioned in 2000).

The fourth *Fermi* Large Area Telescope source catalog (4FGL; Abdollahi et al. 2020), contains the sources in the 50 MeV–1 TeV range, based on the first eight years of data
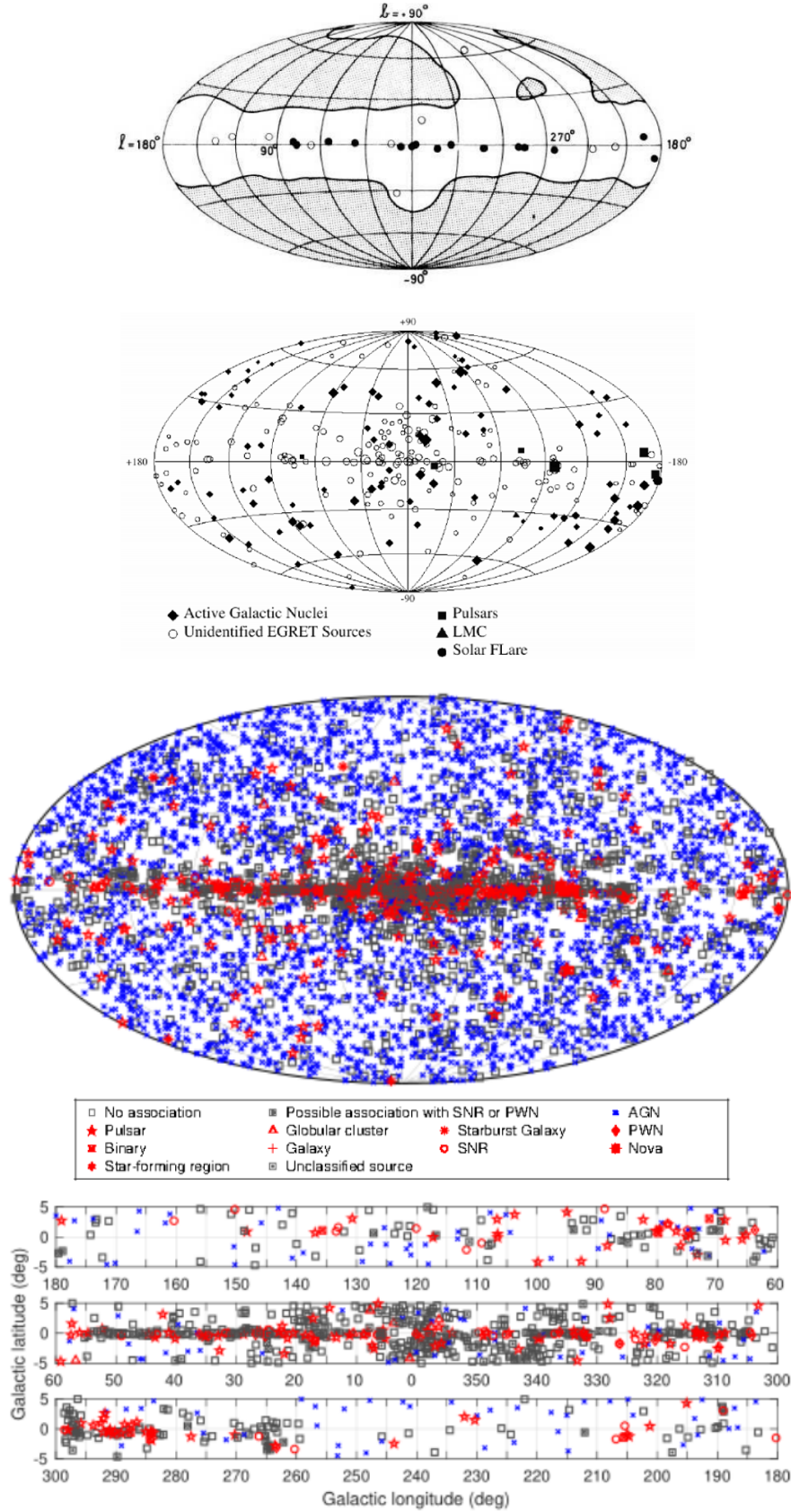
Fig. 2.12.— *Top*: result from COS-B γ-ray satellite. *Middle*: Source locations in galactic coordinates for the third EGRET catalog, 3EG. *Bottom*: Sources of the *Fermi*-LAT fourth catalog by source class. All AGN classes were plotted with the same symbol for simplicity.

(2008 August 4 15:43 UTC - 2016 August 2 05:44 UTC) from the *Fermi* Gamma-ray Space Telescope (GST). The 4FGL also provides source location regions, spectral properties and monthly lightcurves for each source. The largest source class in the 4FGL corresponds to the AGNs. Of these, 3137 sources are blazars, 42 are radio galaxies and 28 belong to other AGN subtypes. The *Fermi* blazars consist of 694 FSRQs, 1131 BL Lacs and 1312 blazar candidates of uncertain type (BCU).
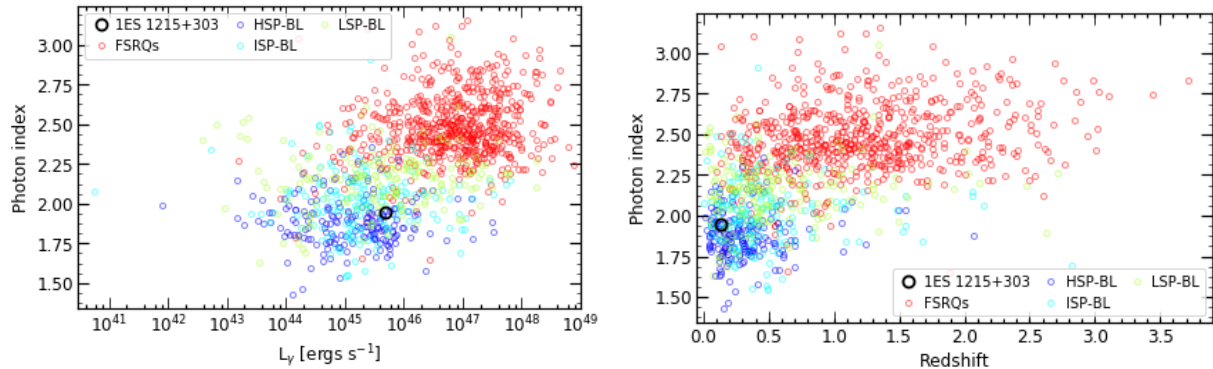

Fig. 2.13.— *Left*: **Photon index against luminosity at HEs.** *Right*: **Photon index versus redshift at HEs. 1ES 1215+303 (black circle), the subject of this work, is shown in both sides. From The *Fermi*-LAT collaboration (2019).**

4LAC comprises all the 4FGL AGNs above $5\,\sigma$ and for latitudes $|b| > 10°$. It provides detailed information on 2863 AGNs, of which 650 are FSRQs, 1052 are BL Lacs and 1092 are BCUs. The FSRQ and BL Lac populations are shown in Figure 2.13, where the trend of higher luminosity with softer HE spectra can be observed, in agreement with the blazar sequence. The right-hand side of the same figure also shows a trend, more distant objects tend to be softer at HEs; something that had not been observed in the previous LAT AGN catalogs.

Each catalog version provides improvements with respect to its predecessor. In particular, the third catalog (3FGL; Acero et al. 2015) did not just provide almost twice as much data as the second catalog, 2FGL, but also analysis and calibration improvements, an updated model for the galactic diffuse emission and improved methods to associate LAT sources with their counterparts at other wavelengths. The 3FGL played an extremely important role in the HE astrophysics field of research for the four years previous to the 4FGL.

The last decades have borne witness to exciting progress in the variability study of blazars. Minute-scale variability has been observed at VHE with the IACTs and at HE with the *Fermi*-LAT (e.g. Shukla et al. 2018; Aharonian et al. 2007). Figure 2.14 shows the variability time scale of a sample of AGNs. This variable behavior along with inconsistent cross-correlation patterns, that is, showing sometimes correlations at different wavelengths and other times not, or even exhibiting flaring activity only in one specific band (i.e. orphan flares) remain a challenge for current theoretical models which generally predict inter-band correlation with time lags that depend on the charged particle cooling
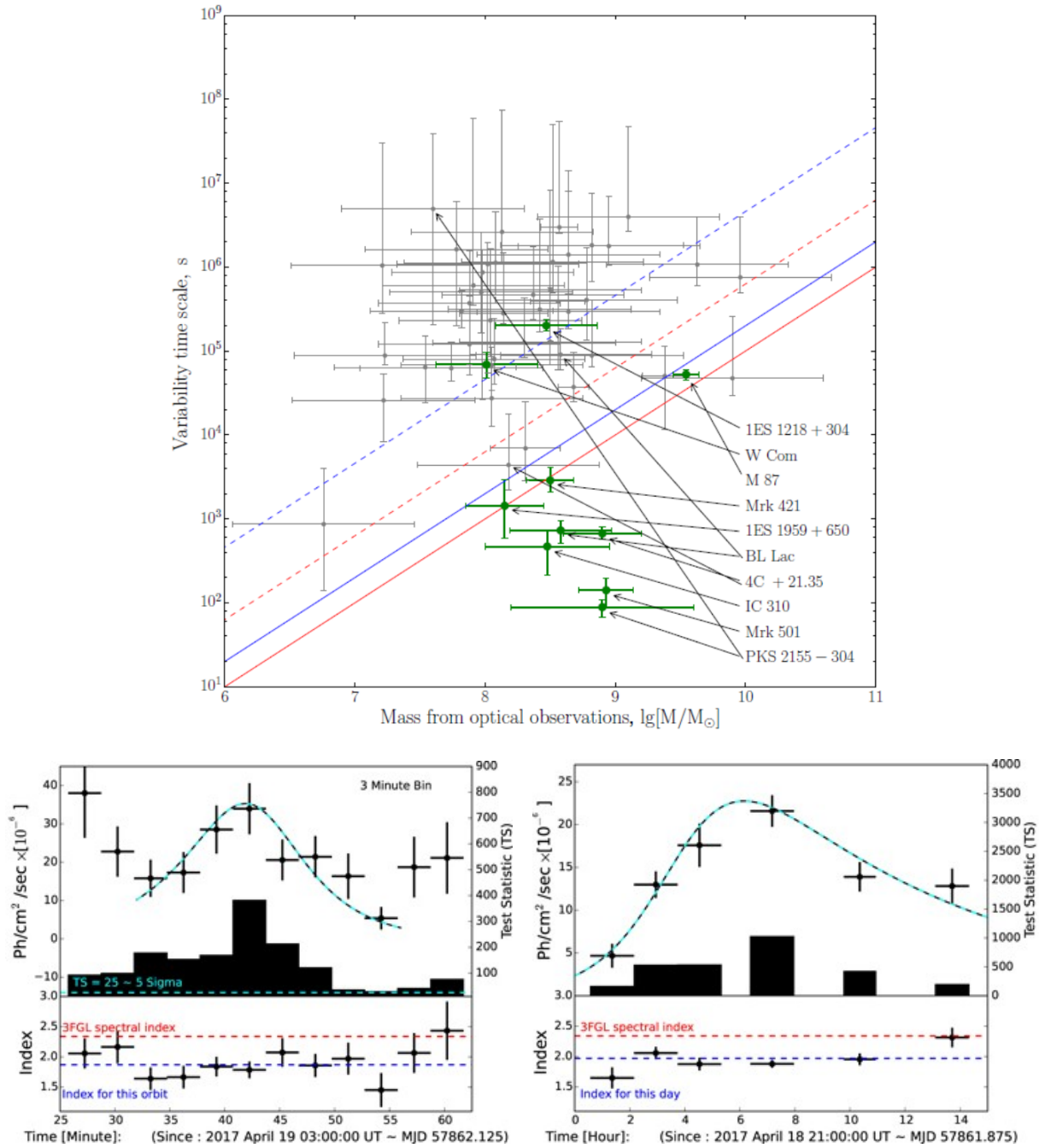
Fig. 2.14.— *Top:* **Population of flares in the variability-time-scale versus black-hole-mass plane. From Barkov (2019).** *Bottom:* ***Fermi*-LAT γ-ray light curves from CTA 102 in April 2017 exhibiting minute-scale variability. From (Shukla et al. 2018).**

or acceleration time scales at different energies (e.g. internal shock model; Böttcher & Dermer 2010). This model would require a very small cross section and an extremely large Doppler factor to barely be able to reproduce the minute scale variability observed. Forcing this model, however, to be very strongly synchrotron or high-energy dominated could enhance the jet large-scale emission, allowing it to reproduce orphan flares (Potter

2018). On the other hand, the shock-in-jet lepto-hadronic scenario is able to link ∼1-day-long flares to extremely long flares delayed by time scales of the order of days. This is because the acceleration time scale for protons is significantly longer than that of electrons (Weidinger & Spanier 2015), so flares that would otherwise seem to be uncorrelated can be linked.
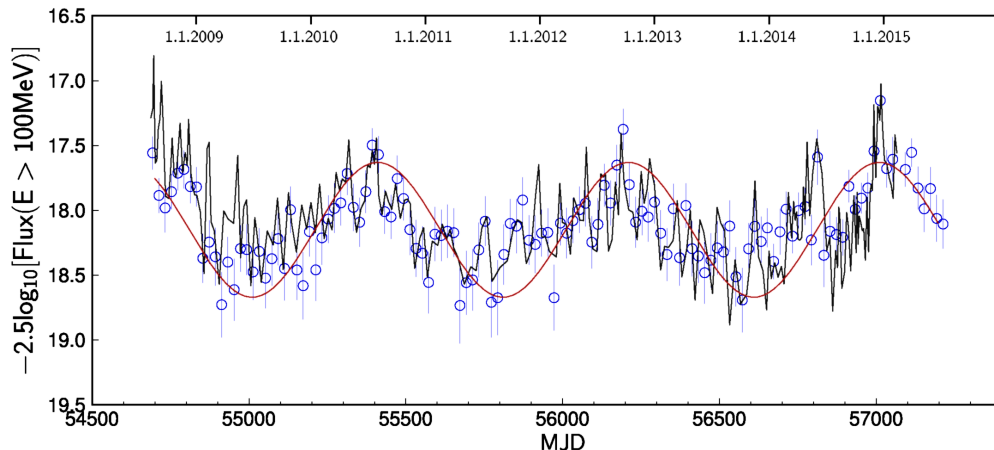

Fig. 2.15.— **20-day binned LAT light curve of PG 1553+113 (blue circles). A sinusoidal curve with period 2.18 years is shown. More cycles are needed in order to test the presence of quasi-periodicity. From Ackermann et al. (2015a).**

The long-term monitoring of blazars has also enabled the community to search for quasi-periodicity in the light curve of these objects. Ackermann et al. (2015a) reported on the possible multi-wavelength periodicity from the BL Lac object PG 1553+113. The radio, optical and γ-ray data suggest a periodicity that would be consistent with a 2.18 ± 0.08 year period (see Figure 2.15). The same authors hypothesize the possible presence of a binary system consisting of two SMBHs. On the other hand, Lico et al. (2020) tested the hypothesis that the possible quasi-periodicity could be related to a jet precession or to pulsational accretion flow instabilities using radio VLBA data. Their results were inconclusive, although they reported a magnetic-field-dominated core.

The availability of these data has also made possible studies on the luminosity function of blazars, which provides us with information on the evolution of BHs. For instance, from a study on the evolution of the luminosity function using LAT data, Ajello et al. (2012) found that the number density of FSRQs increases fast up to redshifts $z \approx 0.5$–2 to then decline, and that this evolution depends on the luminosity of the sources. For most BL Lac though the number density peaks at $z \approx 1.2$. HSPs, on the other hand, show a negative evolution, with the number density increasing for $z <\approx 0.5$ (Ajello et al. 2014). Ajello et al. (2009) and Ghisellini (2015), however, suggest that heavy BH with $M_{BH} > 10^9 M_\odot$ and jets may have formed and started to grow at $z \approx 4$, where their number density reaches a maximum.
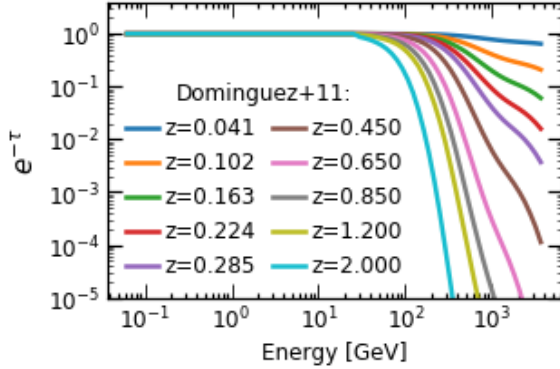
2.5.   Extragalactic background light

Fig. 2.16.— **EBL attenuation dependence of energy for different redshifts (z) according to Domínguez et al. (2011).**

Extragalactic VHE γ-ray astronomy is limited by the absorption of γ-rays by the IR–UV extragalactic background light (EBL), on their path to the Earth, when the center-of-mass energy of the two-photon system is sufficient to create an e^+e^- pair, i.e.

$$\gamma + \gamma_{\text{EBL}} \rightarrow e^+ + e^-$$

The EBL comprises the entire star light emitted throughout the history of the universe. Due to this infrared, optical and UV background light, this absorption effect manifests itself as a modification of the spectra of TeV blazars. The absorption of the γ-rays is a distance- and energy-dependent effect, that is, the higher energy photons suffer more absorption while the spectra from the more distant blazars is more attenuated (see Figure 2.16).
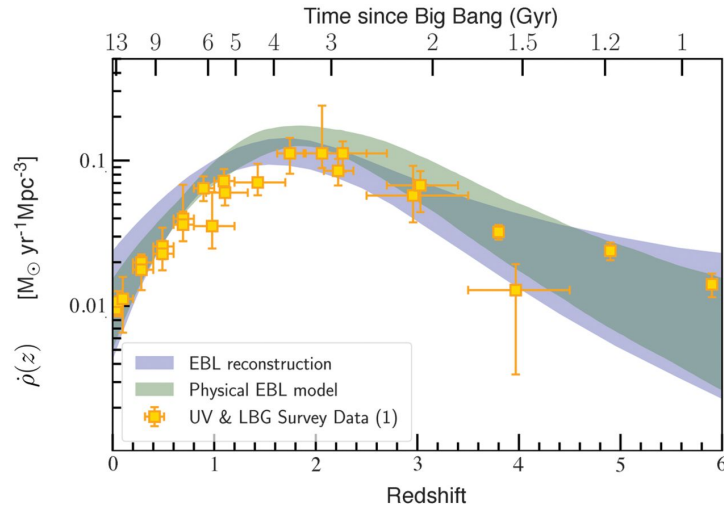
Fig. 2.17.— **Star formation rate against redshift. Shaded areas are $1\,\sigma$ confidence regions. From *Fermi*-LAT Collaboration et al. (2018).**

EBL estimations allow us to measure the density of background photons (e.g. Franceschini & Rodighiero 2017; Domínguez et al. 2011; Finke et al. 2010). This is an important result, since direct measurements of this cosmic radiation are difficult to manage due to galactic foreground. Studies can also be performed the other way around, i.e. to employ TeV measurements to probe EBL models in order to estimate cosmological quantities such as the redshift or the Hubble constant or even probe exotic physics models (Biteau

& Williams 2015; Biteau 2013). The attenuation caused by the EBL on the spectra of blazars can also be used to study the star formation evolution. For instance, *Fermi*-LAT Collaboration et al. (2018) reconstructed the evolution of the EBL from the attenuation observed in hundreds of LAT blazars and one GRB (host galaxy at $z = 4.35$), which allow them to measure the star formation evolution over 90% of the cosmic time. The peak at $z \approx 2$ (See Figure 2.17) they found is consistent with results from optical and IR observations.

3.   THE DETECTORS

The photonic emission from celestial objects can cover the entire electromagnetic spectrum, from radio to γ-rays. Optical detectors have been capturing their visible emission since the early 17th century, while it has been about a century since the start of radio astronomy. Infrared astronomy had its beginnings in the 1830s, however, it became well established in the 1950s after its combined success with the radio detectors. The atmosphere of the Earth is opaque to photons beyond the optical waveband, therefore the advent of space-based experiments was crucial for the development of astrophysics above these wavelengths. The first successful attempts to measure the ultraviolet and X-ray emission from the Sun were in the 1940s, however, it was not until the early 1960s, triggered by the discovery of the first cosmic X-ray source (Giacconi et al. 1962), that continuous strong and successful missions were carried out for astrophysical studies at these wavelengths. Remarkable progress has been made over the last 60 years in the development of the technology necessary for the advent and progress of the high-energy astrophysics domain as well, in the form of both space-based and ground-based detectors. These instruments keep evolving and new missions and large projects including arrays of dozens of telescopes are in preparation.

This chapter is dedicated to the description of the detectors whose data we made use of in our study and to the basics of their functioning. In descending order of energy, these detectors are

- the Very Energetic Radiation Imaging Telescope Array System (VERITAS), for γ-ray observations above ≈ 200 GeV;

- the Large Area Telescope (LAT) on board of the *Fermi* Gamma-ray Space Telescope, for γ-ray observations above ≈ 20 MeV;

- the Neil Geherls *Swift* observatory, for observations at optical, ultraviolet (UV) and X-rays;

- the Tuorla observatory, for observations in the optical R-band;

- the Nordic Optical Telescope (NOT), for polarimetry R-band observations;

- the Owens Valley Radio Observatory, for 15 GHz radio observations;

- the Metsähovi Radio Observatory (MRO), for 37 GHz radio observations;

- and the Very Long Baseline Array (VLBA), for radio observations at 22.2 and 43.1 GHz.

Since this work focuses mainly on the most extreme processes responsible for the γ-ray emission in AGNs, I put a special emphasis on the description of the γ-ray detectors. I provide a detailed description of the VERITAS telescopes and then focus on the *Fermi*-LAT instrument whose data I analyzed and that provided the best sampled dataset. A detailed description of the LAT data reduction process is provided in the next chapter.

3.1.   Ground-based γ-ray astronomy:

The production of astrophysical photons at γ-ray energies decreases steeply with energy as shown in Figure 3.1. For instance, the photon flux detected on Earth from the Crab Nebula, one of the brightest γ-ray sources in the sky, is $\approx$ 6 photons m^{-2} $year^{-1}$ above 1 TeV, whereas above 1 MeV it is $\sim 10^9$ photons m^{-2} $year^{-1}$. Since the Earth's atmosphere is opaque to high-energy (HE, $\geq$ 100 MeV) photons, one might think that the best approach for the study of γ-ray astrophysical sources would be to build space-based detectors; although this works it presents a severe limitation at higher energies due to the rapidly declining γ-ray flux combined with the small collection area of space detectors (≈ 1 m^2) currently launchable.
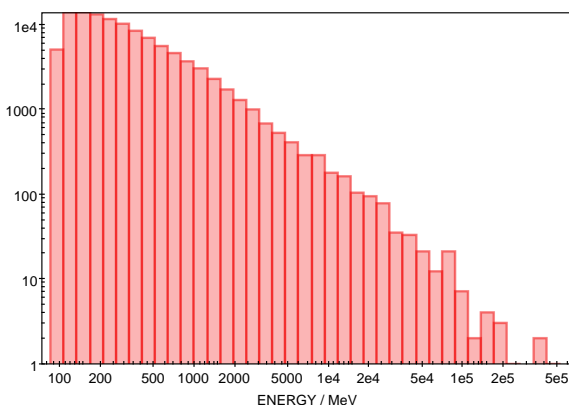
Fig. 3.1.— **Energy distribution of HE events detected by the LAT in logarithmic scale. The very low photon flux at high energies can be visualized from the steeply falling shape of the emission from a 10° region of the sky centered at R. A. $_{(J2000)} = 12^h17^m48.5^s$ and Dec.$_{(J2000)} = +30°07'00''6$, distant from the galactic plane where the γ-ray emission is significantly greater.**

To detect γ-rays in the very high energy (VHE, > 100 GeV) domain, therefore, a different approach is required. In this case, when a VHE γ-ray enters the Earth's atmosphere, it converts into an electron-positron pair (e^-e^+) at high altitude. Each HE e^- and e^+ produces γ-rays through bremsstrahlung, which then convert into e^-e^+ pairs of lower energies. These then radiate γ-rays through bremsstrahlung. This process continues, generating what is known as an electromagnetic air shower. When the average e^- or e^+ energy drops to the critical value of $E_c \approx 84$ MeV where ionization losses start to dominate and the air shower dies out. The maximum number of particles generated is given by E_i/E_c, where E_i is the energy of the incident γ-ray photon.
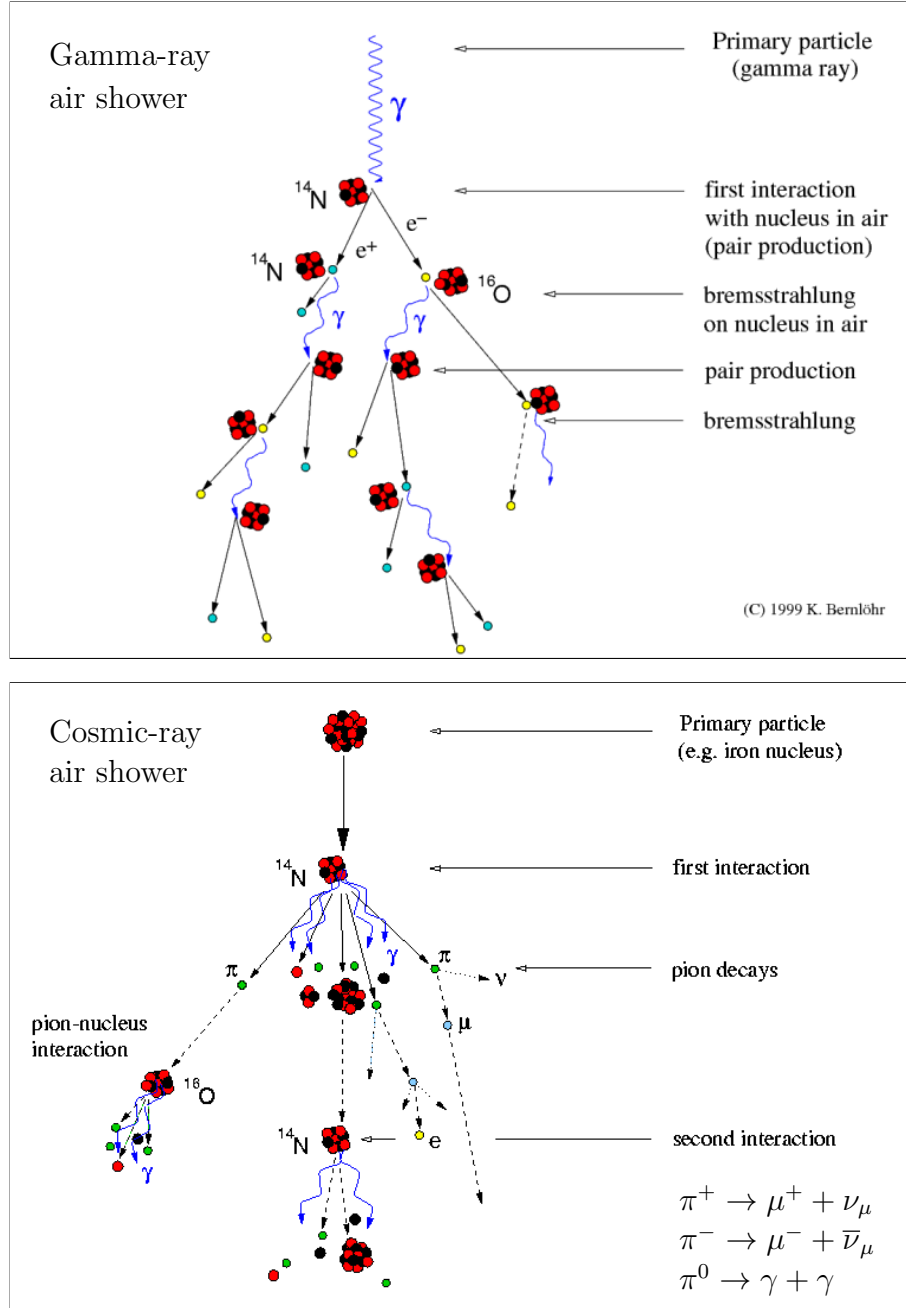
Fig. 3.2.— **Development of electromagnetic (top) and hadronic (bottom) air showers in the atmosphere. Courtesy of K. Bernlöhr.**

When these charged particles have velocities greater than that of the light in the air, on the passage of these particles, visible light is emitted through the Cherenkov effect all along the shower. This mainly consists of blue/UV light and forms a "light pool" of $\sim 10^5$ m^2 on the ground. These optical photons can be collected by a large mirror and this forms the basis of the technique for the VHE detection of γ-rays. By making use of the atmosphere as a natural calorimeter and tracker, an imaging atmospheric Cherenkov telescope (IACT) detects the Cherenkov light from the air showers. The effective detection

area of these telescopes is $\sim 10^5$ m^2. The pulse emitted by Cherenkov photons produced in atmospheric showers last only a few nanoseconds, during which this light can be as intense as the brightest objects in the moonless night sky.

Fig. 3.3.— **Simulations of electromagnetic (*left*) and hadronic (*right*) air showers in the atmosphere, and their images as they would be captured by the IACT cameras. Images captured from showers generated by γ-rays 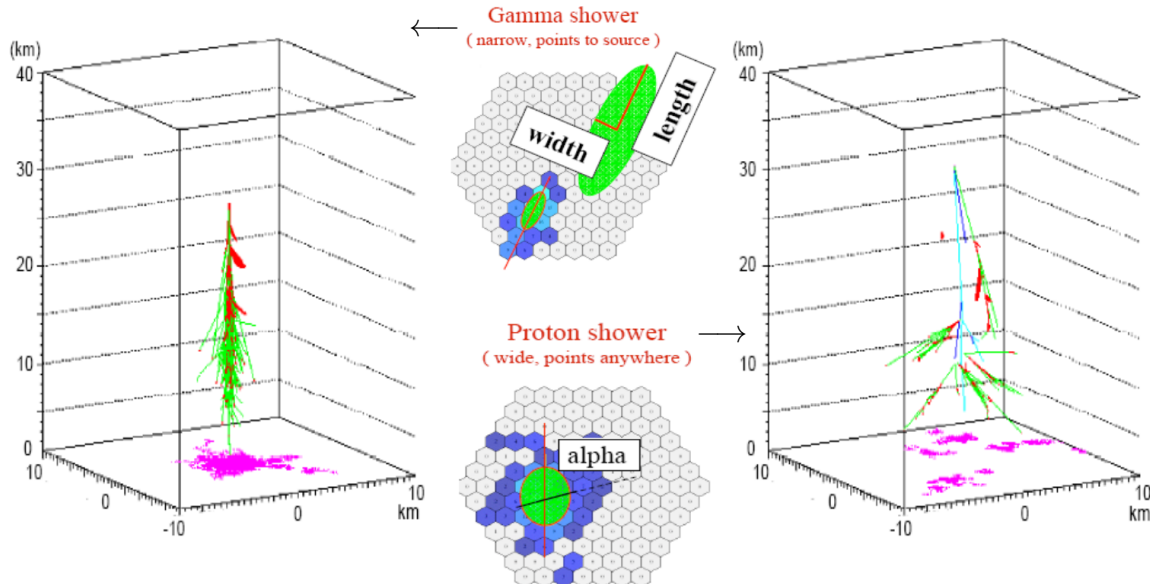have a more compact elliptic shape, compared to the ones produced by the complex hadronic showers due to the sub-showers generated by pions with large transverse momenta and muons. From Di Sciascio (2019).**

Charged relativistic protons and nuclei, known as cosmic rays, also produce cascades in the atmosphere (known as hadronic showers) which represents a huge background compared to the cascades induced by γ-rays. Hadronic interactions through different channels take place within the shower in this case. The particles produced range from secondary nucleons to pions with large transverse momenta, separating them from the axis of the shower. The pions decay before reaching sea level. The charged pions decay into muons and neutrinos, whereas the neutral ones decay into two γ-ray photons, which generate electromagnetic sub-cascades (see Figure 3.2). Muons on another hand live longer and can reach the ground. γ-ray showers provide, therefore, a more compact narrow light pool, with a center very close to the shower axis; as opposed to the wider, more scattered points of fluctuations in hadronic showers. This can be visualized in Figure 3.3. This difference in morphology is one of the key factors that makes it possible to discriminate between γ-ray and cosmic-ray air showers.

The first generation of Atmospheric Cherenkov Telescopes (ACTs) built in the 1950s were not sensitive enough to identify γ-rays even from the strongest sources since they could not discriminate between electromagnetic and hadronic showers because they were not yet parameterizing the images in order to be able to differentiate one type of shower from the other (Jelley & Galbraith 1955). Being able to detect these showers was not

sufficient to search for an excess of Cherenkov events in coincidence with a putative source in the FoV. Over following 30 years, the Whipple Collaboration worked on a series of improvements in both the instrumentation of the focal plane of its 10 m ACT and in the subsequent analysis of the shower images. Implementations of Monte Carlo computer simulations of the shower and Cherenkov emission and detector response together allowed the development of the imaging analysis methods (Hillas 1985) which greatly improved the background rejection. In 1989, these developments resulted in the first ever reliable detection of VHE emission from the cosmos when the Whipple Collaboration announced their discovery of γ-ray emission above 0.7 TeV from the Crab Nebula (Weekes et al. 1989). This was followed by further developments in the techniques and data analysis methods of IACTs (Hillas 2013). Later on, the upgrade of Whipple camera from 37 to 109 pixels enabled the first detection of an extragalactic source, the BL Lac object Markarian 421 (Mrk 421, $z = 0.031$; Punch et al. 1992). By 1995, this had been the only detected object out of a sample of 35 AGNs seen by EGRET (see Section 3.2) that the Whipple Collaboration had been searching at TeV energies. In this context, and after continuous upgrades had taken place, the Whipple Collaboration also carried out observations of other nearby BL Lacs, which led them to the first γ-ray detection from ground of the BL Lac object Markarian 501 (Mrk 501, $z=0.033$; Quinn et al. 1996). This was a major achievement not only because it confirmed that Mrk 421 was not the only extragalactic TeV emitter, but because Mrk 501 had not been reported by EGRET at HEs, which demonstrated the power of the IACTs.

Another important development was achieved by the CAT Collaboration (Barrau et al. 1998), which built a telescope (16 m^2 reflector) with an energy threshold similar to that of the Whipple telescope (60 m^2 reflector), using a considerably smaller mirror, by combining fast photomultiplier tubes (PMTs) with good resolution, fast trigger electronics and a camera with improved granularity[1] and a more sophisticated analysis. In 1997, successful co-ordinated observations and analysis of the BL Lac object Mrk 501 between CAT, HEGRA and Whipple brought much confidence and credit to the field and gave impetus for the building of new facilities combining the best attributes of these three detectors (Degrange & Fontaine 2015), some of which are listed with their main characteristics in Table 3.1. VERITAS, H.E.S.S. and MAGIC are the three major IACT detectors operating today.

The most successful technique for γ-ray discrimination and reconstruction today is the stereoscopic imaging method, and is used by the three major IACTs. Large convex reflectors, such as the ones shown in Figure 3.4, focus the Cherenkov emission from air showers onto a large camera (∼1 m) consisting of hundreds of PMT. The shape, intensity and orientation of the shower captured by the camera is used to determine the characteristics of the incident particle that generated the shower, also known as the shower primary. The term stereoscopic refers to the analysis of the same shower using the images

---

[1]The use of sufficiently small PMTs enabled the discrimination between electromagnetic and hadronic showers.

from an array of telescopes. It was exploited successfully by the HEGRA Collaboration (Daum et al. 1997) and allows for a significantly improved geometrical reconstruction of the shower and much improved background rejection. The IACTs sensitivity is approximately proportional to the square root of the number of telescopes in the array (Holder 2015).

The current IACTs have fields of view (FoV) ranging from 3° to 5°. There are a few reasons for this relatively large size. One is that the air shower images have an extended shape of up to a few degrees. Another reason is that the image could be offset from the position of the source in the FoV depending on the nature of the TeV emitter or on the observation mode being used in order to estimate the background level of the remaining hadronic showers (Berge et al. 2007). For instance, four discrete pointings in the cardinal directions around the source of interest (called the "wobble" mode) could be employed to determine the background to be subtracted from the signal. This allows simultaneous source monitoring and off-source observations.

The use of PMTs as photodetector pixels is suitable for ACTs due to their exceptional signal amplification ($\sim 10^5$) which makes them perfect for single photon detections. PMTs have an efficiency of $\approx$32–34% (Kieda 2011) and a nanosecond response time, ideal for the detection of the very short pulses of Cherenkov light from electromagnetic showers. The implementation of trigger systems is, however, necessary to filter out the signals produced by the fluctuating night sky background (NSB). After the signal recorded by an individual PMT has passed a certain level, a typical trigger would require three neighboring pixels in a camera to have been triggered within a few nanoseconds. A higher level trigger would require at least two telescopes to have been triggered "simultaneously", after having taken into account the different path lengths of the Cherenkov light to and through each telescope.

Table 3.1.   Main characteristics of present major IACT systems.

Experiment	Number of Telescopes	Reflector size (m)	Site	Number of pixels	Pixel size	FoV (ϕ)
HESS I	4	12	Namibia	960	0.16°	5°
MAGIC	2	17	La Palma	1039	0.08° − 0.12°	3.5°
VERITAS	4	12	Arizona, U.S.A.	499	0.15°	3.5°
HESS II	4 (HESS I)	12	Namibia	960	0.16°	5°
(2012 upgrade)	+1	28		2048	0.067°	3.2°

Fig. 3.4.— **The Very Energetic Radiation Imaging Telescope Array System site.**

3.1.1.   VERITAS

The Very Energetic Radiation Imaging Telescope Array System (VERITAS) is an array of four imaging atmospheric Cherenkov telescopes located at the Fred Lawrence Whipple Observatory in southern Arizona, U.S.A. (31° 40'N, 110° 57'W, 1.3 km above sea level) (Holder 2011). Each of the four telescopes (numbered T1, T2, T3 and T4) comprises a spherically curved, segmented-aperture, 12 m diameter reflector, of the Davies Cotton design (Davies & Cotton 1957), and an imaging camera with 499 high-quantum-efficiency PMTs (also referred to as pixels). Each of the reflectors comprises 345 hexagonal mirror facets.

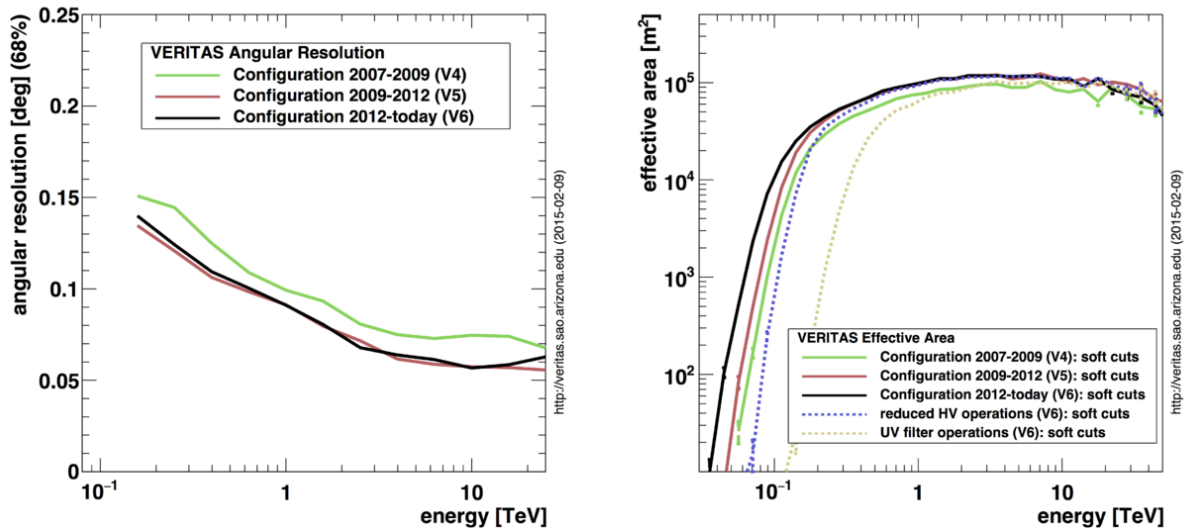**Fig. 3.5.**— **Angular resolution (left) and effective area (right) as a function of energy for an elevation of 70°. A change in the array layout of VERITAS led to a 15% improvement in sensitivity, that is, a ∼ 25% reduction in source detection time. An upgrade of the camera PMTs took place in 2012. The new high-quantum-efficiency PMTs provided an improvement in sensitivity and significantly lowered the energy threshold.**
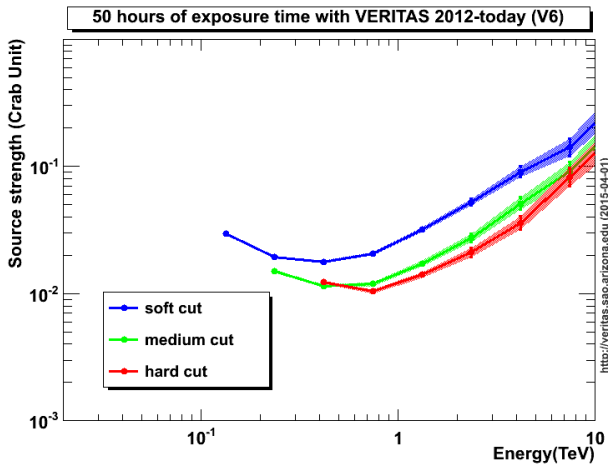
Fig. 3.6.— **VERITAS differential sensitivity.**

The ensemble of telescopes operate in stereo mode to cover a FoV of approximately 3.5° with an angular resolution of 0.08° (68% containment at 1 TeV, see Figure 3.5; Park & VERITAS Collaboration 2015). VERITAS is sensitive to VHE γ-rays in the energy range between ∼85 GeV and >30 TeV (the spectral reconstruction is possible from 100 GeV), with an energy resolution of ∼15-25% (17% at 1 TeV). A point source of 1% of the Crab Nebula flux can be detected by VERITAS with a statistical significance of 5 standard deviations (5σ) in ∼25 hr.; or 10% that of the Crab Nebula in 25 minutes. Figure 3.6 shows the source strength VERITAS can detect with $5\,\sigma$ significance in 50 h. of exposure time at elevations above 70°.
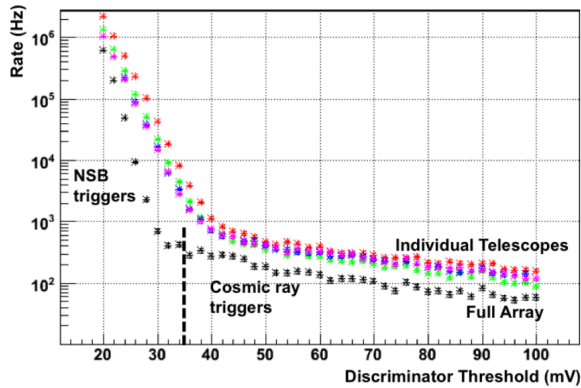

Fig. 3.7.— **Triggers rate vs. discriminator threshold, known as bias curve. Colored curves correspond to individual telescopes. Black points correspond to the ensemble of telescopes after the third level trigger activation. The breaking points separate the NSB fluctuations dominated triggers from the ones dominated by air showers. From Holder (2015).**

A hollow, hexagonal, parabola-shaped Winston cone is located in front of each PMT in the camera in order to concentrate the light and increase the photon collection efficiency. The PMTs work at ∼1000 V, providing a gain of 2.5×10^5. During a moonless night, the current should usually not exceed 10 μA. The pre-amplifiers are connected through coaxial cables to the flash analog-to-digital converter boards located in a trailer beside each telescope. The VERITAS trigger system has three levels. The first level requires the signal in an individual pixel to exceed a predetermined threshold. This threshold is set in the constant fraction discriminator. The second level occurs when the first level is triggered for three pixels adjacent to each other within a short time window (on the order of ≈6 ns). The third-level trigger requires the second-level triggers of at least two telescopes to occur within 50 ns. This happens at a rate of ≈400 Hz, and only when this condition is met will the detected signal be stored.
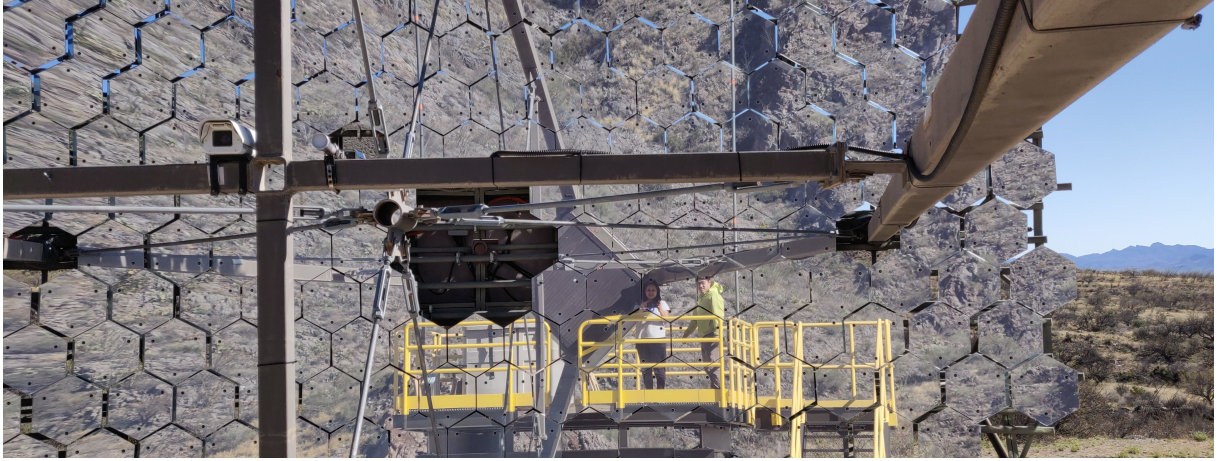
VERITAS has an in-house mirror-coating facility so that the mirrors are recoated periodically (Roache et al. 2008). The reflectivity of the mirrors of each telescope is also

Fig. 3.8.— **T1 view from the focal plane taken by the author. The camera, with the shutter closed, can be seen reflected in the mirrors. The sky and reflectivity cameras are located on the reflector, close to the center where there are no mirrors. The LED flasher is also mounted on the crossbeam. In the picture, the shifters on call start preparing for observations.**

measured for calibration purposes. This procedure starts by installing a white-painted reflective target in front of the camera. Then, the camera located on the reflector is used to simultaneously observe both a star itself and its reflection on the mounted target, in order to obtain the ratio of their intensities (Mirzoyan et al. 2007).

VERITAS has experienced two major upgrades since it started operations in 2007. In 2009, T1, initially located near T4, was moved to its current position, which is the furthest from its neighbors, in order to improve the angular reconstruction and the overall sensitivity of the array. T1 is nowadays the most important telescope for event reconstruction. In 2012, the camera PMTs were replaced by others with higher quantum efficiency; which also contributed to further improving the overall sensitivity and to the reduction of the energy threshold. Therefore, three epochs are distinctive for the VERITAS instrument, each one with its own set of response functions and systematics; the one from 2007 – 2009 before T1 was moved is called V4, the one from 2009 – 2012 after T1 was moved but before the camera upgrade is called V5, and V6 refers to the current epoch after the camera upgrade (see Figure 3.5).

The VERITAS collaboration has been developing and applying other event reconstructions schemes for the VERITAS data analysis, mainly in order to improve their sensitivity and on γ/hadron separation with respect to the standard Hillas based procedure, which is key to obtaining good sensitivity to faint γ-ray sources. One of these methods achieved to reduce the observation time necessary to reach a $5\,\sigma$ detection for weak sources by 20% by extracting image parameters from 2D Gaussian distribution fits using a χ^2 minimization (Christiansen & VERITAS Collaboration 2012) instead of the standard Hillas-based method. In the Hillas (1985) scheme, the clean image of a shower seen in a telescope camera is parameterized as an ellipse whose length and width represent

the longitudinal development and the lateral spread of the shower respectively. The Hillas parameters are: The minor and major axes of the shower ellipse, the number of pixels that comprise the image, the integrated charge of all the pixels, and the distance from the center of the camera to the center of the ellipse (see Figure 3.3). The stereo reconstruction uses the Hillas parameters to geometrically reconstruct, e.g. the core location and the direction. This method, however, loses precision when the shower cores are far from the array so the images are clipped, when the event was not seen by all the telescopes, or when the images are very large ($\gtrsim 30$ TeV primaries) or very small ($\lesssim 0.1$ TeV primaries) so the determination of the axes of the image is ambiguous, and at low elevations when the images have practically parallel major axes. To reconstruct the energy of the primary particle, the fact that the primary energy is approximately proportional to the image size for a given impact distance from the telescope is used. Therefore, the accuracy of this reconstruction depends on the accuracy of the calculation of the impact distance. Another issue presented during the reconstruction analysis is that some pixels may have been removed due to hardware failures or due to contamination from bright stars in the FoV. Christiansen & VERITAS Collaboration (2012) uses the standard Hillas parameters to seed their algorithm, and finds that fitting the 2D Gaussian to the data provides a better directional resolution than the standard parameters. This method is capable of extrapolating beyond the edge of the camera, thus producing a larger effective area. This effect together with the improved angular resolution results in a 20% improved sensitivity for dim sources.

There have been several approaches to improve the methods on γ/hadron discrimination, such as the ones described above. As event selection in IACT data relies on the geometrical differences of γ-ray and hadron showers, the original approach was to find a set of parameters that characterize the showers, to find the distribution of this parameters for each population of showers, and to find an optimal region in the full multidimensional space of shower parameters such that discarding all the events outside these ranges gets rid of a large number of cosmic-ray background events while maintaining the majority of γ-rays. This procedure is known as box cuts. This approach later gave place to the use of supervised machine learning methods, such as the multivariate analysis boosted decision trees (BDTs) and tree classification method called random forest (RF), trained on the use of features extracted from IACT images, which was found to improve their classification performance. Krause et al. (2017), for instance, applied the BDT technique to the analysis of VERITAS data and found that this approach increases the sensitivity of VERITAS for a large variety of sources. The BDT technique had also been applied to the H.E.S.S. data by Becherini et al. (2011), yielding a gain in sensitivity of a factor of $1.2 - 1.8$ (depending on the characteristics of the source) with respect to the standard Hillas analysis; which is equivalent to a reduction in the observation time in a factor of $1.4 - 3.2$. Previous to these studies, Albert et al. (2008) used the RT method for γ/hadron separation in the analysis of MAGIC data, not drawing a clear conclusion on regarding the superiority of the method in comparison with the classical method. Deep learning algorithms, such as deep convolutional neural networks (DCNs) have also been used for γ/hadron discrimination. DCNs are part of class called representation learning where the learning algorithm

is allowed to automatically discover the features to learn from, thus having the potential to access information contained in the images beyond the handcrafted features extracted from them. For instance, Nieto Castaño et al. (2017) used DCNs to demonstrate their capability of classifying simulated IACT images, while Feng et al. (2017) showed their potential to tag muon events. Recently, Nieto Castaño et al. (2019) announced that they are developing a Python package called CTLearn, that aims to help the IACT explore deep leaning models with a focus on DCN-based models. CTLearn uses pixel-wise camera data as input and provides a backend to train deep leaning models for IACT event reconstruction with TensorFlow. This is a work in progress.

3.2.   Space-based γ-ray Astronomy

Table 3.2: Instrumental progress in high-energy space detectors in the last 40 years.

Instrument	EGRET	AGILE	*Fermi*-LAT
Launch	1991 April	2007	2008
Active until	2000	ongoing	ongoing
Energy domain	20 MeV – 30 GeV	30 MeV – 50 GeV	$\approx$ 20 MeV – >300 GeV
Tracker	Spark chamber	silicium strips + W (14 pl.)	silicium strips+ W (18 planes)
Calorimeter	NaI (Tl) 8.5 X_0	CsI (Tl) 1.5 X_0	CsI (Tl) 10 X_0
Effective Area	1200 cm^2 at 1 GeV	700 cm^2 at 1 GeV	10^4 cm^2 at 10 GeV
Field of view	0.20 sr.	2 sr.	2.4 sr.
Angular resolution	1.5° at 1 GeV	0.6° at 1 GeV	0.12° (10 GeV), 4° (100 MeV)
Localization accuracy	5′ to 10′	30′ at 300 MeV	0.4′
ΔE/E	10%	100%	10%
Dead time	0.1 s	< 100 μs	< 100 μs

Note.- EGRET was decommissioned in 2000. AGILE and *Fermi* are still active. *Fermi* was recently approved to continue running for three more years, from the time of writing.

As discussed in the previous section, HE γ-ray astronomy also faces challenges. For instance, γ-rays cannot be focused and must, therefore, interact directly in the detector volume so the effective detection area is restricted to that of the detector ($\approx$1 m^2). In order to fit in the launcher, therefore, the volume attainable with space-based experiments implies that they can be efficient only below $\approx$100 GeV (i.e. HE domain). γ-rays with energies above 100 MeV can be detected only by their $e^- e^+$ pair conversion in matter. The incidence direction can be reconstructed from the electron and positron tracks. This requires converters of short radiation length, however, electrons suffer strong multiple scattering in such materials, which deteriorate the angular resolution. Fortunately, this effect becomes smaller as energy increases, however angular resolutions better than $\approx$ 0.1° have not been reached[2], in contrast with the few arc seconds resolutions of the soft X-ray telescopes. The resolution of the total energy of the $e^- e^+$ pair is typically 15%.

---

[2]`https://www.slac.stanford.edu/exp/glast/groups/canda/lat_Performance.htm`

The strong background of secondary γ-rays produced by cosmic rays in the atmosphere represented a challenge for the first attempts to detect cosmic γ-rays. In 1967–1968 OSO-3 provided clear evidence of γ-ray emission above 50 MeV from the Milky Way, although it did not have imaging capabilities. After that, SAS-2 (1972-1973, $E > 35$MeV) revealed the existence of diffuse emission from our galaxy and discovered γ-ray emission from the Crab and Vela nebulae. Later on, COS-B (1975-1982, $E > 100$MeV) provided a catalog of 25 sources. The progress continued until the launch of the *Fermi* Gamma-ray Space Telescope (GST), which took advantage of the instrumental progress in particle physics. Table 3.2, Table 2.1 and Figure 2.12 summarize the spectacular progress of space-based γ-ray astronomy at HE in the last 30 years. Table 3.2 shows the improvements achieved by the *Fermi* GST, in angular resolution, effective area, FoV, energy resolution and range, and time resolution. It consist of two instruments: The *Fermi* Gamma-ray Burst Monitor (GBM) and the Large Area Telescope (LAT). The GBM localizes and detects gamma-ray bursts (GRBs) in the 10 keV to 25 MeV energy band, and alerts the LAT that a burst is in progress. *Fermi* can change its observing plan autonomously to observe GRBs during and after emission, and rapidly notifies the science community.

The author of this manuscript was responsible for the *Fermi*-LAT data analysis, which provided the richest data set for the study of 1ES 1215+303. I therefore dedicate a special section to the description of this instrument in the following section. Details of the data analysis itself, however, are provided in the next chapter.

3.2.1.   *Fermi* Large Area Telescope

The Large Area Telescope, LAT, on board the *Fermi* Gamma-ray Space Telescope, is an imaging, pair conversion detector that covers the energy range from ≈ 20 MeV to more than 1 TeV (Atwood et al. 2009). The main observation mode of the *Fermi*-LAT is survey mode during which the LAT scans the entire sky every 3 hours. *Fermi* has a circular orbit at 565 km, a period of 96 min and the initial configuration[3] had an inclination of 26°. Table 3.3 summarizes some of the main performance parameters of the instrument.

The LAT consists of an array of 16 tracker modules, 16 calorimeter modules (both mounted to the instrument central structure), and a segmented anticoincidence detector (ACD). Each tracker module consists of 18 XY tracker planes, and each of these planes has an array of (two planes X-Y) silicon-strip tracking detectors (SSD) used for the detection of charged particles. Multiple scattering of the pair components in the first conversion

---

[3]One solar array drive assembly of the *Fermi*-LAT stopped moving on March 2018. It remains functional but fixed since then. The observing program of *Fermi* has been modified in order to provide the spacecraft with sufficient power. The scientific impact of this anomaly is considered minimal due to large FoV of the LAT. This work uses LAT data up to September 2017, therefore, the observing strategy before this anomaly remains valid for this analysis. For details on the current sky survey strategy, which depends on the angle of the Sun with respect to the orbit plane, see: `https://fermi.gsfc.nasa.gov/ssc/observations/types/post_anomaly/`.

plane results in an angular deflection that limits the angular resolution, especially at low energies. Cosmic rays also interact with the tracker, however, the reconstruction of interactions from the tracks identify the type of particle, its energy and direction of incidence. The probability distribution of the reconstructed direction of incident γ-rays from a point source is known as the point spread function (see Figure 3.13). To optimize the PSF at low energies and maximize the effective area at high energies, the tracker was divided in two regions, FRONT and BACK. The FRONT region comprises the first 12 XY planes of tungsten converter material (high Z) of a thickness of 0.035 radiation lengths to minimize the PSF at low energies; while the next 4, at the BACK region, have tungsten plates of a thickness of 0.18 radiation lengths to maximize the effective area. The last 2 planes do not have any converters.

When a γ ray enters the LAT tracker and interacts with the tungsten (high Z), it produces an e^-e^+ pair, which is tracked through the instrument by silicon strip detectors. This pair continues predominantly in the direction of incidence of the γ-ray because of its much larger energy relative to their rest mass. Therefore, again, the reconstruction of the direction of the γ-ray is limited by the multiple scattering of the pair components in the tracker material and its spatial resolution. A Csl(Tl) calorimeter is located at the bottom of the LAT and is sufficiently thick to make an adequate measurement of the pair energy and provide a good background discriminator by imaging the shower development. Each calorimeter module is composed of 96 Csl(Tl) crystals arranged in 8 alternating orthogonal layers. Dual PIN photodiodes at each end of the crystals read the scintillation

Table 3.3: *Fermi* Large Area Telescope instrument parameters and performance.

Parameter	Value or Range
Energy range	< 20 MeV – > 1 TeV
Energy resolution ($1\,\sigma$)	
0.1–1 GeV	9%–15%
1–10 GeV	8%–9%
10–300 GeV	8.5%–18%
>10 GeV	≤6%
Single photon angular resolution, on-axis,	
68% space angle containment radius ($\theta_{68\%}$):	
$E > 10$ GeV	$\theta_{68\%} < 0.15°$
$E = 100$ GeV	$\theta_{68\%} < 3.5°$
on-axis, 95% containment radius:	$< 3 \times \theta_{68\%}$
off-axis, 95% containment radius at 55°	1.7× on-axis value
Field of view	2.4 sr
Timing accuracy	$< 10\ \mu$s
Event readout time (dead time)	26.5 μs
Point source location determination	$< 0'.5$
Point source sensitivity (> 100 MeV)	$< 6 \times 10^{-9}\ \mathrm{ph\,cm^{-2}\,s^{-1}}$,
	$5\,\sigma$ after 1 year sky survey
Background rejection after analysis	$< 10\%$ residual contamination of a high latitude
	diffuse sample for $E = 0.1$–300 GeV.
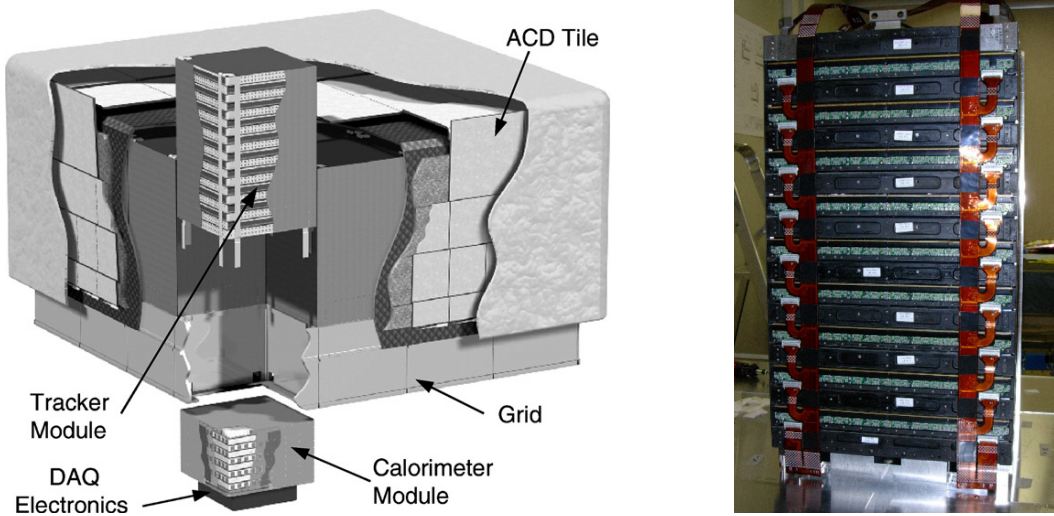
Fig. 3.9.— *Left*: LAT: Each tower in the 4×4 array includes a tracker module and a Calorimeter module. *Right*: LAT Tracker Module. From Atwood et al. (2007, 2009).
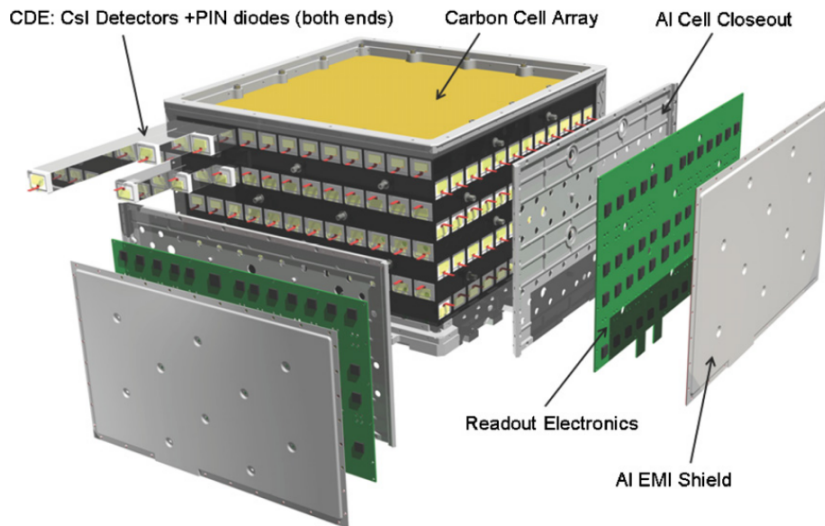
Fig. 3.10.— LAT calorimeter module. From Atwood et al. (2009).

signals. The segmentation and read-out provides precise three dimensional localization of the shower in the calorimeter. The LAT calorimeter is a total absorption calorimeter with excellent energy resolution. Its depth is 8.6 radiation lengths at normal incidence, which enables it to be efficient at high energies. This combined with its segmentation allows it to significantly reject the background. The longitudinal segmentation of the calorimeter also enables measurements up to TeV energies.

Charged cosmic rays that outnumber the γ-rays by factors of 100 to 100000 can produce a huge background in the LAT. In order to reject these events, the LAT is surrounded by an ACD, which consists of scintillator tiles to detect these events and emit a veto signal. Sometimes, secondary charged particles produced in the electromagnetic

shower, created by a potentially valid event HE photon, travel back up through the tracker and cross the ACD. These particles could undergo Compton scattering and create signals and result in vetoed valid γ-rays. In order to suppress this effect, the LAT ACD is segmented (in contrast to the EGRET ACD, in which this was not the case), so that only the events that trigger an ACD tile on the trajectory of the incoming particle are vetoed. As a result, the sensitivity of the LAT is dramatically increased compared to EGRET's.

The ACD has a high detection efficiency for cosmic rays (> 0.9997 for singly charged particles) that allow it to reject this source of background. The ACD also acts as a back-splash (Moiseev et al. 2004) suppressor. These particles are produced when electromagnetic showers produced from high-energy incident photons generate secondary particles, in the energy range from 100–1000 keV, Compton scatter with the ACD generating false signals. The segmentation of the ACD enables the suppression of the backsplash effect so that only the segment of ACD closer to the incident photon candidate is considered.

The data acquisition system (DAQ) of the LAT performs filtering to reduce the background onboard and processes the data into a data stream. It also runs the command, control and instrument monitoring, housekeeping and power switching. The LAT onboard analysis reduces the raw LAT trigger rate from ∼10 kHz, to ∼400 events/s, which are then sent to the ground for further analysis. Typically, 2-5 Hz of these are astrophysical photons. The data for an event that passes the onboard analysis are stored together with the details of the signals from the various LAT subsystems (LAT's primary data product), and are transmitted to the spacecraft's solid state recorder for transmission to the ground.

On ground, each of the several hundreds of events collected per second is then reconstructed. The data is first decompressed and digitalized from the schema used in the electronics to a physically motivated one. For instance, the ACD signals are grouped by tile instead than by readout module. Then, the events are reconstructed by using pattern recognition and fitting algorithms. Finally, event analysis and selection criteria are applied for the various γ-ray classes. This is briefly described below. The processing pipeline verifies the integrity of the data at each step and makes available all the data products related to calibration and performance monitoring of the LAT. Detailed simulations of the particle interactions with a detailed material model of *Fermi*, as well as simulations of the uncalibrated signals produced in the various sensors within the three subsystems, are performed in Geant4 in order to develop filtering, reconstruction and event selection algorithms. These data is simulated as seen by the trigger and on-board software; and is processed with a simulation of the hardware trigger, the same on-board filter algorithms as used on the LAT, and with the same reconstruction and analysis algorithms as for the flight data.

3.2.1.1. Event triggering, filtering and classification

The flux of charged particles is usually thousands of times larger than the γ-ray flux. Therefore, an event triggering an filtering is performed on board in order to reduce the

data volume downlinked to ground. Four stages of the event classification process were implemented in order to account for the contamination of γ-rays by charged particles that might be incorrectly classified as γ-rays:

Firstly, if certain conditions are fulfilled, the triggering process starts when the LAT detects traces of particle interaction. Trigger requests (or primitives) can be issued when three-in-a-row x–y silicon layer pairs (or six consecutive silicon planes) have a signal above threshold of ~ 0.25 minimum ionizing particles (MIP), which might signal the potential presence of a track in a tower. Trigger primitives are also issued when any of calorimeter crystal ends have a signal above the low-energy (~ 100 MeV) or high-energy (~ 1 GeV) trigger thresholds. Signals in any of the ACD tiles above the veto threshold of ~ 0.45 MIP, which indicate a charged particle crossing the tile, or above the "carbon, nitrogen, oxigen" threshold (~ 25 MIP), which indicate the crossing of heavily ionized nuclei, also issue trigger requests. These are five of the eight trigger primitives of the LAT, for further details the reader is referred to, e.g., Ackermann et al. (2012a) and Atwood et al. (2009).

Secondly, if the event in question produces an acceptable trigger pattern, it is read out and passed on to the next stage, the on-board filter, whose software is highly optimized for speed and to terminate the processing of each event as soon as it is able to reach a decision. All events go through three different filters in the nominal science data taking, the γ-ray filter, the heavy ion filter and the diagnostic filter to monitor sensor performance and selection biases.

Thirdly, the event goes through the on-board γ-ray filter. The γ-ray filter rejects: (i) events with patterns of ACD tile hits consistent with cosmic rays and that at the same time do not present a low-energy calorimeter trigger request, which makes it unlikely that the ACD hits were a product of backsplash; (ii) events with patterns of ACD tile hits spatially associated with the tracker towers that launched the trigger ans whose deposited energy in the calorimeter is less than the programmable threshold (~ 350 MeV); (iii) events with a significant energy deposition in the calorimeter ($\gtrsim 100$ MeV) but at the same time the pattern of hits in the tracker is not likely to produce a track; (iv) events whose tracks are consistent with the individual ACD tiles that were hit but the energy deposited in the calorimeter is below the programmable amount (~ 5 GeV); and (v) events with no rudimentary track, which can be performed at an early stage when the tracks are being constructed. Additionally, the γ-ray filter accepts all the events that deposited in the calorimeter a total energy above the programmable threshold (~ 20 GeV).

Lastly, the event in question undergoes more strict selection, for instance, the criteria for individual point source analysis (e.g. Figure 3.11). Event reconstruction algorithms are used in order to a obtain high-level event description. In the Pass 8 (Atwood et al. 2013), the current reconstruction flavor of the event analysis, a tree-based tracking approach is used to look at the conversion in the tracker as the start of a shower and attempts to model the process by linking the hits into tree-like structures. For each tree, the longest and straightest branches, defined as the primary and secondary branches, represent the primary electron and positron trajectories if unique, and the sub-branches represent the
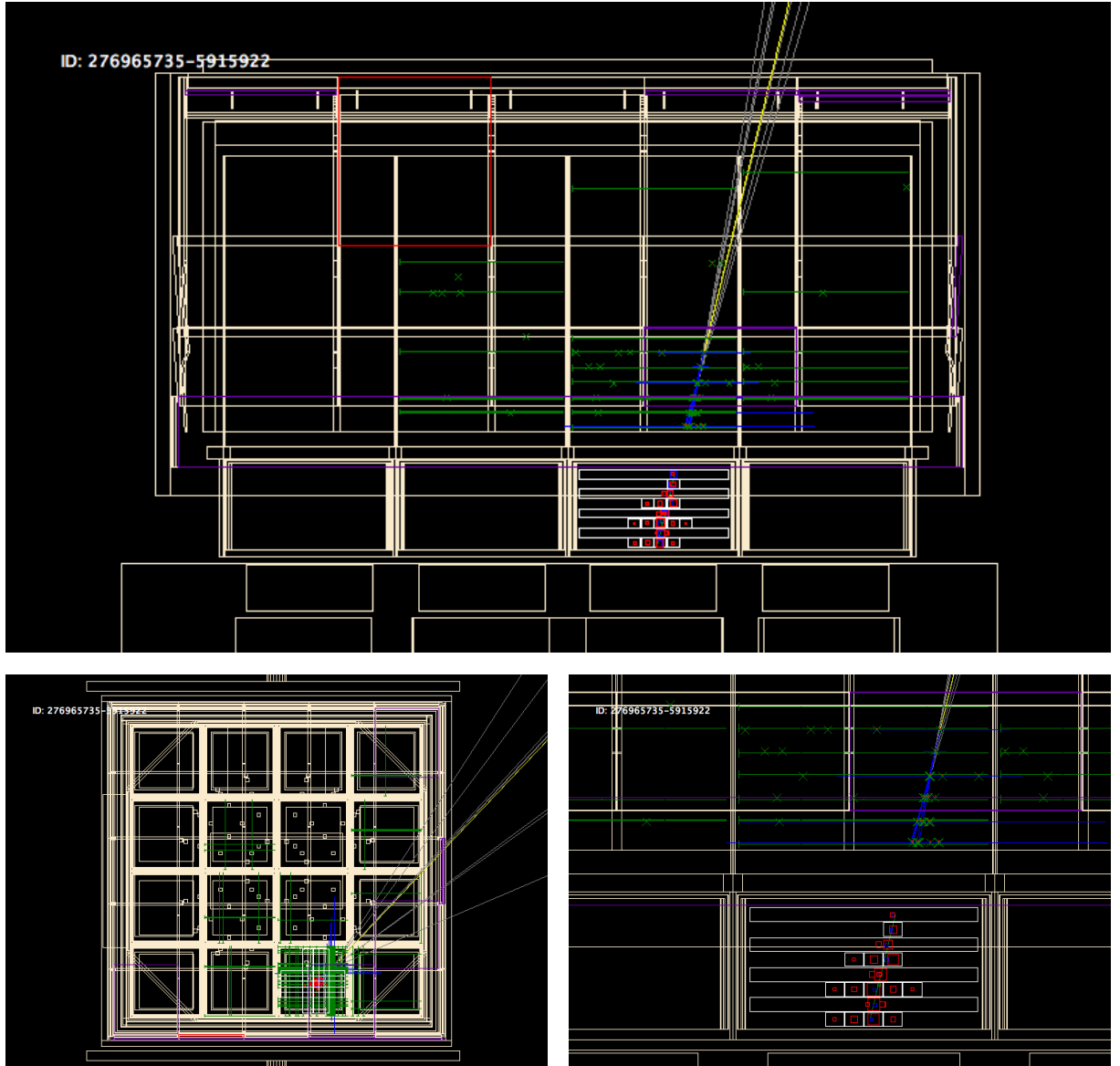
Fig. 3.11.— γ-ray event from 4C +55.17 converted in the back of the tracker, that is contained in one tower and with an estimated energy between 134 GeV and 156 GeV. The small crosses indicate the clusters in the tracker, while the variable size squares represent the reconstructed location and magnitude and energy deposition for each hit crystal in the calorimeter. The green solid line represent the calorimeter axis, the gray solid lines indicate the reconstructed tracker tracks, and the solid yellow line is the true γ-ray direction. Neither the hits in the track nor the hit in the ACD (red square) generated by the backsplash from the calorimeter compromise the algorithm's ability to correctly classify the event as a γ-ray. *Top:* Front view. *Left:* Top view. *Right:* Zoom over the calorimeter. Credits to M. Monzani and the *Fermi*-LAT collaboration.

associated hits originated by the radiation of the electron and positron as they traverse the tracker. The axis of this tree can be found by calculating the moments of inertia of the associated hits, and be used to match the tree to a specific cluster in the calorimeter, which allows the estimation of the energy linked to the tree. Then, up to two tracks

are extracted (primary and secondary branches) and fit using a Kalman Filter technique (Frühwirth 1987) which account for the deviations from multiple scattering and with each track given half the energy from the corresponding cluster. When more than one track is generated, the algorithm attempts to combine them into the vertex expected in a pair conversion.Monte Carlo simulations show that this approach potentially increases the HE acceptance in $15 - 20\%$ with respect to the previous reconstruction flavor (Pass 7; Atwood et al. 2009), and an even greater improvement in the off-axis effective area, especially for photons that convert in the lower part of the tracker.

In the Pass 8 event reconstruction procedure, the three-dimensionality of the calorimeter readout is used to exploit a concept from graph theory, called Minimum Spanning Tree construction, to identify ghost signals that introduce substantial errors in the measurement of the energy, centroid and direction of the shower; which results in genuine γ-ray events being misclassified as background. This approach provides a $5 - 10$ % increment in the effective area above ~ 1 GeV and with a potentially greater effect below a few hundred MeV (where the energy of the ghost signal can be of the same order of magnitude or greater than that of the triggering γ-ray) with respect to that of Pass 7 which made no attempt to identify contamination from ghost signals.

The ACD reconstruction in the Pass 8 incorporates calorimeter information when linking the direction of the incident particle with the energy deposition in the ACD, in addition to the tracks derived from the tracker. Adding the more robust directional information from the calorimeter becomes particularly important for events with high energies or large incident angles, which are more susceptible to tracking errors. Additionally, Pass 8 also uses the fast ACD signals provided to the LAT trigger to attenuate the impact of the ghost signals in the ACD; particularly important at low energies at which the calorimeter backsplash is minimal and a small energy deposition in the ACD can cause the rejection of the event and therefore a potential significant reduction in the effective area.

The LAT Collaboration uses a classification tree analysis to select candidate γ-rays based on the outputs of the event reconstruction process from all the three LAT subsystems briefly explained above. This outputs are event-by-event arrays of quantities such as energy, direction and estimates of the probability a given event is a γ-ray. The classification tree performance is evaluated by combining the background rate and γ-ray acceptance that can be obtained for a given cut on the output signal probability. For instance, a differential background rate equal or not considerably lower than that of the extragalactic background light desirable for point-source analysis (corresponding to the *_SOURCE_*[4] class). All event classes comprise a selection of events with a reconstructed track that deposits ≥ 5 MeV in the calorimeter, a pre-selection of events that such that the reconstructed track points to an activated section of the ACD, and an energy-dependent cut on the classification tree variables for the particle type and the angular reconstruction quality. The event classes are optimally defined for a number of astrophysical source analyses; and are nested, that is, each succeeding selection is a strict subset of the pre-

---

[4]Later, the Pass flavor and version will be specified in the places here occupied by asterisks.

vious one, e.g. passed on-board filter $\supset$ *_TRANSIENT_* $\supset$ *_SOURCE_* $\supset$ *_CLEAN_* $\supset$ *_ULTRACLEAN_*; each class with an even tighter or similar cut on the probability that a given event is a γ-ray than the subset that contains it, among other cuts.
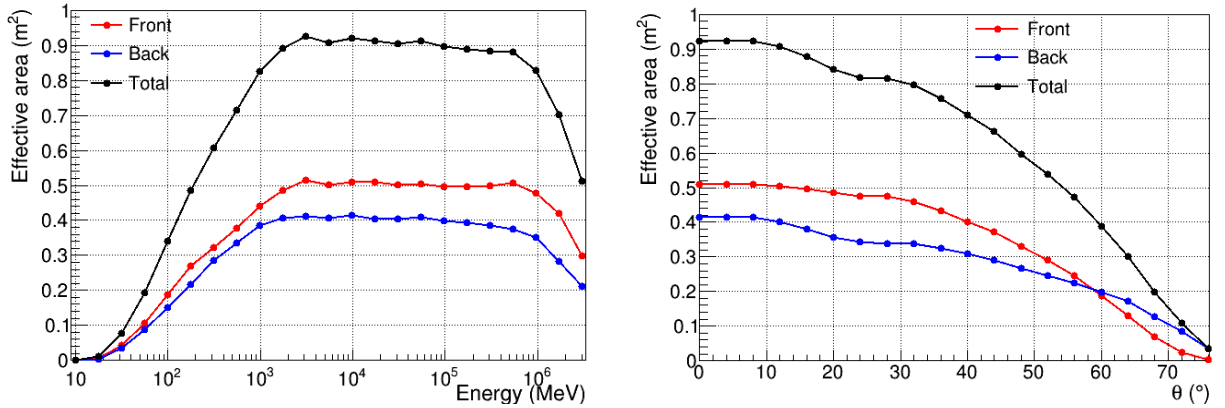
3.2.1.2. Instrument Response Functions

Fig. 3.12.— *Left:* P8R3_SOURCE_V2 **on-axis effective area.** *Right:* P8R3_SOURCE_V2 **effective area averaged over the azimutal angle at 10 GeV. From Atwood et al. (2007) and the** *Fermi*-**LAT collaboration.**

The performance of the LAT detector depends mainly on the instrument design, the event reconstruction software, and the background and event quality selections. A compilation of all this information is called the instrument response functions [5] (IRFs). A number of upgrades to the IRFs have taken place since the start of the mission; as mentioned above, the last major one is called Pass 8 (Atwood et al. 2013). In particular, the Pass 8 selection P8R3 considers after-launch effects, unlike former selections, and also the reduction of the background excess found from the leakage of heavy ions and cosmic rays through the ribbons of the ACD (Bruel et al. 2018). The main detector properties characterized by the IRFs are:

(i) Effective area: this part of the IRFs characterize how the photon collecting area depends on the energy and on the angle of incidence (θ, ϕ).

(ii) Point Spread Function: this part of the IRFs characterize how the reconstructed photons are dispersed around their true direction in the sky as a function of the energy of the incoming photon. Note that it can be difficult to resolve neighboring sources because it is difficult to reconstruct the event associating its true source (see Section 4.7.1 on the search for possible correlations between the results obtained for two close by sources).

(iii) Energy dispersion: this part of the IRFs characterizes how reconstructed photons are dispersed around their true energy.

---

[5]https://www.slac.stanford.edu/exp/glast/groups/canda/lat_Performance.htm
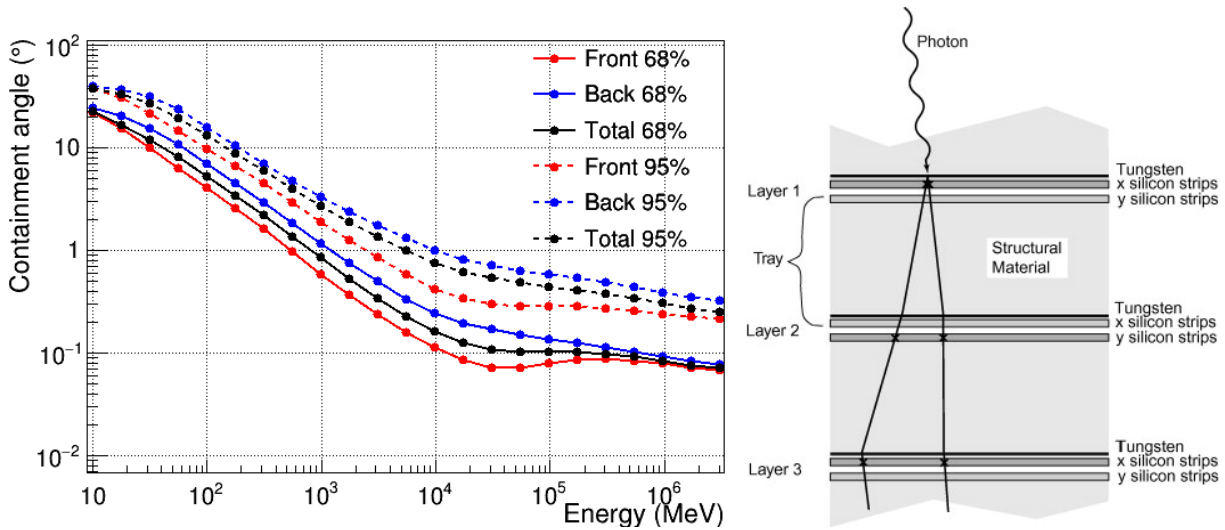
Fig. 3.13.— *Left:* **The weighted point spread function (PSF) at normal incidence for IRF** `P8R3_SOURCE_V2`**.** *Right:* **Pair conversion in the LAT. The scattering in successive layers impacts the angular resolution, or PSF. From Atwood et al. (2007) and the** *Fermi-***LAT collaboration.**

There is a specific set of IRFs for each event class[6]. Additionally, the IRF for each class is divided into FRONT and BACK conversion types. The PSF of the FRONT events (at the front of the LAT) is better by a factor of approximately two than the PSF for the BACK events (at the back of the LAT). As shown in Figure 3.13, multiple scattering in successive layers reduces the angular resolution. The higher the energy of the event, the less impacted the reconstruction is. The thinner the detector layers and the closer to the tungsten foils, the less impacted the event reconstruction is by scattering after the first layer of tungsten. The IRF set employed must complement the event selection used in analysis.

3.3.   The Neil Gehrels *Swift* Observatory

The Neil Gehrels *Swift* Observatory is a multi-wavelength space telescope that carries three coaligned instruments, the Burst Alert Telescope (BAT; Barthelmy et al. 2005) for observations in the 15–150 keV band, the X-Ray Telescope (XRT; Burrows et al. 2005) that covers the 0.2–10 keV band, and the UV/Optical Telescope (UVOT; Roming et al. 2005) that operates in the 170–600 nm wavelength range. *Swift* was launched on 2004 November 20. Originally conceived as a 2-year mission, *Swift* has been active for 15 years and has become one of the most successful missions in the X-ray band, even though it

---

[6]Events are classified according to their photon probability and the quality of the reconstruction. See `https://fermi.gsfc.nasa.gov/ssc/data/analysis/documentation/Cicerone/Cicerone_Data/LAT_DP.html`.

works in pointing mode only. Although it was mainly designed for GRB detection and as a GRB alert generator, it is today one of the main sources of X-ray data for AGN studies. Moreover, it has become the main receptor of target of opportunities (ToO) requests to follow up on the high γ-ray activity of AGNs triggered by the Flare Advocate (FA) monitoring program within the *Fermi*-LAT Collaboration.
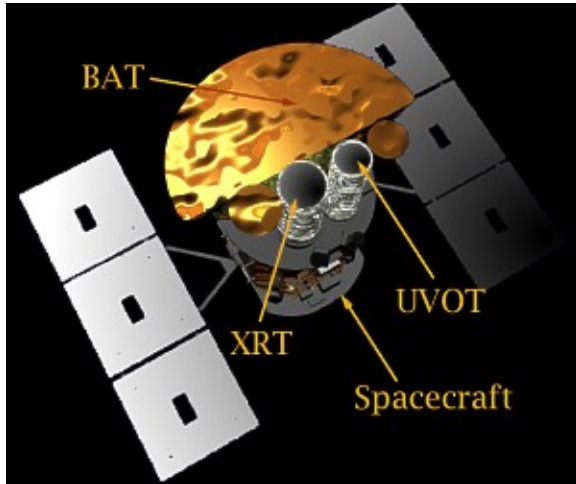

Fig. 3.14.— The Neil Geherls Swift Observatory exhibiting the three detectors on board.

The main task of the wide-FoV BAT is to locate transients, such as GRBs, and to trigger fast alerts within 20 s that would allow the pointing of the other two narrow FoV instruments, XRT and UVOT, to the desired location within 70 s. It has an energy resolution of ≈ 7 keV, a sensitivity of $\approx 10^{-8}\,\mathrm{erg\,cm^{-2}\,s^{-1}}$, and a FoV of 1.4 sr. The BAT works in an all-sky survey mode for the hard X-ray energy band, and has a sensitivity of ≈ 2 mCrab. As an all-sky instrument, the BAT would have been ideal for the study of 1ES 1215+303, however, the source was not found in the *Swift* BAT 105-month hard X-ray survey[7], and the available light curve did not show significant features that we could analyze due

the large uncertainties[8]. Thus we were not able to explore this possibility.

3.3.1. The *Swift* XRT data from 1ES 1215+303

The XRT is a grazing-incidence focusing X-ray telescope with a sensitivity of $2 \times 10^{-14}\,\mathrm{erg\,cm^{-2}\,s^{-1}}$ in 10^4 s (Gehrels et al. 2004). It has an effective area above 120 cm^2 at 1.5 keV and a FoV of 23.6×23.6 arcminutes^2 with an angular resolution of 18 arcseconds. The XRT can also measure the redshift of transients with the Fe emission line, among others. The XRT was designed to rapidly follow-up on the alerts triggered by the BAT in order to measure the position of the burst with high accuracy, its spectrum and light curve.

The instrument requires a number of readout modes in order to optimise the information collected as the flux from the source decreases throughout the seven orders of magnitude in flux that the instrument is capable of covering to exploit its scientific capabilities. In the following, I briefly discuss two of the modes in which the data we made use of were taken; they are the photon counting (PC) mode, and the window timing (WT)

---

[7]https://swift.gsfc.nasa.gov/results/bs105mon/

[8]https://swift.gsfc.nasa.gov/results/transients/weak/QSOB1215p303/

mode. The WT is a high gain and timing resolution mode (2.2 ms) with 1-D position information and spectroscopy in the fluxes in the range 1–600 mCrab. Above these fluxes, more than one X-ray are allowed per pixel, a feature also known as "pile-up", in order to measure positions are high fluxes using a low gain. The PC is a high gain, 2.5 s integration mode with 2-D position information and in the fluxes below 1 mCrab spectroscopy. This mode operates at these low fluxes and with a limited timing information to prevent a pile-up caused by a relatively long integration time.

There were 25 pointed *Swift*-XRT observations within a 10' radius of 1ES 1215+303, 20 of which were taken in PC mode, and five in WT mode. Only five observations were taken after 2013, one on 2014 Feb 9 and four between 2017 Apr 15 and 2017 Apr 23, all of which were triggered by elevated TeV γ-ray fluxes detected by VERITAS. See (Valverde et al. 2020) for details on this analysis.

3.3.2.   The *Swift* UVOT data from 1ES 1215+303

The UVOT has a 17×17 arcminutes^2 FoV, an 11-position filter wheel and is able to detect a B-star of magnitude 24 with white light in 100 s. The UVOT made many observations of 1ES 1215+303 during the time period under study in this manuscript. Specifically, 232 images containing 1ES 1215+303 in the field of view were available (31 with the V filter; 36 with the B filter; 40 with the U filter; 46 with the UVW1 filter; 42 with the UVM2 filter; 37 with the UVW2 filter) and they span the date range from 2009 December 03 (MJD 55168) to 2017 April 23 (MJD 57866). Since UVOT is co-aligned with the XRT, the temporal sampling of the observations from the two instruments is the same. See (Valverde et al. 2020) for details on this analysis.

3.4.   The Tuorla program

Fig.   3.15.— Tuorla Observatory in Finland.

The Tuorla blazar monitoring program (Takalo et al. 2008; Nilsson et al. 2018) started in September 2002 as an optical monitoring support for the VHE MAGIC telescopes in the Roque de los Muchachos Observatory in La Palma, Spain. In 2004, the Kungliga Vetenskapsakademien (KVA) telescope, located also in La Palma, was added to the Tuorla program. Nowadays, the observations have been extended to blazars not necessarily only observed by MAGIC, and also include sources from the southern hemisphere. Thus, the observations were made with two different telescopes, the 1.03 m Dall-Kirkham based at the Tuorla Observatory in Piikkiö, Finland, and the KVA. The Dall-Kirkham telescope has a FoV of 10×10 arcminutes and a focal length of 8.45 m. 3–8 sets of observations of 60 s each are performed, depending on the brightness of the source of interest, using a *R*-band filter. KVA

comprises two telescopes, one of 60 cm and another of 35 cm mounted on the 60 cm telescope. This system is operated remotely from Finland with exposure times of 9–24 min depending on the source brightness. 1ES 1215+303 was monitored in the R-band at the Tuorla Observatory over the past 15 years as part of the Tuorla blazar monitoring program.

Fig.   3.16.— **The Nordic Optical Telescope.**

1ES 1215+303 was monitored with the Nordic Optical Telescope (NOT), making use of the Alhambra Faint Object Spectrograph and Camera [9](ALFOSC) which has a FoV of 6.4 × 6.4 arcminutes[2]. The ALFOSC instrument was used in the standard setup for linear polarization observations ($\lambda/2$ retarder followed by a calcite). The observations were performed in the R-band from 2014 to 2017 two to four times per month. The data were analyzed as in Hovatta et al. (2016) with a semi-automatic pipeline using standard aperture photometry and comparison-star procedures.

3.4.1.   Very Long Baseline Array

Fig.   3.17.— **The transcontinental Very Long Baseline Array radio interferometer.**

The Very Long Baseline Array (VLBA) is a transcontinental interferometer comprising ten 25 m antennas separated by 200–8600 km, that is based in Hawaii, California, Washington, Arizona, New Mexico, Texas, Iowa, New Hampshire and St. Croix-Virgin Islands, U.S.. Each telescope is controlled remotely and their data are taken independently to then be sent to the Science Operations Center in Socorro, New Mexico, to be correlated. VLBA observes the radio sky in the range 0.312–96 GHz in narrow/discrete bands. VLBA can be combined with other very long baseline interferometry (VLBI) in-

---

[9]http://www.not.iac.es/instruments/alfosc/

struments in Europe or the U.S. (such as the Karl G. Jansky Very Large Array, VLA) to improve its sensitivity.

1ES 1215+303 was observed with the Long Baseline Observatory's VLBA at 22 and 43 GHz on 2014 November 11 (with observation code S7017E3). About two hours of on-source integration time was recorded at each frequency, over a total time span of about seven hours.

3.4.2.   OVRO

Fig.   3.18.—   The Owens Valley Radio Observatory at 15 GHz.

The Owens Valley Radio Observatory (OVRO) at 15 GHz is a 40 m radio telescope located in the Owens Valley, California.   In 2007, the OVRO collaboration started the 15 GHz radio monitoring program with this telescope, to coincide with the launch of the *Fermi*-LAT mission.   Today, OVRO monitors more than 1800 blazars, each observed as frequently as twice a week, with a minimum flux of about 4 mJy and 3% uncertainty.   The procedure of the OVRO data reduction and calibration procedures can be found in Richards et al. (2011).

3.4.3.   Metsähovi
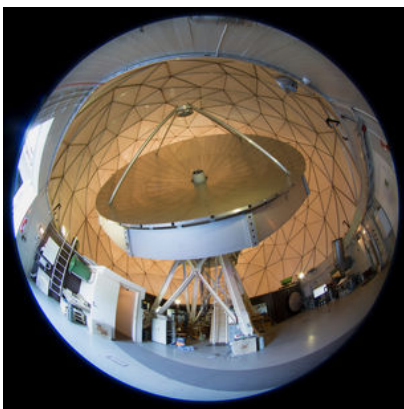
Fig.   3.19.—   The Metsähovi Radio Observatory.   From the Metsähovi Collaboration.

The Metsähovi Radio Observatory[10] (MRO) 37 GHz data reduction and analysis procedure can be found in Teräsranta et al. (1998). 20% of the 37 GHz data points have a $S/N < 4$ and are considered non-detections. Since 2013, the Metsähovi team stores 4σ upper limits from observations. The upper limits of the data before year 2013 can be obtained by multiplying the uncertainty of the non-detection data points by 4. They are therefore not constraining for a faint source such as 1ES 1215+303 at these wavelengths. It should be noted that, in many cases, these upper limits should be interpreted as the source being on the verge of the detection limit. The detection limit of the Metsähovi telescope can vary from

---

[10]https://www.aalto.fi/en/metsahovi-radio-observatory

approximately 0.2 Jy in optimal conditions to approximately 0.5 Jy on a humid and cloudy day. The data are considered of good quality even if the conditions of observation were not optimal, as long as they are stable.

4.   *FERMI*-LAT DATA ANALYSIS

Fig. 4.1.— *Fermi*-LAT sky with seven years of collected data > 1 GeV.

The *Fermi* Large Area Telescope, *Fermi*-LAT or LAT, is the main detector of high energy γ-rays currently in operation[1]. The availability of these data has significantly advanced the studies of many γ-ray emitters including AGN, pulsars, supernova remnants, gamma-ray bursts and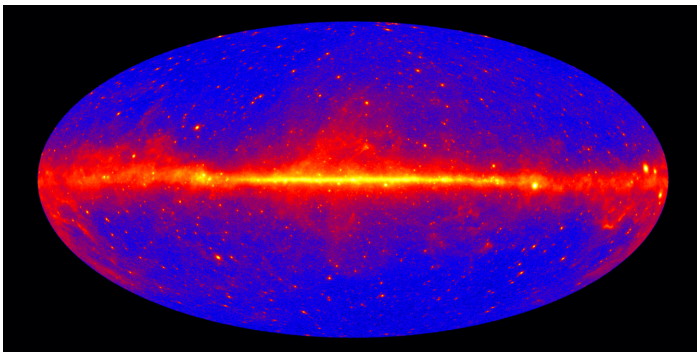 the Sun, while also providing a $3.5\,\sigma$ indication of cosmic neutrinos from a γ-ray blazar (IceCube Collaboration et al. 2018b) thus opening the window on multi-messenger astronomy. I dedicate this chapter to the details of the *Fermi*-LAT γ-ray data reduction, which all of these fields have in common. As mentioned in previous chapters, this manuscript centers on the detailed long-term multi-wavelength study of the BL Lac object 1ES 1215+303, whose LAT data I analyzed. Therefore, even though I provide the detailed views and results from this thorough analysis, the tools and methods employed could equally be applied to the study of most other *Fermi*-LAT sources. The discussion of the physical interpretation of the results presented in this chapter are discussed in Chapter 5.

4.1.   The *Fermi*-LAT γ-ray sky

I adopt the *Fermi*-LAT standard procedure to determine the γ-ray emission from cosmic objects. This consists of assuming the presence of certain objects at a position in the sky that have specific parameterized spectral shapes for their photon emission; the

---

[1]AGILE (30 MeV – 50 GeV Tavani et al. 2009), another major γ-ray telescope has been active since 2007. See Table 3.2.

data collected by the LAT are then fitted to the model built for the emission of all of these sources. The determination of the emission of a source depends, therefore, on how well this model can describe the γ-ray data. In the following, I briefly describe the sources of γ-ray events that are included in this model.
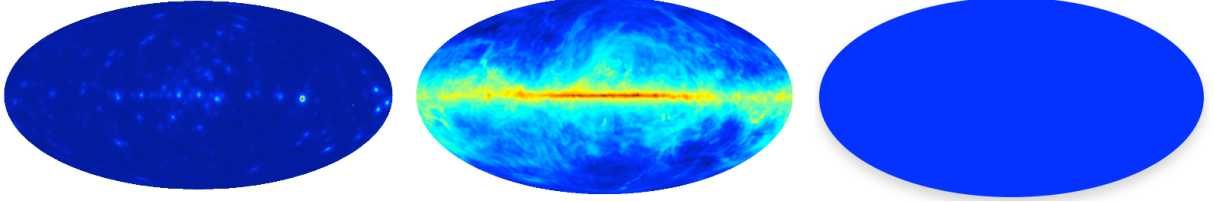
Fig. 4.2.— **The LAT γ-ray sky is parameterized assuming that it comprises three different components classes of astrophysical photons.** *Left:* **Astrophysical sources.** *Middle:* **The galactic diffuse emission consisting of γ-rays produced in the interaction of cosmic rays with galactic gas. From Acero et al. (2016).** *Right:* **Isotropic, unresolved diffuse γ-ray background.**
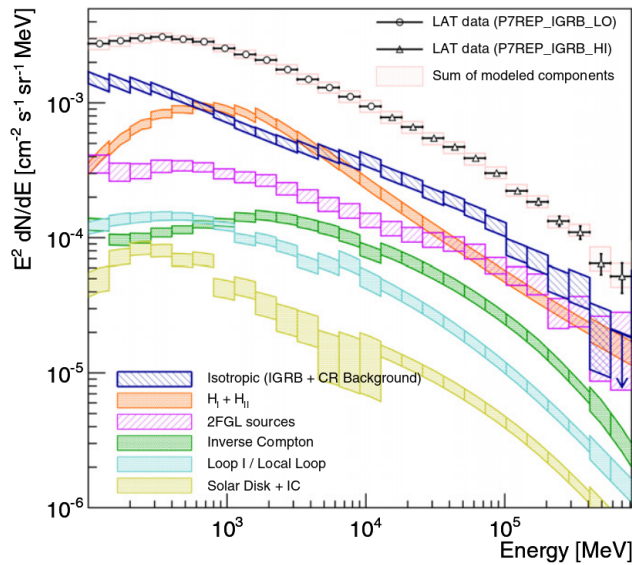
Fig. 4.3.— **Fitted components for LAT γ-ray data with latitudes $|b| > 20°$. From Ackermann et al. (2015b).**

The *Fermi* Space Telescope operates, most of the time[2], in all-sky scanning mode, that is, it collects photons while scanning the entire sky every three hours. Therefore, we need to account for as many sources as there are in the universe to which the LAT is sensitive when modeling the data. Our limited knowledge thus prevents us from building the "perfect" model. Moreover, since the LAT continuously monitors the sky, it allow us to describe its γ-ray emission with a gradually improving precision. The LAT analysis includes the following possible astrophysical sources of γ-ray events in the model file:

(i) Point-like and extended sources: These are celestial objects that have been detected at a significant level by the LAT and include source classes such as AGNs, pulsars,

---

[2]Other modes are pointed observations, such as Targets of Opportunity (ToO) and Automatic Repoint Requests (ARR). Details on the *Fermi* observing timeline can be found in `https://fermi.gsfc.nasa.gov/ssc/observations/timeline/posting/`

supernova remnants, binaries[3] as well as unidentified point sources of γ-rays. The most recent LAT catalog, 4FGL (Abdollahi et al. 2020), described here in Section 2.4, reports on the detection of 5065 ($> 4\,\sigma$) HE γ-ray sources.

Some of these sources tend to vary significantly in time. This is the case for blazars, as discussed in Sections 2.3.1 and 2.4. A temporal analysis can thus provide crucial information on these sources in addition to a spectral analysis. The procedures are later described for both these analyses.

(ii) Galactic diffuse emission: The galactic interstellar medium produces γ-ray photons due to the interaction of interstellar nucleons and photons with energetic cosmic rays (Acero et al. 2016). This emission is thought to originate from the decay of secondary particles produced when hadrons collide (mainly π^0-decay), from the inverse Compton (IC) scattering of the interstellar radiation field by electrons and from their bremsstrahlung emission. The diffuse γ-ray emission from the Milky Way is approximately five times greater than that of the point sources above $50\,\mathrm{MeV}$. It represents a celestial foreground for the detection of γ-ray point sources, which decreases as we look away from the galactic plane.

(iii) Isotropic diffuse γ-ray background (IGRB): This component comprises the residual galactic isotropic foreground and the emission from unresolved sources such as AGNs, star-forming galaxies, radio galaxies as well as other source classes. The IGRB also includes a small contamination from residual charged particles and from the Earth-limb that enter the LAT from the back. The IGRB thus depends on how the events are classified (event class) and on the part of the LAT where the conversion took place (conversion type).

4.2.   Data Structure

The LAT data can be accessed through the *Fermi* astro-server[4]. The coordinates of the source of interest (RA, DEC, in degrees) in addition to the time range of interest (TSTART, TEND, in seconds) must be provided. The search radius (Rad, in degrees) and energy range (EMIN, EMAX, in MeV) must also be specified.

Special care should be taken when providing the search radius. I worked with data of energy above 100 MeV. The highest value that the point spread function (PSF) will attain is at the lowest energy (100 MeV; see Figure 3.13), and corresponds to a radius of approximately 10° around the photon best-fit position. Therefore, for an unbinned analysis (see Section 4.3), a $\approx$10° radius circle (centered at the source of interest) would be minimally necessary. This region is called region of interest (ROI). For a binned analysis

---

[3]For a full list of source classes detected by the LAT see Abdollahi et al. (2020).

[4]`http://fermi.gsfc.nasa.gov/cgi-bin/ssc/LAT/LATDataQuery.cgi`

(see Section 4.3), however, a square ROI containing a $\approx 10°$ circle will be minimally necessary, that is, data up to $\approx 10\sqrt{2}^{°}$ should be included[5]. Therefore, the search radius should be greater than the selected size of the ROI by at least a couple of degrees to avoid the known issue in which the analysis tools interpret data as missing when performing cuts.

The result of the query are files in the Flexible Image Transport System (FITS) format, whose names consist of the query ID string with an identifier appended to indicate which database the file came from, _DDNN. DD=PH for photon file, or SC for Spacecraft file (Spacecraft pointing, livetime and history); NN is the file number. The FITS format has three Header Data Units (HDU); the Primary one (with index= 0) is reserved for an image, even if it is empty; the Events HDU (index= 1) is a table containing all of the data. The GTI header unit (index= 2) details the Good Time Intervals (GTIs) for this file. The photon file contains information on the reconstructed direction, energy, and time of arrival of the events as well as their class and conversion type. The SC file contains information about the spacecraft livetime, position, pointing, functioning mode, the quality of the data, whether it is in the south atlantic anomaly (SAA) region (where the Earth's magnetic field is weaker and therefore the radiation stronger), as well as other house-keeping information. This information is divided into bins of a maximum length of 30 s, which make up the rows in the HDU 1 of the SC file. A detailed description of the content of these files can be found on the *Fermi* Science Support Center (FSSC) page [6].
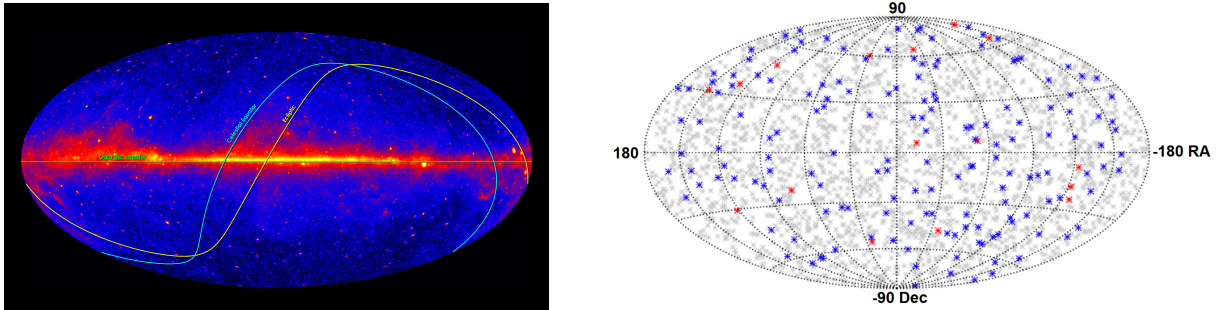
Fig. 4.4.— *Left:* **Annual apparent path of the Sun (ecliptic). From the *Fermi*-LAT collaboration. *Right:* Second *Fermi*-LAT GRB catalog. Gray points are GBM-triggered, while color dots indicate LAT-detected GRBs. From Ajello et al. (2019).**

Before any LAT analysis is undertaken, one must check if any solar flares, gamma-ray bursts or passages of the Moon occurred near the ROI of the source during the time period under investigation. The γ-ray emission from Sun has an extended pattern ($\lesssim 20°$), it is thus expected that the diffuse components results will be biased by its emission. For

---

[5]Data $\approx 10°$ beyond could also be included if the goal were to properly model the other sources in this region, for both, binned and unbinned analyses.

[6]https://fermi.gsfc.nasa.gov/ssc/data/analysis/documentation/Cicerone/Cicerone_Data/LAT_Data_Columns.html

instance, the variation of the normalization of the diffuse components can be observed in Figure A.3 and A.4 for the FSRQ 3C 279 when the Sun is in the ROI. Building templates of the quiescent Sun and Moon to account at least for their baseline emission is therefore advised (Abdo et al. 2011b, 2012). The flux of the quiescent Sun is $F_{0.1-10\,\mathrm{GeV}} \sim 0.5 \times 10^{-6}$ ph cm^{-2} s^{-1}. The Moon flux is $F_{0.1-3\,\mathrm{GeV}} \sim 1 \times 10^{-6}$ ph cm^{-2} s^{-1}. Figure 4.4 shows the ecliptic (annual apparent path of the Sun) in the left panel. Depending on the binning size chosen for the light curve and the brightness of the GRB, they can appear as flaring episodes. It is therefore better to excise the GRB periods and work with a clean dataset. For a list of the GRBs detected during the first decade of the mission, see the second GRB catalog (Ajello et al. 2019).
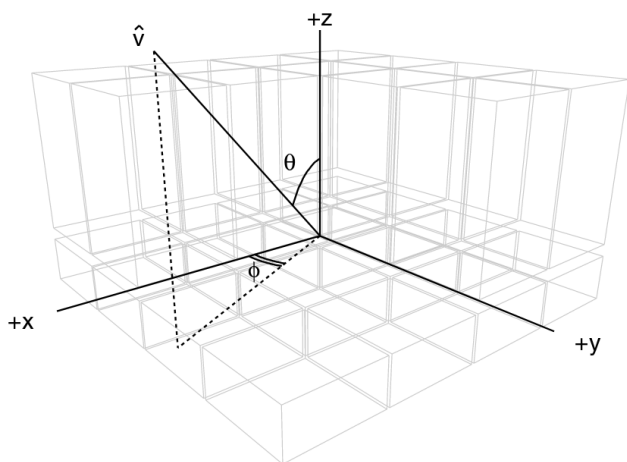

Fig. 4.5.— Definition of the coordinate system and angles (θ, ϕ) used in the LAT. The 16 calorimeter and 12 of the 16 tracker modules are also represented. From Ackermann et al. (2012a).

Simple cuts in the downloaded data allow us to identify the astrophysical photons so that we can study the objects of interest. For most analyses, the FSSC recommends[7] that events with energies 0.1–500 GeV, of the SOURCE class[8] and from both the FRONT and BACK types (internally referred to as evtype = 3) be selected. The FSSC also recommends that only events with a maximum zenith angle, θ (see reference frame in Figure 4.5), of $\theta \leq 90°$ be retained so as to reduce contamination from the Earth's limb. It is also necessary to filter the data so that we only use those taken during the GTIs, and those that are of good quality (DATA_QUAL> 0).

Figure 4.6 shows how the data look after these cuts. In Figure 4.6 (a), the influence of the angular dependence of the effective area can be appreciated, (see the right-hand side of Figure 3.12). Small features or peaks are noticeable in Figure 4.6 (c). They are coincident with the distance of other sources from 1ES 1215+303 in the 10° ROI. The

---

[7]https://fermi.gsfc.nasa.gov/ssc/data/analysis/documentation/Cicerone/Cicerone_Data_Exploration/Data_preparation.html

[8]After the LAT data are downlinked from the spacecraft, the reconstruction of interaction of the events (or their products) with the different parts of the LAT is performed. Then the events are classified based on the quality of the reconstruction and their photon probability. Events are thus classified into classes, which are then subdivided into types. The conversion types are based on the topology (FRONT/BACK), the PSF and the energy dispersion. In this work, the SOURCE class is used (internally referred to as evclass = 128), which is the result of a trade off between lower background contamination and a lower effective area. For details see Section 3.2.1 and: https://fermi.gsfc.nasa.gov/ssc/data/analysis/documentation/Cicerone/Cicerone_Data/LAT_DP.html
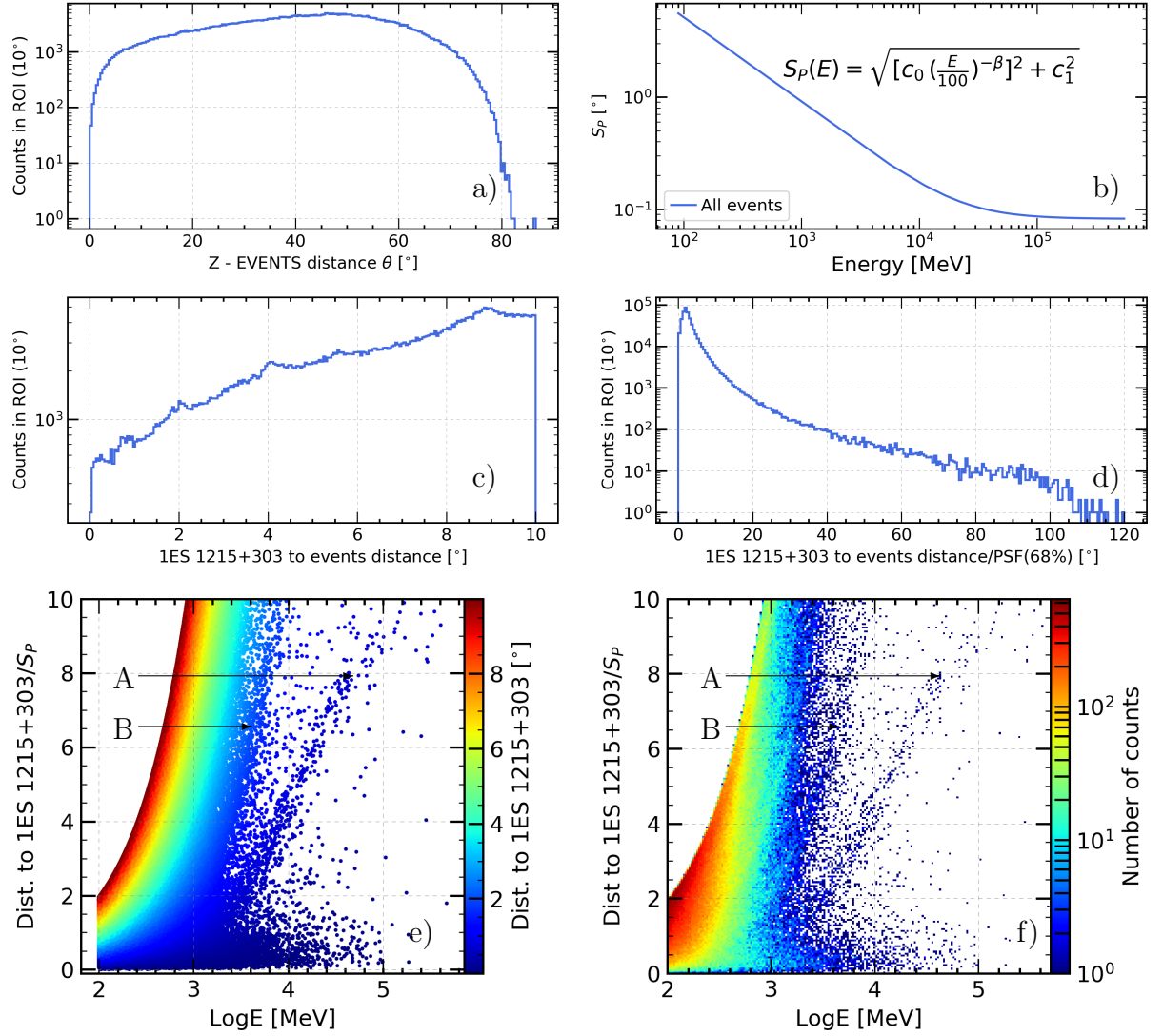
Fig. 4.6.— (a) **Distribution of the distance of the events from the Z-axis.** (b) **Average PSF with 68% containment.** (c) **Distribution of the distance of the events from 1ES 1215+303.** (d) **Distribution of the distance of the events from 1ES 1215+303 divided by the PSF in (b).** (e) **Distribution of event distances from the source (1ES 1215+303) as a function of energy and PSF-scaled distance from the source.** (f) **Distribution of the number of events as a function of energy and PSF-scaled distance from the source. The traces labeled A and B correspond to the blazars 1ES 1218+304 and 3FGL J1225.9+2953 respectively, the closest ones to 1ES 1215+303.**

quantification of the flux and spectrum of the sources in this ROI is the primary goal of the LAT analysis. Figure 4.6 (b) shows the average 68% containment radius curve (PSF 68%). The values of the parameters in this curve are $C_0 = 5.11°$, $C_1 = (8.22 \times 10^{-2})°$ and $\beta = 0.76$. The division of the distance of the events from 1ES 1215+303 by the PSF (68%) provides an idea of the impact of the PSF on the distribution of the events with a possible origin in 1ES 1215+303; the greater the PSF distance, the less likely it is that those photons came from the position of this source. The traces visible in Figures 4.6
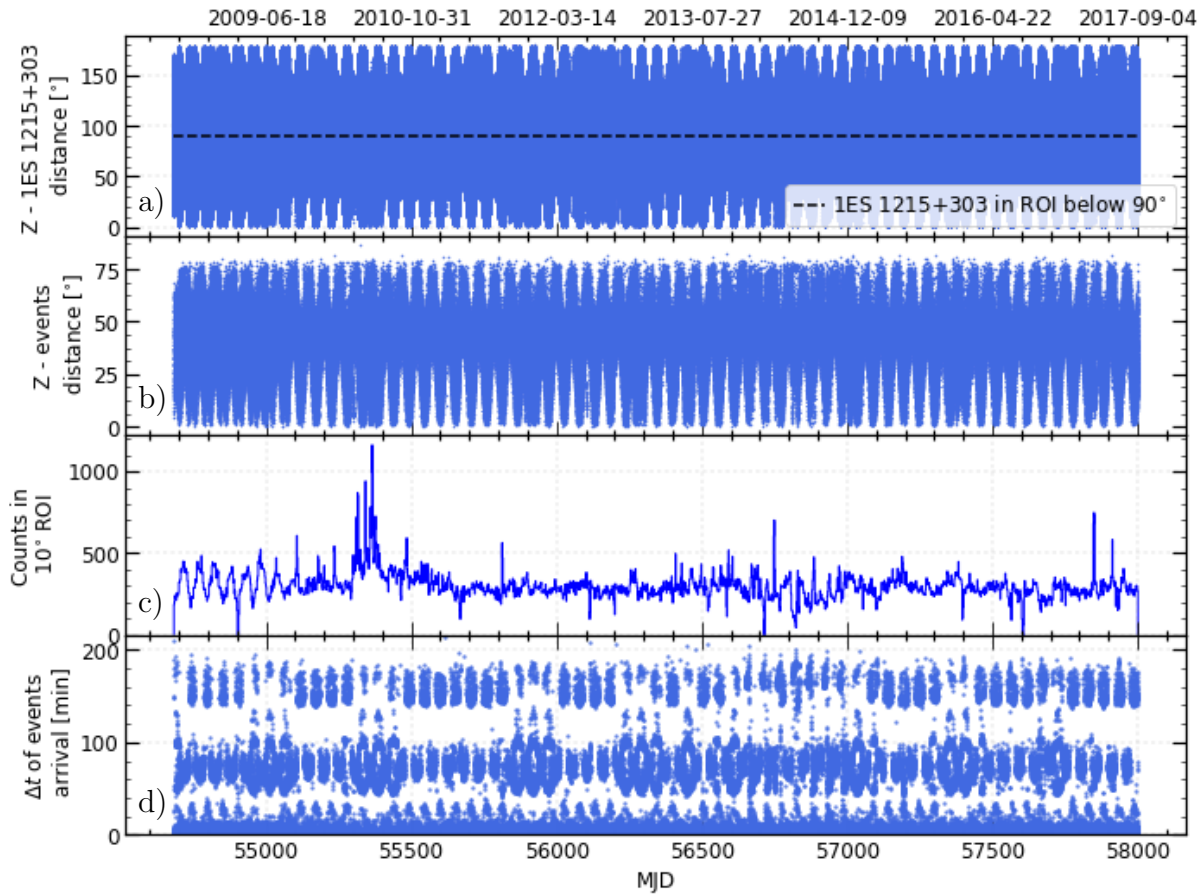
Fig. 4.7.— Panorama of the data in Figure 4.6 as a function of time. (a) Angular distance from the Z-axis to 1ES 1215+303 according to the information in the spacecraft file. The black dashed line indicates the maximum zenith angle cut imposed on the photon data to reduce contamination from the Earth's limb. (b) Angular distance from the events to the Z-axis. Due to the zenith angle cut made, this distance is $\leq 90°$. (c) Distribution of the arrival times of the events from all of the sources in the $10°$ ROI. So far, the exposure has not yet been taken into account. (d) Difference in arrival time from consecutive events versus time of arrival. Notice the clustering of these points around ~ 90 min. and ~ 180 min., the characteristic orbital and one-complete scan period of the *Fermi*-LAT.

(e) and (f) correspond to other point sources in the ROI, in particular, 1ES 1218+304 (labeled A), at a distance of $0.76°$ from 1ES 1215+303, visible in blue almost parallel to the main red contour that represents the events more distant ($\approx 10°$) from the position of 1ES 1215+303. The trace right above this one corresponds to 3FGL J1225.9+2953 (labeled B), $1.77°$ away from 1ES 1215+303. The cuts in ROI size, energy and zenith angle can be noticed throughout these figures.

Due to the fact that the LAT sees the entire sky every 3 hours, one of the most important features of the LAT data is their potential to enable the study of the variability of astrophysical sources. Figure 4.7 provides a panorama of the data in Figure 4.6 as a function of time, since 2008 Aug. 04 (MJD 54682.7), the start of the mission, up until 2017 Sep. 04 (MJD 58001.0). The first panel from the top shows the distance of the

Z-axis of the spacecraft from 1ES 1215+303 for each 30-second bin in the SC file. In the second panel from the top, the zenith angle cut performed on the photon file data of the ROI and the characteristic spacecraft flight period of 54 days[9] are discernible. The next step is to separate the contributions from the known individual sources in the 10° ROI, centered at the position of 1ES 1215+303, from the background photons. The standard method to do this, used by the *Fermi*-LAT Collaboration and recommended by the FSSC, is through a Maximum Likelihood (ML) analysis. In this method, the flux of each of the putative sources in the ROI is parametrized and convolved with the IRFs, as in Equations (4.5) and (4.8), and fitted in order to find the best parameter values for the models used. To this end, a series of tools provided by the *Fermi*-LAT collaboration and the FSSC are used for the preparation of the data for the fit, for the fit itself, and to perform sanity checks. These tools are known as the `Fermi Science Tools`, and are described in Section 4.4.

4.3.   *Fermi*-LAT Statistical Analysis

At this point, we need a method to extract and interpret the measurements with the LAT. We need to address the questions of whether a source is significantly detected, what kind of spectrum it has, or whether it is variable. We need to know whether we can extract information on the flux of the source and its spectral indices. As mentioned before, the LAT uses the ML method to answer these questions, mainly because it provides an unbiased minimum variance estimate of the parameters of interest as the sample size increases; and because it is asymptotically Gaussian, allowing the evaluation of confidence bounds and hypothesis testing (through which the significance is estimated for LAT sources).

The ML requires as input a model that accurately describes the data, which includes the parameters it is to estimate. After this, the first step is to derive the probability density function for the data given the model. This is treated as a function of the model parameters, or likelihood function, which is then maximized with respect to the parameters in order to draw information on the estimation of those parameters. In the following, the spectral parameterizations used to model the emission from LAT active galactic nuclei are presented, then the likelihood functions for two different data processing modes (binned and unbinned) are provided; finally, the hypothesis testing (or test statistics) used in the LAT is introduced.

The sum of the contributions of the individual source spectral and punctual model in each ROI, labeled i and denoted by $S_i(E, \hat{p})$, is given by $S(E, \hat{p}) = \sum_i S_i(E, \hat{p})$, where E and $\hat{p}$ are the true energy and direction vector on the sky. It is assumed that the spatial

---

[9]*Fermi* precesses every 53.4 days so that the 25.6 degree inclination of the axis of its orbit is maintained while enabling the solar panels to point at the Sun for power.

and spectral parts factor, that is $S_i(E, \hat{p}) = s_i(E)\,\tilde{S}_i(\hat{p})$. For instance, for a point source, $S_i(E, \hat{p}) = s_i(E)\,\delta(\hat{p} - \hat{p}_i)$.

The spectral parts of the source models (in units of $\mathrm{cm^{-2}\,s^{-1}\,MeV^{-1}}$) used in this work are:

PowerLaw (PL):

$$s(E) = \frac{dN}{dE}_{PL}(E,\,N_0,\,E_0,\,\Gamma) = N_0 \left(\frac{E}{E_0}\right)^{-\Gamma}, \tag{4.1}$$

where N_0 is the prefactor (in $\mathrm{cm^{-2}\,s^{-1}\,MeV^{-1}}$), Γ is the photon index or spectral parameter, and E_0 is the scale (in MeV).

LogParabola (LP):

$$s(E) = \frac{dN}{dE}_{LP} = N_1 \left(\frac{E}{E_b}\right)^{-(\alpha + \beta \log(E/E_b))}, \tag{4.2}$$

where, N_0 is the norm (in $\mathrm{cm^{-2}\,s^{-1}\,MeV^{-1}}$), α and β are the spectral parameters and the scale, E_b (in MeV), is usually set near the lower energy range of the spectrum being fit and fixed (Massaro et al. 2004).

Power-law Sub Exponential Cutoff (plSECO):

$$s(E) = \frac{dN}{dE}_{plSECO} = N_2\,(E/E_0)^{-\gamma_1}\,e^{-(E/E_c)^{\gamma_2}}, \tag{4.3}$$

where E_c is the cutoff energy (in MeV) and γ_1 and γ_2 are the spectral parameters. When referring to these models, we call $N_{0,1,2}$, the flux parameter, which is in units of $\mathrm{cm^{-2}\,s^{-1}\,MeV^{-1}}$.

The instrument response is given by

$$R(E', \hat{p}'; E, \hat{p}, t) = A(E, \hat{p}, t)\,P(\hat{p}'; E, \hat{p}, t)\,D(E'; E, \hat{p}, t), \tag{4.4}$$

where E' and $\hat{p}'$ are the photon measured energy and direction, $P(\hat{p}'; E, \hat{p}, t)$ denotes the PSF, and $D(E'; E, \hat{p}, t)$ is the energy dispersion, both given by probability density functions. $A(E, \hat{p}, t)$ represents the effective area of the LAT, which is the cross-section for detecting an incident photon with energy E from direction $\hat{p}$ at time t. The time dependence in this expression is necessary, since the sky coordinates of the direction, $\hat{p}$, are not fixed because the LAT pointing changes in time.

The distribution of observed γ-rays is given by:

$$\begin{aligned} M(E', \hat{p}', t) &= \int_{SR} dE\,d\hat{p}\,R(E', \hat{p}'; E, \hat{p}, t)S(E, \hat{p}) \\ &= \sum_i \left[\int_{SR} dE\,d\hat{p}\,R(E', \hat{p}'; E, \hat{p}, t)S_i(E, \hat{p})\right] = \sum_i M_i(E', \hat{p}', t), \quad (4.5) \end{aligned}$$

where SR stands for source region.

4.3.1. Binned Likelihood

For data binned in energy and space $(E', \hat{p}')$, with n_j events in bin j, and θ_j predicted events in this bin, where

$$\theta_j = \int dt \int_j dE' d\hat{p}' M(E', \hat{p}', t), \tag{4.6}$$

over the duration of the observation j (Mattox et al. 1996), the likelihood is given by

$$L = \prod_j \frac{\theta^{n_j} e^{-\theta_j}}{n_j!}. \tag{4.7}$$

4.3.2. Unbinned likelihood

The total number of predicted counts for the ROI then is:

$$N_{\text{pred}} = \int dt \int_{E_{\min}}^{E_{\max}} dE' d \int_{\Omega_{\text{ROI}}} d\hat{p}' M(E', \hat{p}', t). \tag{4.8}$$

If the bins are considered small enough to allocate 0 or no more than 1 event per bin, from Equation (4.6),

$$\theta_j = \delta t \delta E' \delta \hat{p}' M(E'_j, \hat{p}'_j, t),$$

where j labels each event detected by the LAT. In Equation (4.7), since n_j can take values 0 or 1 and for sufficiently small differentials,

$$
\begin{aligned}
\log L &= \sum_j n_j \log \theta_j - \theta_j - \underline{\log n_j!} = \sum_j n_j \log \theta_j - N_{\text{pred}} \\
&= \sum_j \log M(E'_j, \hat{p}'_j, t_j) - \underline{N_{\text{obs}} \log(\delta t \delta E' \delta \hat{p}')} - N_{\text{pred}}
\end{aligned}
\tag{4.9}
$$

4.3.3. *Fermi*-LAT Test Statistic

Hypothesis testing consists in comparing the likelihoods of two hypothesis to find out which one is better supported by the data. A hypothesis in this case would be an assumption about the model that describes the data, in which the parameters have some presumed true values. This is called the null hypothesis. In the case of the LAT analysis, for a specific source or interest, the null hypothesis consists in assuming that this source is not in the ROI, i.e. its presence is removed from the model that describes the data.

The *Fermi*-LAT test statistic (TS) is thus defined as:

$$\text{TS}_{\text{NH}} = -2 \log \frac{L_{\max,0}}{L_{\max,1}}, \tag{4.10}$$

where the ML computed from the null hypothesis (NH) is denoted by $L_{\mathrm{max},0}$, and the one computed using ML for all parameters (i.e. including the parameters of the source of interest) is denoted by $L_{\mathrm{max},1}$.

In the limit of a large number of counts, Wilk's Theorem (Wilks 1938) states that the TS for the null hypothesis is asymptotically distributed as $\chi^2(N)$ where N is the number of parameters, or degrees of freedom (d.o.f.), characterizing the source of interest.

As a basic rule of thumb, the signal from a source is considered significant if a $5\,\sigma$, or equivalently a p-value $\approx 5,7 \times 10^{-7}$, detection was measured. As the TS is distributed as a $\chi^2(N)$, the p-value is given by:

$$\mathrm{p - value} = 1 - F(\chi^2, N),$$

where F is the cumulative distribution function for the χ^2 distribution.

For instance, if the source has one parameter under evaluation in the ML calculation, i.e. 1 d.o.f or $N = 1$, the significance is given by the $\sqrt{\mathrm{TS}}$. Hence, a source with $N = 1$ would be significant if its TS is found to be ≥ 25. On the other hand, a source with $N = 2$ would require a TS ≥ 28.7 to be considered significant.

4.4.   Data Analysis

The *Fermi*-LAT data are analyzed using the `Fermi Science Tools`, (briefly described below), developed by the FSSC and the *Fermi*-LAT instrument team. As mentioned above, spectral and temporal analyses are crucial in the study of blazars, and they consist, at this level, of three parts:

(i) Global analysis: Having chosen the time and energy range of interest, what will be called a "complete analysis" is performed, which is described in Section 4.4.1. In this analysis, the average values for the parameters of the sources in the ROI, for the selected time and energy ranges are calculated. To enable a more rapid convergence, these values are used as the initial values for the model files for later spectral and temporal analyses, which are performed for smaller energy and time ranges. For each source in the model file, a flux and the spectral parameters (e.g. photon index for a power-law model; photon index and break and break energy for a broken power-law model) are calculated.

(ii) Spectral analysis: This step allows us to obtain the source flux in each energy bin. The entire energy range used for the global analysis is divided into a number of parts, usually equally distanced logarithmically. For each of these energy bins, the spectral parameters of each source in the model file are frozen to those found in the global analysis. A complete analysis is then performed for each of these energy bins. The optimal flux for each energy bin is thus calculated and can be plotted versus the energy to show that source's spectrum, known as the spectral energy distribution (SED) when plotted with $E^2\frac{dN}{dE}$ on y-axis.

(iii) Temporal analysis: This step allows us to produce a time-dependent flux curve, also known as a light curve. Having decided the size of the time bins, a complete analysis is run for each of them. As a starting point, the model parameters are set to those that were found in the global analysis. For what we will call a "standard light curve" analysis in this work, the spectral parameters are frozen to those global values with just the flux parameters free to vary for each time bin.

Before entering into the details of these steps, let us see what a complete analysis consists of.

4.4.1.   A Complete Analysis

As mentioned above, the `Fermi Science Tools` are designed for the analysis of the LAT data, from the performance of cuts to the maximum likelihood fits and all of the steps in between, including sanity checks, and diagnostics. The analysis procedure recommended by the FSSC states the `P8R2_SOURCE_V6` IRFs[10] be used for point-source analysis. All of the steps in a standard global analysis from *gtselect* to *gtmodel* are detailed in Table 4.4.1. The name of each `Fermi Science Tool` along with its corresponding cuts and parameters as well as a description of its function is provided. In this table, *farith* which is not part of the `Fermi Science Tools`, but of the `FTOOLS` [11], a software designed to manipulate fits files, is also included. The number of events per file quoted corresponds to one year of data for a known blazar. These values are shown in order to give the reader an idea of how the tools and cuts work. Observe how the number of events (rows) decreases as the cuts are progressively performed. Note that *gtselect* allows only for mission elapsed time (MET) units. *gtlike* [12] is perhaps the heart of the process. It performs the likelihood analysis. The value of STAT can be BINNED or UNBINNED statistics, for binned or unbinned analysis (see Section 4.3). A very important input of *gtlike*, known as "the model file", is described in the next section.

Throughout this document, the term "complete analysis", or complete maximum likelihood analysis, is used to refer to the process of having applied all the steps above, from *gtselect* to (at least) *gtlike*, to a *Fermi*-LAT dataset.

---

[10]At the time this study started, this was the latest class of data available. As of the day of writing, further improvements have been made in the LAT data classification and are found on the FSSC site. The current source IRFs to be used is `P8R3_SOURCE_V2`.

[11]`https://heasarc.gsfc.nasa.gov/docs/software/ftools/ftools_menu.html`

[12]`https://fermi.gsfc.nasa.gov/ssc/data/analysis/scitools/help/gtlike.txt`

Table 4.1:: Description of the Fermi Science Tools.

Tool	Description	Parameters	IN files	OUT files	OUT files description HDU			
					Index	Name	Type	Dimension
GTSELECT	Makes cuts.	ra=RA, dec=DEC, rad=Rad, tmin=TSTART, tmax=TEND, emin=EMIN, emax=EMAX, zmax=90, evclass=128, evtype=3	PH files	*_ev_roi_raw.fits	0	Primary	Null	
					1	Events	BinTable	$23c \times 107827r$
					2	GTI	BinTable	$2c \times 5593r$
GTMKTIME	Update GTI and cut data based on ROI.	DATA_QUAL>0, LAT_CONFIG==1, abs(ROCK_ANGLE)<180, roicut=NO	*_ev_roi_raw.fits, SC file	*_ev_roi.fits	0	Primary	Null	
					1	Events	BinTable	$23c \times 107778r$
					2	GTI	BinTable	$2c \times 5614r$
make3FGLxml.py	Make model file.		*_ev_roi.fits, gll_psc_v16.fit	*_model.xml	XML model file that contains the initial values for the ML fit.			
GTBIN	Make counts map and cube.	algorithm=CMAP, nxpix=200, nypix=200, binsz=0.1, coordsys=CEL, xref=RA, yref=DEC, axisrot=0, proj=STG	*_ev_roi.fits, SC file	*_map.fits	0	Primary	Image	Int4(200 × 200)
					1	GTI	BinTable	$2c \times 5614r$
		algorithm=CCUBE nxpix=200 nypix=200 binsz=0.1 coordsys=CEL xref=RA yref=DEC axisrot=0 proj=STG ebinalg=LOG emin=EMIN emax=EMAX enumbins=37	*_ev_roi.fits, SC file	*_ccube.fits				

Continues on the next page

table continues

| Tool | Description | Parameters | IN files | OUT files | OUT files description | | | |
| | | | | | HDU | | | Dimension |
					Index	Name	Type	
		algorithm=CCUBE nx-pix=484 nypix=484 binsz=0.1 coordsys=CEL xref=RA yref=DEC axisrot=0 proj=STG ebinalg=LOG emin=EMIN emax=EMAX enumbins=37	*_ev_roi.fits, SC file	*_extended_ccube.fits				
GTLTCUBE	Make livetime and cube.	dcostheta=0.025 binsz=1 zmax=90	*_ev_roi.fits, SC file	*_expCube.fits	0	Primary	Null	
					1	Exposure	BinTable	$3c \times 49152r$
					2	Weighted_Exposure	BinTable	$3c \times 49152r$
					3	CTHETABOUNDS	BinTable	$2c \times 40r$
					4	GTI	BinTable	$2c \times 5614r$
GTEXPMAP	Make a exposure map. Skip for in binned analysis mode.	irfs=P8R2_SOURCE_V6, srcrad=20.0, nlong=80, nlat=80, nenergies=37	*_ev_roi.fits, *_expCube.fits, SC file	*_expMap.fits				
GTEXPCUBE2	Make binned exposure cube.	irfs=P8R2_SOURCE_V6, bincalc=EDGE, emin=EMIN, emax=EMAX, enumbins=37	*_expCube.fits, *_extended_ccube.fits	*_binExpMap.fits	0	Primary	Image	Real14($484 \times 484 \times 38$)
					1	Energies	BinTable	$1c \times 38r$
					2	GTI	BinTable	$2c \times 5614r$
GTSRCMAPS	Make model counts maps as an input of the likelihood analysis by taking each source in the XML model file, multiplying it by the exposure at the position of the source and convolving it with the PSF. Run before GTLIKE only in binned analysis mode.	irfs=P8R2_SOURCE_V6, ptsrc=yes	SC, *_expCube.fits, *_ccube.fits, *_binExpMap.fits, *_model.xml	*_srcMaps.fits	0	Primary	Image	Real4($200 \times 200 \times 37$)

table continues

Tool	Description	Parameters	IN files	OUT files	OUT files description			
					Index	Name (HDU)	Type (HDU)	Dimension
GTDIFFRP	convolves a diffuse source model with the IRF.	irfs=P8R2_SOURCE_V6, convert=yes	*_ev_roi.fits, *_model.fits, SC file	Adds two columns to the events file.	1	GTI	BinTable	$2c \times 5614r$
					2	EBOUNDS	BinTable	$3c \times 37r$
					3–90	Name of sources	Images	Real4(200×200×38)
GTLIKE	Likelihood analysis.	irfs=P8R2_SOURCE_V6, statistic=STAT, optimizer=MINUIT, ftol=1e-08, toltype=ABS, tsmin=no, chatter=3	*_srcMaps.fits, *_binExpMap.fits, *_expCube.fits, *_model.fits	*_fitmodel.xml, *_results.dat, *_counts_spectra.fits	0	Primary	Null	
					1	COUNTS_SPECTRA	BinTable	$128c \times 37r$
					2	FLUXES	BinTable	$125c \times 37r$
					3	EBOUNDS	BinTable	$2c \times 37r$
GTMODEL	Make a model map to be compared with the counts map.	irfs=P8R2_SOURCE_V6	*_srcMaps.fits, *_binExpMap.fits, *_expCube.fits, *_fitmodel.xml	*_modelmap.fits	0	Primary	Image	Real4(200×200)
FARITH	Make a residual map, excess of counts with respect to the model.	SUB	*_map.fits, *_modelmap.fits	*_residualmap.fits				

* Source label.

Note.– For a detailed description of these tools with runtime examples and up to date software, visit the FSSC page:

https://fermi.gsfc.nasa.gov/ssc/data/analysis/scitools/likelihood_tutorial.html

4.4.2. The XML Model File

The model file is an extensible markup language (XML) file that contains all of the initial parameters for the chosen model of the sky that *gtlike* uses as input. The tool `make3FGLxml.py` creates the model XML file using the events file (i.e. *gtmktime* output) and the XML model file combining the descriptions of all of the sources in the LAT catalog, in our case the 4-year source catalog (3FGL; Acero et al. 2015). The spectral and positional information of the sources are organized in blocks, one block per source, as seen in the portion of the model file for the 1ES 1215+303 ROI shown here:

```xml
<?xml version="1.0" ?>
<source_library title="source_library">

<!-- Point Sources -->

<!-- Sources between [0.0,4.0) degrees of ROI center -->
<source ROI_Center_Distance="0.000" name="3FGL_J1217.8+3007" type="PointSource">
        <spectrum apply_edisp="false" type="PowerLaw">
        <!-- Source is 0.0 degrees away from ROI center -->
                <parameter free="1" max="1e4" min="1e-4" name="Prefactor" scale="1e-12"
                    value="3.25"/>
                <parameter free="1" max="10.0" min="0.0" name="Index" scale="-1.0" value=
                    "1.97448"/>
                <parameter free="0" max="5e5" min="30" name="Scale" scale="1.0" value="
                    1360.154663"/>
        </spectrum>
        <spatialModel type="SkyDirFunction">
                <parameter free="0" max="360.0" min="-360.0" name="RA" scale="1.0" value=
                    "184.465"/>
                <parameter free="0" max="90" min="-90" name="DEC" scale="1.0" value="
                    30.1178"/>
        </spatialModel>
</source>
<!-- Diffuse Sources -->
<source name="gll_iem_v06" type="DiffuseSource">
        <spectrum apply_edisp="false" type="PowerLaw">
                <parameter free="1" max="10" min="0" name="Prefactor" scale="1" value="1"
                    />
                <parameter free="0" max="1" min="-1" name="Index" scale="1.0" value="0"/>
                <parameter free="0" max="2e2" min="5e1" name="Scale" scale="1.0" value="1
                    e2"/>
        </spectrum>
        <spatialModel file="$(FERMI_DIR)/refdata/fermi/galdiffuse/gll_iem_v06.fits" type=
            "MapCubeFunction">
                <parameter free="0" max="1e3" min="1e-3" name="Normalization" scale="1.0"
                    value="1.0"/>
        </spatialModel>
</source>
<source name="iso_P8R2_SOURCE_V6_v06" type="DiffuseSource">
        <spectrum apply_edisp="false" file="$(FERMI_DIR)/refdata/fermi/galdiffuse/
            iso_P8R2_SOURCE_V6_v06.txt" type="FileFunction">
                <parameter free="1" max="10" min="1e-2" name="Normalization" scale="1"
                    value="1"/>
        </spectrum>
        <spatialModel type="ConstantValue">
                <parameter free="0" max="10.0" min="0.0" name="Value" scale="1.0" value="
                    1.0"/>
        </spatialModel>
</source>
</source_library>
```

Fitting spatial model parameters has not been implemented yet due to overhead related to computing the energy dependent response functions per source component.

In 3FGL, the latest catalog available when this study started, 626 out of 662 BL Lacs were well-fit by a Power-law (PL), the other 36 by a LogParabola(LP). The power-law model has only two free parameters, the log-parabola has three and the power-law sub exponential Cutoff (plSECO) has four. However, because the 3FGL provided analysis results for the first 4 years of data, and since six more years have since passed, I also checked if a curved model (i.e. LP, plSECO) would better fit the data. The diffuse sources make reference to two files, `gll_iem_v06.fits` and `iso_P8R2_SOURCE_V6_v06.txt`. They describe the extragalactic and galactic diffuse emission, respectively. All of the extended sources require the input of a template file that provides the necessary information on the spatial extension. These are provided as part of the Science Tools. The model file contains 127 sources, 8 of them LogParabola type, 2 DiffuseSource type and the rest PowerLaw type. 23 of these sources, (2 of these diffuse), have parameters with the flag 'free="1"' which means that it has been left free (= "0" for frozen). 3FGL contains only sources detected with a statistical significance of $> 4\,\sigma$, the `make3FGLxml.py` tool freezes the parameters of the ones below $5\,\sigma$ significance. This tool also fixes the spectral and flux parameters of the sources outside the ROI (sources fixed in a $10°$ annulus exterior to the ROI for this work). At a separation of $> 10°$ from 1ES 1215+303, they are too distant for their variation to influence the results for its flux and spectrum, but are kept in the model so that their emission is accounted for to a certain level.

The parameter values found with *gtlike* are not reliable if the likelihood has not been accurately maximized, especially the uncertainties, which tend to be underestimated. The latest *Fermi*-LAT source catalogs provide a very good estimate of the parameter values of the sources, therefore making it easier to reach convergence (or accuracy or fit quality = 3) when analyzing datasets longer than the period covered by the catalog. The analyses of smaller time ranges of data, however, can be more challenging, especially if there are variable sources in the ROI, whose spectral parameters might shift far from the average provided by the catalog. In particular, sources in a faint state (i.e. with low or relatively low TS) tend to cause convergence difficulties. Therefore editing the model file and re-running *gtlike* is necessary to achieve convergence. I have found the following particularly helpful and uses them as guidelines to reach convergence:

- Never fix the source of interest or sources spatially close to them, e.g. sources within $1°$ of the source of interest or very bright and variable sources, so that correlated effects between them can be explored.

- Erase sources with TS < 0 from the model file, their contributions are not being taken into account by *gtlike*.

- Fix spectral parameters whose fit results show unlikely values, to those provided by the LAT catalog. For instance, a fit photon index value of 5.

- If all the values look reasonable but convergence has not been attained, try allowing

gtlike to continue from where it stopped during the last run, that is, replace the input model file (∗_model.xml) with the output model file from *gtlike* (∗_fitmodel.xml).

- Systematically fix the parameters of the faintest sources. For instance, try first fixing sources with TS < 4, then the ones with TS < 9, then the ones with TS < 16, and so on.

Once *gtlike* has converged, some sanity checks should be performed. These include examining the residual map and its pixel distribution and verifying that the counts spectra and its residuals look reasonable.

4.5.   Global Analysis

In what follows, the term "global analysis" refers to the process of applying a complete ML analysis to the entire ROI dataset. The global analysis of the first 9 years of *Fermi*-LAT data from the BL Lac object 1ES 1215+303 converged after two *gtlike* iterations, the second one using as input the output model file of the first run. These results are shown in Table 4.2.

Table 4.2: Global Analysis results for the 1ES 1215+303 ROI: 2008-08-04 − 2017-09-04.

Object name 3FGL	Dist. to center (°)	Npred	TS	Prefactor (MeV^{-1} cm^{-2} s^{-1})	Photon Index	Flux$_{.1-500\ \text{GeV}}$ (10^{-8} cm^{-2} s^{-1})
J1221.4+2814[a]	2.04	8224.3	5576.8	$(3.65 \pm 0.08) \times 10^{-12}$	2.11 ± 0.02	4.30 ± 0.14
J1149.1+2815	6.53	1165.2	56.1	$(4.43 \pm 0.78) \times 10^{-12}$	2.87 ± 0.18	0.81 ± 0.19
J1217.8+3007[b]	**0**	**16045.1**	**20808.1**	$\mathbf{(4.72 \pm 0.07) \times 10^{-12}}$	**1.92 ± 0.01**	**7.70 ± 0.16**
J1236.6+3901	9.71	238.5	83.6	$(2.44 \pm 0.59) \times 10^{-12}$	1.94 ± 0.14	0.18 ± 0.06
J1230.3+2519[c]	5.53	8413.6	6964.2	$(4.05 \pm 0.09) \times 10^{-12}$	2.09 ± 0.02	4.55 ± 0.14
J1220.2+3434	4.48	1399.6	379.3	$(3.45 \pm 0.26) \times 10^{-12}$	2.14 ± 0.06	0.73 ± 0.09
J1301.5+3333	9.90	388.0	56.3	$(2.37 \pm 0.44) \times 10^{-12}$	2.30 ± 0.15	0.40 ± 0.13
J1243.1+3627	8.25	2481.4	3399.2	$(3.20 \pm 0.11) \times 10^{-12}$	1.74 ± 0.02	1.20 ± 0.07
J1136.4+3405	9.63	1213.2	151.0	$(5.32 \pm 0.52) \times 10^{-12}$	2.74 ± 0.09	1.24 ± 0.16
J1150.3+2417	8.43	3381.0	1414.0	$(6.55 \pm 0.28) \times 10^{-12}$	2.25 ± 0.03	2.28 ± 0.13
J1258.1+3233	8.94	3078.6	1216.0	$(2.21 \pm 0.09) \times 10^{-12}$	2.34 ± 0.04	2.21 ± 0.14
J1136.9+2551	9.98	234.0	65.9	$(5.08 \pm 1.29) \times 10^{-12}$	1.94 ± 0.18	0.24 ± 0.11
J1231.7+2847	3.31	3509.5	2515.6	$(0.74 \pm 0.03) \times 10^{-12}$	1.96 ± 0.03	1.74 ± 0.98
J1249.7+3705	9.62	308.2	205.6	$(1.79 \pm 0.21) \times 10^{-12}$	1.76 ± 0.08	0.19 ± 0.04
J1221.3+3010[d]	0.76	3719.6	4126.7	$(1.71 \pm 0.06) \times 10^{-12}$	1.70 ± 0.02	1.62 ± 0.10
J1224.5+2436	5.70	1932.0	1292.4	$(15.19 \pm 0.78) \times 10^{-12}$	1.88 ± 0.04	0.96 ± 0.09

				Norm (MeV^{-1} cm^{-2} s^{-1})	α	β ($\times 10^{-2}$)	Flux$_{.1-500\ \text{GeV}}$ (10^{-8} cm^{-2} s^{-1})
J1224.9+2122[e]	8.88	49888.0	90566.7	$(3.82 \pm 0.03) \times 10^{-12}$	2.28 ± 0.01	3.97 ± 0.41	37.30 ± 0.30
J1159.5+2914[f]	4.08	23040.5	24247.2	$(6.25 \pm 0.08) \times 10^{-12}$	2.16 ± 0.01	6.71 ± 0.75	12.30 ± 0.20
J1225.9+2953	1.77	1173.2	1074.7	$(5.64 \pm 0.35) \times 10^{-12}$	1.85 ± 0.08	40.93 ± 6.24	0.40 ± 0.06

Note.− Association names of six of the brightest sources in the FoV: a) W Comae, b) 1ES 1215+303, c) ON 246, d) 1ES 1218+304, e) PKS 1222+216, f) Ton 0599.
The results shown are from a global analysis using a power-law spectral model for 1ES 1215+303.

By looking at the TS of column of Table 4.2, we notice that 1ES 1215+303 is the third brightest source in the ROI after PKS 1222+216 and Ton 0599. There are three free sources in the ROI described as having a log-parabola spectrum according to the 3FGL catalog; all the other free sources are modeled with power-law spectra. The correlations
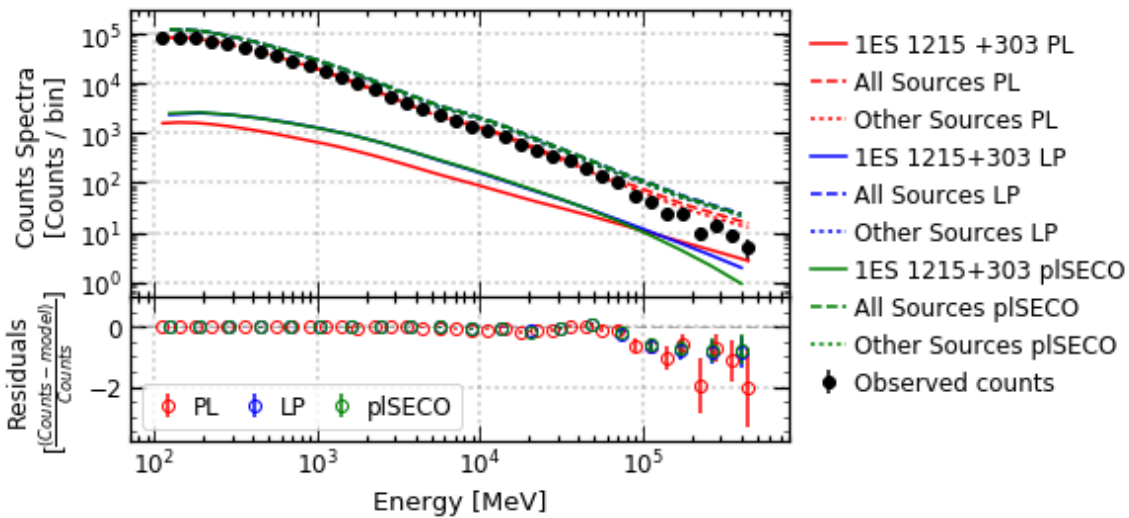
Fig. 4.8.— *Top:* **Counts spectra from the three different spectral models used for 1ES 1215+303 for data from 2008 Aug. 04 to 2017 Sep. 04, power-law (PL), log-parabola (LP) and power-law sub-exponential cutoff (plSECO). The addition of the spectra of all the sources in the 10° ROI are also shown (in dashed lines and labeled as All Sources), which matches the profile of the observed counts for the three spectral models tested for 1ES 1215+303. The addition of the spectra of all the sources but 1ES 1215+303 are also shown (in dotted lines and labeled as Other Sources).** *Bottom:* **Counts spectra residuals. The curved models show less residuals at higher energies.**

(ρ) obtained in the ML fit between the parameters of 1ES 1215+303 and all of the other free sources in the ROI are $|\rho| < 0.25$. 1ES 1215+303 and 1ES 1218+304 are possibly the closest extragalactic point sources in the 3FGL. Given that the distance between them, $0.76°$, is of the order of the 68% PSF we pay special attention to the correlations obtained between the parameters of these sources. We also pay close attention to the correlation of the 1ES 1215+303 parameters with those of the two diffuse model components and also to the cross-correlation of the diffuse source model components.

When fitting the data, *gtlike* divides the data into 37 energy bins; the result for each individual bin can be seen in the counts spectra plot in Figure 4.8. We observe that the three models used provide reasonable fits, and that the curved models, log-parabola and power-law sub exponential cutoff, present smaller residuals than the power-law. We also observe that the three models overestimate the number of counts ≥ 100 GeV, possibly due to the low statistics at these energies, or because none of the models are a good representation of the data. Alternatively, it could mean that the PSF has room for improvements at these energies[13]. The counts map, model map and residual map obtained for the global analysis are presented in Figure 4.10. The residual map and its pixel value

---

[13]A possibility worth testing would be to account to EBL absorption in the fit, especially if we consider that with more than eleven years of collected data we might start to have enough statistics at higher energies to do this test.

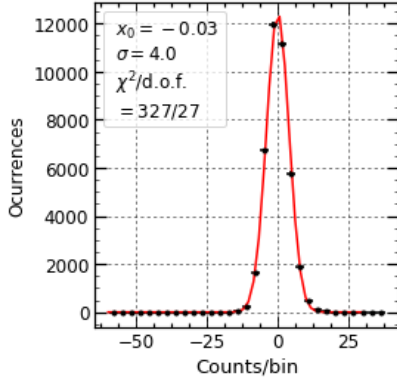distribution (see Figure 4.9) do not show any evidence for an excess.

Fig. 4.9.— **Pixel distribution of the residual map from the ML analysis for the ROI data centered at 1ES 1215+303 from 2008 Aug. 04 to 2017 Sep. 04.**

We may want to see how our results match the distributions of the data presented in Figures 4.6 and 4.7. In order to do that I make use of a `Fermi Science Tool` not yet presented, *gtsrcprob*[14]. For each photon, this calculates the probability that it came from each of the sources in the output model file of *gtlike*. Figure 4.11 presents the probability-weighted distributions of some quantities for the six brightest sources in the ROI, the diffuse contributions (galactic and isotropic) and the total observed counts.

The probability-weighted distributions of the right ascension, declination and distance to 1ES 1215+303 of six of the brightest sources in the ROI are plotted on top of those of the diffuse backgrounds in panels a), b) and c) of this figure. A compatible pattern can be observed between the location of the peaks for the different sources and the total observed counts. Probability-weighted temporal and energy distributions are shown in panels d), e) and f) for the same sources, where the dominance of the diffuse backgrounds and PKS 1222+216 in the ROI is observed.

Table 4.3: *Fermi*-LAT spectral analysis. Time range: 2008-08-04 – 2017-09-04.

1ES 1215+303 spectral model	$-\log L_1^a$	$-\log L_0^b$	$\mathrm{TS_{NH}}$
PL	5616649.5	5624985.7	16672.3
LP	5616623.3	5624985.7	16724.7
plSECO	5616621.4	5624985.7	16728.6

(a) L_1 is the maximum likelihood of a fit with 1ES 1215+303 present in the model. (b) L_0 is the maximum likelihood value of a fit in the absence of 1ES 1215+303 in the model.

To calculate the preference between the spectral models used for 1ES 1215+303, we re-run *gtlike* with a model file without 1ES 1215+303 in it, and use Equation (4.10) to calculate the TS from the null hypothesis. The results are shown in Table 4.3. Since the likelihood test only allows us to compare nested models (i.e., models which can be described using the same set of parameters), we cannot compare the log-parabola and power-law sub exponential cutoff models to each other. I find, however, that, by using the likelihood test

$\mathrm{TS_{curve}} = 2(\log \mathrm{L_{curved}} - \log \mathrm{L_{PL}}) \approx 50$, each of the curved models is thus preferred over the power-law at the $7\,\sigma$ level. This is further discussed in Section 5.9, where the spectra of 1ES 1215+303 obtained are shown in Figure 5.20.

---

[14]https://fermi.gsfc.nasa.gov/ssc/data/analysis/scitools/help/gtsrcprob.txt
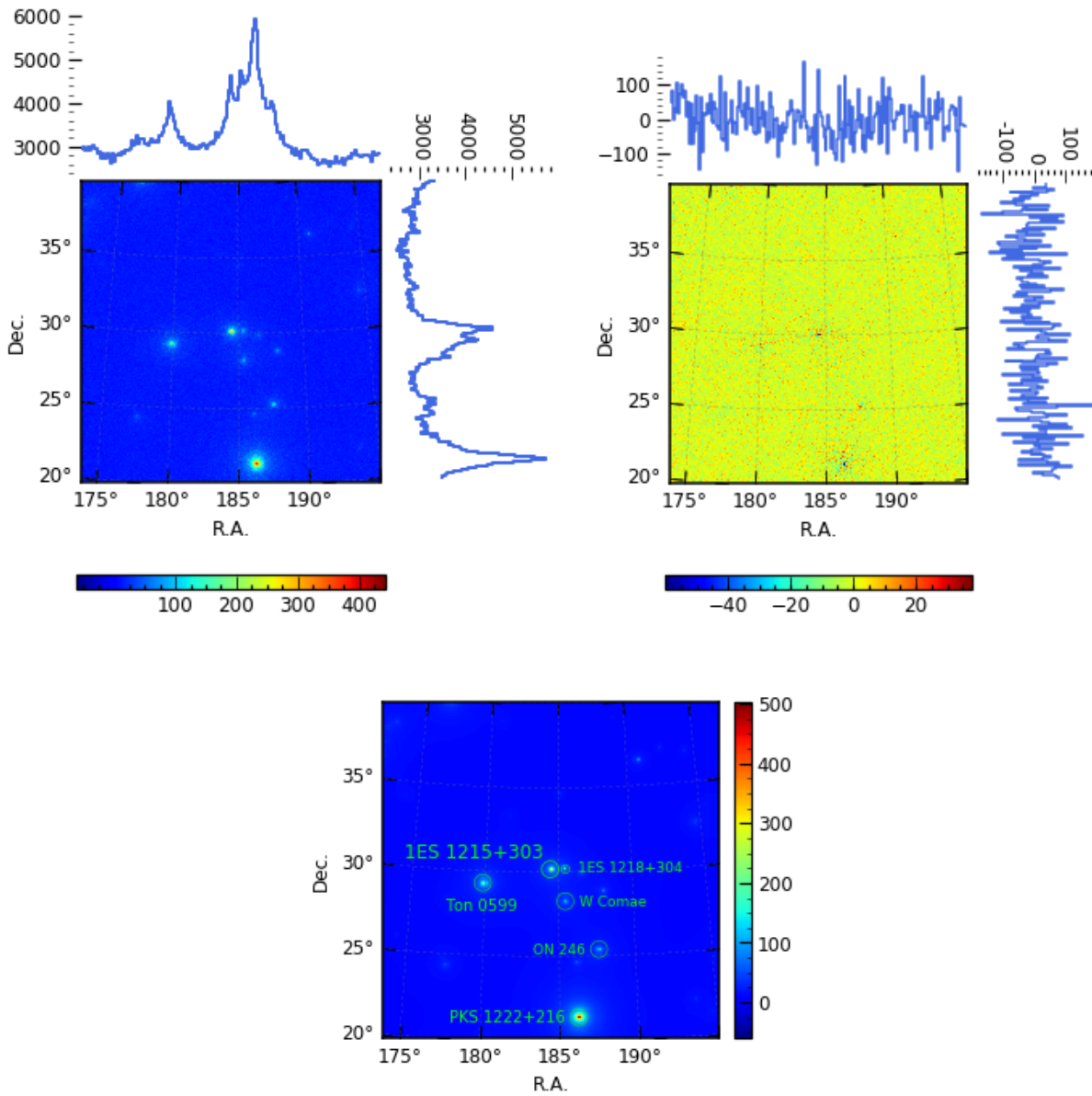
Fig. 4.10.— *Top left:* **Counts map of the events in the ROI centered at 1ES 1215+303 from 2008 Aug. 04 to 2017 Sep. 04. The color bar indicates the number of counts. Pixel distributions on the horizontal and vertical axes are provided.** *Bottom:* **Model map of the same data. The six brightest sources are labeled.** *Top right:* **Residual map of the same data. Pixel distributions on the horizontal and vertical axes are provided.**

4.6.   Spectral Analysis

For this step, the 100 MeV–500 GeV energy range is evenly binned in the logarithm of energy. The energy range is divided into a number of bins ensuring that the statistics are sufficient to ensure a significant ($\geq 2\,\sigma$) detection in each energy bin. A complete ML analysis is then run for each of these energy bins. In order to obtain an initial input model file for these analyses, the final output model file for *gtlike* for the global analysis
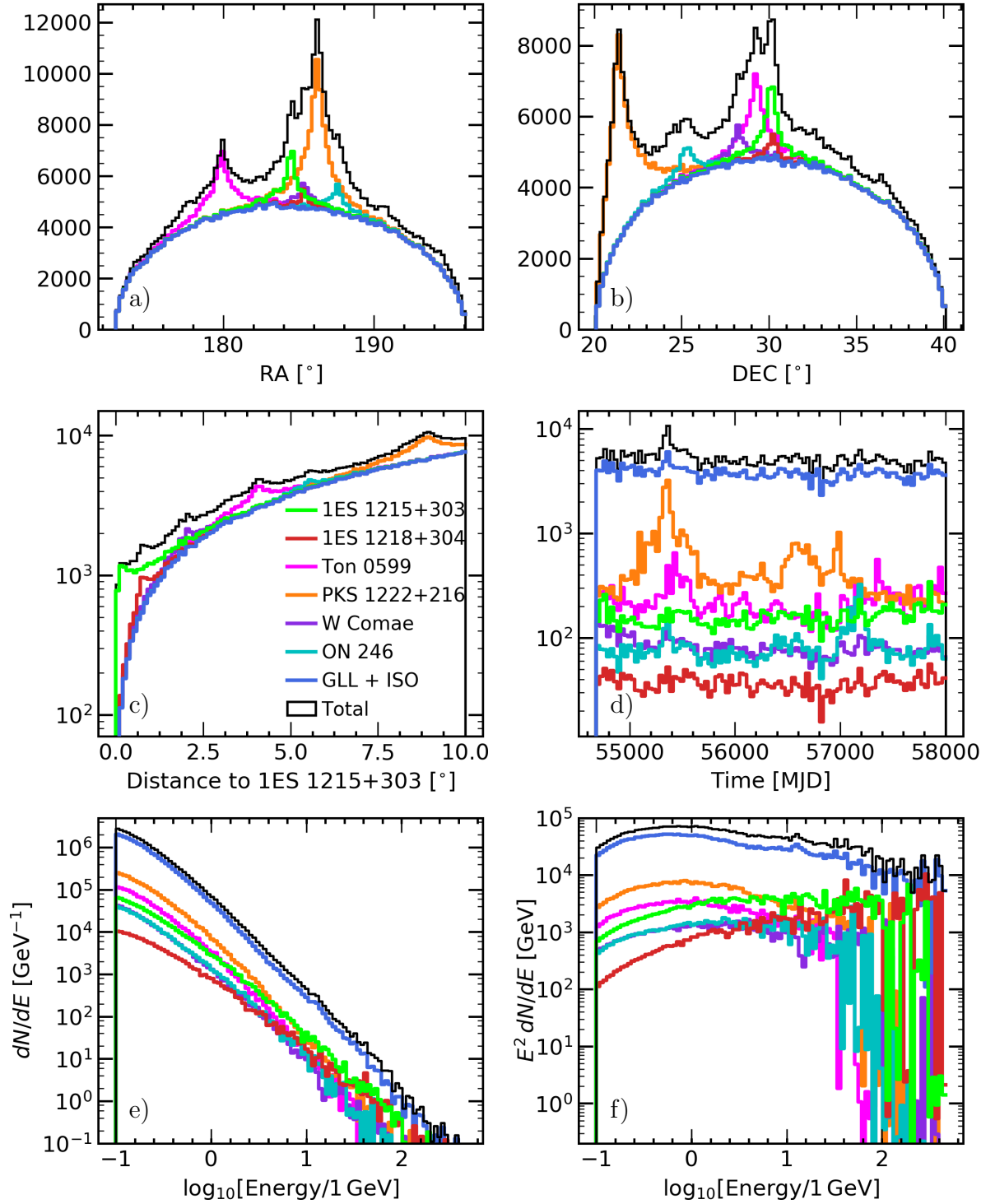
Fig. 4.11.— a) **Probability-weighted distribution of the right ascension for the six brightest sources plotted on top of that of the contribution from the diffuse backgrounds. b) Probability-weighted distribution of the declination for the six brightest sources plotted on top of that of the contribution from the diffuse backgrounds. c) Probability-weighted distribution of the distance of the six brightest sources from 1ES 1215+303 plotted on top of that from the contribution of the diffuse backgrounds. d) Probability-weighted temporal distribution of the events. e) and f) Probability-weighted energy distributions of the events. The legend in panel c) is valid for all of the other panels.**

is used and the photon indices of all the sources are fixed. This edited file is then used as the input model file for each of the energy bins.

Depending on the source, time range, energy range and binning chosen, it is sometimes possible to obtain significant results (conventionally accepted as significance of above 5σ or, equivalently, above TS = 25) for all of the energy bins. Convergence is reached within a small number of iterations. Such is the case for the long-term spectral analysis of 1ES 1215+303, whose results are shown in Table 4.4 and Figure 5.20, which is discussed in the next chapter. However, it often happens that the source is very faint at higher energies, or that there are no events at all in the ROI at these energies. In these cases, upper limits can be calculated using the general method of Helene (1983).

The "butterfly" contour consists of the curves $\frac{dN}{dE} \pm \sigma_{\frac{dN}{dE}}$, where $\frac{dN}{dE}$ is given by, depending on the model used, Equations (4.1), (4.2) or (4.3). These butterfly contours are frequently included in the spectra of AGNs to check for consistency or for the SED modeling. The rms of the logarithm of the flux according to a power-law model is given by Equation (4.11).

$$\sigma^2_{\log(\frac{dN}{dE})_{\mathrm{PL}}}(N_0, \Gamma) \approx \frac{\mathrm{Cov}(N_0, N_0)}{N_0^2} + \mathrm{Cov}(\Gamma, \Gamma) \log^2\left(\frac{E}{E_0}\right) - 2\frac{\mathrm{Cov}(N_0, \Gamma)}{N_0} \log\left(\frac{E}{E_0}\right)$$

(4.11)

where $\mathrm{Cov}(N_0, N_0)$, $\mathrm{Cov}(\Gamma, \Gamma)$, and $\mathrm{Cov}(N_0, \Gamma)$ are terms of the covariance matrix provided by *gtlike*.

The rms of the logarithm of the flux according to a log-parabola model is given by Equation (4.12).

$$\begin{aligned}
\sigma^2_{\log(\frac{dN}{dE})_{\mathrm{LP}}}(N_0, \alpha, \beta) \;\approx\;& \frac{\mathrm{Cov}(N_0, N_0)}{N_0^2} + \mathrm{Cov}(\alpha, \alpha) \log^2\left(\frac{E}{E_b}\right) + \mathrm{Cov}(\beta, \beta) \log^4\left(\frac{E}{E_b}\right) \\
-\;& 2\frac{\mathrm{Cov}(N_0, \alpha)}{N_0} \log\left(\frac{E}{E_b}\right) - 2\frac{\mathrm{Cov}(N_0, \beta)}{N_0} \log^2\left(\frac{E}{E_b}\right) \\
-\;& 2\,\mathrm{Cov}(\alpha, \beta) \log\left(\frac{E}{E_b}\right).
\end{aligned}$$

(4.12)

where all of the covariance terms are provided by *gtlike*.

The rms of the logarithm of the flux according to a power-law sub-exponential cutoff model is given by Equation (4.13).

$$\begin{aligned}
\sigma^2_{\log(\frac{dN}{dE})_{\mathrm{plSECO}}}(N_0, E_c, \gamma_1, \gamma_2) \;\approx\;& \left(\frac{dN}{dE}_{PL}(E, N_0, E_0, \gamma_1)\right)^2 + \sigma_G^2(E, E_c, \gamma_2) \\
-\;& 2\frac{dN}{dE}_{PL}(E, N_0, E_0, \gamma_1)\,\sigma_G(E, E_c, \gamma_2),
\end{aligned}$$

(4.13)

where $G(E, E_c, \gamma_2) = (E/E_c)^{\gamma_2}$,

$$\begin{aligned}
\sigma_G^2(E, E_c, \gamma_2) \;=\;& \left(\frac{E}{E_c}\right)^{2\gamma_2} \left[\mathrm{Cov}(E_c, E_c)\frac{\gamma_2^2}{E_c^2} + \mathrm{Cov}(\gamma_2, \gamma_2) \log^2\left(\frac{E}{E_c}\right)\right. \\
&\left. +\; 2\,\mathrm{Cov}(\gamma_2, E_c) \log\left(\frac{E}{E_c}\right) \frac{\gamma_2}{E_c}\right]
\end{aligned}$$

(a) .1 - .3 GeV.

(b) .3 - 1 GeV.

(c) 1 - 3 GeV.

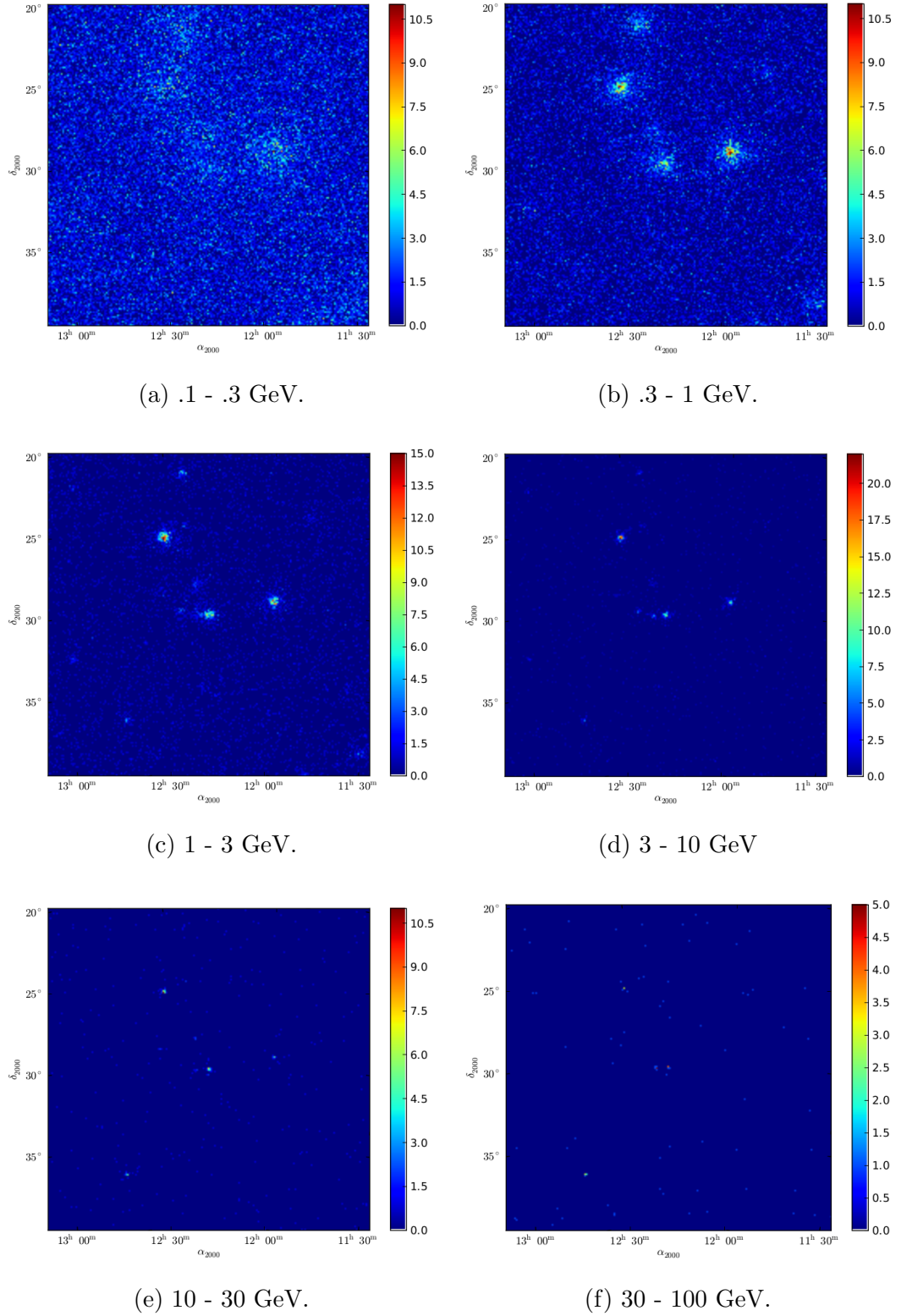(d) 3 - 10 GeV

(e) 10 - 30 GeV.

(f) 30 - 100 GeV.

Fig. 4.12.— **Counts Maps of the ROI centered on 1ES 1215+303, for each bin for the data from 2015. The color bars show the number of counts. It can be observed that the resolution improves as the energy increases (1 GeV to 100 GeV). This is due to the PSF which is larger at lower energies. As expected, the number of events in the ROI decreases with increasing energy.**

and all of the covariance terms are provided by *gtlike*.

The three spectral models are shown in Figure 4.13. The spectral points shown in Table 4.4 and in Figure 4.13 (black points) were obtained using the power-law model for 1ES 1215+303 in each bin. One of the reasons for the choice of the power-law parameterization is that the preference for the curved spectral models starts to be observed ($> 5\sigma$) with 8 years of data. No preference is detected in any of the smaller subsets, even for yearly data with TS∼5000. Another reason is that in a relatively small energy bin, the SED of an AGN can be approximated to a power-law, as the 3FGL and other LAT catalogs assume by default. These results are discussed in detail in Section 5.9.
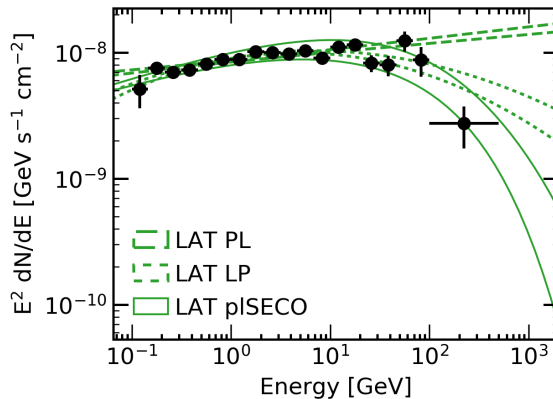

Fig.   4.13.— SED of the entire *Fermi-LAT* data set (2008-08-04 – 2017-09-04). The data were analyzed with three different models, power-law (dashed), log-parabola (dotted) and power-law sub-exponential cutoff (solid line). The black circles show the result of the individual spectral analyses for each of the LAT energy bins.

4.7.   Lightcurves

Blazars are indeed variable sources. For instance, the outburst of the BL Lac object 1ES 1215+303 and FSRQs PKS 1222+216 and Ton 0599 can be noticed in the yearly (360-day to be precise) sky maps for the 10° ROI centered in 1ES 1215+303 shown in Figure 4.14; where a counts map, a model map and a residual map are provided for each year since 2008 Aug. to 2017 Sep. In order to study the variability of blazars we need information on the changes of the photon flux from these objects reconstructed with data from time ranges as small as the statistics allow. We thus need light curves.

There are different ways in which the light curve analysis can be performed. What I called a "standard light curve", is the conventional light curve widely used by researchers. This standard light curve is built using bins of equal duration and the global analysis output file having fixed all of the spectral indices, including those of the source of interest. Another method consists in letting the photon index of the source of interest free. A more strict method consists in letting all the indices in the ROI free initially, although many of these might get frozen later while looking for convergence. These "indices free" methods allow fluctuations in the mean integral flux best values, and an increment in the size of the uncertainties, which I discuss later in this chapter.

The binning size for the light curve is chosen depending on the significance of the source obtained in the global analysis, and on the science goals. However, in order to obtain (relatively) significant points, the author has found that a good number of bins

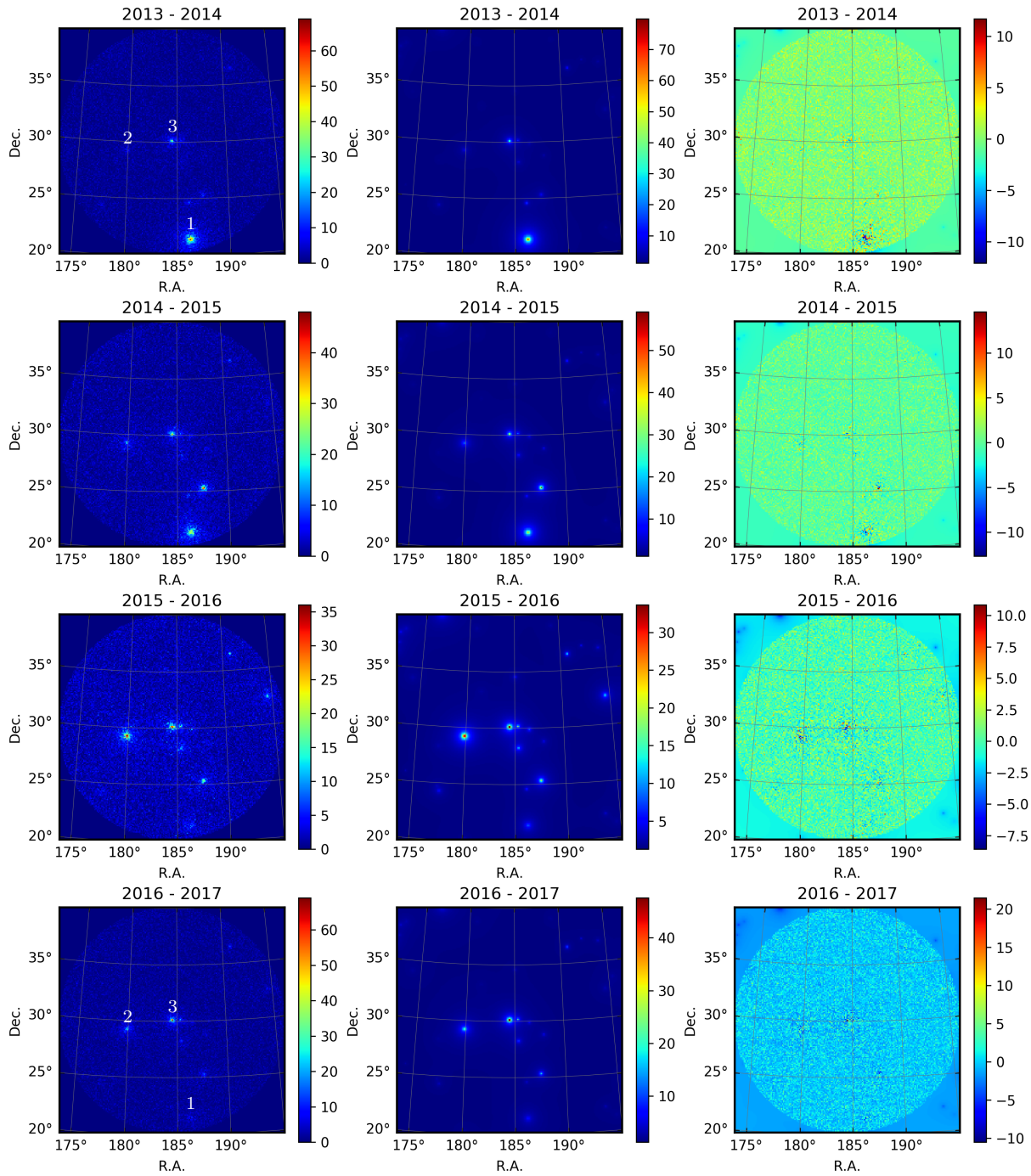Counts Maps:

Model Maps:
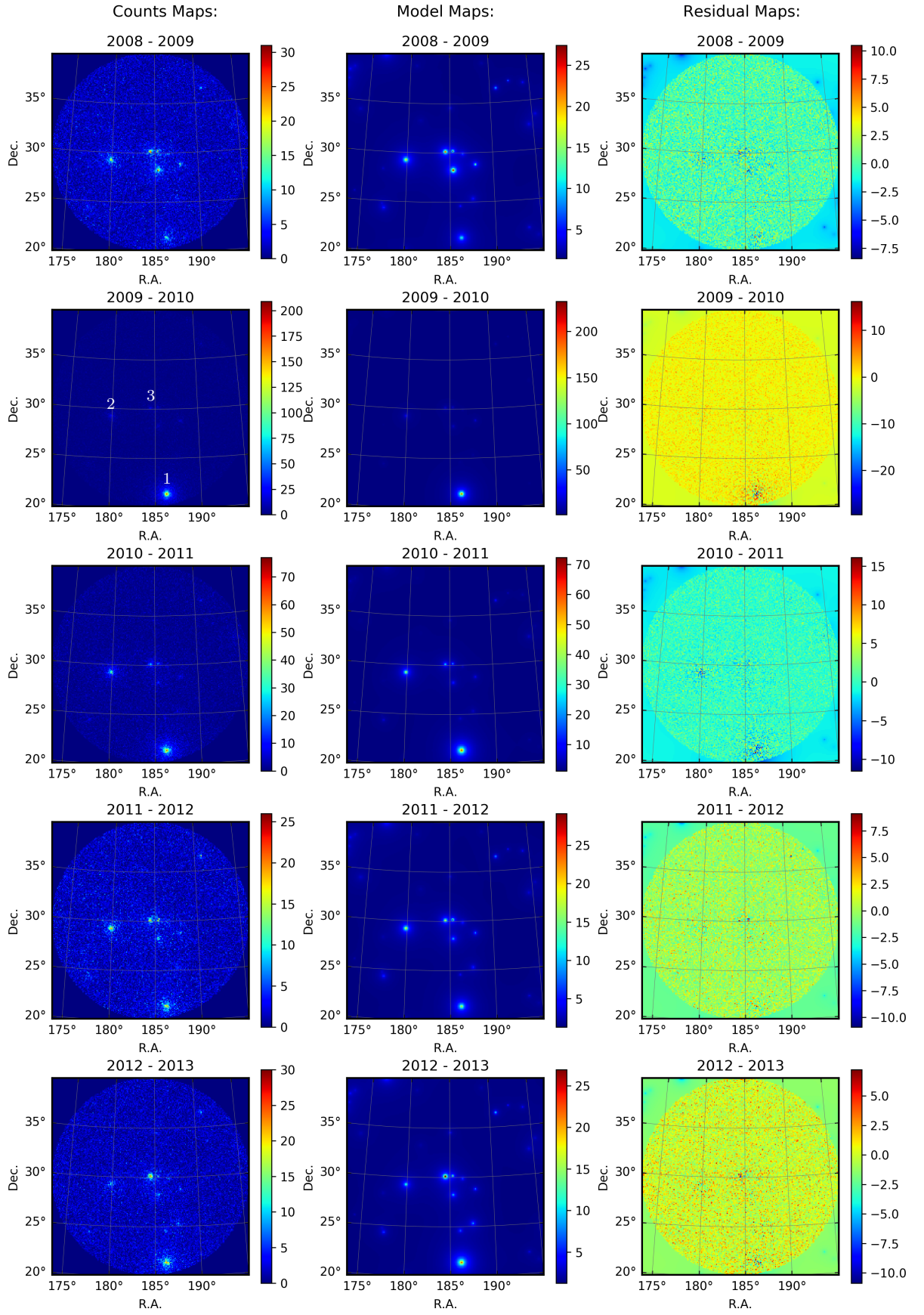
Residual Maps:

Fig. 4.14.— Sky maps of the yearly-binned LAT data from 2008 to 2017: counts maps (left), model maps (middle) and residual maps (right). The variability of AGNs at γ-ray energies can be noticed here. For example, the extremely bright outburst experienced by PKS 1222+216 (labeled "1") from ∼2009 Sep. to 2010 Oct. that outshone the rest of the point sources in the ROI is observed (see Figure A.1 in Appendix A.1). The outburst of 1ES 1215+303 (labeled "3") in 2014 outshone most of the sources in the sky; while during the outburst of 2017, the brightness of 1ES 1215+303 turned to that of the level of Ton 0599 (labeled "2"; see Figure A.2 in Appendix A.2) and PKS 1222+216 became comparatively quiet. These are the three brightest sources in the ROI.
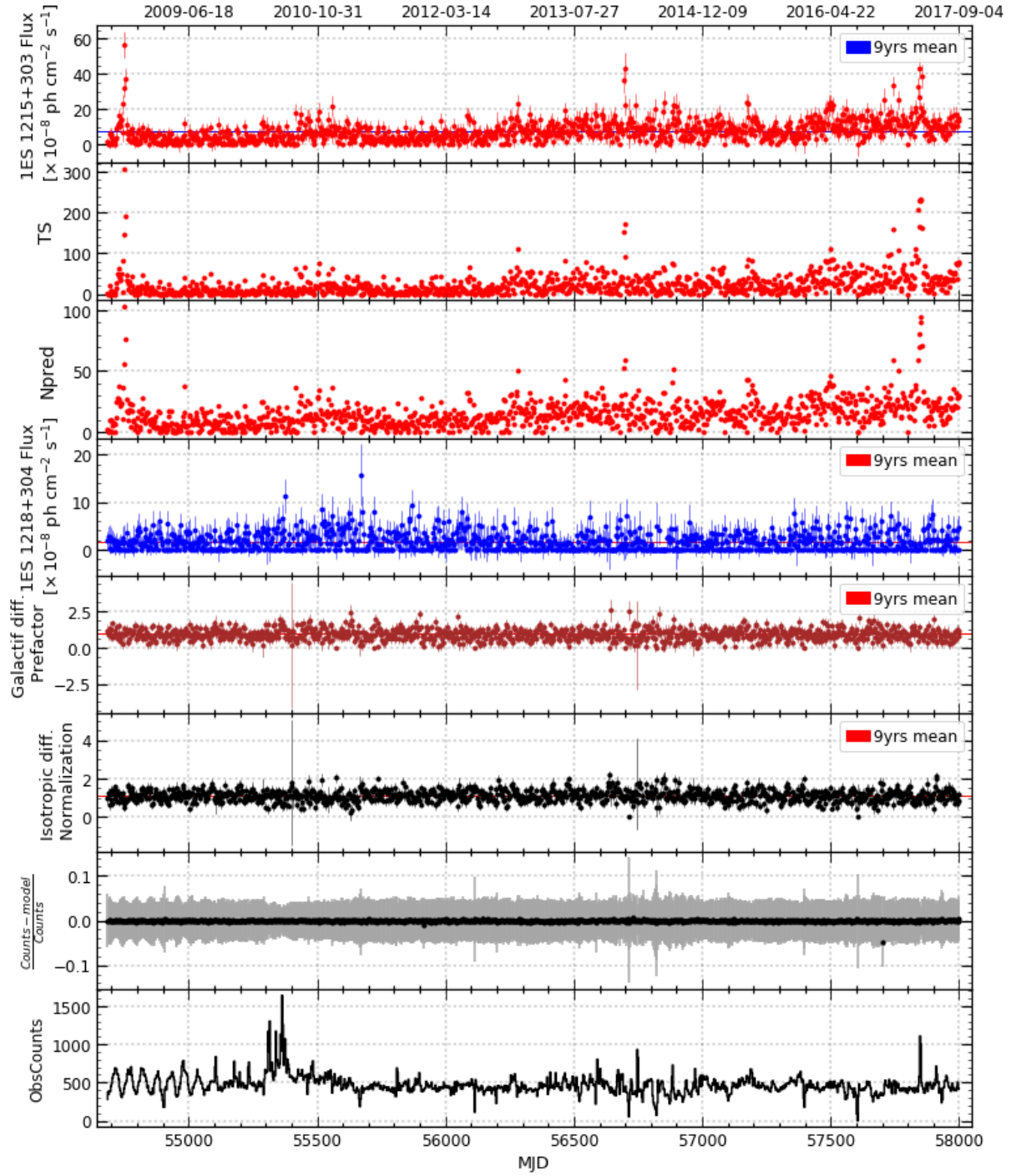
Fig. 4.15.— From top to bottom: 1ES 1215+303 standard light curve above 100 MeV, TS, predicted number of counts (Npred), 1ES 1218+304 light curve, galactic diffuse prefactor parameter, isotropic diffuse normalization parameter, residuals per bin (means are shown in black while the uncertainties are shown in gray), and observed counts per bin vs time. All of these data correspond to the light curve analysis for 1ES 1215+303 from 2008 Aug. 04 to 2017 Sep. 04.

to start with is $TS_{Global}/50$, especially if the source of interest is known to be variable;

otherwise the division recommended would be over 25 ($\equiv 5\sigma$ significance). Choosing a bin length close to integer fractions of one that can interfere with any of the LAT characteristic periods should be avoided, for instance, the orbital precessional period of 53.7 days.
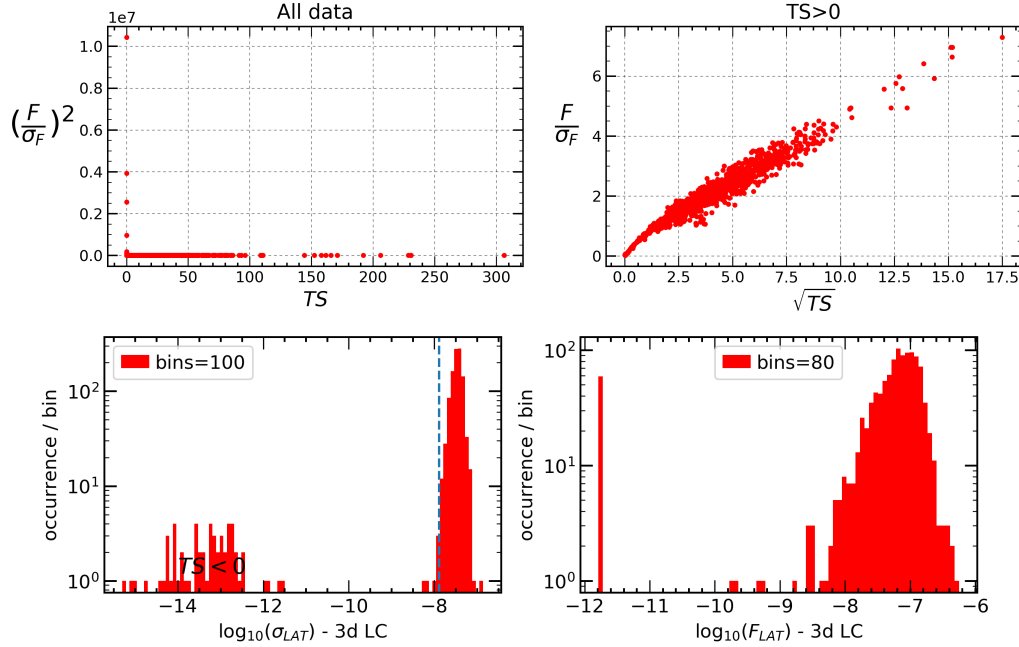

Fig. 4.16.— *Top:* **The proportionality of the ratio $\frac{Flux}{\Delta Flux}$ and the significance ($\sqrt{|\mathrm{TS}|}$) of the source is observed for bins with TS > 0, while the bins with TS ≤ 0 are outliers.** *Bottom:* **These outliers are also observed when the distribution of the logarithm of the uncertainties is plotted (left), see the text.**

Figure 4.15 shows the 3-day binned light curve obtained for 1ES 1215+303 from 2008 Aug. 04 to 2017 Sep. 04. Convergence for all of the bins was reached by following the recommendations provided in Section 4.4.2, obtaining a total of 1106 flux points. A method to test the goodness of the *gtlike* results is based on the fact that ratio $\frac{Flux}{\Delta Flux}$ should be proportional to the significance ($\sqrt{|\mathrm{TS}|}$) of the source. Through this method, 59 outliers from this linear dependence are found, all of them having TS < 0 and very small uncertainties, see top panels of Figure 4.16. Another sanity check consists in verifying the good behavior of the distribution of the uncertainties obtained. The bottom left panel of Figure 4.16 shows that the outliers with TS < 0 clearly misbehave. These were excluded from the light curve. Further cuts, in addition to those suggested in this plot are at the discretion of the researcher; this is discussed later in Section 4.7.2. No cuts due to the presence of solar flares, the Moon or GRBs were necessary for the analysis of the 10° ROI centered on 1ES 1215+303 since this ROI is not within the ecliptic path and since there were no LAT GRB detections reported in this region in the second LAT GRB catalog.

In order to verify that the bins with a low value for the test statistic (TS < 0) for 1ES 1215+303 are indeed due to the faintness of the source during those time ranges and

not the result of a change in the observation mode of the LAT[15], a "sliding-window" analysis is performed around these bins. This consists of taking overlapped slides around the bins in question whilst maintaining the same bin size. Figure 4.17 shows this method applied to one of these bins, which is, by construction, centered around the sliding-window data. We can see that the results from the sliding-window analysis are consistent with the original light-curve analysis; the flux falls significantly towards the middle points. The same behavior was observed in the other low-TS bins, which confirms the low flux state of 1ES 1215+303 during these time ranges. When an analysis resulted in a TS < 4, I calculated upper limits using the method of Helene (1983).
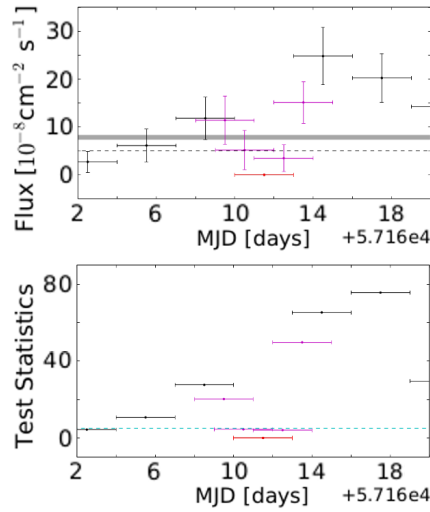

Fig. 4.17.— **Zoom around an outlier (in red), showing the sliding-window results (in magenta).** *Top:* **The dotted line represents the arithmetical mean flux of the dataset. The gray band represents the flux found in the global analysis.** *Bottom:* **The dotted line represents TS = 4.**

One of the main differences between the probability-weighted temporal distribution of events in Figure 4.11 and the light curve in Figure 4.15 obtained for 1ES 1215+303 is the exposure. The flux measured for an object does not only depend on the number of counts measured, but also on the amount of time for which it was being observed and on its position relative to the center of the LAT FoV. For the LAT, the amount of time of observation is given the parameter called "Livetime" which depends on the off-axis angle θ. The total livetime (integrated over θ) is shown in the top panel of Figure 4.18 for a portion of the 1ES 1215+303 light curve (from 2016 Oct. to 2017 Sep.). The two top panels of Figure 4.18 show the livetime-dependent off-axis θ as a function of time. In the second panel from the top, the peak in the observed counts in the ROI around MJD 57850 does not correspond to a flaring episode of 1ES 1215+303, but to an increase in the exposure of the region due to a ToO on M 87, at an angular separation of $\sim$18° from 1ES 1215+303, from 2017 April 4-9 inclusive. The 54 day characteristic LAT period can be observed in the three top panels of the figure. The livetime parameter can be extracted

---

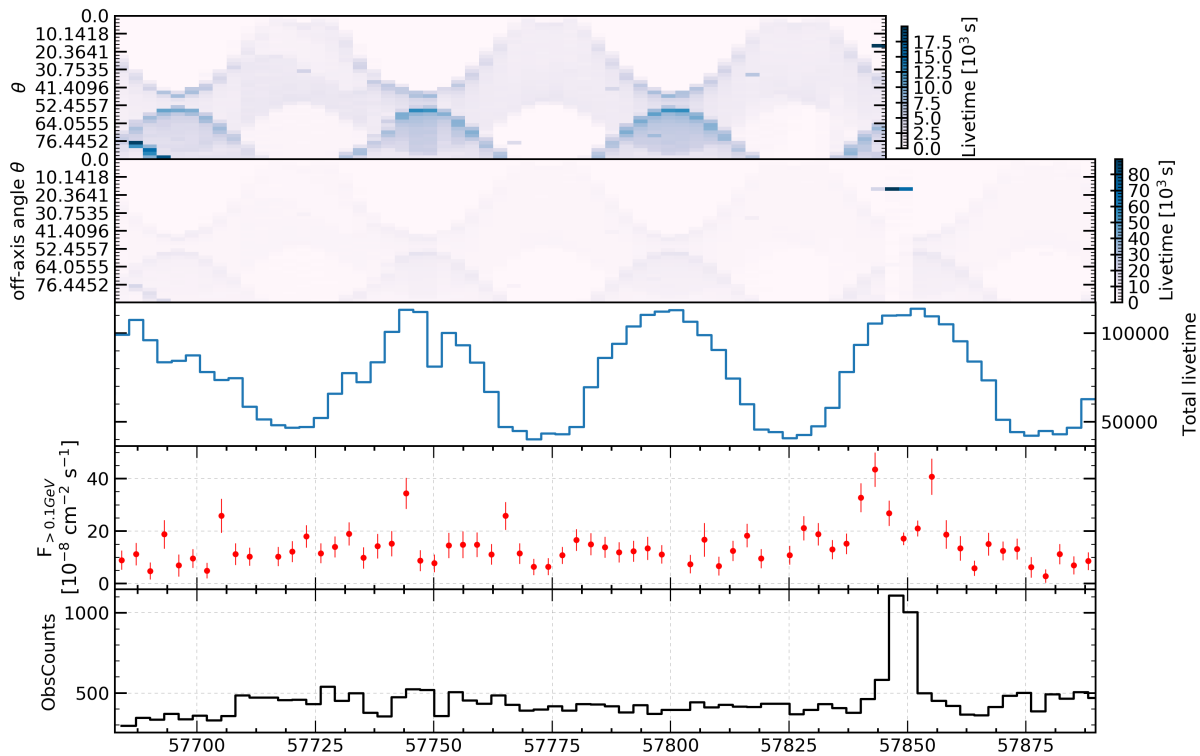[15]For instance, from all-sky survey to pointing due to a ToO.

Fig. 4.18.— **From bottom to top: The observed counts in the 10° ROI centered in for 1ES 1215+303, the 1ES 1215+303 light curve, the total livetime vs time, the color map of the livetime-dependent θ vs time from 2016 Oct. to 2017 Sep., and color map of the livetime-dependent θ vs time from 2016 Oct. to 2017 Mar., which was added for an improved visualization outside the ToO. See text for a description.**

from the output of *gtltcube* by identifying the EXPOSURE HDU, and selecting the row with the closest position to the source of interest. The information on exposure as a function of the off-axis angle is stored there.

4.7.1. Search for correlations between 1ES 1215+303 and its closest neighbors

There is another complex intrinsic aspect of the ML fit that needs to be checked; the possible correlations between the results obtained for different sources, and the correlation between their parameters.

From Figure 4.19, no flux-flux correlation is observed between 1ES 1215+303 and 1ES 1218+304, or between these sources and the diffuse contributions. The galactic diffuse and the isotropic diffuse, on the other hand, are anti-correlated. It is reasonable that the fit is not able to disentangle these sources at high latitudes such as that of 1ES 1215+303 where the galactic diffuse is basically uniform.
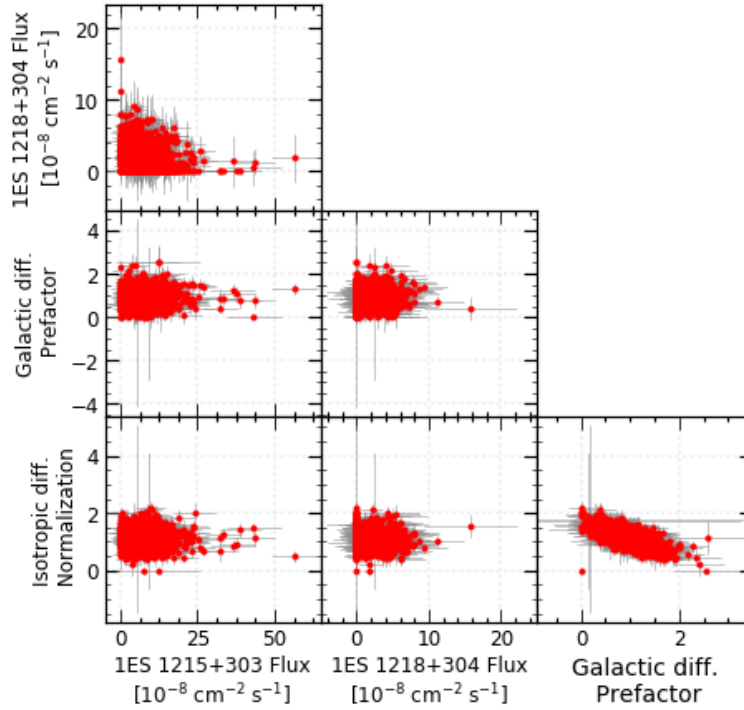
Fig. 4.19.— **Correlation between 1ES 1215+303 and objects close by. All of these data correspond to the light curve analysis for 1ES 1215+303 from 2008 Aug. 04 to 2017 Sep. 04. See text.**

The covariance terms for the free parameters of 1ES 1215+303 and 1ES 1218+304 were also carefully monitored throughout this work. For instance, Figure 4.20 shows the correlation coefficient between their prefactors (in blue), as given by *gtlike*, in the third panel from the top. This coefficient is most of the time negative and above -0.5, approaching this value during the faintest states of 1ES 1218+304. There is no evidence for correlations between the parameters of 1ES 1215+303 and those of the diffuse components.

The correlation between different methods of building light curves was also analyzed before the method itself to be used in this study was determined. Separate analyses leaving the indices free for the brightest sources in the ROI of 1ES 1215+303, for a portion of the light curve (namely 2016-2017) were performed. Given the strong anti-correlation of the diffuse components, the case with no isotropic diffuse in the model file was also analyzed. In Figure 4.21, method M1 is the case of a 3-day binned light curve with all indices fixed (standard), and method M4 is the case with all indices initially free (the indices of some of the sources in the ROI were later fixed in order to reach convergence with reasonable values; this happened more frequently for the fainter sources). Methods M2 and M3 are the analogous cases but with no isotropic diffuse component included in the model file.

We notice that in the cases with the indices free we obtain a more scattered F/σ_F vs $\sqrt{TS}$ correlation than in the cases of an analysis with the indices fixed. This is possibly an indication of larger uncertainties. From Figure 4.22, we observe that there is no advantage to erasing the isotropic diffuse from the model, and that there is possibly a trend for higher

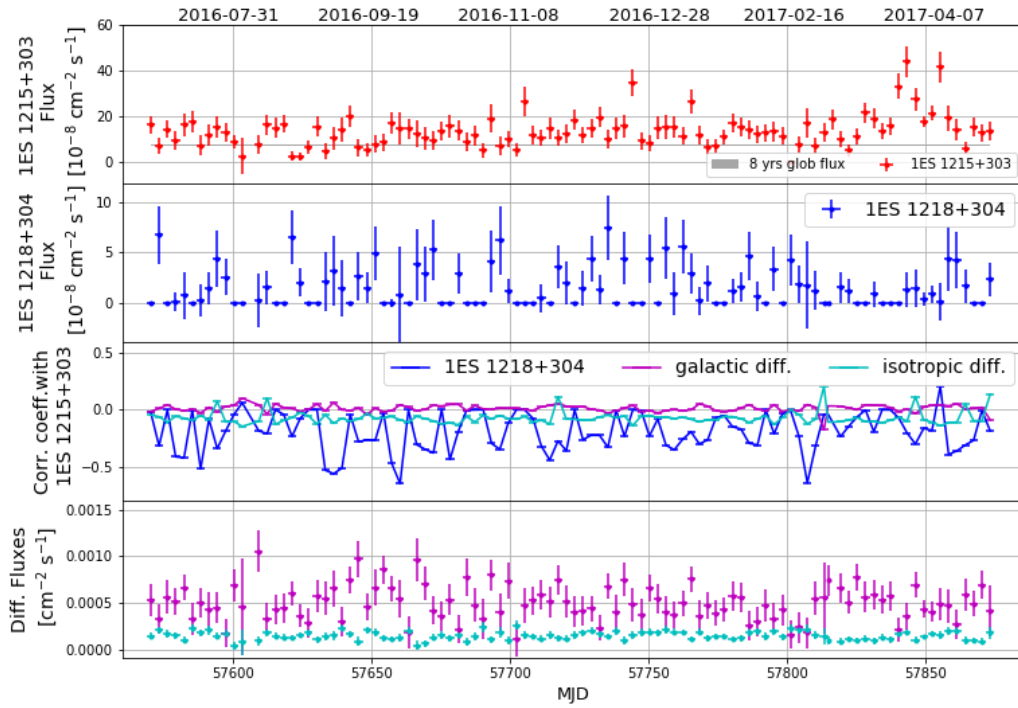**Fig. 4.20.**— From top to bottom: 1ES 1215+303 standard light curve, 1ES 1218+304 standard light curve, correlation coefficient between the flux parameters of close-by sources and 1ES 1215+303, and the light curves from the galactic and isotropic diffuses; for 1ES 1215+303 ROI analysis from 2016 Oct. to 2017 Sep.
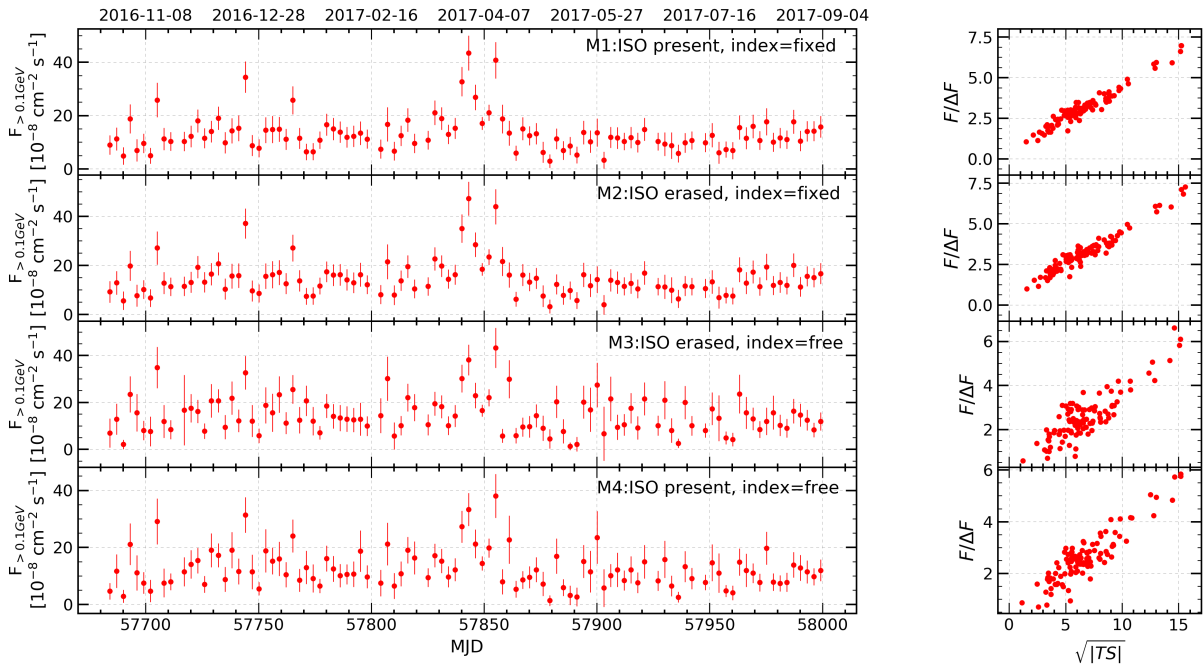

Fig. 4.21.— Four methods to build the light curves for 1ES 1215+303 were investigated, see text.
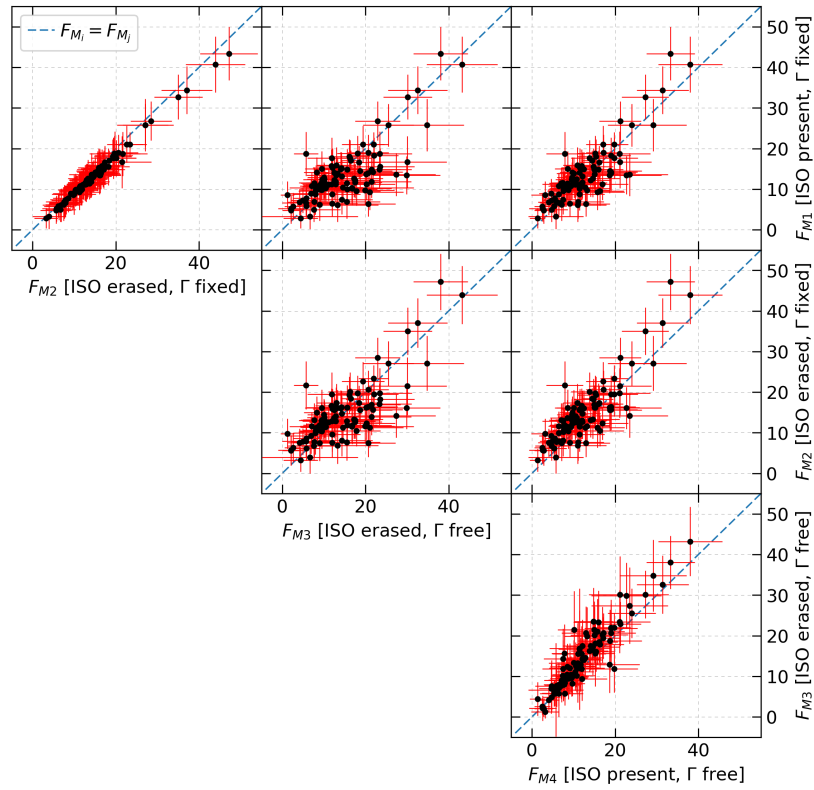
Fig. 4.22.— **Correlations between the four methods used to build the light curves shown in Figure 4.21.**

fluxes for 1ES 1215+303 when the isotropic diffuse is not included in the model.

Figure 4.23 offers an overview of the differences and ratios between the fluxes measured with the four different analysis methods. That is, deviations of M_i with respect to M_j, with $i, j = 1, 2, 3, 4$. No uncertainties were included. This figure confirms the larger scatter of the methods with photon indices free and the absence of any advantage to erasing the isotropic diffuse component from the model file.

The left panel of Figure 4.24 shows a comparison between the uncertainties obtained by fixing the indices or leaving them free, that is, M1 and M4 respectively. A line of slope= 1 was drawn for visualization. The middle panel shows the distributions of these uncertainties, where the broadening for the case with indices free (M4) is evident. The obtention of larger uncertainties with the method where the photon indices are free is also apparent. No clear difference is observed in the distribution of the fluxes in the right-hand side panel of the same figure.

Having obtained a more defined distribution of the uncertainties and no clear difference in the distribution of the fluxes, we were inclined towards the use of method M1, that is, indices fixed.

It was possible to implement all of the rigorous analyses and sanity checks on this
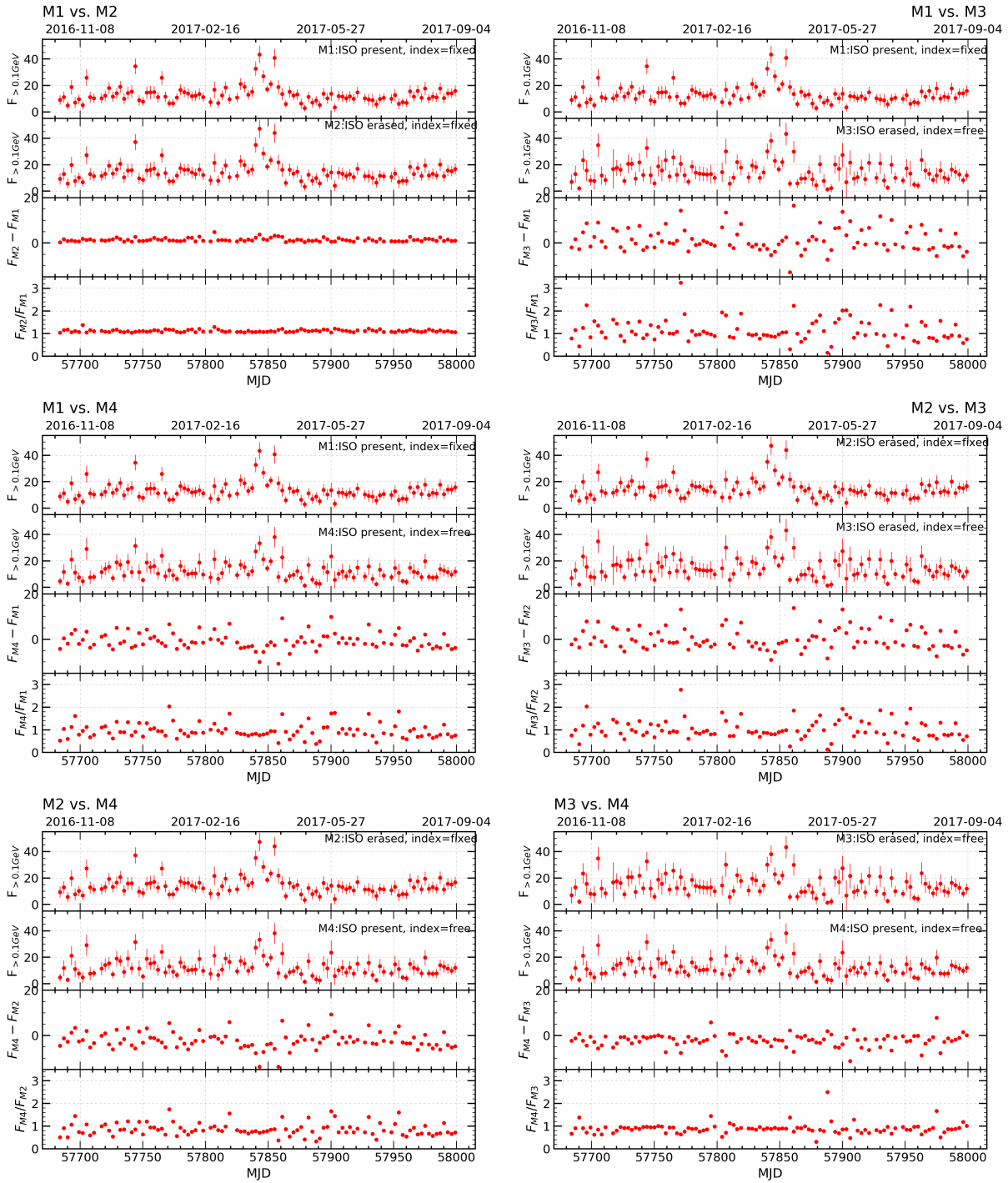
Fig. 4.23.— Overview of the differences and the ratios between the fluxes measured with the different methods for 1ES 1215+303 from 2016 Oct. to 2017 Sep.

extensive data set detailed throughout this chapter due to the implementation of scripts written by the author that automated the procedure for the obtention of LAT light curves. One of them consists of a code implemented in Python that parses and extracts the information from the folders where the results of a complete analysis is stored for each bin; dictionaries are built and results are written to tables. Another script uses the
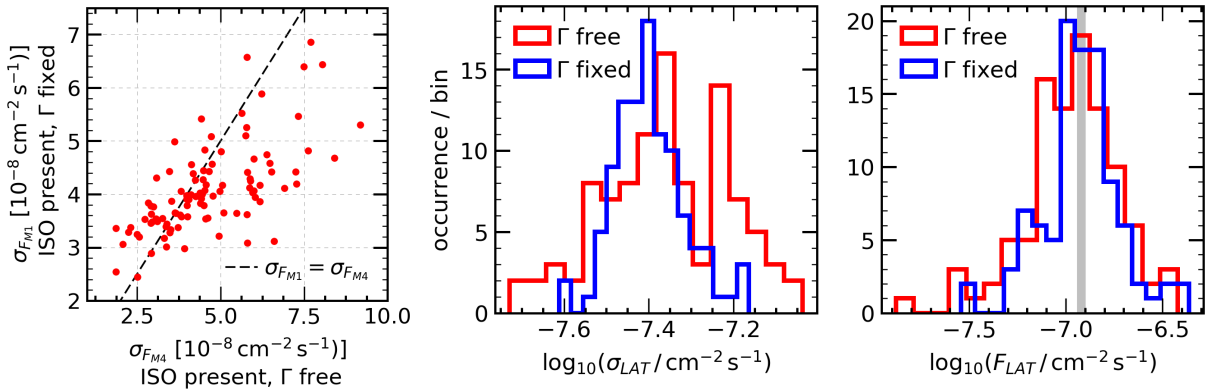
Fig. 4.24.— *Left:* Correlation between the uncertainties obtained with methods M1 and M4. *Middle:* Distribution of the uncertainties for methods M1 and M4. *Right:* Distribution of the uncertainties for methods M1 and M4. Data from **3-day binned light curve for 1ES 1215+303 from 2016 Oct. to 2017 Sep.** The gray region represents the average flux of the source reconstructed with the data in the 2016 Oct. – 2017 Sep. time range.

dictionary with the information that all of the analyses generated, and erases or fixes the parameters of the sources according to the user specifications. It can also replace the model files with the fitmodel file from the previous run so that the user can re-run the analyses from the values reached in the previous attempt. The model file in each folder is modified independently from the information in the other folders, and a `.log` of the changes made is generated.

4.7.2. Variability analysis: Bayesian blocks

The Bayesian blocks representation (Scargle et al. 2013, henceforth S13) addresses the issue of identifying and characterizing statistically significant localized variations in sequential data, e.g. light curve features that last a sub-range of the total observation time. This method finds the optimal segmentation of data in the observation interval, separating like this the statistically significant features from random observational errors. The Bayesian blocks representation is used in Section 5.3.2 as one of the methods to study the flux variability of 1ES 1215+303 and select high states caused by its outbursts (also known as flares). Therefore, I dedicate this section to briefly introduce and highlight the benefits of this method.

The Bayesian blocks method is a kind of segmentation analysis (or change-point detection), in which the range of the independent variable is divided into sub-intervals, or blocks; and the dependent variable is modeled as a constant within errors within the block. The result is thus a step-function which represents the changes in the data. In the case of this work the independent variable is the time, the dependent variable is the flux and the constant within the block is the average of the fluxes of the data points in each block.

Bayesian statistics involves defining a prior distribution (often simply called "prior") through which we incorporate our subjective belief about a parameter, retrieving data, and updating the prior distribution with the data to obtain a posterior distribution through: posterior $\propto$ prior $\times$ likelihood (Bayes' Theorem; Tanabashi et al. 2018a). S13 imposes the following geometric prior on the number of blocks (N_{blocks}):

$$P(N_{\mathrm{blocks}}) = \begin{cases} P_0 \gamma^{N_{\mathrm{blocks}}}, & \text{for } 0 \leq N_{\mathrm{blocks}} \leq N, \\ 0, & \text{otherwise,} \end{cases} \tag{4.14}$$

where $P_0 = \frac{1-\gamma}{1-\gamma^{N+1}}$[16], and N is the number of cells (a cell usually contains one datum). In almost all applications γ is chosen to be < 1 to indicate the belief that a smaller number of blocks is a priori more likely than a larger number. The expected number of blocks is then given by:

$$\langle N_{\mathrm{blocks}} \rangle = P_0 \sum_{N_{\mathrm{blocks}}=0}^{N} N_{\mathrm{blocks}} \gamma^{N_{\mathrm{blocks}}} = \frac{N\gamma^{N+1}+1}{\gamma^{N+1}-1} + \frac{1}{1-\gamma} \tag{4.15}$$

As mentioned before, the goal of the method is to find the best step-function (or piecewise constant model) fit to the data, defined by maximizing a specific fitness measure (see S13 for details on the fitness functions). This algorithm relies on the fitness being block-additive:

$$F[\mathcal{P}(\mathcal{T})] = \sum_{k=1}^{N_{\mathrm{blocks}}} f(B_k), \tag{4.16}$$

where $F[\mathcal{P}(\mathcal{T})]$ is the total fitness of the partition $\mathcal{P}$ of the interval $\mathcal{T}$, and $f(B_k)$ is the fitness of the block k. The method ignores the possibility of having correlated errors, which would at the same time correlate the fitness of a block with those of its neighbors. All of the parameters in the model are marginalized except for the block edges; on which the total fitness depends. Thus the best model is found by maximizing F over all possible such partitions.

The basic algorithm follows the spirit of mathematical induction, and at each step the analysis makes use of results, fitness and change points, stored from all previous steps; and the position of the change points are not necessarily fixed until the very last iteration. As mentioned above, the output of the algorithm depends on γ. Although for moderately large signal-to-noise ratio, the results are quite insensitive to the value of γ. There is a tradeoff involved in choosing the value of γ. One might have to choose between not being misled by noise fluctuations but taking the risk of missing potential changes, which would be a conservative posture, or one can choose to better capture the changes but at the

---

[16]γ, in this section only, is not to be confused with gamma-ray as in the rest of the manuscript.

same time allowing some false detections. Running the algorithm with different values of γ could lead to finding a range over which the block representation is reasonable and not very sensitive to the parameter γ.

To help with calibrating γ as a function of the number of data points, S13 find it useful to relate γ to the relative frequency with which the algorithm falsely reports the detection of a change point in data when no signal is present, i.e. the false positive probability. The authors conveniently make use of the complementary quantity, that is, the frequency with which the algorithm correctly rejects the presence of a change-point in pure noise, i.e. the correct detection rate:

$$p_0 \equiv 1 - \text{false positive probability}. \tag{4.17}$$

S13 finds the needed γ-p_0 relationship by noting that the rates of correct and incorrect responses to fluctuations in simulated pure noise data can be controlled by adjusting the value of γ. By applying the algorithm to the simulated pure noise data for a number of γs, selecting the smallest values that yield a false detection frequency equal or less than the desired rate, and averaging over a number of realizations of the random data; they find that γ depends only on the number of data points and the adopted value of p_0. Review S13 for details on the results of these simulations for different model fitness functions and data modes (event data, binned data and point measurements with normal errors).
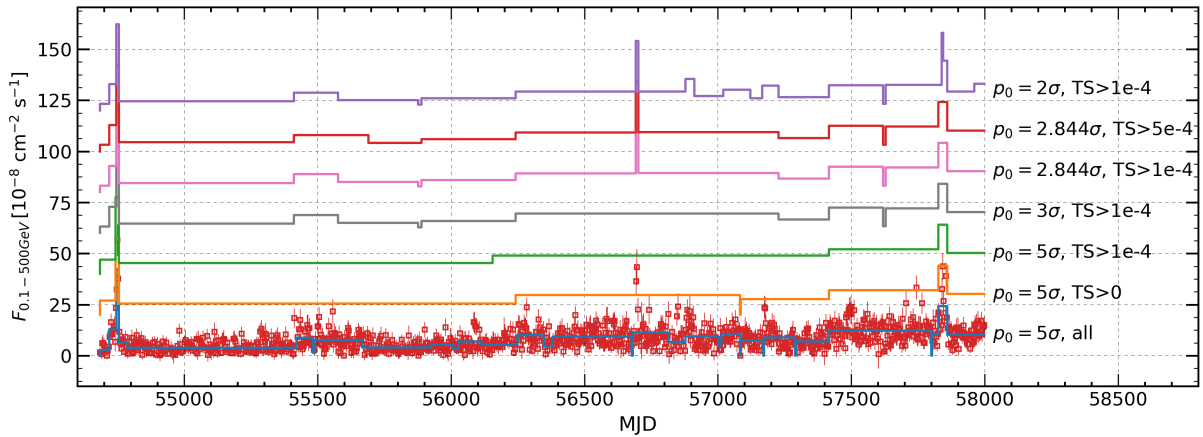
Fig. 4.25.— **Bayesian blocks for different values of false positive rates p_0 and data selections. All of these data correspond to the light curve analysis for 1ES 1215+303 from 2008 Aug. 04 to 2017 Sep. 04. The Bayesian blocks have been translated on the y-axis with an offset flux of $20 \times 10^{-8}\,\mathrm{cm}^{-2}\,\mathrm{s}^{-1}$ between each other for visibility purposes.**

In the following, the Bayesian blocks `astropy` implementation was used[17]. This code is based on the algorithm developed by S13. Figure 4.25 shows a 3-day binned light curve from 1ES 1215+303. As is expressed in Equation (4.15), the number of blocks depends

---

[17]https://docs.astropy.org/en/stable/api/astropy.stats.bayesian_blocks.html

on the number of points (N) and on γ. As mentioned above, the γ depends on N and on the correct detection rate, p_0 as defined in Equation (4.17). Therefore, the number of blocks depends on N and p_0. Figure 4.25 shows the blocks obtained for different values of p_0 (in σs) and datasets (applying cuts in TS, see Figure 4.16). Clearly, modifying p_0 and N changes the number blocks, and has an impact on the block heights.

The cuts made were triggered by the flux/uncertainty vs $\sqrt{\text{TS}}$ lack of linearity for data with TS< 0 (see Figure 4.16), whose uncertainties have a separate distribution with respect to those from data with TS> 0. If these cuts are not applied, the blocks show depths not consistent with the local behavior of the data due to small uncertainties during notably faint states. As discussed in Section 5.3.2, a false positive rate of $p_0 = 2.844\,\sigma$ and a cut in the LAT data that rejected the points with TS $< 5 \times 10^{-4}$ were chosen so that the flaring periods that were selected using method I (see Section 5.3.2) would also be detected by the Bayesian blocks method.

Table 4.4: *Fermi*-LAT SED. Time range: 2008 Aug. 04 - 2017 Sep. 04.

Energy (GeV)	Sig. (σ)	Flux ($\mathrm{cm^{-2}\,s^{-1}}$)	Predicted counts
0.100 - 0.146	10.9	$(1.62 \pm 0.48) \times 10^{-8}$	1893.8
0.146 - 0.215	22.1	$(1.65 \pm 0.19) \times 10^{-8}$	2766.9
0.215 - 0.316	24.8	$(1.03 \pm 0.09) \times 10^{-8}$	2198.6
0.316 - 0.464	30.7	$(7.36 \pm 0.44) \times 10^{-9}$	1857.2
0.464 - 0.681	38.6	$(5.58 \pm 0.25) \times 10^{-9}$	1608.2
0.681 - 1	44.9	$(4.12 \pm 0.16) \times 10^{-9}$	1319.3
1 - 1.467	47.3	$(2.81 \pm 0.11) \times 10^{-9}$	992.1
1.467 - 2.154	51.8	$(2.20 \pm 0.09) \times 10^{-9}$	820.0
2.154 - 3.162	50.4	$(1.48 \pm 0.07) \times 10^{-9}$	559.7
3.162 - 4.641	43.9	$(9.82 \pm 0.55) \times 10^{-10}$	366.0
4.641 - 6.812	40.0	$(7.07 \pm 0.47) \times 10^{-10}$	258.5
6.812 - 10	32.4	$(4.23 \pm 0.36) \times 10^{-10}$	155.8
10 - 14.677	32.5	$(3.52 \pm 0.32) \times 10^{-10}$	129.9
14.677 - 21.544	27.9	$(2.50 \pm 0.27) \times 10^{-10}$	91.4
21.544 - 31.622	20.4	$(1.22 \pm 0.18) \times 10^{-10}$	45.2
31.622 - 46.415	16.2	$(8.02 \pm 1.50) \times 10^{-11}$	30.5
46.415 - 68.129	18.4	$(8.51 \pm 1.54) \times 10^{-11}$	32.4
68.129 - 100	12.9	$(4.10 \pm 1.09) \times 10^{-11}$	15.6
100 - 500	7.3	$(2.19 \pm 0.79) \times 10^{-11}$	8.2

5. THE CASE OF 1ES 1215+30, A BL LAC OBJECT

Most studies of TeV γ-ray blazars focus on short timescales, especially during flares. With a decade of observations from *Fermi*-LAT and VERITAS and our multi-wavelength partners, this manuscript describes our investigation of the multi-frequency, cross-comparison and cross-correlation variability and broadband emission of the blazar 1ES 1215+303 using multi-wavelength (MWL) observations from radio to γ-rays, covering the past decade, and with a strong focus on its γ-ray emission.

5.1. A brief introduction
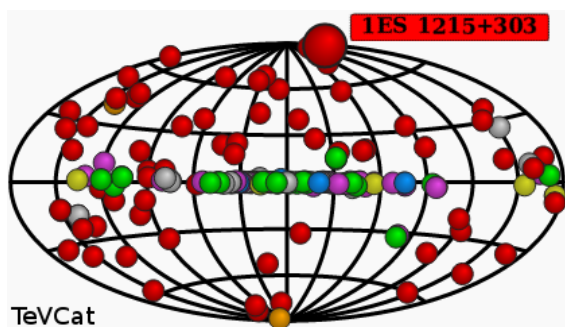
Fig. 5.1.— **Map showing the known TeV sources at the time of writing. The position of 1ES 1215+303 is highlighted. From TeVCat.**

1ES 1215+303 (B2 1215+30, ON 325, 3FGL J1217.8+3007, 4FGL J1217.9+3007) is a blazar located at R. A.$_{(J2000)} = 12^h17^m48.5^s$ and Dec.$_{(J2000)} = +30°07'00''6$. It was first reported in the 1970 B2 408 MHz Bologna Northern Cross telescope radio catalog (Colla et al. 1970) (hence the name B2), and has been observed at other wavelengths since then, including its first detection at VHE on 2011-01-[02-05] by the MAGIC collaboration (ATel #3100[1]; Aleksić et al. 2012). 1ES 1215+303 exhibits a double-humped spectral energy distribution typical of all high-energy blazars, with the synchrotron peak between radio and X-ray energies and the high-energy peak at GeV – TeV energies. Throughout the last decades, 1ES 1215+303 has been reported to belong at different times to different classes of BL Lacertae object types. It was classified as a

---

[1] http://www.astronomerstelegram.org/?read=3100

high-frequency peaked (HSP) with $\nu_{\text{syn}} > 10^{15}$ by Ackermann et al. (2011). Nieppola et al. (2006) reported it as an intermediate-frequency peaked BL Lac[2] (IBL) based on a measurement of $\nu_{\text{sy}} = 10^{15.58}$ Hz while Ackermann et al. (2015a) classified it as a high-frequency peaked BL Lac (HBL) with $\nu_{\text{syn}} = 10^{15.205}$ Hz. Akiyama et al. (2003) measured a redshift of $z = 0.13$, which was confirmed to be $z = 0.131$ with high signal-to-noise ratio optical spectroscopic data (Paiano et al. 2017).

There have been two separate detections of γ-ray flaring activities from 1ES 1215+303 at VHE reported by VERITAS (Abeysekara et al. 2017), and another two at HE, detected with the *Fermi*-LAT, reported by Abdo et al. (2010b) and Abeysekara et al. (2017). The first HE flare for this source occurred on 2008-10-[10-15] with a reported flux of $F_{(E>300\text{MeV})} \sim 15 \times 10^{-8}\text{cm}^{-2}\text{s}^{-1}$ in a weekly light curve as part of a broader study of variability that included another 105 blazars (Abdo et al. 2010b). The second HE flare occurred with a coincident counterpart at VHE on 2014-02-08 and was described in a detailed publication (Abeysekara et al. 2017), which also reported the 2013-02-07 VHE flare. Additionally, 1ES 1215+303 was the subject of a 4-year multi-wavelength study (Aliu et al. 2013) that covered the time range from 2008 to 2012 with a 8.9 σ significance for energies greater than 200 GeV.

5.2.   The multi-frequency data

For this project, the broadband emission of 1ES 1215+303 was investigated, using MWL observations summarized in Table 5.1 and plotted in Figure 5.2. These observations covered the past decade, and in this study we focus, in particular, on the γ-ray data. These MWL observations allow us to study the variability of the flux of the source at different wavelengths, as well as the evolution of the broadband spectral energy distribution (SED). Given the fact that one luminous γ-ray flare has already been detected from 1ES 1215+303, we were interested in exploring the long-term temporal behavior of the source over a ten year time period using the γ-ray observations of *Fermi*-LAT and VERITAS. This analysis gives access to an unprecedented archival data set from *Fermi*-LAT and VERITAS and is the longest temporal study of 1ES 1215+303 at γ-ray energies to date. Multiple strong γ-ray flares and a long-term increase in the γ-ray and optical flux baseline of the source were observed over the ten-year period.

---

[2]The class boundaries set by Nieppola et al. (2006) were $\nu_{\text{sy}} \approx 10^{13-14}$ Hz for LBLs, $\nu_{\text{sy}} \approx 10^{15-16}$ Hz for IBLs, and $\nu_{\text{sy}} \approx 10^{17-18}$ Hz for HBLs. They were therefore different than those described in Section 2.3.1, hence the apparent contradiction in the classification of this source.

Table 5.1: Overview of the dataset presented in this study.

Instrument	Waveband	Energy range	Date range	No. of observations[a]
VERITAS	VHE-γ-ray	> 200 GeV	2009 - 2017	87
Fermi-LAT	HE-γ-ray	0.1 - 500 GeV	2008 - 2017	1045[b]
Swift-XRT	X-ray	0.3 - 10 keV	2009 - 2017	25
Swift-UVOT	UV-optical	170 - 650 nm[c]	2009 - 2017	232
Tuorla	Optical	R-band	2003 - 2017	424
NOT	Optical[d]	R-band	2014 - 2017	49
OVRO	Radio	15 GHz	2008 - 2017	475
Metsähovi	Radio	37 GHz	2002 - 2016	53
VLBA (MOJAVE)	Radio	15.3 GHz	2009 - 2016	10
VLBA	Radio	22.2 & 43.1 GHz	2014	2

[a] We list here the number of flux points shown in Figure 5.2 to give an indication of the sampling at each wavelength. For the VLBA observations, we just provide the number of images that were recorded.
[b] Number of flux points in the 3-day binned light curve.
[c] The UVOT data were taken with six different filters with central wavelengths of 544 nm (V filter), 439 nm (B filter), 345 nm (U filter), 251 nm (UVW1 filter), 217 nm (UVM2 filter) and 188 nm (UVW2 filter) (Roming et al. 2005).
[d] The NOT provided polarization measurements at optical wavelengths.

5.2.1.   Very-high-energy γ-ray Data: VERITAS

1ES 1218+304 ($z = 0.182$), one of a list of blazars that VERITAS monitors frequently as part of its long-term monitoring program, has been regularly observed by VERITAS since 2008 December. Due to the proximity of this blazar to 1ES 1215+303 (the angular distance between the two is $\sim$0.76°) and the FoV of VERITAS, a rare long-term TeV dataset is also made available for 1ES 1215+303 through this study by the VERITAS Collaboration.

The observations were taken in "wobble mode" (Fomin et al. 1994) with either 1ES 1215+303 or 1ES 1218+304 offset by 0.5° from the center of the FoV. The total exposure with 1ES 1215+303 in the FoV between 2008 Dec and 2017 May amounts to 175.8 hr, after quality selection, before dead-time correction and without accounting for the difference in sensitivity between observations on the two sources. The VERITAS results for this source between 2008 December and 2012 May are archival data from Aliu et al. (2013), and those between 2013 January and 2014 May were reported in Abeysekara et al. (2017).

The VERITAS data were analyzed using two independent analysis packages (Cogan 2008; Daniel 2008), and consistent results were obtained. Cuts optimized for each analysis package for a point source of 2% to 10% of the Crab Nebula flux with a power-law photon index between 2.5 and 3.0 (Park & VERITAS Collaboration 2015) were used. The detection significance value was calculated using Equation (17) from Li & Ma (1983). It was found that a power-law model (see Equation (4.2)) provides a good fit to the VER-
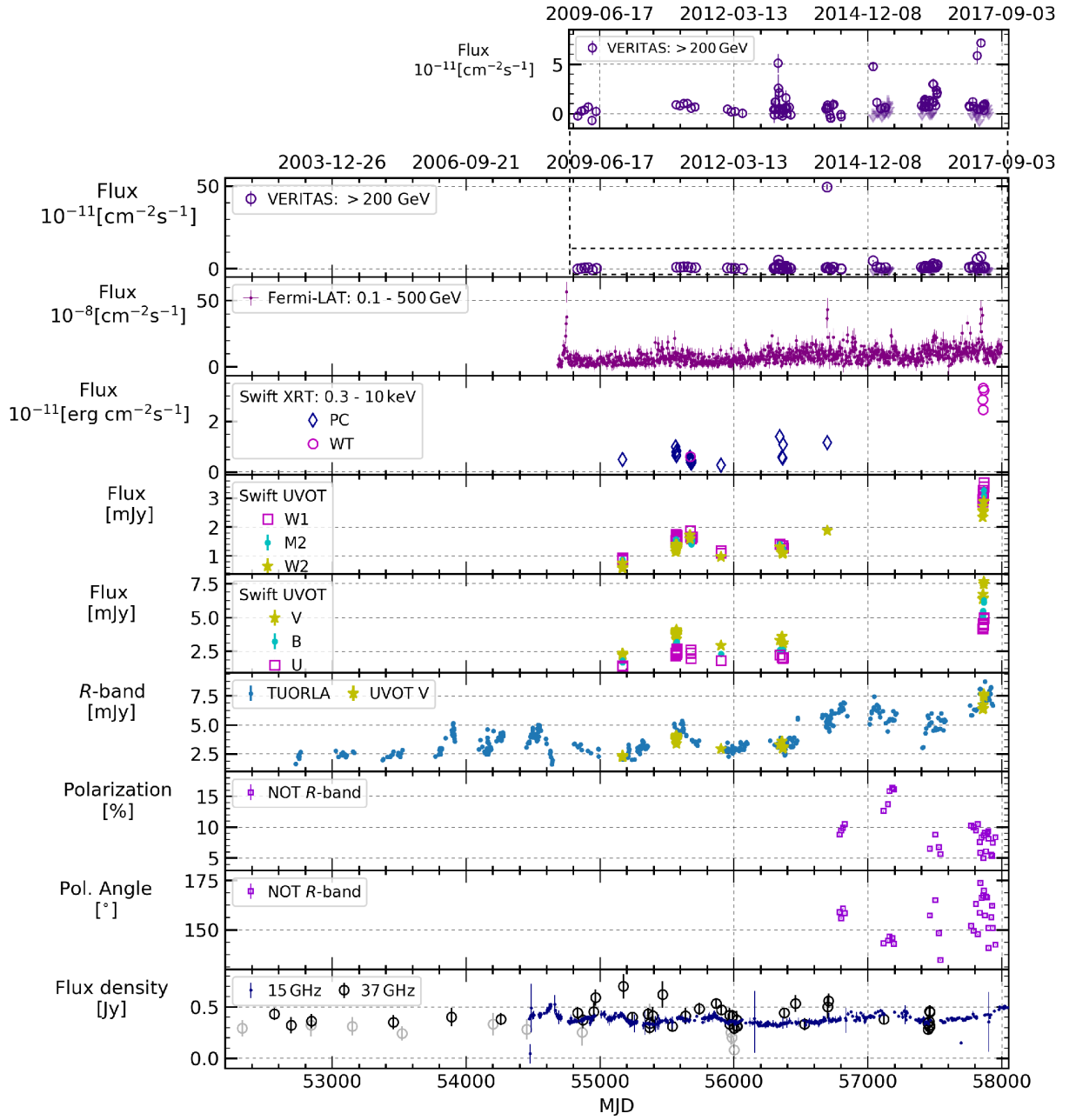
Fig. 5.2.— From top to bottom, the light curves for the various wave bands are shown in descending order of energy. A zoom is provided on the VERITAS data which excludes the GeV – TeV flare during 2014. For the radio panel, the 37 GHz data with signal to noise ratio S/N< 4 are shown in gray.

ITAS spectrum of 1ES 1215+303. The best-fit TeV γ-ray fluxes and photon indices of 1ES 1215+303 for different epochs and states (flare and non-flare) are provided in Table 5.2. The data from the 2014 season were re-analyzed in order to extract the spectrum from the non-flaring state, which resulted in an upper limit.

The top left panel of Figure 5.3 shows the cumulative significance for the 2015 season. Notice the peak within the first 150 min. caused by the outburst of 2015 Jan. 17, the

Table 5.2: VERITAS observations of 1ES 1215+303 from 2008 December to 2017 May. The VERITAS observing season runs from the end of the monsoon season ($\approx$ September) until the start of the monsoon season the following year ($\approx$ July) and is divided into periods called "darkruns" that are centered on the new moon.

Epoch	Exposure (hr)	Flux >200 GeV ($\mathrm{cm^{-2}\,s^{-1}}$)	Photon Index
2008-2009	33.8	$< 4.5 \times 10^{-12}$	-
2010-2011	41.9	$(8.0 \pm 0.9) \times 10^{-12}$	3.6 ± 0.4
2011-2012	17.5	$(2.8 \pm 1.1) \times 10^{-12}$	-
2012-2013 non-flare	10.8	$(6.0 \pm 1.2) \times 10^{-12}$	3.9 ± 0.6
2013 Feb 07 (2)	0.5	$(5.1 \pm 1.0) \times 10^{-11}$	3.7 ± 0.7
2013-2014 non-flare †	7.4	$< 7.2 \times 10^{-12}$	-
2014 Feb 08 (3)	0.9	$(5.0 \pm 0.1) \times 10^{-10}$	3.1 ± 0.1
2014-2015 non-flare	14.4	$(4.2 \pm 0.8) \times 10^{-12}$	2.8 ± 0.4
2015 Jan 17 (4)	0.9	$(5.3 \pm 0.5) \times 10^{-11}$	3.0 ± 0.2
2015-2016 non-flare	22	$(1.3 \pm 0.1) \times 10^{-11}$	3.3 ± 0.1
2016 Apr 09 (5)	0.9	$(3.7 \pm 0.5) \times 10^{-11}$	3.1 ± 0.3
2016-2017 non-flare	24.6	$(8.0 \pm 0.8) \times 10^{-12}$	3.9 ± 0.3
2017 Mar 05 (6)	0.9	$(5.9 \pm 0.9) \times 10^{-11}$	2.5 ± 0.4
2017 Apr 01 (7)	2.5	$(9.5 \pm 0.6) \times 10^{-11}$	3.6 ± 0.1

The enumeration in parenthesis after the date of a flare corresponds to the flare identification number (ID). I refer to Sections 5.3.2 and 5.10 for details on the flare ID and the simultaneity of observations with the *Fermi*-LAT.
† The 2013 – 2014 season was re-analyzed for the non-flare data and we report here the upper limit of those observations.

first observation of the season performed on this source. The top-right panel of Figure 5.3 shows the distribution of significance for the results of the 2015 season. The blue line represents the distribution of excesses after subtracting 1ES 1218+304; while the red line represents the distribution of the excesses after subtracting 1ES 1215+303. The background (black solid line) is seen to follow a Gaussian function centered at zero with a width of one, as is expected from background fluctuations after having excluded both neighboring sources, validating the results obtained.

5.2.2. High-energy γ-ray Data: *Fermi*-LAT

I analyzed the *Fermi*-LAT data for 1ES 1215+303 from 2008 Aug 04 (MJD 54682.7), the start of the science operations phase of the mission, up until to 2017 Sep 04 (MJD 58001.0). The data were analyzed using the `Fermi Science Tools package`[3] and following the standard procedures described in Chapter 4. As explained there, I restricted our

---

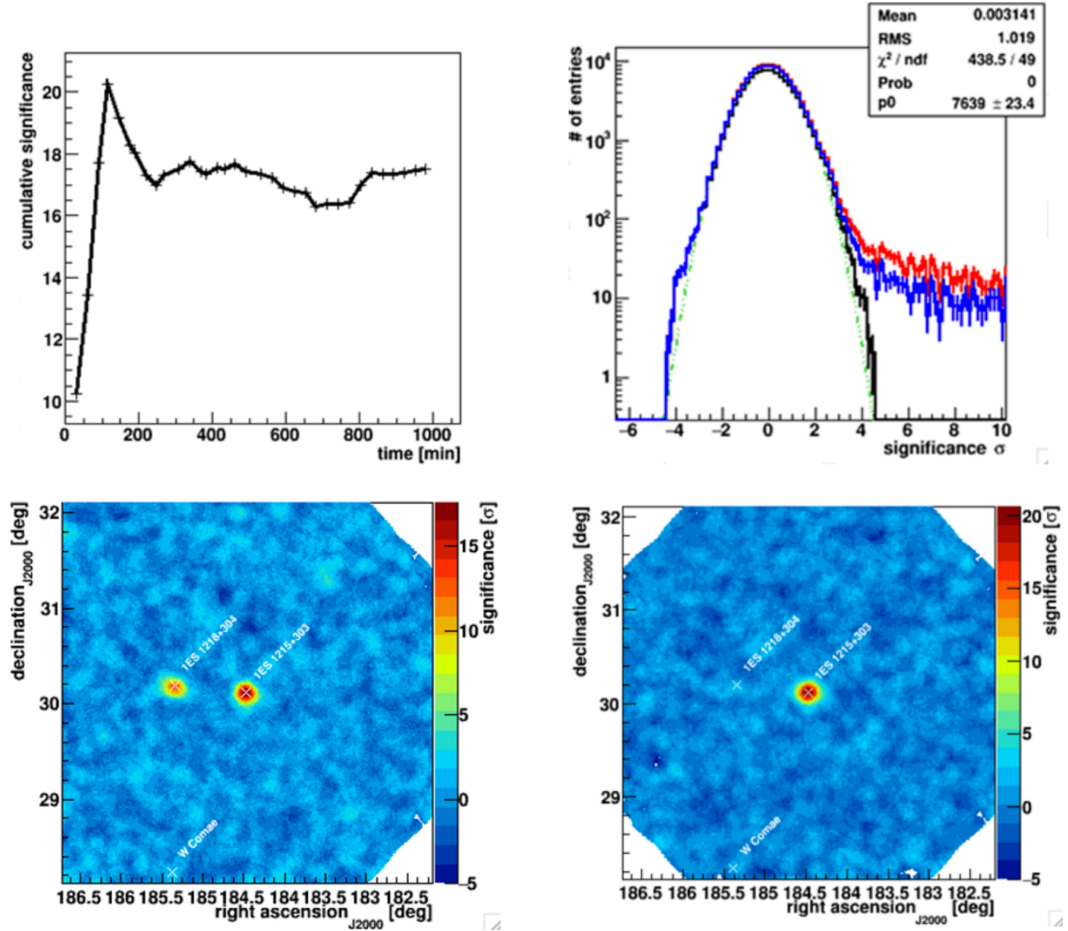[3]Version `v10r0p5`; Instrument response functions `P8R2_SOURCE_V6`.

Fig. 5.3.— 1ES 1215+303: *Top left:* Cumulative significance as a function of time from the 2015 season data. *Top right:* Distribution of significance in the 2015 season data (see the text). *Bottom left:* 2015 season skymap. *Bottom right:* Skymap of the region during the flare of 2015 January 7th. Notice that the comparatively hard BL Lac object 1ES 1218+304 is outshone by 1ES 1215+303 during this 114 min. time range. Courtesy of G. Noto and the VERITAS Collaboration.

photon selection to those that had a zenith angle of less than 90° in order to reduce contributions from the Earth's limb. Photons with energies between 100 MeV and 500 GeV were considered and analyzed using unbinned statistics. These consisted of photons in a circle of radius 10° centered on the position of 1ES 1215+303, the ROI[4].

For the modeling of the 1ES 1215+303 ROI, I used the maximum likelihood fit method, implemented in *gtlike* within the `Fermi Science Tools`. Three different spectral models were considered to describe the spectrum of 1ES 1215+303 as measured by the LAT. These comprised a power-law (PL), a log-parabola (LP) and a power-law sub-exponential cutoff model (plSECO), as described in Section 4.6. As is discussed in Section 5.9, both of the curved models were found to be preferred over the power-law model. For

---

[4]Since the PSF of the *Fermi*-LAT can attain ≈10° at 100 MeV.

Table 5.3: *Fermi*-LAT flux and spectral shape of 1ES 1215+303 from 2008 Aug 04 to 2017 Sep 05.

Epoch	State	Sig. σ	Flux $_{>0.1\ \mathrm{GeV}}$ $10^{-8}\ \mathrm{cm}^{-2}\ \mathrm{s}^{-1}$	Γ
2008-11-17 - 2010-08-12			4.3 ± 0.3	1.98 ± 0.03
&	Low	49.0		
2011-04-15 - 2012-04-09				
2008-08-04 - 2009-07-30	Total	38.4	5.3 ± 0.4	1.94 ± 0.04
2008-08-04 - 2009-07-30	Non-Flare	31.6	4.3 ± 0.4	1.94 ± 0.04
2008-10-04 - 2008-10-17	Flare 1	26.4	35.0 ± 3.5	1.92 ± 0.06
2009-07-30 - 2010-07-25	Total	29.3	4.6 ± 0.5	2.01 ± 0.05
2010-07-25 - 2011-07-20	Total	40.9	7.2 ± 0.5	1.97 ± 0.04
2011-07-20 - 2012-07-14	Total	32.8	5.4 ± 0.5	2.00 ± 0.04
2012-07-14 - 2013-07-09	Total	47.0	7.5 ± 0.5	1.92 ± 0.03
2013-07-09 - 2014-07-04	Total	54.0	10.1 ± 0.6	1.94 ± 0.03
2013-07-09 - 2014-07-04	Non-flare	50.4	10.0 ± 0.6	1.95 ± 0.03
2014-07-04 - 2015-06-29	Total	50.4	8.7 ± 0.5	1.91 ± 0.03
2015-06-29 - 2016-06-23	Total	54.7	9.1 ± 0.5	1.90 ± 0.03
2016-06-23 - 2017-06-18	Total	70.1	12.0 ± 0.5	1.86 ± 0.02
2016-06-23 - 2017-06-18	Non-Flare	63.7	11.2 ± 0.5	1.88 ± 0.02
2017-03-25 - 2017-04-05	Flare 7	25.9	25.2 ± 2.8	1.74 ± 0.06
2017-04-09 - 2017-04-16	Flare 8	18.9	28.4 ± 4.0	1.83 ± 0.08
2017-04-15 - 2017-04-23	Post-flare	8.6	9.5 ± 2.3	1.89 ± 0.34

Sig. stands for significance,while Γ represents the power-law photon index.

the estimation of the integrated flux data points in the light curves and for the individual spectral data points, only the power-law model was used for 1ES 1215+303, since for these small data sets, no preference for curved models was found. The photons above 10 GeV with the highest probability of coming from 1ES 1215+303 were calculated with the *gtsrcprob* tool, and using the output model file of *gtlike*.

Table 5.3 shows the best-fit values for the power-law spectral shape parameter and for the flux obtained for the different epochs, flaring, low state, post-flare, 360-day binned (approximately yearly), and 360-day binned outside flares (non-flare) results. The flare selection and the definition of the low state (2008 November 17 – 2010 August 12 or MJD 54787–55421; and 2011 April 15 – 2012 April 10 or MJD 55666–56027) were guided by a variability analysis which included the use of the Bayesian block method. This is discussed in Section 5.3.2. Additional LAT analyses, constrained to the periods of time of VERITAS flares, were also performed; they are discussed in Section 5.10.

5.2.3.   X-ray – optical data

The *Swift* − XRT and UVOT analysis is described in Valverde et al. (2020).

1ES 1215+303 was monitored in the *R*-band at the Tuorla Observatory over the past

15 years as part of the Tuorla blazar monitoring program (Takalo et al. 2008; Nilsson et al.
2018). We also made use of optical polarization data from the NOT program (Hovatta
et al. 2016). We show the long-term R-band flux density in Figure 5.2. The long coverage
of the R-band data allows us to compare the optical and γ-ray emission on timescales as
long as a year.

5.2.4.   Radio Data: VLBA

1ES 1215+303 was observed with the VLBA at 22.2 and 43 GHz on 2014 November
11. About two hours of on-source integration time was recorded at each frequency, over
a total time span of about seven hours. These images are shown in Figure 5.4; both show
fractional polarization increasing down the jet, relative to the core. Circular Gaussian
models were fit to these data. A total of three jet components were detected at 22.2 GHz,
and a total of four jet components were detected at 43 GHz (labeled as "2, 3 and 4"
to correspond to those at 22.2 GHz), with an additional component (labeled as "5")
appearing between the innermost 22.2 GHz component and the core. The parameters of
the Gaussian model components are shown in Table 5.4.

1ES 1215+303 was also observed at 15.4 GHz with the Monitoring Of Jets in Active
galactic nuclei with VLBA Experiments (MOJAVE; Lister et al. 2019) program for 10
epochs between 2009 and 2016[5].
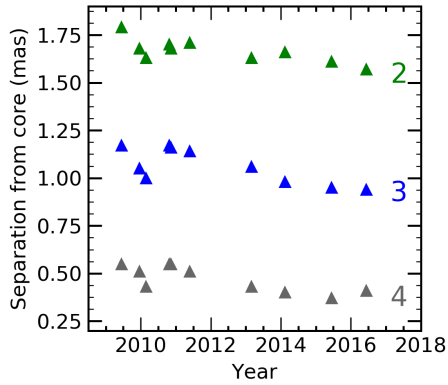

Fig. 5.6.— **Zoom on the separation between knots 2, 3 and 4 and the core.**

Emission features derived from a Gaussian model fit to the interferometric visibility data have been identified in the VLBA images at 15.4 GHz. The separations between these emission features and the core as at the time of each epoch of observation are shown in the right panel of Figure 5.5, revealing three innermost quasi-stationary emission features (components) labeled as 2, 3 and 4. The majority of TeV HBLs exhibit stationary features (e.g., Kharb et al. 2008; Hervet et al. 2016; Piner & Edwards 2018). The mean and standard deviation of the angular separation between the three quasi-stationary knots to the core over all epochs are 0.44 ± 0.07 mas, 1.04 ± 0.09 mas, and 1.64 ± 0.06 mas, as shown in Table 5.4. These three stationary knots are also resolved in the 22 and
43-GHz images, and the parameters of these three Gaussian components are consistent
between the three frequencies. There is an additional component observed at 15.3 GHz
(labeled as "1" in Figure 5.5 and Table 5.4) at a much larger distance from the origin
of the images, at a position consistent with a very-long-baseline interferometry (VLBI)

---

[5]Publicly available on: physics.purdue.edu/astro/MOJAVE/sourcepages/1215+303.shtml

Table 5.4: VLBA 43.1, 22.2, and 15.3 GHz Gaussian model components.

Flux (Jy)	r (mas)	P.A. (°)	$a^\dagger$ (mas)	Freq (GHz)	I.D.
(1)	(2)	(3)	(4)	(5)	(6)
0.127	0.03	−16.1	0.04	43.1	0
0.044	0.13	155	0.1	43.1	5
0.014	0.47	155	0.2	43.1	4
0.003	1.04	153	0.30	43.1	3
0.003	1.62	147	0.39	43.1	2
0.207	0.04	−24.4	0.02	22.2	0
0.038	0.37	155	0.11	22.2	4
0.008	1.1	151	0.30	22.2	3
0.004	1.72	145	0.25	22.2	2
0.265	0.03	323.1	0.03	15.3‡	0
0.033	0.47	152.5	0.12	15.3	4
0.011	1.06	150.3	0.2	15.3	3
0.009	1.67	145.6	0.34	15.3	2
0.013	16.20	143.5	4.41	15.3	1

Columns: (1) flux density of the component,
(2) and (3) the distance (r) and the position angle (P.A.) of the center of the component relative to the origin of the image,
(4) the full width at half maximum (FWHM) of the circular Gaussian component,
(5) measurement frequency, (6) Identification number of features from (or consistent with) Lister et al. (2019). Zero indicates core feature.
† The standard deviations of the best-fit Gaussian components are approximately 20% of the FWHM beam dimensions.
‡ The 15.3 GHz data correspond to fits using all data from the 10 epochs observed between 2009 and 2016.

stationary component found at 1.6 and 5 GHz (Giroletti et al. 2006), shown in Figure 2.2. The components 2, 3, and 4 show subluminal inward apparent speeds respectively of 0.170 ± 0.036 c, 0.246 ± 0.055 c, and 0.194 ± 0.040 c estimated by MOJAVE. The fact that they have similar inward motions, all consistent with an inward speed of $0.2\,c$, suggests that they are due to a downstream shift of the radio core. Indeed, if the three features are stationary shocks, a core shift predicts a similar inward motion for all of them. Such a shift of the radio core can be explained by a slow increase of the jet power over years, which would increase the distance from the supermassive black hole (SMBH) where the jet becomes optically thin in radio. Such a slow power increase is supported by the multi-year increase of the γ-ray and optical luminosities reported in Section 5.3.2. Similar inward motions have been detected in other BL Lac sources by MOJAVE such as UGC 00773, 3C 66A, and Mrk 421 (Lister et al. 2019). Since the emission features are quasi-stationary, we show a stacked image of the 15.4 GHz intensity in the left panel of Figure 5.5. The five best-fit Gaussian components from the last epoch on 2016 June 9
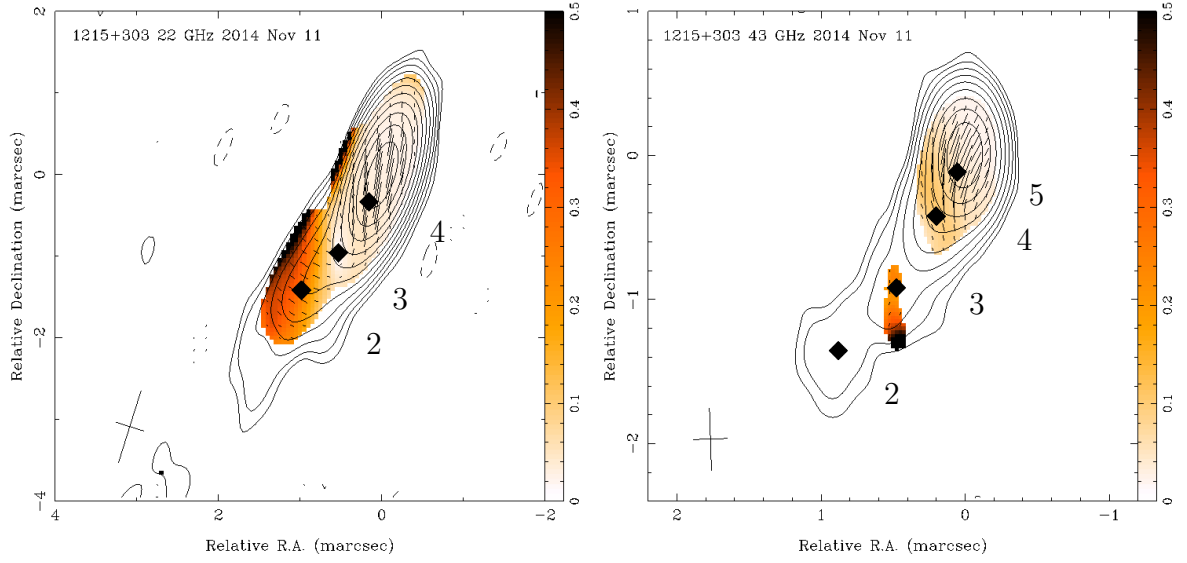
Fig. 5.4.— *Left*: VLBA image at 22.2 GHz. Contours show total intensity, with the lowest contour at 0.129 mJy beam^{-1}, and subsequent contour factors of two higher. The peak flux density is 229 mJy beam^{-1}. The naturally-weighted beam size is 0.914 by 0.358 mas at $-17.4°$. The sticks show the magnitude of the linearly polarized flux density (with a scale of 0.1 mas mJy^{-1}) and the direction of the electric vector position angle (EVPA). The color scale indicates fractional polarization. *Right*: VLBA image at 43.1 GHz. The lowest contour is 0.308 mJy beam^{-1}; the peak flux density is 152 mJy beam^{-1}. The naturally-weighted beam size is 0.432 by 0.241 mas at 1.9°. The polarized flux density scale is 0.05 mas mJy^{-1}. The centers of the Gaussian jet components are shown by filled diamonds. The beams are shown in the bottom left-hand corner of each panel as a plus symbol "+".
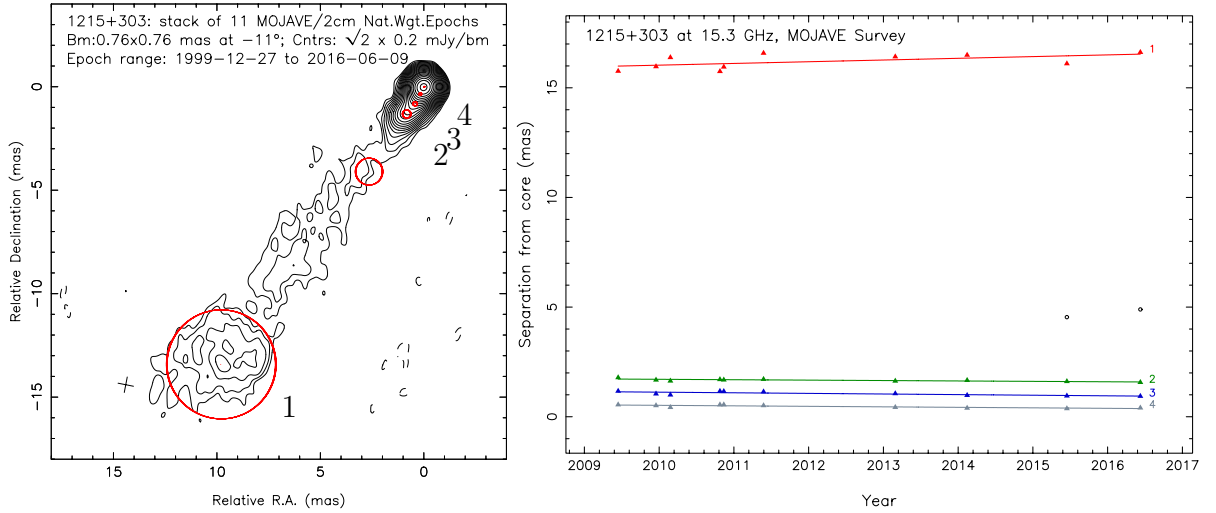
Fig. 5.5.— *Left*: The stacked MOJAVE image with the five best-fit Gaussian components from the last epoch on 2016 Jun 9 overlaid. The contours show the total intensity, starting at a baseline of 0.2 mJy beam^{-1}, and incrementing by factors of $\sqrt{2}$. *Right*: The separation between knots and the core at the time of each epoch of observation. The innermost three knots (designated with number 2, 3, and 4) are quasi-stationary.

are shown as red circles[6].

5.2.5.   OVRO 15 GHz and Metsähovi 37 GHz radio data

The radio flux density of 1ES 1215+303 measured by the OVRO at 15 GHz over the past decade (2008-2017) is shown in Figure 5.2, where a total of 475 data points are presented. We also show the radio flux density measured by Metsähovi Radio Observatory (MRO) at 37 GHz in Figure 5.2. The duration of the MRO data are longer than those from OVRO, but the sampling is generally more sparse. The radio data were also used in the SED modeling in Section 5.11, providing constraints on the less variable jet component.

5.3.   Temporal studies

In this section I describe the various analyses performed on our rich dataset including the study of its temporal evolution, MWL cross-correlations and flux distributions. The LAT data are explored in detail in order to study the evolution of the hardness of 1ES 1215+303 and its highest energy photons. Subsequently, we perform a search for periodicities and characterize the selected γ-ray flares.

5.3.1.   The γ-ray dataset

We show the nightly VERITAS light curve integrated above 200 GeV in the top panel of Figure 5.2. The 3-day LAT standard light curve is shown in the middle panel of the same figure (see Section 4.7). Flux values and their $1\,\sigma$ statistical uncertainties are shown only if the data result in a significance value of at least $2\,\sigma$, otherwise 95% flux upper limits are shown.

1ES 1215+303 flared a number of times at γ-ray energies during the past decade. The γ-ray flares are labeled from 1 to 8, in chronological order, independently of whether they were detected only at HE, only at VHE or in both wavebands. Six VERITAS flares were observed, Flares 2 to 7 (see Table 5.2). Two of these were found to have a GeV counterpart, Flares 3 and 7; the others were not detected, possibly due to insufficient exposure time. The details of the flaring episodes and their observations are discussed in Sections 5.3.2 and 5.10. Flares 2 and 3 had a dedicated study reported in Abeysekara et al. (2017). Flare 1 was analyzed along with other 105 sources in Abdo et al. (2010b) and it has not been subjected to a detailed, individual analysis here. We focus on the

---

[6]The red circle between components 1 and 2, corresponds to an additional non-robustly cross-identified feature that is thus not considered in this document.

unpublished observations and, in particular, on Flare 7[7] that occurred on 2017 April 01 since this is the only unpublished flare with simultaneous LAT-VERITAS data.

5.3.2.   Increasing flux trend and the selection of flares

The top and middle panels of Figure 5.7 show a more detailed view of the VERITAS nightly and LAT 3-day light curves. In the following variability analyses, the low flux values were used instead of upper limits. The LAT light curve shows peaks of apparent flaring epochs on top of a noisy but still possibly not completely inactive quieter "base line". In order to characterize this base line, I first fit the light curve to a constant flat line ($\chi^2_{\rm red} = \chi^2/{\rm d.o.f.} = 2.26$), to a linear function ($\chi^2_{\rm red} = 1.90$) and to a broken linear function (BLF, $\chi^2_{\rm red} = 1.88$). A likelihood ratio test shows that the increasing line is preferred at the $19.4\,\sigma$ level to the constant fit, and that the broken linear function (black dashed line in Figure 5.7) is preferred at the $5.5\,\sigma$ level over the linear function. This broken linear fit is composed by first a constant part given by $(4.0 \pm 0.2) \times 10^{-8}$ cm^{-2} s^{-1}, consistent with the Bayesian blocks results (described in Section 4.7.2 below in this section); and a linear function of slope $(2.8 \pm 0.3) \times 10^{-11}$cm^{-2} s^{-1} MJD^{-1} which starts at the breaking point MJD 55834 ± 134, i.e. around 2011 Sep. (see Table 5.5).

Table 5.5: Results of the fit of the *Fermi*-LAT 3-day light curve and Tuorla averaged data.

Model	a $(\mathrm{cm^{-2}\,s^{-1}\,MJD^{-1}})$	b $(\mathrm{cm^{-2}\,s^{-1}})$	$t_{\rm break}$ (MJD)	$\chi^2/{\rm d.o.f.}$
		Fermi-LAT		
Const.	NA	$(5.57\pm0.14)\,10^{-8}$	NA	2361/1043
Linear	$(1.92\pm0.14)\,10^{-11}$	$-(1.02 \pm 0.08)\,10^{-6}$	NA	1984.7/1042
BLF	$(2.75 \pm0.27)\,10^{-11}$	$(4.00\pm0.20)\,10^{-8}$	55834 ± 134	1954.1/1041
		Tuorla R-band		
Const.	NA	$(2.92\pm0.25)\,10^{-3}$	NA	102.8/13
Linear	$(5.46\pm1.10)\,10^{-7}$	$-(2.67 \pm 0.60)\,10^{-2}$	NA	35.4/12
BLF	$(1.73\pm0.44)\,10^{-6}$	$(2.58\pm0.15)\,10^{-3}$	55515 ± 297	24.0/11

For a linear function $ax + b$, a is the slope and b is the independent term. For a constant function a is not applicable (NA). For the BLF, a is the slope of the linearly increasing section, and b is the value in the constant section.

A similar preliminary analysis was performed for the Tuorla R-band data, where it was found that a linear increasing function is preferred at the $206\,\sigma$ level over a constant function, and the broken line ($\chi^2_{\rm red} = 121.1$) is preferred at the $126.0\,\sigma$ level over the linear function. The break point found for the Tuorla data is MJD 56124 ± 68, i.e. about a hundred days after the break time obtained for the LAT data. The large reduced χ^2s

---

[7] http://www.astronomerstelegram.org/?read=10270

obtained are an indication that none of the functions used are a satisfactory representation of the data, although the BLF provides a relatively better representation. I therefore performed an analysis on the Tuorla R-band data averaged per season (black squares in the bottom panel of Figure 5.7) to eliminate the daily variability. I found that a linear function is preferred at the $8.2\,\sigma$ level over a constant function, and that the broken linear function (in the same panel of Figure 5.7; with $\chi^2_{\text{red}} = 2.2$) is preferred at the $3.4\,\sigma$ level over the linear function. The break point for the Tuorla data was found to be MJD 55515±297 (around 2010 Nov.), i.e., consistent with the LAT break time. See Table 5.5 for details on the results for the Tuorla data averaged per season. Lindfors et al. (2016) searched for long-term variability trends in the Tuorla and 15 GHz radio light curves from 2008 to 2013. They did not find a significant trend in radio or optical data during this time period, which is not incompatible with the results found in this work where the long term flux increase starts around the end of 2010 and become especially visible after 2013. Lindfors et al. (2016) also reported having found both decreasing and increasing trends for a number of other sources in the radio and optical bands.

In order to identify the flaring epochs in the LAT data, two different methods were implemented. In Method I, the data were first recursively fit to the broken linear function. Only those points that deviated by no more than $3\,\sigma$ from the broken linear function were included. This resulted in an improved fit ($\chi^2_{\text{red}} = 1.3$) that was still consistent with that found previously. The points (outliers) that deviated by $\geq 3\sigma$ from this broken line are shown in black in the middle panel of Figure 5.7 and on the top panel of Figure 5.8. Out of these, only those with at least two neighboring outliers, also above 3σ (Chang et al. 2015), were used to define flares. This resulted in the identification of four LAT flares. To summarize, this method consists of the following steps:

- choose a base-line function that best represents the light-curve data,

- select a level N_{th} (in σs) of deviation of the outliers from the baseline (F_{BL}):

$$\frac{|F_i - F_{\text{BL}}|}{\sigma_{F_i}} \geq N_{\text{th}}, \tag{5.1}$$

  where F_i are the values of each flux point,

- recursively fit the data that deviated no more than $N_{\text{th}}\,\sigma$ from the base-line until the base-line and the outliers obtained are stable.

- choose the minimum number of consecutive points, N_p, which must satisfy Equation (5.1) in order to be identified as a flare[8].

The four *Fermi* flares identified using Method I are referred to as Flares 1, 3, 7 and 8. Their durations are shown by arrows in the insets of the middle panel of Figure 5.7,

---

[8]This method applied to a brighter source, 3C 279, is shown in Figure A.5; where a linear function as a base-line and the values of $N_{\text{th}} = 5\,\sigma$ and $N_p = 3$ were used.
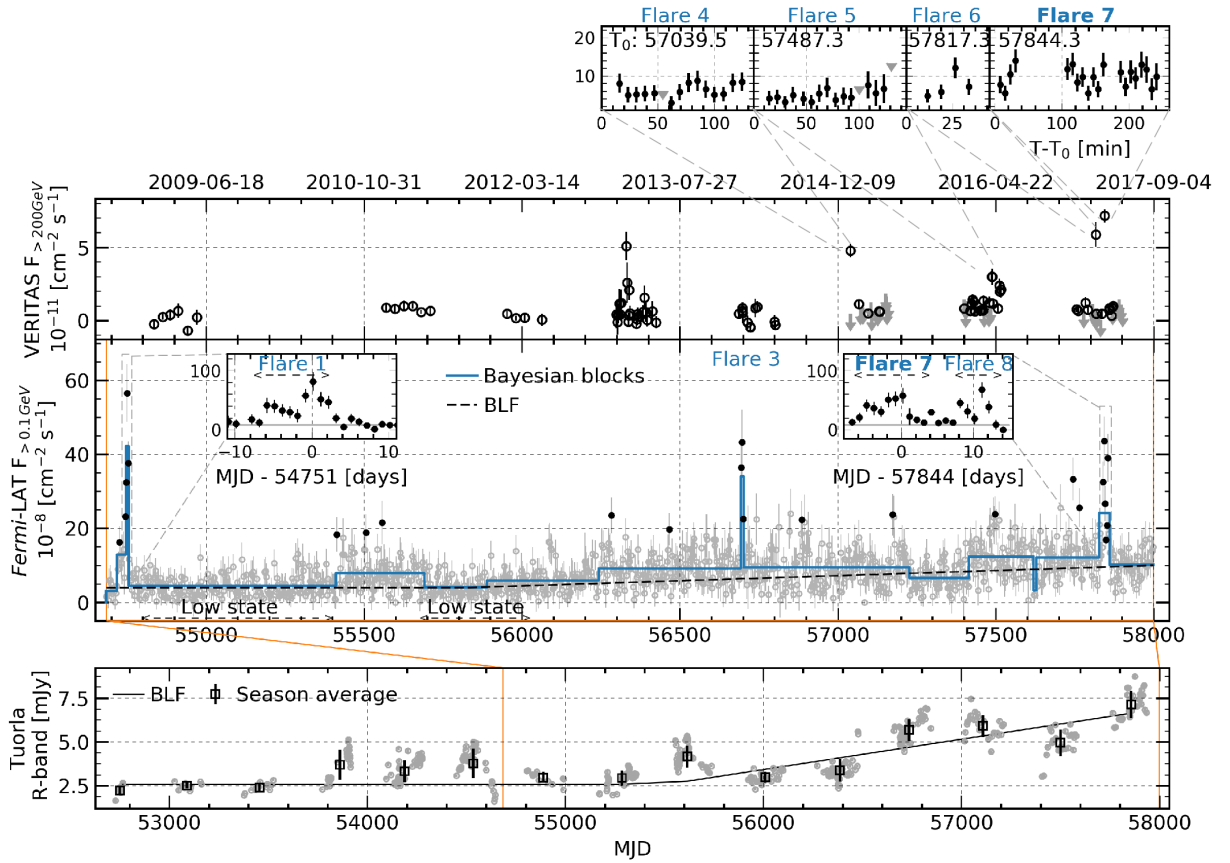
Fig. 5.7.— **The Optical and GeV-TeV γ-ray dataset.** *Top:* **The VERITAS light curve (> 200 GeV), with detailed zoom down to the minute scale in the VHE flares, from year 2015 onwards. VERITAS Flare 3 has been excluded from this panel.** *Middle: Fermi-***LAT light curve (> 100 MeV) with daily zoom for the four flares defined for this source in this energy range. 3σ deviated data points from the broken linear function (BLF, dashed line) are shown in black. From these, only the points with two neighbors were used to select the four LAT flares. Bayesian blocks are shown in light blue. These guided the definition of the low state.** *Bottom:* **Optical R-band light curve in gray, exhibiting seasonal average square points in black. The last nine years are contemporaneous to the time range for the LAT and VERITAS in the upper panels.**

where 1-day light curves show in more detail their structure. The durations are also given in Table 5.3. Flare 1 had its peak on 2008 Oct. 12 (MJD 54751) before the VERITAS observatory began routine observations of 1ES 1215+303; Flare 3 on 2014 Feb. 8 (MJD 56696; Abeysekara et al. 2017), Flare 7 on 2017 Apr. 01 (MJD 57844), and Flare 8 on 2017 Apr. 12 (MJD 57856). The peak day of the Flare 7 is coincident between *Fermi* and VERITAS observations and is annotated in bold font in the insets of Figure 5.7. Details on the search for simultaneous observations between the LAT and VERITAS are provided in Section 5.10.

In Method II, Bayesian blocks (Scargle et al. 2013) were also used to explore the LAT data. Following the discussion in Section 4.7.2, a false positive rate of $p_0 = 2.844\,\sigma$ and a cut in the LAT data that rejected the points with TS $< 5 \times 10^{-4}$ were chosen so that the
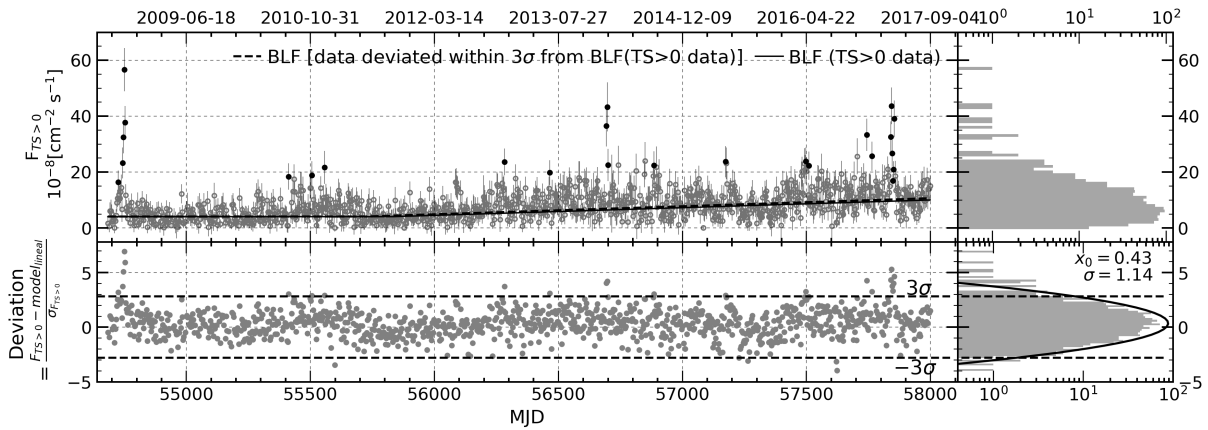
Fig. 5.8.— **LAT light curve base-line analysis and flare selection, Method I.** *Top left:* **Base-lines of all the data (solid, TS > 0, $\chi^2_{\rm red} = 1.9$) and of the data that deviated by no more than $3\,\sigma$ that was recursively fitted (dashed, $\chi^2_{\rm red} = 1.3$). The outliers that deviated by $\geq 3\,\sigma$ are shown as black points.** *Bottom left:* **Deviation of the data from the base-line (broken linear function, BLF).** *Right:* **Flux (top) and deviation (bottom) distributions of the LAT 3-day light curve data.**

flaring periods that were selected using method I would also be detected by this method; that is, *Fermi* Flares 1, 3, 7 and 8. The Bayesian blocks are in general agreement with the increasing trend, i.e., the flux of the blocks shows a mostly increasing trend starting approximately at the break time. This method also guided the definition of the "low state" (from 2008 Nov. 17 to 2010 Aug. 12 and from 2011 Apr. 15 to 2012 Apr. 10, see Figure 5.7) and the 2017 post-flare state (2017 Apr. 15–23) for the SED modeling in Section 5.11. No flaring epochs were reported at any wavelength during the low or post-flare states. As is discussed in Section 5.11.4, no other instrument other than the LAT and VERITAS performed observations of 1ES 1215+303 during the outburst of 2017 Apr. 01 (Flare 7). There was, however, simultaneous coverage of the emission of this source by the LAT, VERITAS, *Swift* and Tuorla during the post-flare state triggered by an enhanced activity alert that the *Fermi*-LAT Collaboration sent to the MWL community[9]. It should be noted that due to the long-term increasing flux trend found, the post-flare fluxes are not at the level of those of the low state, but belong to an elevated state of the source. The details can be found in Table 5.3.

The VERITAS light curve is characterized by a baseline at $\approx 2\%$ of the Crab Nebula flux. No preference for a long-term linear trend was found. The flares at this wavelength were selected when the photon flux rose above 10% of the Crab Nebula flux[10]. Between 2013 and 2017, these outbursts were observed at least once per year from 1ES 1215+303. No strong intra-night variability on sub-hour timescales was observed in the light curves with 8-min binning intervals, as can be seen in the insets on the top panel of Figure 5.7.

---

[9]http://www.astronomerstelegram.org/?read=10270

[10]This is the standard protocol used to define flares for VERITAS data.

5.3.3. Searches for harder-when-brighter behavior in the LAT data

In order to search for evidence of spectral evolution, various supplementary analyses were performed. The significance of the source is sufficiently high to allow for binning on 30-day timescales while still being able to extract information on the time evolution of the photon indices, (see the top and middle panels in Figure 5.9). I also analyzed the data in 60-day bins to calculate the hardness ratio (HR) between two energy ranges, 0.1–1 GeV and 1–500 GeV. No evidence for significant changes in the HR of the source was found (see the bottom panel of Figure 5.9). Lastly, I analyzed each year of the LAT data both including and excluding the flaring epochs. This resulted in different datasets only for those three years which included flaring
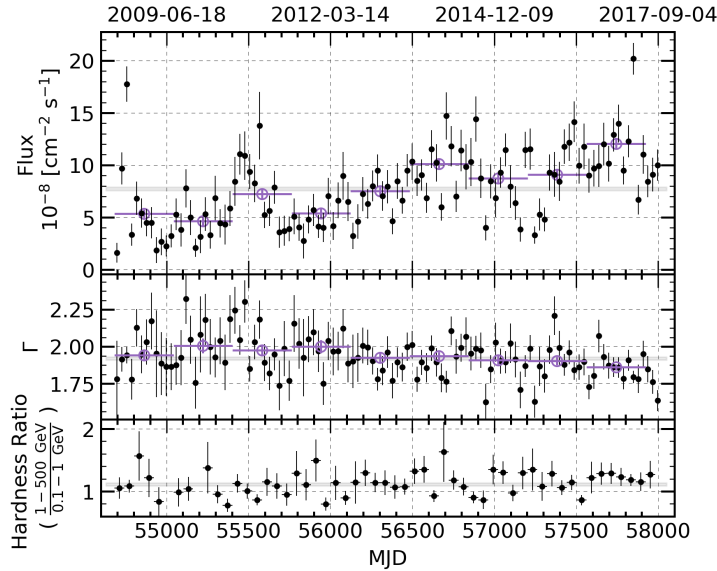
Fig. 5.9.— *Top:* **30-day bins light curve (black points) and the 360-day binned light curve (violet points).** *Middle:* **Monthly spectral shape for the 30-day binned (black) and 360-day binned (violet) data. A 5 σ long-term hardening is observed in the 30-day binned data.** *Bottom:* **Hardness ratio for 1ES 1215+303 in 60-day bins.**

episodes (2008 Oct., 2014 Feb. and 2017 Apr.). These results are also shown in the top and middle panels of Figure 5.9 and in Table 5.3. The gray shading represents the flux and photon index values obtained in the global analysis (2008 Aug.–2017 Sep.).

Table 5.6: Results of the fit of the yearly *Fermi*-LAT data.

Model	Total			Non-flare		
function	a	b	χ^2/d.o.f.	a	b	χ^2/d.o.f.
Constant	NA	1.92±0.02	17.8/7	NA	1.93±0.01	14.2/7
Linear	$-(1.61 \pm 0.35) \times 10^6$	2.06±0.03	4.5/6	$-(1.41 \pm 0.48) \times 10^6$	2.05±0.04	6.3/6
Preference			3.6 σ			2.8 σ

For a linear function $ax+b$, a is the slope and b is the independent term. For a constant function a is not applicable (NA).

I find strong evidence for a long-term hardening of this source, reaching the 5.0 σ level with the 30-day binned data, (4.7 σ including the trials factor for having also looked at the 30, 60 and 360-day binned data); 3.6 σ level for the yearly data bins and 3.2 σ outside flares with this same binning. A long-term brightening is observed with this binning as well, reaching the 12.8 σ level for the yearly data bins, and 13.4 σ outside flares.
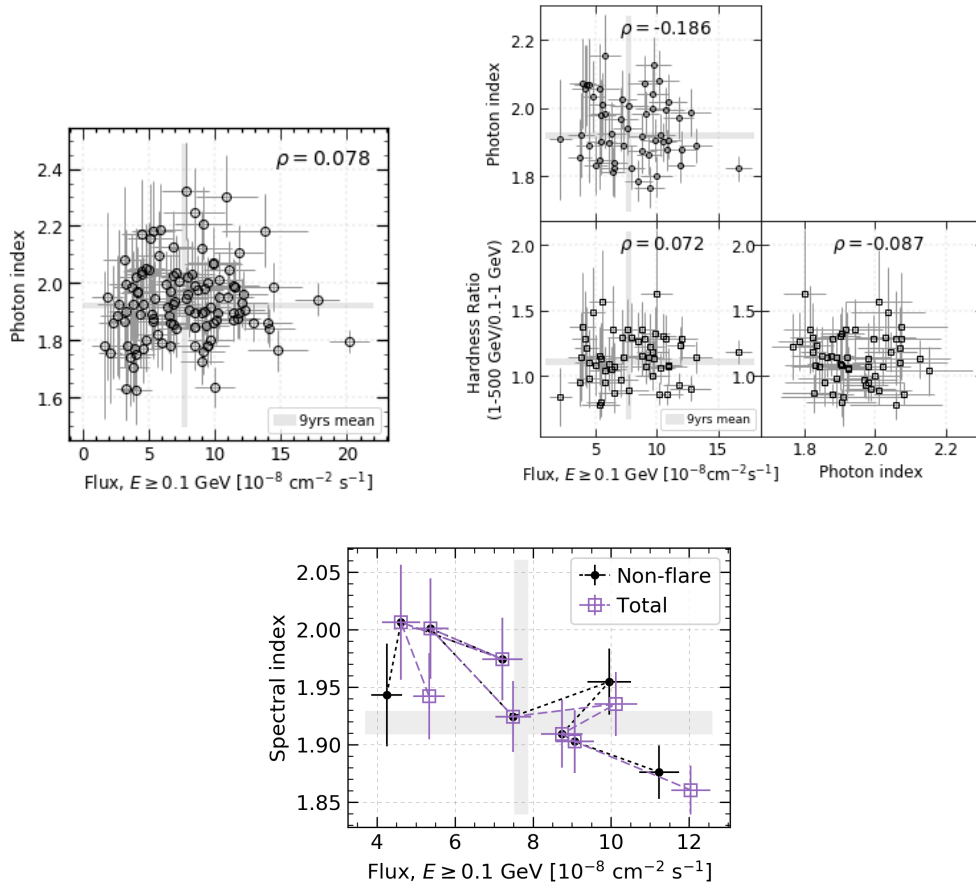
Fig. 5.10.— *Top left:* **30-day binned LAT data. No flux-photon index correlation is observed.** *Top right:* **60-day binned LAT data. No photon index‑flux or HR‑flux or HR‑photon index correlation was observed for the 30-day or 60-day binned data, respectively.** *Bottom:* **Power-law photon index against flux for the 360-day binned *Fermi*-LAT data. The violet squared points show the average value per bin, while black points show the non-flaring state values (which are different from the total only for the three bins that include flaring epochs). The 360-day light curve and photon indices against time are shown in the top and middle right panels of Figure 5.9 in violet as well. The shaded areas correspond to the results for the total dataset.**

No photon index‑flux or HR‑flux correlation was observed for the 30-day or 60-day binned data, respectively. For the 360-day binned data, however, a Pearson correlation parameter of -0.86 between the photon index and the flux is obtained for the total data set (violet points in the bottom panel of Figure 5.10), and a value of -0.74 for the non-flare data (black points in the same figure). A likelihood ratio test shows a $3.4\,\sigma$ preference, including trials factor (by having looked at the 30, 60 and 360-day binned data), for a linearly decreasing dependence over a constant between the photon index and the flux, which indicates a possible overall "harder-when-brighter" trend in this source. The yearly data outside flares also showed a preference at the $2.8\,\sigma$ level for a linearly decreasing dependence over a constant. These data, as well as the linear fits, are shown in Figure 5.10 and the details of the fit parameters can be found in Table 5.6. This "harder-

when-brighter" trend has been observed in the *Fermi*-LAT data for flat-spectrum radio
quasars and BL Lacs (Abdo et al. 2010c; Katarzyński et al. 2001a).

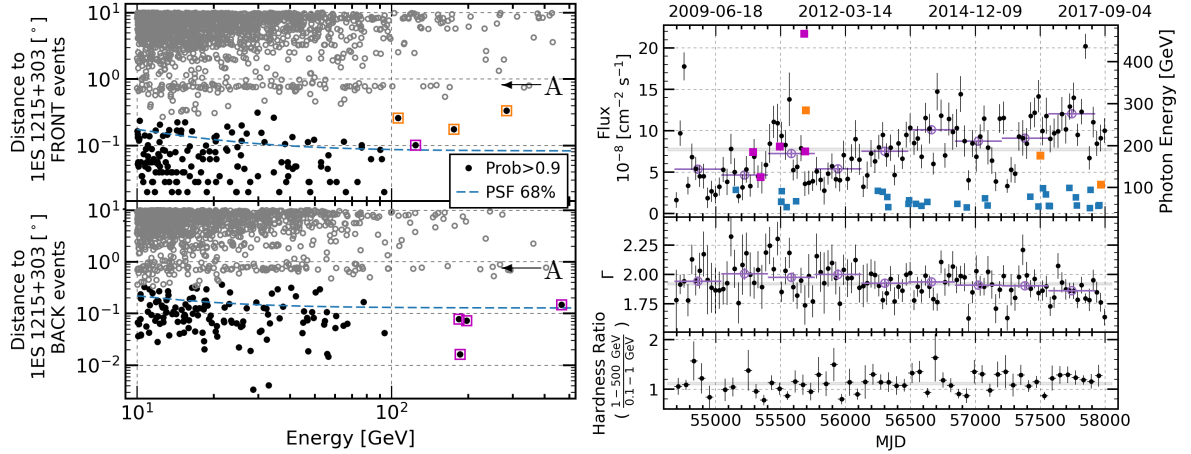## 5.3.4.   High energy γ-ray photons detected by the LAT

Fig. 5.11.— *Left:* **LAT photons above 10 GeV. The vertical axis represents the distance
(in degrees) from the photon to 1ES 1215+303. Photons above 100 GeV, close to, or below
the 68% containment radii curves are highlighted with magenta squares. VHE photons
clearly above this curve, but with probability > 0.9 of having originated in 1ES 1215+303,
are highlighted with orange squares. *Right:* The same plot as Figure 5.9 with the addition
of the 90% probability photons above 50 GeV in light blue. The magenta and orange points
(in both the left and right panels) represent the photons above 100 GeV that are more likely
to have come from 1ES 1215+303 (described in Table 5.7).**

I performed an analysis of the highest energy photons detected from the direction of
1ES 1215+303; a detailed description is provided in the following. When a photon converts
in the LAT, it does so either in the "FRONT" or "BACK" section of the detector and
is thus labeled as a FRONT or a BACK event. The layers of tungsten are finer and
are interspersed with more silicon tracking layers in the FRONT section of the detector
allowing for a more precise tracking of the charged particles' positions and, therefore, a
lower PSF. In the BACK section, the tungsten layers are thicker so as to encourage pair
conversion of the γ-ray. The tracking capabilities are therefore degraded slightly with
respect to those for front-converting events leading to a larger PSF.

The left-hand side of Figure 5.11 shows the FRONT and BACK events within the
ROI and above 10 GeV. The vertical axis represents the distance, in degrees, between
the photons and 1ES 1215+303. The events with at least 90% probability of coming from
1ES 1215+303 are shown in black. We observe that most of these highest probability
photons between 50 GeV and 100 GeV are close to or below the 68% containment radii
or PSF; they have been plotted in light blue on top of the 30-day binned light curve on
the right-hand side of Figure 5.11 for visualization. According to *gtsrcprob*, there are

Table 5.7: LAT VHE photons from 1ES 1215+303 with probability> 0.9.

E^a (GeV)	1ES 1215+303 prob.	dist.^{b} (°)	1ES 1218+304 prob.	dist.^{c} (°)	gll^d prob.	iso^e prob.	MJD	Type
466.498	0.9838	0.15	0.0123	0.68	0.0003	0.0036	55682.3	Back
197.614	0.9990	0.07	0.0006	0.76	0	0.0003	55494.8	Back
185.928	0.9998	0.02	0.0002	0.75	0	0	55691.6	Back
184.408	0.9987	0.07	0.0008	0.75	0.0001	0.0004	55289.9	Back
124.287	0.9977	0.10	0.0009	0.68	0.0002	0.0012	55347.2	Front
283.275	0.9636	0.33	0.0059	0.95	0.0028	0.0277	55696.7	Front
175.895	0.9957	0.17	0.0010	0.87	0.0004	0.0029	57502.9	Front
106.104	0.9443	0.26	0.0315	0.55	0.0029	0.0213	57968.5	Front

(a) Photons above 100 GeV. The top five photons are the closest to or contained within the PSF 68% (magenta points in Figure 5.11). (b) Event distance to 1ES 1215+303. (c) Event distance to 1ES 1218+304. (d) Galactic diffuse background. (e) Isotropic diffuse background.

eight high probability photons above 100 GeV, which is in very good agreement with the *gtlike* predictions in this energy range (see Figure 5.20 and Table 4.4). These LAT VHE photons are shown on the right-hand side of Figure 5.11 as well, and in Figure 5.12. A detailed description of the eight photons above 100 GeV is provided in Table 5.7, where the probabilities that those photons came from each source are listed.
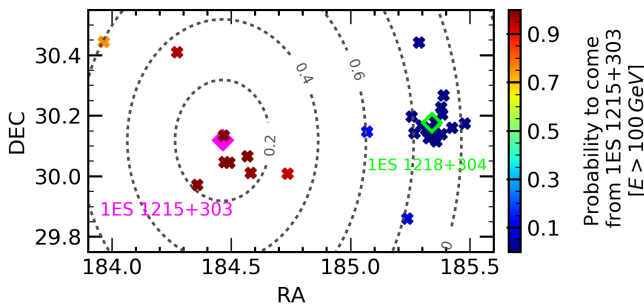

Fig.   5.12.— LAT photons with energy > 100 GeV in the region around 1ES 1215+303. The eight photons in Table 5.7 that are within 0.33° of 1ES 1215+303 and shown in the reddish colour. Gray concentric contours are shown to visualize the distance to 1ES 1215+303.

Of these eight events, however, only five (in magenta) are close to or below the PSF 68% curve, which strengthens the *gtsrcprob* results; the other three (in orange) are a bit further above, closer to the neighbor 1ES 1218+304, which is 0.76° from 1ES 1215+303. Notice in Figure 5.11 left the linear patterns in gray; these correspond to the neighboring sources located at those distances, in particular, 1ES 1218+304, labeled as "A" in that figure.

The highest energy photon obtained from 1ES 1215+303 in these nine years has an energy of 466 GeV and was detected on 2011 May 1, during a relatively high state of the source that lasted for approximately 13 months. During this high state, five other photons above 100 GeV were also detected, along with four photons with energies between 50 GeV and 100 GeV. Notice that the defined low state and, in particular, the second half of 2015 are almost devoid of photons above 50 GeV. These photons above 50 GeV are in accordance with high overall LAT fluxes, however not strictly associated with flaring episodes; possibly

due to the short duration of these outbursts which limits the statistics, especially at the highest energies.

5.4.   Flux-flux cross-comparisons and cross-correlations

Attempts to search for flux-flux MWL correlations using daily time bins were inconclusive due to the large statistical uncertainties. Furthermore, the cross-correlation function analyses performed showed no evidence for significant inter-band correlation for the data shown in Figure 5.2 (see Section 5.6 for details). To circumvent the large statistical fluctuations associated with the short-term low-state flux measurements in the flux-flux correlation, and to allow us to further investigate the apparent long-term increasing trend in the optical and GeV fluxes, I performed a likelihood analysis of the LAT data using the R-band seasonal intervals to define the time bin edges. This corresponds to the time periods during which the source was visible to optical telescopes. I made use of the averaged optical data per season, and of the corresponding non-flaring VERITAS data in Table 5.2. These quiescent VERITAS data comprise six data points, whereas there are LAT data dating back to 2008, thus providing 9 data points. The seasonal flux-flux correlations which result from these analyses are shown in Figure 5.13, in logarithmic scale.

The least-squares fits and Pearson correlation coefficient for the logarithms of the seasonal fluxes of these energy bands can be found in Table 5.8. A strong long-term correlation is revealed between the optical and HE γ-ray bands. I find the following correlation between the *Fermi*-LAT (F_{LAT}) and optical (F_{opt}) flux data:

$$\log_{10} F_{\mathrm{LAT}} = a \ \log_{10} F_{\mathrm{opt}} - b \tag{5.2}$$

(dashed line in Figure 5.13), yielding a slope $a = 0.86 \pm 0.21$ and $b = 5.05 \pm 0.49$ with a $\chi^2/\mathrm{d.o.f.} = 41/6$, and Pearson correlation coefficient of 0.86. The uncertainties on a and b are obtained after having re-scaled the measurement uncertainties to $\chi^2/\mathrm{d.o.f.} = 1$ (Tanabashi et al. 2018b).

Table 5.8: Seasonal flux logarithm correlations.

Energy bands	Pearson corr. coefficient	Linear fit[†] slope	$\chi^2/\mathrm{d.o.f.}$
LAT - Optical	0.86	0.86±0.21	41/6
VERITAS - LAT	0.59	0.63±0.62	43/3
VERITAS - Optical	0.44	0.06±0.80	54/3

[†] Uncertainties scaled to $\chi^2/\mathrm{d.o.f.}$
The linear fit slope corresponds to a in a fit to: $\log(f_1) = a \log(f_2) + b$, where f_1 and f_2 are the seasonal fluxes in two different energy bands.
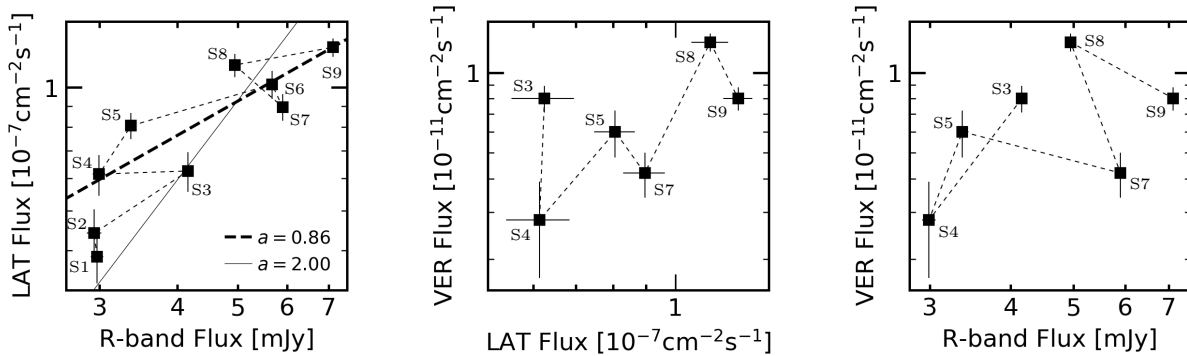
Fig. 5.13.— Seasonal flux-flux diagrams for **VERITAS**, the *Fermi*-**LAT** and **TUORLA** (R-band) energy ranges (in logarithmic scale). The data is labeled from Season 1 (S1), in 2009, to Season 9 (S9), in 2017. The dotted lines join the data chronologically, going approximately from left to right due to the long-term brightening observed in the GeV and optical light curves. The dashed line represents the fit to the expression $\log_{10}(F_{\mathrm{LAT}}) = a \, \log_{10}(F_{\mathrm{opt}}) - b$. The solid line is the fit to the same expression with $a = 2$.

To our knowledge, this is the first time that such a strong global GeV-optical correlation (over nine years) and brightening (over six years) has been observed over such an extended period of time[11]. The optical emission most likely comes from the synchrotron process and if the γ-ray photons originate from inverse Compton scattering (ICS), this strong, almost linear ($a = 0.86$) correlation is consistent with a long-term variability induced by changes of the Doppler factor or magnetic field of the emitting zone, if we consider a synchrotron-self-Compton (SSC) scenario. It is also consistent with the γ-ray emission originating from inverse-Compton scattering of an external photon field (e.g. Bonnoli et al. 2011).

In a SSC scenario, if a change in the number of emitting particles is the cause of the long-term variability, this would induce a quadratic flux-flux correlation ($a = 2$ line in Figure 5.13) between the optical and the γ-ray data. However, a slope of $a = 2$ is found to be disfavored at the $5.4\,\sigma$ level. In order to account for the daily variability of the source in the fit, if instead of $\chi^2/\mathrm{d.o.f.}$ re-scaling, we add quadratically a source variability (of $\approx 30\%$), obtained from the excess variance analysis per season as in Section 5.5, we obtain $a = 0.83 \pm 0.33$, which would be preferred over $a = 2$ at the $3.6\,\sigma$ level.

No evidence for a clear correlation was found between the HE and VHE bands. A weaker correlation is found between the VHE and the optical bands. This is likely due to the relatively sparse sampling and to the seasonal visibility gaps in the VHE γ-ray observations, which do not allow us to draw conclusions about the relationship between

---

[11]Abeysekara et al. (2015) found significant long-term GeV-optical and GeV-radio correlations for the FSRQ PKS 1441+25 over a period of seven years since 2008; which also showed significant brightening at the three wavelengths during the last year of this dataset.

the production mechanisms of these two energy bands. Similarly, a less strong correlation is found between the VHE and the optical bands. No long-term correlation was observed between the OVRO data (15 GHz) and the optical data or the γ-ray data (i.e. the Pearson correlation coefficient had an absolute value below 0.5).

5.5.   Flux distributions and variability

In this section I analyze the flux distribution of the best-sampled light curves obtained, i.e., the OVRO radio, the R-band Tuorla, the LAT 3-day binned and the VERITAS nightly binned. These light curves are probed in order to search for log-normality behavior such as that studied in other blazars, such as BL Lacertae (Giebels & Degrange 2009), 1ES 1011+496 (Sinha et al. 2017), (Ackermann et al. 2015c) and bright *Fermi* blazars (Shah et al. 2018). Log-normal distributions have the property that their mean values and fluctuations behave linearly on average, and are of interest because they have multiplicative properties rather than additive ones (Aitchison & Brown 1973). In the following, I present the results of these tests, using as the fluctuations the rms corrected for the Poisson noise defined by Vaughan et al. (2003), the excess rms or excess variance σ_{XS}, described below.
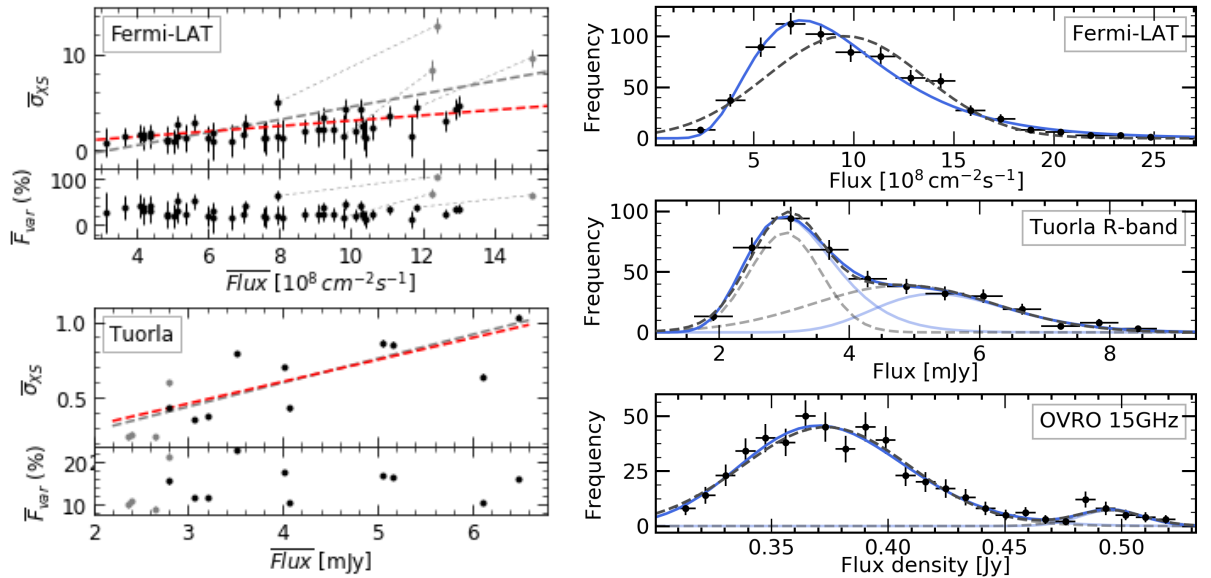

Fig. 5.14.— *Left*: **LAT, Tuorla and OVRO flux distributions. The (bi)log-normal best fit is shown in dashed lines and the (bi)normal in dotted lines. The components of the bi-functions are shown in gray.** *Right*: **The excess variance ($\overline{\sigma}_{XS}$) and variability amplitude ($\overline{F}_{\mathrm{var}}$) for the *Fermi*-LAT and Tuorla data.**

To investigate the relationship between the fluctuations and the mean fluxes, I binned the light curves into segments of equal duration ensuring at the same time that I had at least 20 measurements of flux for each bin (flux data points shown in Figure 5.2). The

time binning of these flux measurements varied depending upon the waveband. They are shown on the left-hand side of Figure 5.14. It is frequently postulated (Tavecchio et al. 2011; Chiaberge & Ghisellini 1999; Marscher & Gear 1985; Giannios et al. 2010) that the flaring states correspond to different physical processes than the "quiescent" (or baseline) state, whose variability we are interested in characterizing, so I performed the binning both including and excluding data from the flaring periods. Points containing data outside flares are shown in black and their best fit as a dashed red line in the same panels. I calculated the following parameters for each of the bins: the arithmetic mean, the excess variance $\sigma_{XS}^2 = \frac{1}{N}\Sigma_N^{i=1}(x - \overline{x})^2 - \overline{\sigma_i^2}$ with its uncertainty (Vaughan et al. (2003) Section B) and the variability amplitude $\overline{F}_{\mathrm{var}}$ (Vaughan et al. 2003). For the LAT data, a fit outside flares resulted in $\sigma_{XS} \propto (0.25 \pm 0.05)\overline{\mathrm{Flux}}$ ($\chi_{\mathrm{red}}^2 = 0.66$) and a Pearson correlation coefficient, ρ, of 0.54. The data containing the flaring epochs in 2008, 2014 and 2017 are shown in gray in the top-left panels of Figure 5.14, and have $\sigma_{XS} \propto (0.61 \pm 0.01)\overline{\mathrm{Flux}}$, $\chi_{\mathrm{red}}^2 = 3.3$, $\rho = 0.64$.

The Tuorla data are more sparsely sampled (424 data points in total) than the LAT data, making it difficult to have at least 20 points per bin for every segment. During the first, second, third and sixth years of observation, there are between 11 and 18 optical data points per segment for the Tuorla data (gray points in the bottom-left panels of Figure 5.14). These belong to optical low states of the source. At all other times, there were 20 data points per segment for the Tuorla data. A linear fit to these data outside of the low states yields $\sigma_{XS} \propto (0.15 \pm 0.05)\overline{\mathrm{Flux}}$ ($\chi_{\mathrm{red}}^2 = 172.5$, $\rho = 0.74$), while a linear fit to the total data set results in $\sigma_{XS} \propto (0.16 \pm 0.04)\overline{\mathrm{Flux}}$ ($\chi_{\mathrm{red}}^2 = 134.4$, $\rho = 0.80$). A similar analysis on the OVRO data did not show significant correlation ($\rho = -0.20$). Lastly, the method would not apply to the VERITAS data since we have only 76 flux points over nine years and rebining them to 20 points per bin would produce only a few new points not which do not represent the variability of the data, nor do they allow the fitting.

Table 5.9: Widths (σ) and goodness of fits (χ_{red}^2) for normal, bi-normal, log-normal and bi-log-normal fits to the LAT, Tuorla and OVRO flux data.

Dataset	normal		bi-normal			log-normal		bi-log-normal		
	σ	χ_{red}^2	σ_1	σ_2	χ_{red}^2	σ	χ_{red}^2	σ_1	σ_2	χ_{red}^2
VERITAS	0.38±0.05	0.76	-	-	-	0.63±0.06	0.97	-	-	-
LAT	3.9±0.3	4.12	-	-	-	0.43±0.02	1.42	-	-	-
Tuorla	-	-	0.5±0.1	1.4±0.3	1.48	-	-	0.22±0.02	0.19±0.04	1.08
OVRO	-	-	$(3.6\pm0.2)\times10^{-2}$	$(1.5\pm0.4)\times10^{-2}$	0.67	-	-	$(9.5\pm0.4)\times10^{-2}$	$(2.7\pm0.6)\times10^{-2}$	0.82

The log-normal function is given by $f(x) = \frac{N}{x\sigma\sqrt{2\pi}} \exp\left[-\frac{(\log x - \mu)^2}{2\sigma^2}\right]$. A dash in a given column indicates that the particular function was not fit to that dataset.

The flux distributions of the *Fermi*-LAT, Tuorla and OVRO 15 GHz data, and their best fits to the (bi)log-normal (solid light blue) and (bi)normal (gray dashed) functions are shown on the right-hand side of Figure 5.14. Both bi-functions consist of two components each, which are shown in lighter colors in the same figure. In the case of the LAT data, flaring states as they were defined in the previous section, were excluded so as not to favor the logarithmic fit, due to a possible bias produced by the elongated tail. A Shapiro-Wilk test on the LAT data rejects the normal distribution with a p-value of 4.2×10^{-16} and

a test statistic of $w = 0.87$ (Shapiro & Wilk 1965). The χ^2 fits improve after Poisson noise reduction during faint epochs (that is, excluding light curve data with low statistics), reaching the best fit for data with significance above $3\,\sigma$ (in fact, approximately 60% of the data below $3\,\sigma$ is located within the low state defined in Section 5.3.2). The distribution of these data is shown in the top right-hand panel of Figure 5.14. The results of fits to normal ($\chi^2/\text{d.o.f.}= 49.4/12$) and log-normal ($\chi^2/\text{d.o.f.}= 17.0/12$) functions shown in the same figure, are presented in Table 5.9, where it is observed that the log-normal function provides a much better fit. The right middle and bottom panels of the same figure show the Tuorla and OVRO flux distribution respectively, where contributions from the two different states are observed. There were no flaring state exclusions in their cases due to the relative sparsity in the sampling of these light curves. A double-peaked structure is observed in their flux distributions, possibly due to the fact that both quiescent and flare data are included, or due to the presence of a brighter second quiescent state. The bi-log-normal function does not provide a clear improvement to the fit with respect to the bi-normal function, nor vice-versa, in the case of the Tuorla and OVRO data (see Table 5.9). The two states of the Tuorla distributions are consistent with the states before and after the break time calculated in Section 5.3.2. The bi-normal fit results of the OVRO distributions are consistent with the flux density of the states interpreted as quiescent and flaring components by Liodakis et al. (2017), which includes data up to February 2016 for this source. Two log-normal states were also previously observed at the IR-optical wavelengths in FSRQ PKS 1510-089 (Kushwaha et al. 2016).

An analogous analysis performed on the VERITAS data outside flares did not show evidence of a preference for a Gaussian ($\chi^2_{\text{red}} =0.76$) model over a log-normal function ($\chi^2_{\text{red}} =0.97$). In fact, the Shapiro-Wilk test was found to reject the normal hypothesis for the VERITAS ($w = 0.21$, p-value$= 3.1 \times 10^{-18}$), Tuorla ($w = 0.93$, p-value$= 6.6 \times 10^{-13}$) and OVRO data ($w = 0.91$, p-value$= 3.9 \times 10^{-17}$). Similarly, I performed Shapiro-Wilk tests on the logarithm of the fluxes of the VERITAS ($w = 0.92$, p-value$= 0.2 \times 10^{-3}$), Tuorla ($w = 0.98$, p-value$= 2.1 \times 10^{-5}$) and OVRO ($w = 0.67$, p-value$= 6.3 \times 10^{-30}$) data. However, the normal hypothesis would be rejected in the case of the OVRO data, but not for the VERITAS or Tuorla data if a level of rejection of the normal hypothesis of 5.7×10^{-7} (i.e. $5\,\sigma$) was chosen.

The preference for log-normality in the flux distributions of the LAT and Tuorla data could be evidence that multiplicative processes (Aitchison & Brown 1973) are occurring at these wavelengths, which are, as is discussed in Section 5.4, strongly correlated over the long term, and which could also be connected due to SSC scattering. Several hypotheses have been discussed in the literature regarding the nature of the processes behind these observations. For instance, Uttley & McHardy (2001) attribute them to large, long-time-scale energy releases in the corona, possibly due to magnetic reconnection, initiating avalanche sub-division, which is later superimposed on short-time-scale emissions of energy proportional to the original division. They also mention the natural appearance of these linear relationships in the mechanism proposed by Lyubarskii (1997) due to radius-dependent mass-accretion-rate fluctuations producing variations on all time scales in the

disk and corona. However, an interpretation based on additive processes by Biteau & Giebels (2012), the mini-jets-in-a-jet model, predicts that skewed flux distributions (such as log-normal) could be obtained from the summation of contributions of a large number of mini-jets under specific conditions.

5.6.   ZDCF

To further quantify the inter-band flux-flux correlation from the source, we calculated the z-transformed discrete cross-correlation function (ZDCF; Alexander 2013) between the light curves from different energy bands, as shown in Figure 5.15. The ZDCF method offers a conservative, more efficient estimate of cross-band correlation in light curves, compared to regular discrete cross-correlation function.

The ZDCF method uses the Fisher's z-transform (Fisher 1921) and an equal population binning with a minimum of 11 data points per bin, and discards dependent pairs to avoid bias. Therefore, it has only the minimum number of points per bin as a free parameter, while the discrete cross-correlation function (DCF; Edelson & Krolik 1988) has two. Additionally, the ZDCF does not depend on the number of observations, which is an advantage in the analysis of unequally sampled light curves. The ZDCF method is shown to out-perform the DCF and the interpolated cross-correlation function methods under a wide range of conditions (Alexander 2013).
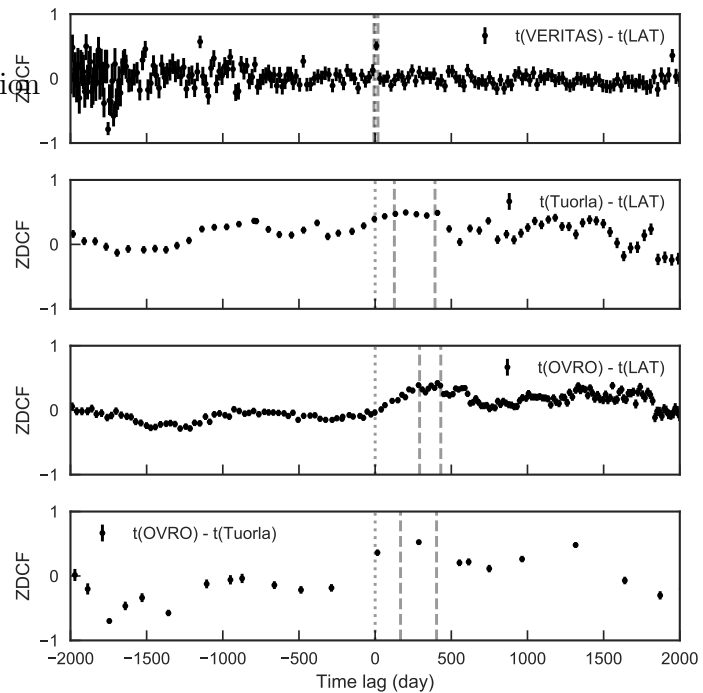

Fig. 5.15.— The ZDCFs between light curves measured at different wavelengths. The pair of wavelengths in each panel is shown in the legend. A positive time lag $(t(X) - t(Y) > 0)$ between band X and band Y means the emission in band X lags behind that in band Y. The vertical dotted lines show the time lag of zero, and the vertical dashed lines show the 1-σ confidence interval around the maximum-likelihood peak time lag.

The local peak time lag between the 3-day *Fermi*-LAT and VERITAS light curve data obtained with this method is $t(\text{VERITAS}) - t(\text{LAT}) = 8^{+11}_{-16}$ days compatible with a zero lag (a positive value indicates that the VERITAS flux is lagging behind the LAT flux). There are no significant peaks in the ZDCFs for the optical and γ or the radio and

γ or the optical and radio fluxes (this last one consistent with Lindfors et al. (2016)).

5.7. Power spectral density and periodicity analysis

The source exhibited a typical power-law power spectral density (PSD) distribution, commonly observed in AGN. The PSD calculated from LAT data and a simple power-law fit are shown in the left panel of Figure 5.16. A geometric binning by factors of 1.2 was used to obtain the red squares from the black points. For those bins with more than five PSD points, the standard deviation is used as the uncertainty of the re-binned PSD. For those bins with five or fewer PSD points, we use the mean PSD value itself as the conservative uncertainty, since the PSD points are expected to follow an exponential distribution (i.e. the mean and standard deviation are equal). Since power-law PSDs can be distorted by power leakage from longer and shorter timescales, we simulated 1000 light curves at a range of power-law indices between 0 and 1.2 in steps of 0.02, following the method described in Timmer & Koenig (1995).
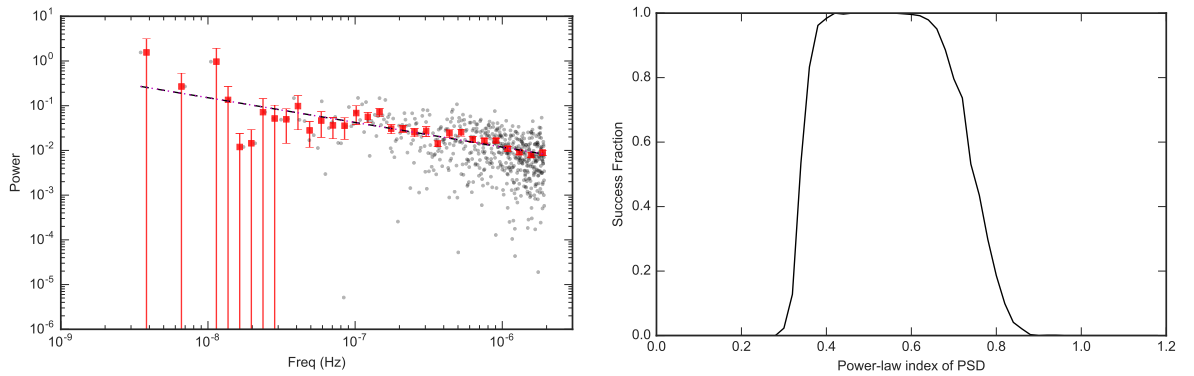

Fig. 5.16.— *Left:* **The power spectral density distribution of the 3-day-binned *Fermi*-LAT light curve. The black points are the periodogram from the data. The red squares are the re-binned periodogram. The dashed line shows a simple power-law fit to the re-binned periodogram.** *Right:* **The "Success Fraction" of simulated light curves at different power-law index of the power spectral density distribution.**

We then adopted a "success fraction" (SuF) to estimate whether the data are in agreement with a simulated light curve of a particular PSD power-law index, following the method described in Uttley et al. (2002). The SuF curve is shown in the right panel of Figure 5.16. The best-fit power-law index, 0.6 ± 0.1 is consistent with the relatively wide 90% SuF range of 0.38 to 0.68. The SuF curve drops to 0 at indices of 0.3 and 0.9. This suggests that the PSD distribution of 1ES 1215+303 is relatively flat compared to the typical values between 1 and 2 found in AGN (e.g. Uttley et al. 2002).

To test for any periodicity in the flux of 1ES 1215+303, we calculated the weighted wavelet Z-transform (WWZ; (Foster 1996)) and the Lomb-Scargle periodograms (LSP; Scargle 1982) of the *Fermi*-LAT and Tuorla light curves, as shown in Figure 5.17.
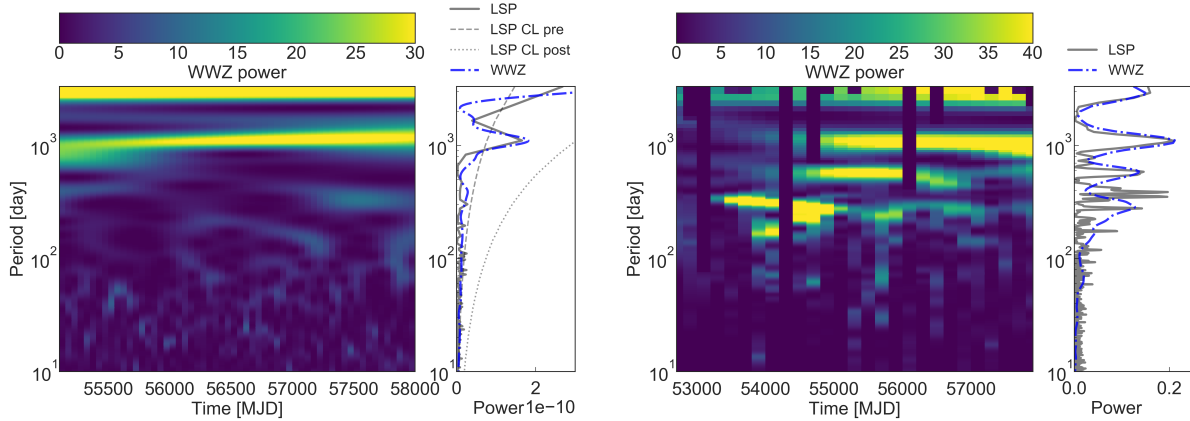

Fig. 5.17.— **The scalograms from WWZ transform of the *Fermi*-LAT (left) and Tuorla (right) light curves. The Lomb-Scargle periodogram (solid gray line) and the marginal WWZ periodogram (dash-dot blue line) are shown in the right panel of each plot. 90% confidence limits from a purely stochastic model with power-law PSD generated using the method of Emmanoulopoulos et al. (2013) are also shown, including (dotted gray line) and excluding (dashed gray line) the effect of the 553 trial frequencies.**

Both the WWZ and LSP methods are suitable for detecting quasi-periodic oscillations (QPOs) in unevenly sampled light curves. An excess power at a ≈ 3-year period appears persistently in the WWZ and LSP of both the *Fermi*-LAT and Tuorla data throughout the observational period. Slightly lower excess power at about a half and a quarter of the ≈ 3-year period, and the effect of sampling gaps in the optical data are apparent in the WWZ time-frequency plot (scalogram). The *Fermi*-LAT LSP is noisy at shorter periods, while the periodogram (PSD) and the WWZ are much cleaner and are consistent with each other.

The right panel of the *Fermi* plot of Figure 5.17 shows the PSD from the data compared with the 90% confidence limits (CL) calculated from 4.7×10^6 simulated light curves generated using the method of Emmanoulopoulos et al. (2013) assuming that the underlying stochastic process has a power-law PSD, and using the flux probability density function (PDF) from the right-hand panels of Figure 5.14. The dashed gray curve shows the CL for an *a priori* frequency. The dotted gray curve shows the CL that includes the penalty for selecting the frequency with the largest excess *a posteriori* from the 553 trial frequencies in the PSD. Assuming that the PSD is fully described by this stochastic process, it should be expected that at the 90% CL none of the measured PSD powers exceed this dotted gray curve, and indeed none do. Our simulations show that the apparent peaks in the LSP power at a ≈ 3 year period are not significant when the PSD of the underlying stochastic process and the trials factor are taken into account. The fact that the optical data show the same peak at ≈ 3 years does not necessarily lend credence

to the presence of a true QPO; this should be expected if a single stochastic process is responsible for the optical and γ-ray light curve.

The simulated light curves are also used to test whether the trend of linearly increasing flux found in Section 5.3.2 is inconsistent with a stationary stochastic process. We find that a linearly increasing or decreasing trend with a magnitude equal to or greater than that seen in the LAT data is present in approximately 1 in 1,000 simulations ($p = 9.6 \times 10^{-4}$), equivalent to a significance of $\approx 3.3\,\sigma$. The linear trend is therefore only moderately inconsistent with the stochastic modeling.

5.8.   Characterizing the 1ES 1215+303 flares

Of the four LAT flares defined, Flare 1 and Flare 3 appear in previous publications. Flare 1 was mentioned in Abdo et al. (2010b) for this source, together with another 105 sources, and did not have a detailed analysis. Flare 3 on the other hand was the subject of a detailed analysis in Abeysekara et al. (2017), therefore, the analysis here focuses on Flare 1, Flare 7 and Flare 8 (see Figures 5.18 and 5.19), with an emphasis on Flare 7, since its peak has a coincident flaring detection by VERITAS.

I calculated the decay time of *Fermi* Flares 1, 7 and 8 by fitting the 1-day binned light curve to:

$$F(t) = F_0 + F_1 \times 2^{-(t-t_0)/t_{\mathrm{var}}}. \qquad (5.3)$$

The size, R, and Doppler factor, δ, of the γ-ray emitting region are related, due to causality, to the variability timescale through: $R\delta^{-1} \leq ct_{\mathrm{var}}/(1 + z)$. The values found are shown in

Table 5.10: LAT flares halving times.

Flare	MJD	t_{var} UL(90%) days	$R\delta^{-1} \leq$ 10^{15} cm
Flare 1	54751	1.57	3.6
Flare 7	**57844[a]**	**0.90**	**2.1**
Flare 8	57855	1.24	2.8

[a] Coincident with a VHE flare.

Table 5.10. A similar fit was performed to the nightly TeV γ-ray light curve around the time of the flare on 2017 Apr. 01. The exponential decay time was relatively well constrained to 10 ± 2 days. While the rise time is less constrained by the fit, we estimate the doubling time to be < 4 days based on an upper limit measured eight days before the flare. Out of these flares, the one that puts the strongest constraint on the halving time is LAT Flare 7.

From the SED modeling that we performed (as described in Section 5.11), the Doppler factor for the blob is estimated to be $\delta = 25.0$. From fundamental plane-derived velocity dispersion, Woo & Urry (2002) estimated the SMBH mass of the source to be $1.3 \times 10^8 M_\odot$, which corresponds to a Schwarzschild radius of $R_s \sim 3.9 \times 10^{11}$ m. Therefore, the strongest constraint on the size of the emitting region based on the fastest observed γ-ray variability (shown in Table 5.10) is
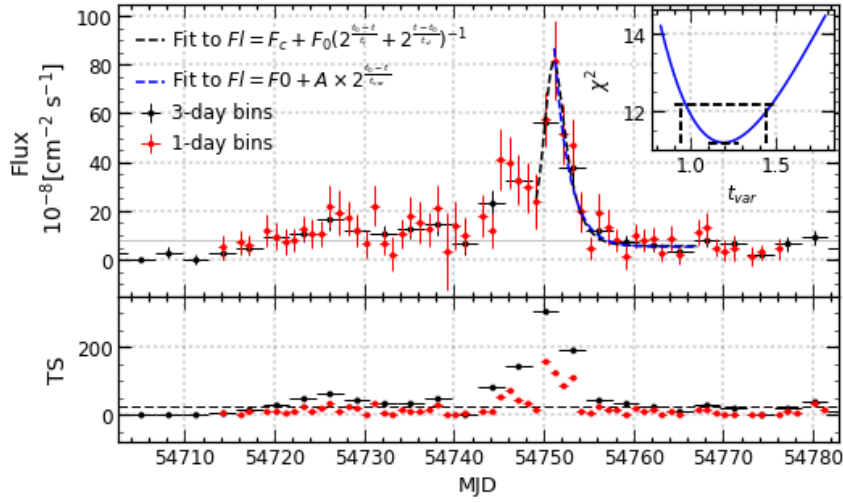
$$R \leq 1350 R_{\mathrm{S}}.$$

Fig. 5.18.— *Top: Fermi-*LAT Flare 1 in 3-day binned (black points) and 1-day binned (red points) light curves. A fit to a power function is shown (black dashed line) for visualization. A falling function (Equation (5.3)) was used to calculate the halving time (the best fit function is shown by a blue dashed line). The inset provides a view of the profile built to calculate the 90% upper limits for the halving time. *Bottom:* TS values of the corresponding 3-day and 1-day light curve data in the top panel. A dashed horizontal black line was drawn at TS=25.

Fig. 5.19.— *Fermi-*LAT Flare 7 (left outburst) and 8 (right outburst) in 3-day binned (black points) and 1-day binned (red points) light curves. A simple function (Equation (5.3)) was used to calculate the halving time (best fit functions are shown in blue dashed lines). The top panels provide a view of the profiles built to calculate the 90% upper limits for the halving times. *Bottom:* TS values of the corresponding 3-day and 1-day light curve data in the top panel. A dashed horizontal black line was drawn at TS=25.
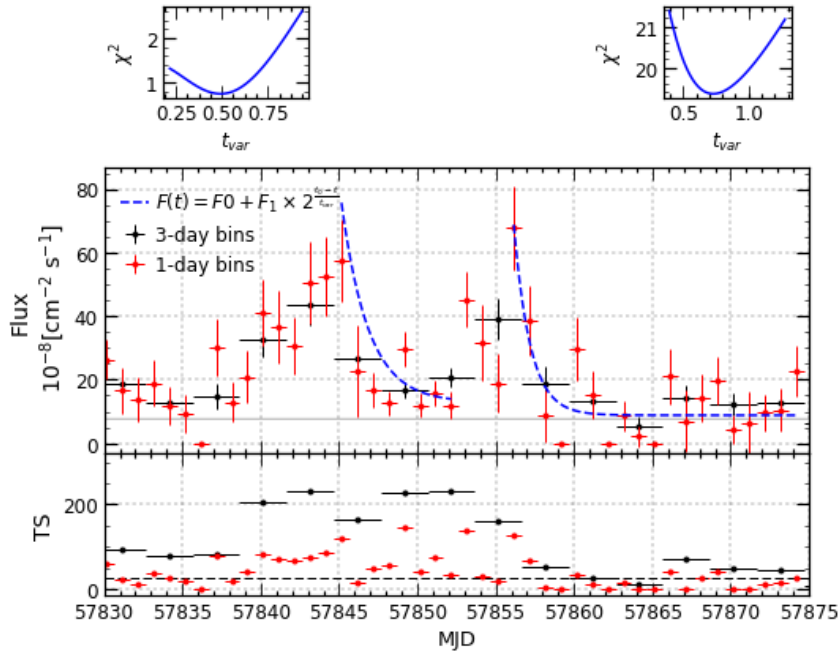
5.9.   Long-term spectral analysis

I fitted the *Fermi*-LAT complete
data set with three different spec-
tral models. The power-law model,
$dN/dE = N_0(E/E_0)^{-\Gamma}$, resulted in
an integral flux of $(7.7 \pm 0.2) \times$
10^{-8} photons cm^{-2}s^{-1} with a signif-
icance of 144σ and a photon index
$\Gamma = 1.92 \pm 0.01$ at $E_0 = 1.36$ GeV.
The log-parabola model fit, $dN/dE =$
$N_0(E/E_b)^{-(\alpha+\beta \log(E/E_b))}$, where N_0 is
the normalization and α and β are
the spectral parameters at energy E_b,
provided an integral flux of $(6.9 \pm$
$0.2) \times 10^{-8}$ photons cm^{-2} s^{-1} with a
significance of 166σ, a spectral slope
$\alpha = (1.86 \pm 0.01)$ and a curva-
ture parameter $\beta = 0.039 \pm 0.006$ at
$E_b = 1$ GeV. From a power-law sub-
exponential cutoff (plSECO) model,
$dN/dE = N_0(E/E_b)^{-\gamma_1}e^{-(E/E_c)^{\gamma_2}}$,
an integral flux of $(7.7 \pm 0.2) \times$
10^{-8} photons cm^{-2} s^{-1} was obtained
with a significance of 144σ, a $\gamma_1 =$
1.74 ± 0.03, a $\gamma_2 = 0.40 \pm 0.06$, at
cutoff energy $E_c = 21.98$ GeV and
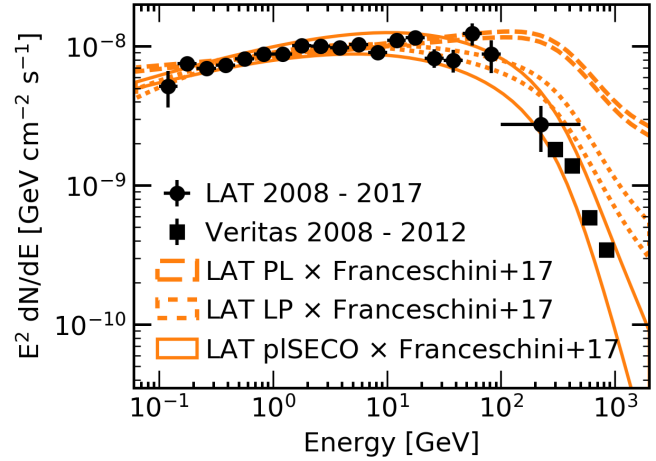$E_0 = 1.36$ GeV.

**Fig.   5.20.— SED of the entire *Fermi*-LAT
data set (2008-08-04 – 2017-09-04).   The data
were analyzed with three different models, power-
law (dashed), log-parabola (dotted) and power-law
sub-exponential cutoff (solid line). The black cir-
cles show the result of the individual spectral anal-
yses (Section 4.6) for each of the LAT energy bins.
To visualize the connection with the TeV data, the
VERITAS SED for integrated data from 2008 to
2012 (Aliu et al. 2013)) was added. The LAT but-
terflies were extrapolated to the VHE regime and
EBL absorption was applied.**

Since the PL and LP as well as the PL and plSECO are nested models, I use a
likelihood ratio test in order to compare them, $TS_{\mathrm{curve}} = 2(\log L_{\mathrm{curved}} - \log L_{\mathrm{PL}})$, where
L is the maximum likelihood of the fit. LP and plSECO are not nested, therefore, I do
not compare them. As a result, it is observed that the LP is preferred to the PL model
with 7.2σ significance. Analogously, the plSECO is preferred over the PL with 7.5σ
significance. These results indicate a preference for curved models, which at the same
time could be an indicator of internal curvature, even before entering the VHE range
where the extragalactic background light (EBL) absorption has a considerable impact on
the reduction of the VHE flux. A similar analysis was performed for shorter time scales
(per year, per season), which gave no evidence for a preference for a curved model, since
there is not enough statistics above ∼30 GeV - ∼100 GeV, where the SED of this source
begins to turn over.

The three spectral models are shown in Figure 5.20. I refer the reader to Section 4.6
and Table 4.4 for details on this analysis. Absorption for three different EBL models were

applied to each of the spectra, Franceschini & Rodighiero (2017) ($z = 0.131$ interpolated), Domínguez et al. (2011) ($z = 0.132$) and Finke et al. (2010) ($z = 0.13$); and good agreement between these models was found. Only the absorption with the model of Franceschini & Rodighiero (2017) are shown in the same figure. The VERITAS spectrum for the data from 2008 to 2012 (Aliu et al. 2013)) is shown for visualization. A very good connection between the GeV and TeV data is observed. The LAT spectra corresponding to the curved models are in better agreement with the VERITAS data, in this case corresponding to an average quiescent state.
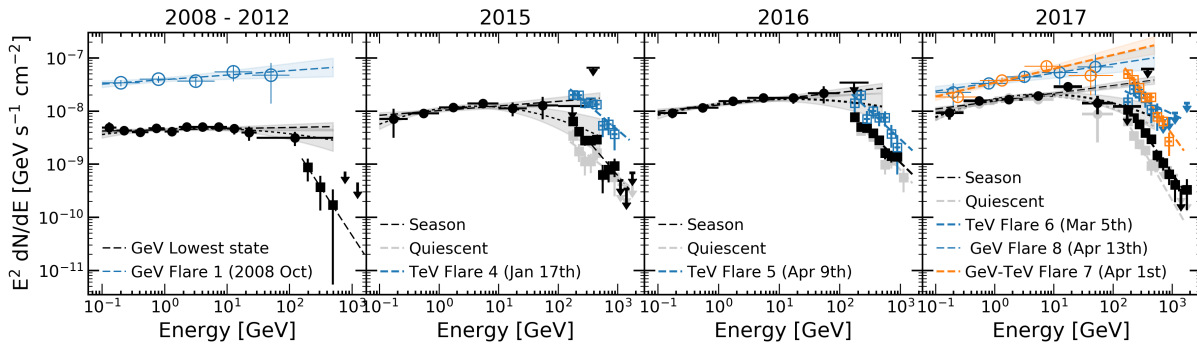
5.10.   1ES 1215+303 GeV-TeV SEDs

Fig. 5.21.— **SEDs for the previously unpublished LAT and VERITAS flares. Circular points correspond to the *Fermi*-LAT data, while the square data points correspond to the VERITAS data. Data and butterflies for the flaring states are shown in light blue and orange. Data for the quiescent state are shown in gray. Notice the rare VERITAS low state detection of $\approx 6\,\sigma$ over a period of about 3 years in the first panel on the left. For years 2015 to 2017, the black data points correspond to the season total data sets. Power-law and log-parabola butterflies are shown for the black spectra. Only power-law butterflies are shown for the flaring states. Non-coincident GeV-TeV flare SEDs are shown in light blue, while the orange SED represents Flare 7 which had a peak on 2017 Apr. 01, coincident with a TeV flare.**

    LAT-VERITAS SEDs for the previously unpublished VHE data are shown in Figure 5.21. In 2008, the brightest flare (Flare 1) at GeV energies was detected. There were no corresponding VHE data, since VERITAS observations of 1ES 1215+303 did not commence until 2008 Dec. The first panel on the left shows Flare 1, and the GeV–TeV lowest state SED, as defined in Table 5.3; which is a rare VERITAS low state detection of $\approx 6\,\sigma$ over a period of about 3 years.

    During Flare 4 at VHE in 2015, there were approximately 40 minutes of simultaneous observations between the LAT and VERITAS; see top panel of Figure 5.22 and Figure 5.23. During Flare 5, also at VHE, in 2016, there were approximately 80 minutes of simultaneous observations between the LAT and VERITAS; see second panel of Figure 5.22 and Figure 5.24. No significant HE emission was detected during these simultaneous
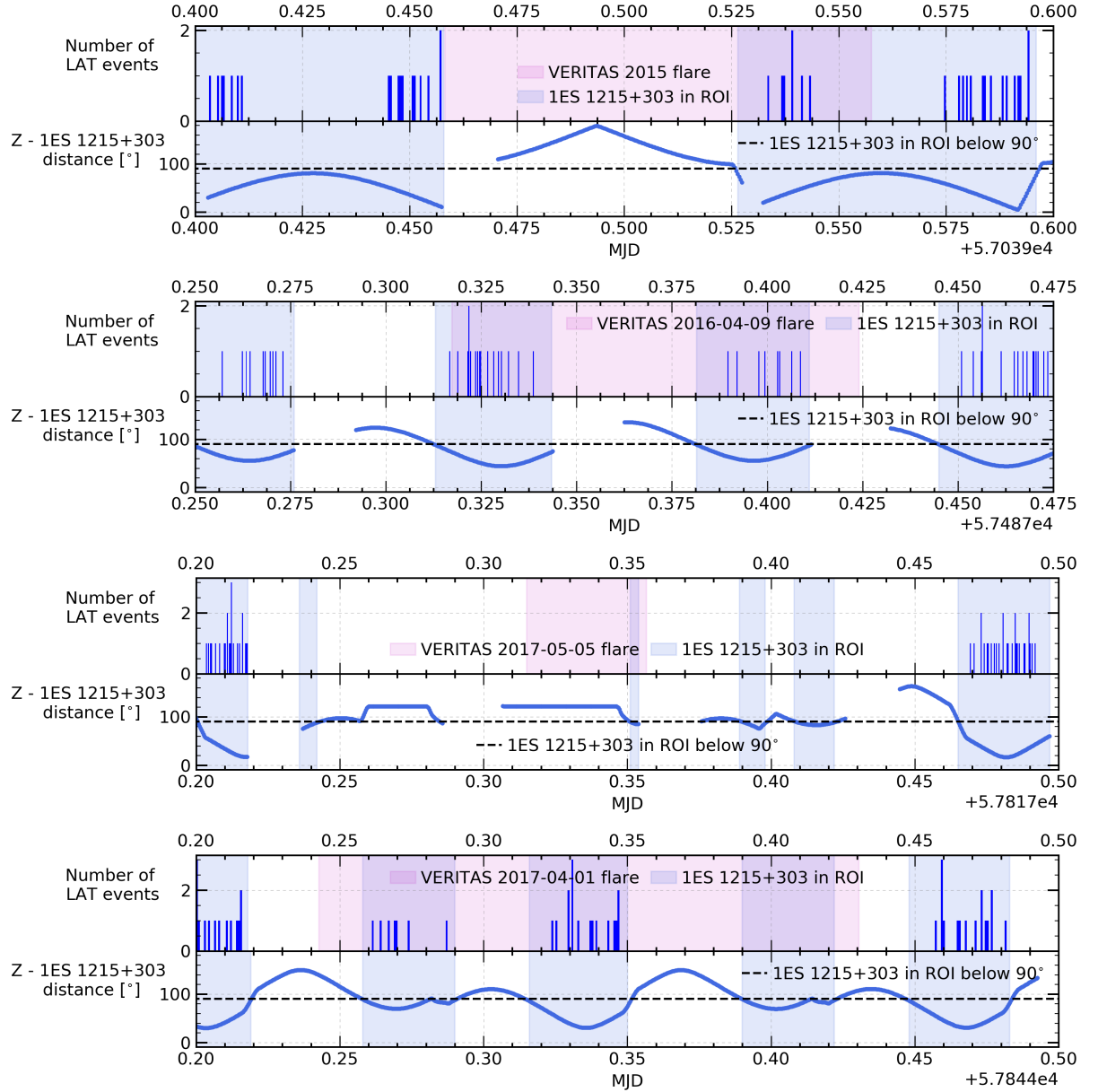
Fig. 5.22.— Distribution of events versus time (upper panels). The angular distance of the Z-axis from 1ES 1215+303 is shown in the lower panels. 1ES 1215+303 is in the FoV when this distance is < 90° (indicated by the dashed line). *Top, 2015 Flare 4:* There are 40 min. of simultaneous observations between the LAT and VERITAS (intersection of blue and pink shaded areas), although no significant detection is found. *Second from top, 2016 Flare 5:* There are 80 min. of simultaneous observations between the LAT and VERITAS (intersection of blue and pink shaded areas), although no significant detection is found. *Third from top, 2017 Flare 6:* There is no simultaneous observations between the LAT and VERITAS; 1ES 1215+303 was not in the LAT FoV. 1ES 1215+303 had been in the FoV of the LAT approximately 2.5 hours before VERITAS started observations, and re-entered the LAT FoV approximately 1 hour after VERITAS finished observing this source during that night. *Bottom, 2017 Flare 7:* Simultaneous observations of 1ES 1215+303 by the LAT and VERITAS. A significant detection by the LAT at the 5.8 σ level is found. Upper limits are represented by arrows.

observations; and no elevated flux was observed in the LAT data for these days. VERITAS
detected another flare on 2017 March 05, Flare 6, at a time during which 1ES 1215+303
was not in the LAT FoV. 1ES 1215+303 had been in the FoV of the LAT approximately 2.5
hours before VERITAS started observations, and re-entered the LAT FoV approximately
1 hour after VERITAS finished observing this source during that night. See third panel of
Figure 5.22. No evidence for an elevated flux was found when the LAT data for this day
were analyzed. In 2017, two flares were measured by the LAT with peaks on April 01 and
13 (Flares 7 and 8, respectively; refer to Table 5.3 for the duration of these flares). LAT
Flare 7 had a VHE counterpart (orange), while VERITAS was not observing at the time
of Flare 8 at GeV energies (blue). See the bottom panel of Figure 5.22 and Figure 5.25. A
view of my searches for simultaneous LAT observations is provided in Figures 5.22–5.25.
A significant detection by the LAT at the $5.8\,\sigma$ level is found for a simultaneous coverage
of Flare 7 by the LAT and VERITAS on 2017 Apr. 01, that lasted for about 4 hours.
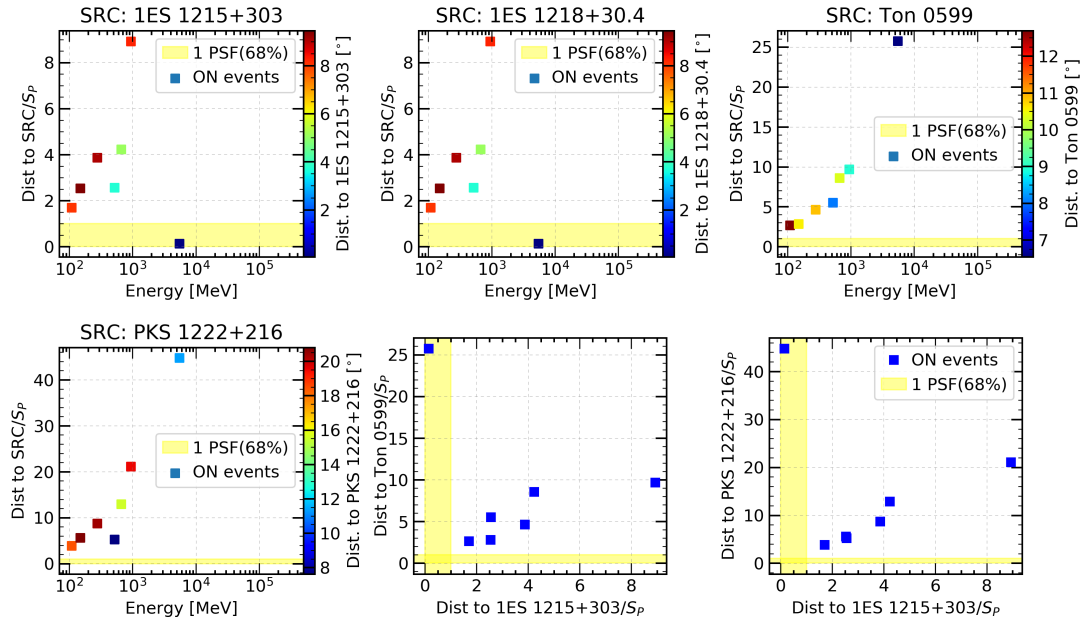The results of this analysis are used in the next section for the SED modeling[12].

Fig. 5.23.— **VERITAS Flare 4 simultaneous observations, 2015: LAT event distances
from the source as a function of energy and PSF-scaled distance from the source. The
two bottom-right panels show the PSF-scaled distance from 1ES 1215+303 versus the PSF-
scaled distance from the two brightest sources in the ROI. One ($\approx$ 6 GeV) of the seven
photons in the ROI is consistent with the position of 1ES 1215+303 or 1ES 1218+304;
which is consistent with the results of a maximum likelihood analysis.**

---

[12]For this analysis in particular, different consistency checks were performed due the very short expo-
sure. While the flux parameters for the diffuse backgrounds would usually be let free, the analysis was
repeated by fixing each of these parameters, or both at the same time. The results were verified to be
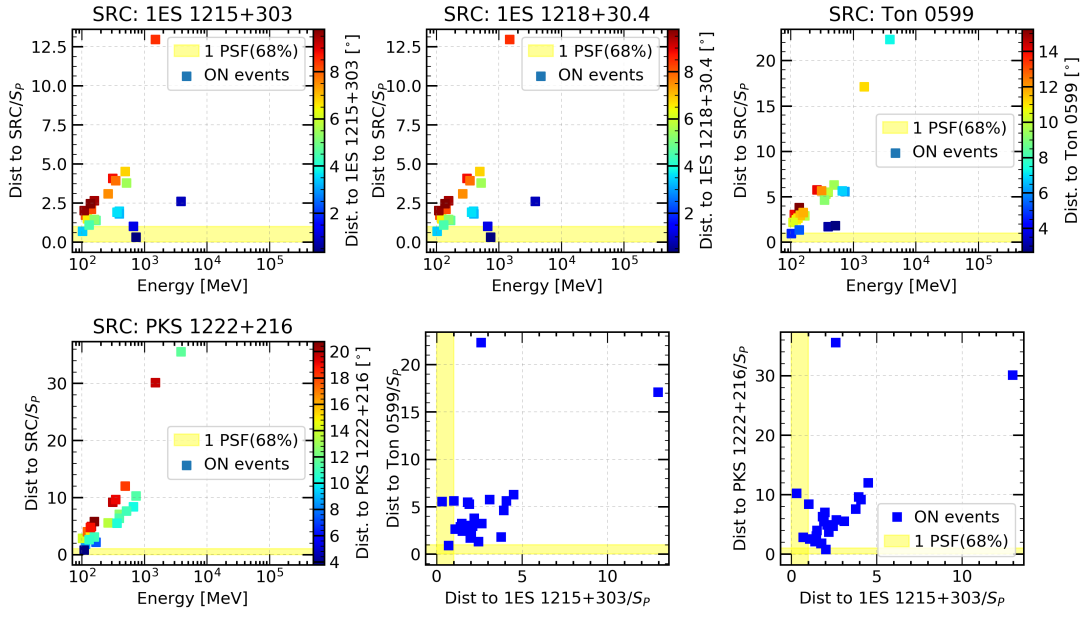consistent.

Fig. 5.24.— **VERITAS Flare 5 simultaneous observations, 2016: Analogous to Figure 5.23.** ≈ 2 **of the 24 photons in the ROI are consistent with the position of 1ES 1215+303 or 1ES 1218+304; consistent with the results of a maximum likelihood analysis.**
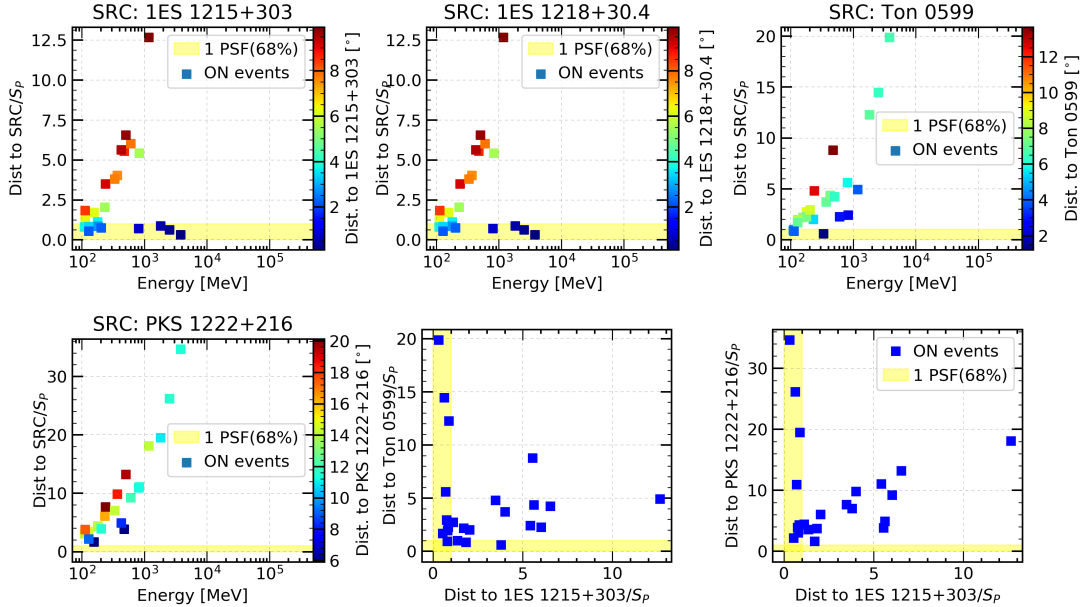
Fig. 5.25.— **VERITAS Flare 7 simultaneous observations, 2017: LAT event distances from the source as a function of energy and PSF-scaled distance from the source. The two bottom-right panels show the PSF-scaled distance from 1ES 1215+303 versus the PSF-scaled distance from the two brightest sources in the ROI. Of the 34 photons in the ROI** ≈ 6 **are consistent with the position of 1ES 1215+303 (or 1ES 1218+304). Significant results are obtained in this case with a maximum likelihood analysis, that associates six photons with 1ES 1215+303, therefore consistent with these plots.**

Table 5.11: Gamma-ray contemporaneous spectral analysis.

Year	VERITAS						Fermi-LAT					
	All		Flare		Non-flare		All		Flare		Non-flare	
	Γ	Flux	Γ	Flux	Γ	Flux	Γ	Flux	Γ	Flux	Γ	Flux
2015	3.32 ± 0.18	0.61 ± 0.14	2.96 ± 0.18	4.36 ± 0.99	2.84 ± 0.39	0.56 ± 0.27	1.91 ± 0.04	5.6 ± 0.3	–	–	–	–
2016	3.12 ± 0.13	1.07 ± 0.16	3.06 ± 0.28	2.93 ± 0.89	3.27 ± 0.14	0.78 ± 0.13	1.88 ± 0.03	7.2 ± 0.3	–	–	–	–
2017	3.62 ± 0.10	$0.013 \pm 0.003^{\dagger}$	3.56 ± 0.13	$0.073 \pm 0.023^{\dagger}$	3.94 ± 0.32	0.21 ± 0.10	1.85 ± 0.03	8.6 ± 0.3	1.61 ± 0.32	52.3 ± 25.1	1.85 ± 0.04	8.0 ± 0.5

The flux value for VERITAS is the normalization (N_0) of the differential flux (dN/dE) at energy of 1 TeV in units of $10^{-12} \mathrm{TeV}^{-1} \mathrm{cm}^{-2} \mathrm{s}^{-1}$.

The flux value for *Fermi*-LAT is the normalization (N_0) as well, at the energy of 1.36 GeV, in units of $10^{-12} \mathrm{MeV}^{-1} \mathrm{cm}^{-2} \mathrm{s}^{-1}$.

† Normalization at 3 TeV.

5.11.   1ES 1215+303 SED Modeling

The large multi-wavelength dataset described in this paper allows us to build broadband SEDs for different periods and states of activity of the source. In this section, three activity states that have not been examined in previous works, are studied: a low steady state corresponding to the lowest observed *Fermi*-LAT activity as defined by the Bayesian Block method, the 2017 Apr 01 GeV-TeV flare (Flare 7), and the subsequent post-flare state from 2017 Apr. 15 to 23.

These three states are modeled using the "blob-in-jet" radiative code from Hervet et al. (2015), where we consider the main emission zone as a spherical compact plasma blob moving at a significant Lorentz factor close to the line of sight. We assume that this blob is filled by an electron (or electron/positron) population in an isotropic magnetic field. The particle energy distribution follows a canonical broken power-law function as

$$N_e(\gamma) = \left\{ \begin{array}{ll} K_1 \gamma^{-n_1} & \text{for } \gamma_{\min} \leqslant \gamma \leqslant \gamma_{\mathrm{brk}} \\ K_2 \gamma^{-n_2} & \text{for } \gamma_{\mathrm{brk}} \leqslant \gamma \leqslant \gamma_{\max} \end{array} \right. , \tag{5.4}$$

with $K_2 = K_1 \gamma_{\mathrm{brk}}^{(n_2 - n_1)}$, and K_1 the particle density factor set as $K_1 = N_e(1)$.

This blob is moving through a conical leptonic plasma jet that has a larger radius and lower Lorentz factor. The jet is partitioned into 50 discrete conical slices which, for the sake of simplicity have their particle density spectra considered as simple power-law functions. Both the blob and the jet are radiating in synchrotron and SSC. We include the effects of the absorption by the EBL following the model of Franceschini & Rodighiero (2017). The broadband spectral modeling presented in this work consists in a "fit by eye" procedure due to the strong degeneracies between the parameters of the SSC models, which make the minimization algorithm extremely challenging. This complexity is intensified when considering multi-zone models, as is our case. Therefore, the proposed model solutions are not statistically best results; they are, however, consistent with our assumptions about the underlying emission scenario. In the following, the χ^2/d.o.f. provided are for informational purposes only.

5.11.1.   Low state of 1ES 1215+303

The time period corresponding to the low state of the source was defined using the results of the Bayesian block method that was applied to the 10 year *Fermi*-LAT light curve (see Fig. 5.7). Two periods between 2008 and 2012 can be considered as the lowest activity state: 2008 Nov. 17 - 2010 Aug. 12 (MJD 54787 - 55421) and 2011 Apr. 15 - 2012 Apr. 10 (MJD 55666 -56027). We ensured that no outburst was detected at any other wavelength during these time periods by examining our multi-wavelength light curves. Such a long cumulated time of 33 months of low state allows us to have a very well-defined *Fermi*-LAT spectrum, as well as having a well-sampled multi-wavelength SED at lower energies. Additionally, data from the *Planck PCCS2* catalog (Planck Collaboration et al.

2016) and the AllWISE Multiepoch Photometry Database[13] were taken during this low-state period, thus increasing the broadband coverage. The resulting SED with the favored associated radiative model is presented in Figure 5.26, and the model parameters are shown in Table 5.12. The favored model has a $\chi^2/\text{d.o.f.} = 364./49 = 7.4$. The fit quality is strongly, however, impacted by the extremely small uncertainties of the averaged *WISE* data. Without taking into account the *WISE* data, we have $\chi^2/\text{d.o.f.} = 106./45 = 2.4$.
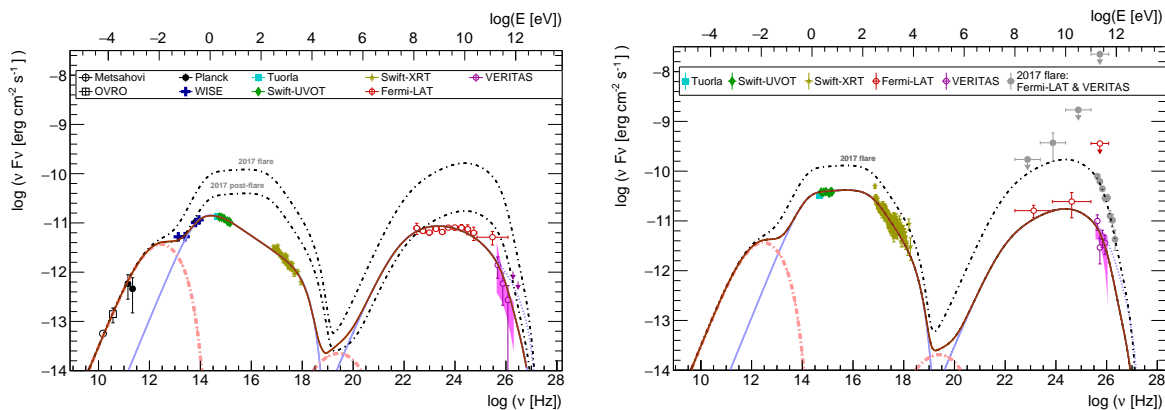

Fig. 5.26.— **Multi-wavelength SEDs and models of the source low state (*left*), 2017 flare and 2017 post-flare (*right*). Plain blue lines are the blob synchrotron and SSC, dotted-dashed pink lines are the jet synchrotron and SSC, blue dotted line is the intrinsic SSC emission without EBL absorption. The thick brown and thick black dotted-dashed lines are the sums of all components.**

5.11.2. Compact blob

The multi-wavelength SED from the IR to γ-rays is assumed to be emitted from a compact emission zone, referred to above as the "blob". The SED shows two clear bumps, one peaking in the IR-optical range considered as synchrotron emission and one peaking at high energy considered to be dominated by SSC emission. The apparent contradiction with this observed low frequency synchrotron peak and the HBL classification of the source is further discussed in Section 5.12.

Neither the thermal signature of accretion disc radiation nor a sharp peak at high energy, which would indicate the presence of the external inverse-Compton (EIC) process on the nucleus thermal radiation field, are detected. We therefore consider this process negligible, as is usually done for HBL sources.

The wide gap of about ten orders of magnitude in energy between the synchrotron and SSC peaks requires a very low internal $\gamma - \gamma$ opacity in order to explain the observed energies of $E > 100$ GeV. A satisfactory solution is found by considering a high Doppler

---

[13]http://wise2.ipac.caltech.edu/docs/release/allwise/

factor value of $\delta = 25$, associated with the maximum theoretical angle with the line of sight $\theta \simeq 2°$. The radius of the emitting region is calculated by taking into account the fastest observed variability of 0.9 day (see Section 5.8).

The minimal energy of the radiative electron is set at the relatively high value of $\gamma_{min} = 4.7 \times 10^3$. While not exceptional in blazar radiative models, such a high γ_{min} is often specifically used to describe extreme HBLs (e.g Aliu et al. 2014; Archer et al. 2018). The blob is matter-dominated with an equipartition ratio between the magnetic field energy density U_B and the particle energy density U_e of $U_B/U_e = 1.6 \times 10^{-2}$.

5.11.3.   Radio jet

The *WISE* SED shows a clear luminosity excess in its lowest energy band with a hard spectral index power law spectrum, as would be expected for the optically thick blob synchrotron emission.

This excess could be associated with broader jet emission, dominating the low energy part of the SED from the radio to the far infrared. Although not often modeled, this jet signature is not a rare HBL feature (e.g. Katarzyński et al. 2001b; Archer et al. 2018).

With 9 free parameters and only one obvious spectral signature in the radio to far IR, the jet parameters are naturally degenerate. So in order to have parameters as physically consistent as possible while keeping a good fit to the data, we constrain several other parameters in addition to the density and Doppler factor that were discussed above. We consider an identical spectral slope for the injected particle spectrum between the blob and the jet and we also assume that the jet is in equipartition.

The apparent opening angle of the 15 GHz radio-jet was measured at $\alpha_{app} = 13.8 \pm 0.1$ deg by Pushkarev et al. (2017) via a stacking of the multiple observations of the VLBA referenced in the MOJAVE database. This value confirms the former measurement of $\alpha_{app} = 14$ deg by Hervet et al. (2016), from the same database but based on the evolution of the referenced radio-knots sizes. The fact that these two measurements are similar indicates that the jet does not present a significant

Table 5.12: Model parameters used for the multi-wavelength low state.

Parameter	Value	Unit
θ	2.0	deg
Blob		
δ	25	–
K_1	1.8×10^6	cm^{-3}
n_1	2.82	–
n_2	3.7	–
γ_{min}	4.7×10^3	–
γ_{max}	7.0×10^5	–
γ_{brk}	1.5×10^4	–
B	2.35×10^{-2}	G
R	5.1×10^{16}	cm
Jet		
δ	15	–
K	1.3×10^4	cm^{-3}
n	2.82	–
γ_{min}	9.0×10^2	–
γ_{max}	3.5×10^3	–
B_1	3.5×10^{-2}	G
R_1	1.0×10^{17}	cm
L^*	1.0×10^2	pc
$\alpha/2^*$	2.4×10^{-1}	deg

*: *Host galaxy frame.*

change of its direction with the line of sight over time, and that the radio-knots occupy
the full jet cross-section.

From the observed jet apparent opening angle and the angle with the line of sight
set at $\theta = 2$ deg, we can deduce the intrinsic jet opening angle used for the model via the
relation

$$\tan(\alpha/2) = \tan(\alpha_{\mathrm{app}}/2)\sin(\theta), \tag{5.5}$$

which leads to $\alpha/2 = 0.24$ deg.

5.11.4.   2017 April flare and post-flare

On 2017 Apr 01 (MJD 57844), VERI-
TAS detected its second brightest flare from
1ES 1215+303 (referred to as Flare 7). This
strong γ-ray activity was simultaneously de-
tected by *Fermi*-LAT and was followed by a
secondary *Fermi*-LAT outburst 10 days later
which we call Flare 8 (see Fig. 5.7). Unfortu-
nately 1ES 1215+303 was not being monitored
at any other energies at this time, which pre-
vents us from being able to derive any accurate
emission scenario for this 2017 Apr. 01 event.

From 2017 Apr.   15 to 23 (MJD
$57858 - 57866$), the source was monitored at
many wavelengths and showed historically high
fluxes in the optical, UV, and X-ray bands (see
Fig. 5.2). It is plausible then that the emission
zone responsible for Flares 7 and 8 was still in
its cooling phase during this period.

Table 5.13: Model parameters used for
the multi-wavelength 2017 April 01 flare
and post-flare states.

Parameter	Value	Unit
θ	2.0	deg
Blob		
δ	25	–
K_1 (flare)	$\mathbf{5.5 \times 10^6}$	cm^{-3}
K_1 (post-flare)	$\mathbf{1.8 \times 10^6}$	cm^{-3}
n_1	2.9	–
n_2	4.5	–
γ_{min}	4.7×10^3	–
γ_{max}	7.0×10^5	–
γ_{brk}	9.0×10^4	–
B	5.2×10^{-2}	G
R	5.1×10^{16}	cm

Given the many multi-wavelength observations available during this post-flare period
we focus primarily on it to derive realistic physical parameters from the modeling. As
shown in Figure 5.26 and Table 5.12, a particle density decrease of a factor ~ 3 of the
emission zone is enough to pass from the flare to the post-flare state. Such a decrease
matches an interpretation of a flare from a jet overdensity crossing a standing shock.

The radio jet is assumed to keep a roughly steady flux between all of the studied
states. The jet model used for the low state is kept for the 2017 flare/post-flare, and
plays only a very minor role in the total radiative output.

We considered the same emission zone for all of the SED modeled, with a constant
plasma flow speed (same Doppler factor and size). The low- and high-state SEDs can be
well represented by changing the particle spectrum and the magnetic field parameters as
follows: an increase of the magnetic field B ($\times 2.2$), an increase of the particle spectral

break energy γ_{brk} ($\times 6.0$), and a softening of the particle index after the break n_2 ($\times 1.2$). Interpretations of such changes are discussed throughout Section 5.12. The fit quality of the flare and post-flare states is $\chi^2_{\mathrm{flare}}/\mathrm{d.o.f.} = 10.5/0$ and $\chi^2_{\mathrm{p-flare}}/\mathrm{d.o.f.} = 385/184 = 2.1$ respectively.

5.12. Discussion

5.12.1. Extreme shift of the synchrotron peak frequency

In many ways 1ES 1215+303 shows typical features of a classical HBL source: it has an FR I radio jet with multiple stationary radio components as can be seen from VLBI (Hervet et al. 2016; Piner & Edwards 2018); it does not show a thermal accretion disc signature in the blue-UV, nor does it exhibit strong inverse-Compton dominance in the broadband SED.

An unusual feature however, is the dramatic change of the synchrotron bump (shape and peak frequency) between the low and high activity states. The high state, as observed in the 2017 flare and post-flare SED, presents a synchrotron peak between the UV and soft X-rays, typical of HBLs. Due to the relative flatness of the synchrotron bump it is difficult to determine the precise peak frequency value, but the favored post-flare model shows a synchrotron peak at $\log_{10}(\nu_{\mathrm{peak}}/\mathrm{Hz}) = 15.75$. The low state is characterized by a much more constrained peak frequency $\log_{10}(\nu_{\mathrm{sy}}) = 14.49\pm^{0.17}_{0.54}$ Hz from the model, with boundaries from the IR and optical data. Thus, if only this low state were considered, this source would be classified as an IBL.

Fits to a cubic polynomial function were also performed on the synchrotron bump of the broadband SED; since this is the method followed in the Fourth Catalog of AGNs detected by the *Fermi*-LAT (4LAC; The *Fermi*-LAT collaboration 2019). The results were consistent with the blob-in-jet modeling, and are illustrated in Figure 5.27.

Up to now, the only ever extreme peak frequency shift observed from mid-IR to X-ray is from the IBL VER J0521+211, with however, a lack of optical-UV data during its flare, which prevents any reliable peak shift estimation (Archambault et al. 2013). HBLs are also subject to synchrotron peak shifts during flares but, for instance, within the same band, as between soft/mid to hard X-rays, making a transition possible between regular to extreme HBL (e.g Ahnen et al. 2018; Tavecchio et al. 2001). Thus, the reported frequency shift in this study is a first for this kind of source, which further increases the diversity of behaviors observed for BL Lacs and raises many questions about the causes of such a phenomenon.

A critical parameter illustrating this synchrotron peak shift is the Lorentz factor break of the electron spectrum, γ_{brk}, which increased by a factor of 4.5 between the low and high states. Following the common broken power-law description of the particle spectrum, the γ_{brk} parameter represents the energy from where the radiative cooling is taking over from
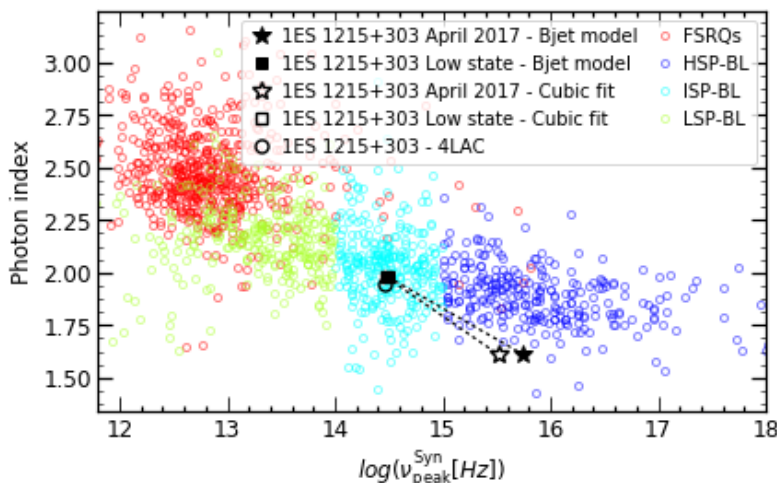
Fig. 5.27.— **Photon index versus the logarithm of the frequency of the synchrotron peak. Color markers represent classifications, indicated in the legend, for GeV-detected blazars as published in the 4LAC. 1ES 1215+303 shows a spectral shape characteristic of IBLs during the low state, while exhibiting HBL-like properties during the high state in April 2017. This extreme shift is observed with both the results of the blob-in-jet modeling and the cubic polynomial fit (see text for details).**

the adiabatic (or advective) one (e.g Inoue & Takahara 1996). A significant increase of γ_{brk}, as suggested by the SED modeling, points towards a more efficient adiabatic cooling when flaring. In order to picture a flare with a more efficient non-radiative cooling, the model shown in Figure 5.26 induces a strong increase of the population of injected particles in addition to a local increase of the magnetic field. Due to the degeneracy between the magnetic field and the Doppler factor in blazar SSC models, a local increase of the Doppler factor instead of the magnetic field is also a possible explanation.

The linear flux-flux correlation between the optical and the GeV γ-ray bands discussed in Section 5.4, in particular, the slope ($a = 0.86$) of less than 1 is consistent with the fact that the variation of the synchrotron peak luminosity is larger than the variation of the SSC luminosity between the low state and the 2017 post-flare state. The exclusion of a quadratic flux-flux correlation indicates that a change in the number of radiative particles is not the major criterion explaining the common observed variability. However this could be favored for the strongest flares, such as that of 2017 Apr 01 (see Figure 5.26 and Table 5.13).

5.12.2. Multi-year flux increase

The broken-line fit of the long-term light curves is strongly favored over the linear fit for the *Fermi*-LAT dataset ($5.5\,\sigma$ level), and moderately favored for the optical dataset ($3.4\,\sigma$ level). The times where the break occurs in both datasets are compatible within $1\,\sigma$, strengthening the case for a MWL increase of the source activity starting approximately

at the time of MJD 55780 ± 122 ($\sim$ 2011 August).

Even though the LAT linear trend is inconsistent with the stochastic model only at the $3.3\,\sigma$ level (see Section 5.7), this long-term flux increase of at least 6 years is intriguing and can be caused, in theory, by various possible processes including jet precession, or an increase in the accretion rate.

The multiple radio-VLBI observations of the source indicating the lack of non-radial motions in the jet rule out any significant jet precession. Also, jet precession would make the jet width, from stacked radio images, broader than the measured knot sizes (Section 5.11.3). We thus consider that the most likely cause of this multi-year flux increase is related to the black hole accretion process.

Tidal disruption events (TDEs) are often mentioned when observing multi-year-long flares of supermassive black holes. These should be at a particularly high rate in AGNs due to the interaction of their accretion disc/torus with nearby stars (Karas & Šubr 2007). However it is very challenging to differentiate a TDE from the natural high-amplitude variability of the accretion disc itself. A TDE is usually identified by its strong nuclear ionization and by a specific decreasing flux profile. We do not have access to these observables with our gathered data, which prevents us from any relevant testing of the TDE hypothesis.

This long-term flux increase can be, however, compared to typical timescales of natural changes that occur in the accretion rate. HBLs are known to be the least powerful blazars and have been associated with a weak accretion mode known as the "advective dominated accretion flow" (ADAF). In this case, the accretion timescale is roughly given by the free-fall timescale τ_{ff}. From Manmoto et al. (1996) we have

$$\tau_{ff} = 4.63 \times 10^{-5} \left(\frac{r}{1.0 \times 10^3 r_g} \right)^{3/2} \left(\frac{M_{\mathrm{BH}}}{10 M_\odot} \right) \mathrm{days}. \qquad (5.6)$$

By considering a perturbation from the outer part of the ADAF disk, at $r \sim 3.0 \times 10^3 r_g$ (Narayan et al. 1996), and the black hole mass $1.3 \times 10^8 M_\odot$ (as discussed in Section 5.8), we obtain a typical timescale of τ_{ff} of 8.7 years. This timescale is in agreement with the reported long-term flux increase in Section 5.3.2 which started around the 2011 Aug.

We found evidence (significance of $4.7\,\sigma$) for a long-term spectral hardening trend accompanied with the flux increase (see Section 5.3.2). Such a "harder-when-brighter" trend is typically observed in γ-ray flat-spectrum radio quasars, in IBLs and in LBLs (e.g., Abdo et al. 2010c). Similar behavior has been observed in radio galaxies and HBLs, most commonly in the X-ray band (e.g., Brown & Adams 2011; Ahnen et al. 2018). From our SED modeling above, the GeV γ-ray spectra during higher flux states are indeed harder then the lowest flux state, lending support to the "harder-when-brighter" phenomenon.

5.12.3.   Optical polarization

The optical polarization fraction over the 3 years covered by the NOT observations is relatively stable, with values between 5 and 15 %. This relatively low blazar polarization is well within the range of small values typical of HBL sources (Angelakis et al. 2016). In the same paper, it was noted that HBLs tend to concentrate their polarization angle around preferred directions, which is also the case for 1ES 1215+303 with small angle variations from 130° to 175°. This indicates a stable, nearly toroidal magnetic field structure at the location of the optical emission zone that we described as a compact blob.

The NOT observations provide good optical polarization coverage around the γ-ray flare of 2017 April 01. During this epoch, the polarization angle reached its highest value (173°), remaining above 166° during the post-flare state. At the same time, the polarization fraction reached its local minimum during the post-flare state. The polarization angle local minimum of the season was 140.6°, varying a total of 38.4° in 2017; while the polarization fraction changed between 5% and 10.5%.

Although this angle shift is much less dramatic that what has been observed in some blazars (e.g. Abdo et al. 2010a; Marscher et al. 2010), it follows a common behavior associated with γ-ray flares (Blinov et al. 2018), i.e. larger polarization angles and smaller polarization fraction. The weak amplitude of the polarization angle shift could find a natural explanation in a toroidal magnetic structure and widely matter-dominated blob, as suggested from the modeling.

6. CONCLUSION

This project summarized the long-term observations of the HBL 1ES 1215+303 from 2008 to 2017 from radio to VHE γ-ray energies. We summarize the main observational properties of the source that we have gathered from the data.

- The observations performed by *Fermi*-LAT in γ-rays and the Tuorla Observatory in optical show a clear long-term increase of flux over the ten-year period. Both datasets favor a start of this increase around August 2011 ($\approx$ MJD 55780$\pm$122). No conclusive interpretation is found to explain such a behavior; however, the timescale of this flux increase, while limited by our dataset, is consistent with a process driven by the accretion disk. We can also reject jet precession as the cause of this behavior since precession is not in agreement with the multiple radio-VLBI observations.

- The HE LAT fluxes and the Tuorla optical bands are found to be strongly temporally correlated with one another ($a = 0.86$). This almost linear correlation does not favor the change of particle density in a SSC scenario, or a change of Doppler factor in an EIC scenario. Beyond this, the interpretation remains open.

- An extreme shift of the synchrotron peak frequency from the low state to the 2017 flaring state of the source from IR to soft X-rays is observed. This indicates that the source exhibits IBL behavior during quiescent states and HBL characteristics during high states. This is consistent with a higher break energy of the emitting particles in the flaring state, likely associated with a more efficient adiabatic cooling.

- Strong evidence for a long-term hardening at the $5\,\sigma$ level is found in the 30-day LAT light curve data ($4.7\,\sigma$ including the trials factor). A harder-when-brighter trend at the $3.4\,\sigma$ level, including the trials factor, is found for this source. The LAT data are found to prefer the log-parabola and power-law sub exponential cutoff parameterizations over the power-law parameterization at the $7\,\sigma$ level, indicating a possible curvature of at the source before entering the VHE domain where the EBL has a considerable impact.

- Time-resolved modeling of the SED of the source indicates that the individual flares observed have different characteristics and are likely to have different origins.

- Three stationary radio knots in the innermost jet region are found in the VLBA data at 43.1 GHz, 22.2 GHz, and 15.3 GHz. A single-epoch VLBA observation at 43.1 GHz resulted in the highest resolution image yet (at the time of this article) of the jet in this blazar, revealing a knot (unresolved at lower frequencies) very close (0.16 mas) to the core. Stationary knots in the vicinity of the radio core are a typical phenomenon in HBLs. Combining the SED modeling with this radio behavior, we conclude that this source is a typical HBL, although the synchrotron peak sometimes lies in the IBL region of the SED.

- We were able to use a two-component ("blob-in-jet") SSC model to describe multiple flux states of the source. The flaring state is sufficiently described using the same model parameters for the jet component but different values for the particle spectral distribution and the magnetic field strength of the blob component.

- The fluxes measured by the LAT in the HE regime and by Tuorla at optical energies are found to favor a log-normal over a normal distribution; which suggests the existence of multiplicative underlying processes.

- We searched for evidence of a periodic signal in the Tuorla optical data and in the *Fermi*-LAT data, the two datasets for which we have the best-sampled light curves. No evidence for periodicity on any timescale was detected.

- None of the $E > 50$ GeV photons we found in the LAT data were associated with flaring episodes; they were, however, associated with relatively high states. The highest energy photon detected by the LAT had an energy of 466 GeV and was detected on 2011 May 01 during a relatively high state of the source that lasted 13 months.

- Method I, based on the recursive search of neighboring outliers, and Method II, based on the Bayesian blocks, were found to be well suited for the selection of flares and the characterization of the baseline in the LAT light curves. In particular, the Bayesian blocks guided the definition of the different states of activity of source (quiescent, flaring, post-flaring) based on its flux information.

- A detailed framework of the LAT data analysis is provided. This includes the thorough efforts employed in validating the methods used and the sanity checks performed on the results obtained. This could serve as a guideline for researchers interested in the field.

In the future, studies such as the ones presented here should be performed on larger data sets, covering different emission states of the source being studied. Such data are expected to be provided at γ-ray energies by the Cherenkov Telescope Array (Cherenkov Telescope Array Consortium et al. 2019).

6.1.   Potential areas of improvement

- As of the day of writing, a systematic multiwavelength variability study and inter-band cross-correlation analysis at different time scales on LAT blazars has not been performed; possibly due to the large computing power and project management investment that would be required. This investigation would allow us to constrain the parameters of current emission models and also to perhaps challenge the basis of certain models. This would take us closer towards the understanding of ultrafast variability, orphan flares and the apparent non-consistent correlations at different wavelengths.

- A bonus of this systematic study would be its unbiased nature giving us access to the quiescent, flaring and intermediate epochs of the sources. This would give a broader perspective of the current blazar classification scheme. Indeed, Figure 5.26 shows the extreme shift of the synchrotron peak observed when the data are separated according to the different activity states of the source (definition guided by the Bayesian blocks). This blazar behaves as an ISP during the quiescent states, and as a HSP during the high states. This was the first reliable extreme shift ever reported, and begs the question of whether this behavior is to be found in other blazars as well and between other blazar subclasses.

- Evaluating the possibility of implementing the multi-wavelength cross-correlations flux-flux results in TeVCat. This could serve as a valuable library for researchers, in particular during the CTA era; and at the same time trigger low-state observations of sources. It should be pointed out here that, presently, (most of) the data on non-monitored sources from detectors that work in the pointing mode is biased, since they are mainly triggered by alerts of high activity coming from detectors that work on the scanning mode, such as the *Fermi*-LAT.

- A clear definition of what a flare is does not exists to this day; it evolves with our knowledge of the variability of the γ-ray sky. A few years ago, a level of activity above 2.5 times the average value from the LAT source catalog would be used as an indicator of flaring activity by the Flare Advocate program of the *Fermi*-LAT Collaboration; while for the brightest sources a flux above 10^{-6} ph cm^{-2} s^{-1} would be required. Both Methods I and II in Section 5.3.2 are flux-driven methods to select flares. A possible implementation in the future would be to take into account the evolution of the photon indices in time for the selection of flares. Of course, this would only be possible for sufficiently bright sources.

APPENDIX A.   Projects in progress

The author continues her quest to untangle the intricate nature of blazars. With the tools acquired and developed during this thesis, she has undertaken the task to collaborate with the VERITAS colleagues in the study of a number of flat spectrum radio quasars (FSRQ, below) and apply the tools and the lessons learned with 1ES 1215+303 to this endeavor.
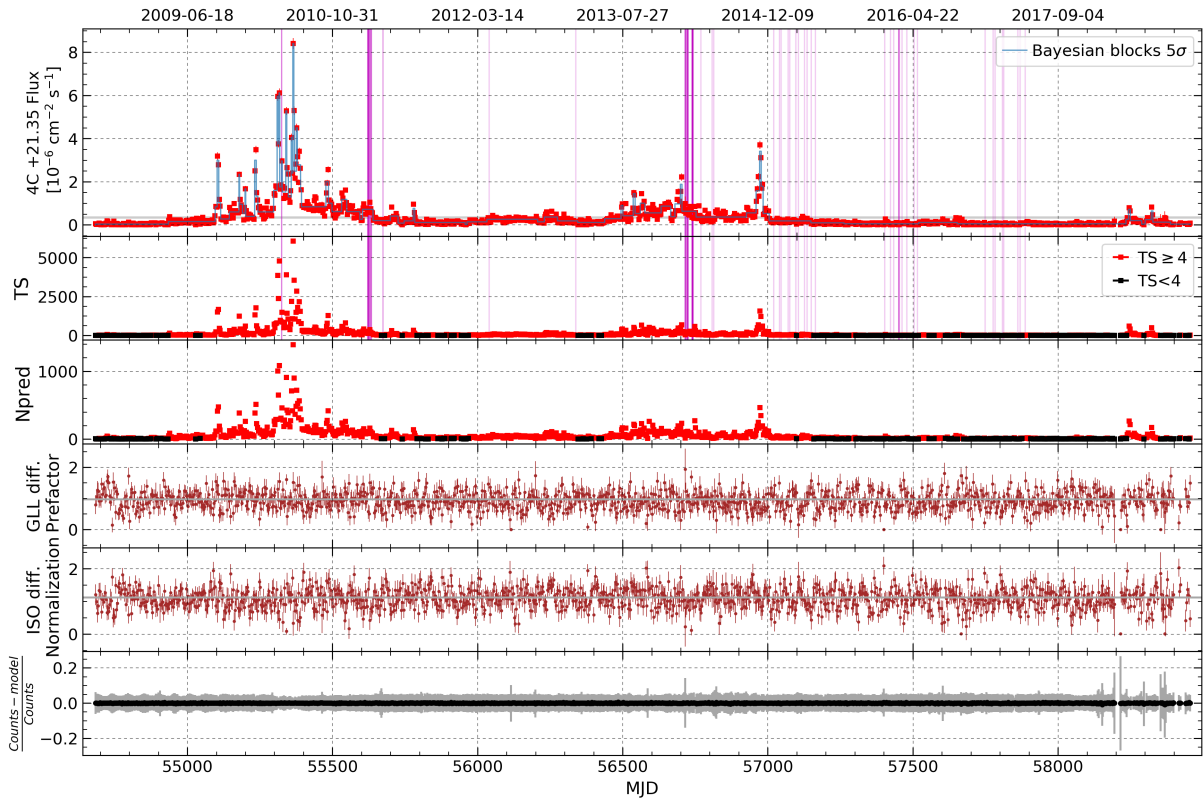
A.1.   PKS 1222+216

Fig. A.1.— **3-day standard light curve from PKS 1222+2016. Shaded regions in magenta represent the periods of VERITAS observations. The extremely large outburst from ∼2009 Sep. to 2010 Oct. can be noticed.**

The FSRQ PKS 1222+216, with redshift $z = 0.435$, was first detected at above > 70 GeV in 2010 June 17 by the MAGIC Collaboration (Aleksić et al. 2011). Following an alert of a bright outburst from this source by the *Fermi*-LAT Collaboration, VERITAS reported on the detection of PKS 1222+216 at the $6\,\sigma$ level from data spread over 10 nights between 2014 Feb. 26 to Mar 10[1].

A.2.   Ton 0599

FSRQ Ton 599, with redshift $z = 0.715$ is part of the *Fermi*-LAT Very Important Project (VIP) list of active galactic nuclei; which consists of a few dozens of sources that appear to provide strong prospects for scientific advances.
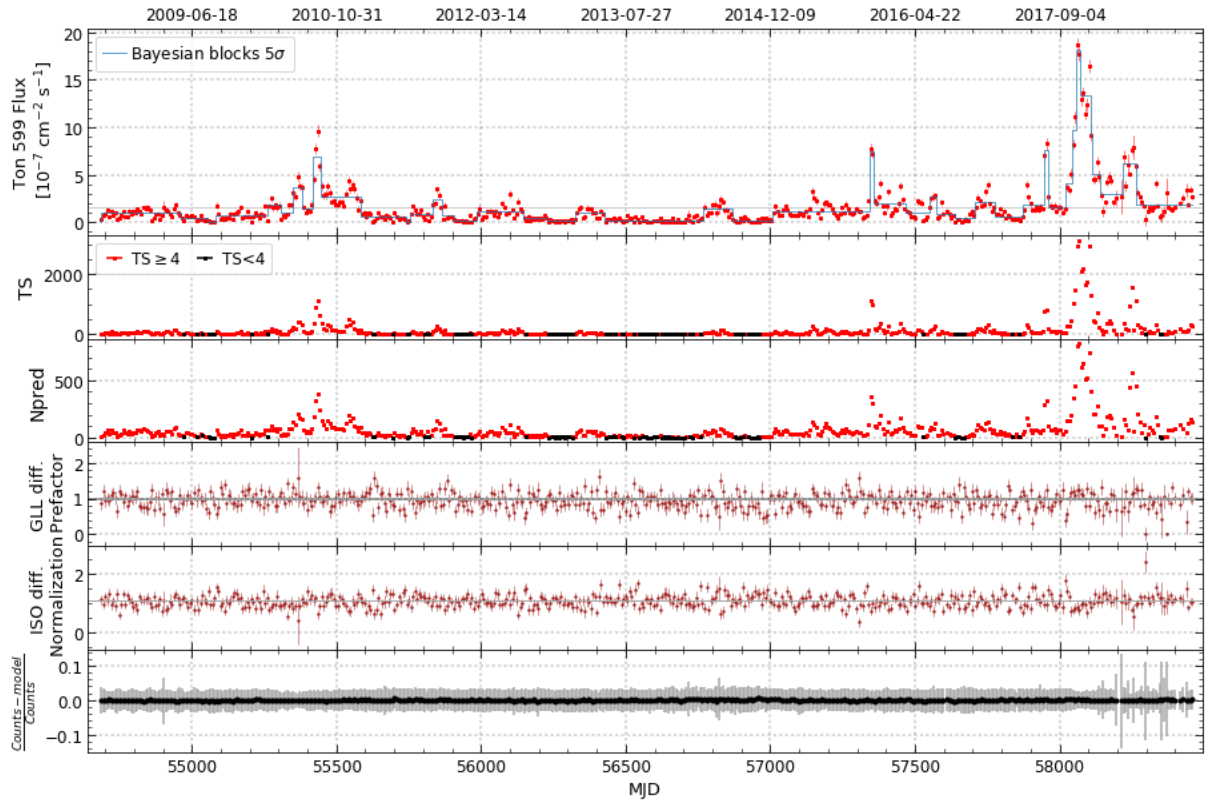

Fig. A.2.—— 7-day standard light curve from Ton 0599. The luminous outburst from ~2017 Sep. that lasted almost ten months can be noticed.

---

[1] http://www.astronomerstelegram.org/?read=5981

A.3.   3C 279

Fermi-LAT has detected several flares from this 3C 279 with extensive follow-up including in December 2013[2], April 2014[3], and June 2015[4]. VERITAS took (nearly) simultaneous observations of these three events, resulting in upper limits. Recent LAT flares occurred in January 2018[5], April 2018[6] and June 2018. No publications yet exist for the two latest flares.
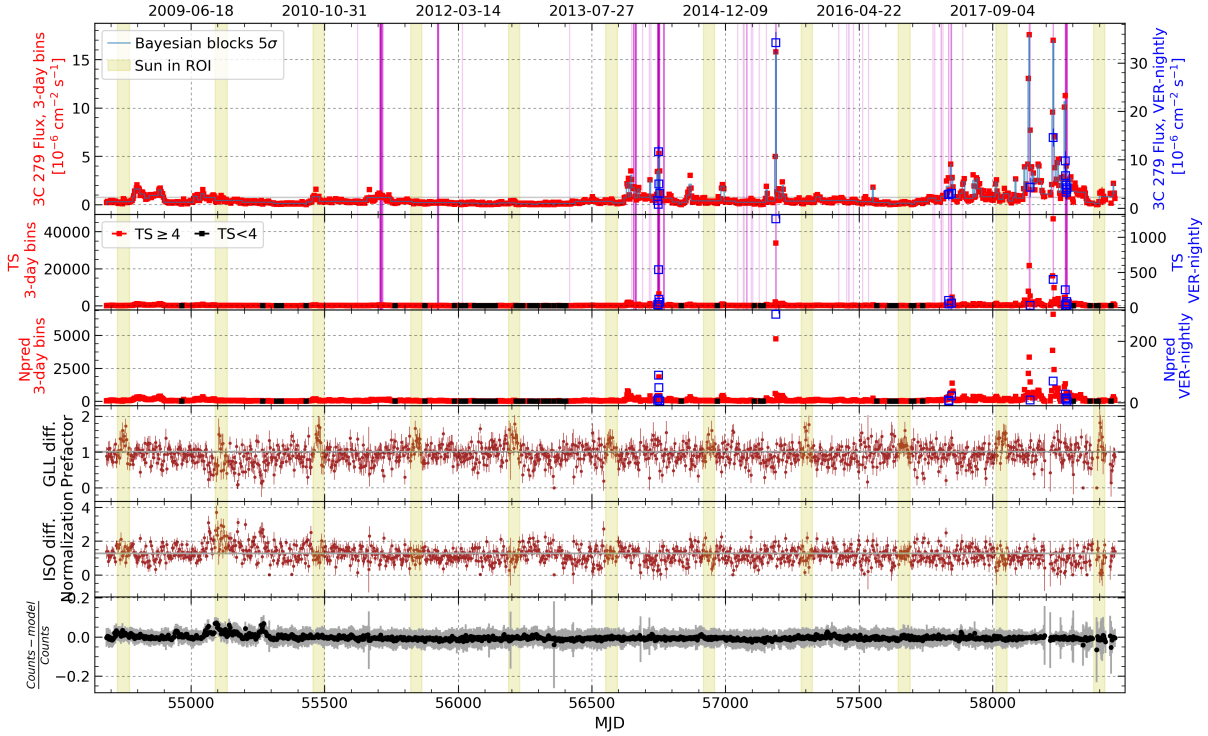

Fig. A.3.—— 3-day standard light curve from 3C 279 (red points). Shaded regions in magenta represent the periods of VERITAS observations. Shaded regions in yellow correspond to periods where the Sun is in the ROI; the assimilation of this emission by the diffuse backgrounds can be noticed. The blue points correspond to LAT significant detections restricted to the time of observations of VERITAS.

[2]http://www.astronomerstelegram.org/?read=5680

[3]http://www.astronomerstelegram.org/?read=6036

[4]http://www.astronomerstelegram.org/?read=7633

[5]http://www.astronomerstelegram.org/?read=11189

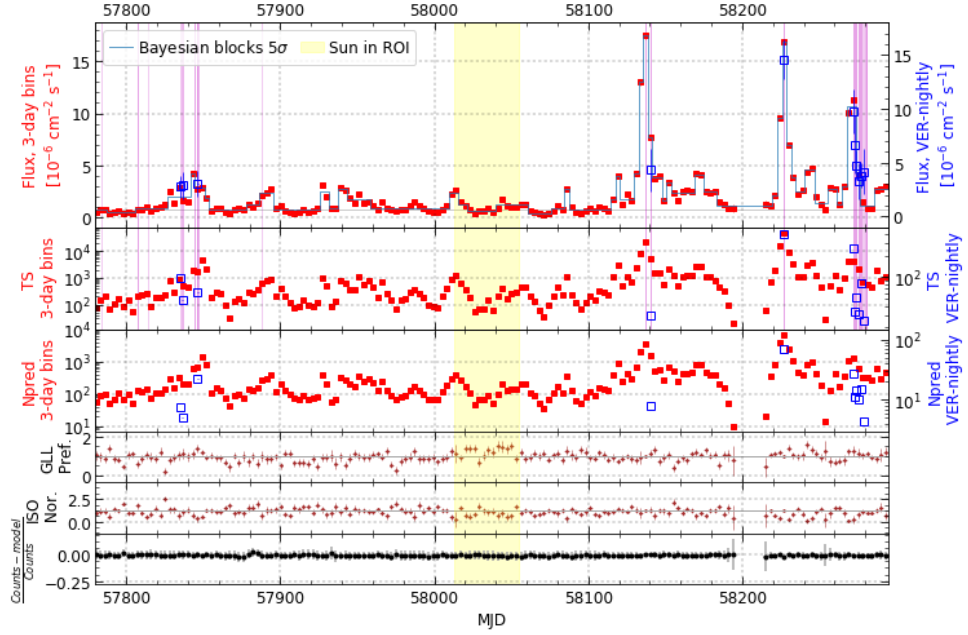[6]http://www.astronomerstelegram.org/?read=11542

Fig. A.4.— Zoom of the 3-day standard light curve from 3C 279 (red points) around flares in 2018. Shaded regions in magenta represent the periods of VERITAS observations. Shaded regions in yellow correspond to periods where the Sun is in the ROI; the assimilation of this emission by the diffuse backgrounds can be noticed. The blue points correspond to LAT significant detections restricted to the time of observations of VERITAS.
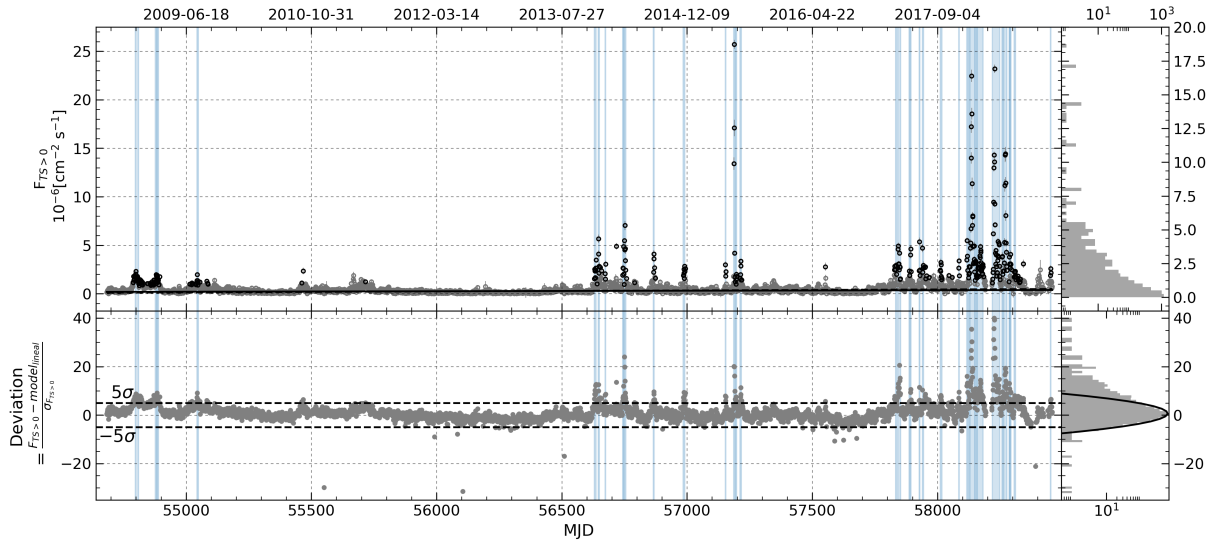

Fig. A.5.— Method I to select flares applied to the 1-day light curve from 3C 279. A linear function as a base-line and the values of $N_{th} = 5\,\sigma$ and $N_p = 3$ were used. See Section 5.3.2.

REFERENCES

Abdalla, H., et al. 2019, Nature, 575, 464

Abdo, A. A., et al. 2009, ApJ, 706, L138

—. 2010a, Nature, 463, 919

—. 2010b, ApJ, 722, 520

—. 2010c, ApJ, 710, 1271

—. 2011a, ApJ, 736, 131

—. 2011b, ApJ, 734, 116

—. 2012, ApJ, 758, 140

Abdollahi, S., et al. 2020, ApJS, 247, 33

Abeysekara, A. U., et al. 2015, ApJ, 815, L22

—. 2017, ApJ, 836, 205

Acero, F., et al. 2015, ApJS, 218, 23

—. 2016, ApJS, 223, 26

Ackermann, M., et al. 2011, ApJ, 743, 171

—. 2012a, ApJS, 203, 4

—. 2012b, Science, 338, 1190

—. 2015a, ApJ, 813, L41

—. 2015b, ApJ, 799, 86

—. 2015c, ApJ, 810, 14

Aharonian, F., et al. 2007, ApJ, 664, L71

Aharonian, F. A. 2002, MNRAS, 332, 215

Ahnen, M. L., et al. 2018, A&A, 620, A181

Aitchison, J., & Brown, A. C. 1973, Cambridge University Press, 60, 104

Ajello, M., et al. 2009, ApJ, 699, 603

—. 2012, ApJ, 751, 108

—. 2014, ApJ, 780, 73

—. 2017, ApJS, 232, 18

—. 2019, ApJ, 878, 52

—. 2020, ApJ, 890, 9

Akiyama, M., Ueda, Y., Ohta, K., Takahashi, T., & Yamada, T. 2003, ApJS, 148, 275

Albert, J., et al. 2008, Nuclear Instruments and Methods in Physics Research A, 588, 424

Aleksić, J., et al. 2011, ApJ, 730, L8

—. 2012, A&A, 544, A142

Alexander, T. 2013, arXiv e-prints, arXiv:1302.1508

Aliu, E., et al. 2013, ApJ, 779, 92

—. 2014, ApJ, 782, 13

Angelakis, E., et al. 2016, MNRAS, 463, 3365

Angioni, R., Valverde, J., & Ojha, R. 2018, The Astronomer's Telegram, 11854

Archambault, S., et al. 2013, ApJ, 776, 69

Archer, A., et al. 2018, ApJ, 862, 41

Atwood, W., et al. 2013, arXiv e-prints, arXiv:1303.3514

Atwood, W. B., et al. 2007, Astroparticle Physics, 28, 422

—. 2009, ApJ, 697, 1071

Barkov, M. 2019, High Energy Phenomena in Relativistic Outflows VII (HEPRO VII) conferences

Barrau, A., et al. 1998, Nuclear Instruments and Methods in Physics Research A, 416, 278

Barthelmy, S. D., et al. 2005, Space Sci. Rev., 120, 143

Becherini, Y., Djannati-Ataï, A., Marandon, V., Punch, M., & Pita, S. 2011, Astroparticle Physics, 34, 858

Beckmann, V., & Shrader, C. 2012, in Proceedings of "An INTEGRAL view of the high-energy sky (the first 10 years)" - 9th INTEGRAL Workshop and celebration of the 10th anniversary of the launch (INTEGRAL 2012). 15-19 October 2012. Bibliotheque Nationale de France, Paris, France, 69

Bennett, A. S. 1962, MmRAS, 68, 163

Berge, D., Funk, S., & Hinton, J. 2007, A&A, 466, 1219

Biteau, J. 2013, arXiv e-prints, arXiv:1309.5738

Biteau, J., & Giebels, B. 2012, A&A, 548, A123

Biteau, J., & Williams, D. A. 2015, ApJ, 812, 60

Blandford, R. D., & McKee, C. F. 1982, ApJ, 255, 419

Blandford, R. D., & Payne, D. G. 1982, MNRAS, 199, 883

Blandford, R. D., & Znajek, R. L. 1977, MNRAS, 179, 433

Blinov, D., et al. 2016, MNRAS, 457, 2252

—. 2018, MNRAS, 474, 1296

Blumenthal, G. R., & Gould, R. J. 1970, Reviews of Modern Physics, 42, 237

Bonnoli, G., Ghisellini, G., Foschini, L., Tavecchio, F., & Ghirlanda, G. 2011, MNRAS, 410, 368

Böttcher, M., & Dermer, C. D. 2010, ApJ, 711, 445

Brown, A. M., & Adams, J. 2011, MNRAS, 413, 2785

Bruel, P., Burnett, T. H., Digel, S. W., Johannesson, G., Omodei, N., & Wood, M. 2018, arXiv e-prints, arXiv:1810.11394

Burbidge, G. R. 1961, Nature, 190, 1053

Burrows, D. N., et al. 2005, Space Sci. Rev., 120, 165

Cerruti, M., Zech, A., Boisson, C., & Inoue, S. 2015, MNRAS, 448, 910

Chang, S. W., Byun, Y. I., & Hartman, J. D. 2015, ApJ, 814, 35

Cherenkov Telescope Array Consortium et al. 2019, Science with the Cherenkov Telescope Array, ed. World Scientic Publishing Co. Pte. Ltd., LCCN 2018017444, ISBN 9789813270084, ISBN 981327008X

Chiaberge, M., & Ghisellini, G. 1999, MNRAS, 306, 551

Christiansen, J., & VERITAS Collaboration. 2012, in American Institute of Physics Conference Series, Vol. 1505, American Institute of Physics Conference Series, ed. F. A. Aharonian, W. Hofmann, & F. M. Rieger, 709–712

Cogan, P. 2008, in International Cosmic Ray Conference, Vol. 3, International Cosmic Ray Conference, 1385–1388

Colla, G., et al. 1970, A&AS, 1, 281

Collin-Souffrin, S., Dumont, S., Heidmann, N., & Joly, M. 1980, A&A, 83, 190

Costamante, L., Bonnoli, G., Tavecchio, F., Ghisellini, G., Tagliaferri, G., & Khangulyan, D. 2018, MNRAS, 477, 4257

Curtis, H. D. 1918, Publications of Lick Observatory, 13, 9

Daniel, M. K. 2008, in International Cosmic Ray Conference, Vol. 3, International Cosmic Ray Conference, 1325–1328

Daum, A., et al. 1997, Astroparticle Physics, 8, 1

Davidson, K. 1972, ApJ, 171, 213

Davies, J. M., & Cotton, E. S. 1957, Solar Energy, 1, 16

de Naurois, M. 2019, The Astronomer's Telegram, 13052, 1

Degrange, B., & Fontaine, G. 2015, Comptes Rendus Physique, 16, 587

Dermer, C. D., & Giebels, B. 2016, Comptes Rendus Physique, 17, 594

Di Sciascio, G. 2019, in Journal of Physics Conference Series, Vol. 1263, Journal of Physics Conference Series, 012003

Domínguez, A., et al. 2011, MNRAS, 410, 2556

Drake, J. F., Swisdak, M., Schoeffler, K. M., Rogers, B. N., & Kobayashi, S. 2006, Geophys. Res. Lett., 33, L13105

Edelson, R. A., & Krolik, J. H. 1988, ApJ, 333, 646

Emmanoulopoulos, D., McHardy, I. M., & Papadakis, I. E. 2013, MNRAS, 433, 907

Falomo, R., Scarpa, R., Treves, A., & Urry, C. M. 2000, ApJ, 542, 731

Fath, E. A. 1909, Lick Observatory Bulletin, 5, 71

Feng, Q., Lin, T. T. Y., & VERITAS Collaboration. 2017, in IAU Symposium, Vol. 325, Astroinformatics, ed. M. Brescia, S. G. Djorgovski, E. D. Feigelson, G. Longo, & S. Cavuoti, 173–179

Fermi, E. 1949, Phys. Rev., 75, 1169

Fermi-LAT Collaboration et al. 2018, Science, 362, 1031

Finke, J. D., Razzaque, S., & Dermer, C. D. 2010, ApJ, 712, 238

Foffano, L., Prandini, E., Franceschini, A., & Paiano, S. 2019, MNRAS, 486, 1741

Fomin, V. P. Stepanian, A. A., Lamb, R. C., Lewis, D. A., Punch, M., & Weekes, T. C. 1994, Astroparticle Physics, 2, 137

Foster, G. 1996, AJ, 112, 1709

Franceschini, A., & Rodighiero, G. 2017, A&A, 603, A34

Frühwirth, R. 1987, Nuclear Instruments and Methods in Physics Research A, 262, 444

Gallant, Y. A., & Achterberg, A. 1999, MNRAS, 305, L6

Gehrels, N., et al. 2004, ApJ, 611, 1005

Ghisellini, G. 2015, Journal of High Energy Astrophysics, 7, 163

Ghisellini, G., Celotti, A., Fossati, G., Maraschi, L., & Comastri, A. 1998, MNRAS, 301, 451

Giacconi, R., Gursky, H., Paolini, F. R., & Rossi, B. B. 1962, Physical Review Letters, 9, 439

Giannios, D., Uzdensky, D. A., & Begelman, M. C. 2010, MNRAS, 402, 1649

Giebels, B., & Degrange, B. 2009, A&A, 503, 797

Giroletti, M., Giovannini, G., Taylor, G. B., & Falomo, R. 2006, ApJ, 646, 801

Greenstein, J. L. 1963, Nature, 197, 1041

Gunn, J. E., & Peterson, B. A. 1965, ApJ, 142, 1633

Hauser, M. G., & Dwek, E. 2001, ARA&A, 39, 249

Hazard, C., Mackey, M. B., & Shimmins, A. J. 1963, Nature, 197, 1037

Helene, O. 1983, Nuclear Instruments and Methods in Physics Research, 212, 319

Hervet, O., Boisson, C., & Sol, H. 2015, A&A, 578, A69

—. 2016, A&A, 592, A22

Hillas, A. M. 1985, International Cosmic Ray Conference, 3

—. 2013, Astroparticle Physics, 43, 19

Holder, J. 2011, International Cosmic Ray Conference, 12, 137

—. 2015, arXiv e-prints, arXiv:1510.05675

Hovatta, T., et al. 2016, A&A, 596, A78

Hoyle, F., Burbidge, G., & Sargent, W. 1966, Nature, 209, 751

Hoyle, F., & Fowler, W. A. 1963a, Nature, 197, 533

—. 1963b, MNRAS, 125, 169

IceCube Collaboration et al. 2018a, Science, 361, eaat1378

—. 2018b, Science, 361, 147

Inoue, S., & Takahara, F. 1996, ApJ, 463, 555

Jelley, J. V., & Galbraith, W. 1955, Journal of Atmospheric and Terrestrial Physics, 6, 304

Karas, V., & Šubr, L. 2007, A&A, 470, 11

Katarzyński, K., Sol, H., & Kus, A. 2001a, A&A, 367, 809

—. 2001b, A&A, 367, 809

Kembhavi, A. K., & Narlikar, J. V. 1999, Quasars and active galactic nuclei : an introduction

Kharb, P., Lister, M. L., & Shastri, P. 2008, International Journal of Modern Physics D, 17, 1545

Kieda, D. 2011, in International Cosmic Ray Conference, Vol. 9, International Cosmic Ray Conference, 14

Krause, M., Pueschel, E., & Maier, G. 2017, Astroparticle Physics, 89, 1

Kristian, J. 1973, ApJ, 179, L61

Kuehr, H., Witzel, A., Pauliny-Toth, I. I. K., & Nauber, U. 1981, A&AS, 45, 367

Kushwaha, P., Chandra, S., Misra, R., Sahayanathan, S., Singh, K. P., & Baliyan, K. S. 2016, ApJ, 822, L13

Li, T.-P., & Ma, Y.-Q. 1983, ApJ, 272, 317

Lico, R., et al. 2020, A&A, 634, A87

Lindfors, E. J., et al. 2016, A&A, 593, A98

Liodakis, I., Pavlidou, V., Hovatta, T., Max-Moerbeck, W., Pearson, T. J., Richards, J. L., & Readhead, A. C. S. 2017, MNRAS, 467, 4565

Lister, M. L., Aller, M. F., Aller, H. D., Hodge, M. A., Homan, D. C., Kovalev, Y. Y., Pushkarev, A. B., & Savolainen, T. 2018, ApJS, 234, 12

Lister, M. L., et al. 2019, ApJ, 874, 43

Lynden-Bell, D. 1969, Nature, 223, 690

Lyubarskii, Y. E. 1997, MNRAS, 292, 679

MAGIC Collaboration et al. 2019, A&A, 623, A175

Manmoto, T., Takeuchi, M., Mineshige, S., Matsumoto, R., & Negoro, H. 1996, ApJ, 464, L135

Marscher, A. P., & Gear, W. K. 1985, ApJ, 298, 114

Marscher, A. P., et al. 2010, ApJ, 710, L126

Massaro, E., Perri, M., Giommi, P., & Nesci, R. 2004, A&A, 413, 489

Mattox, J. R., et al. 1996, ApJ, 461, 396

Mirzoyan, R. 2019, The Astronomer's Telegram, 12390, 1

Mirzoyan, R., Garczarczyk, M., Hose, J., & Paneque, D. 2007, Astroparticle Physics, 27, 509

Moiseev, A. A., Ormes, J. F., Hartman, R. C., Johnson, T. E., Mitchell, J. W., & Thompson, D. J. 2004, Astroparticle Physics, 22, 275

Mortlock, D. J., et al. 2011, Nature, 474, 616

Mücke, A., Protheroe, R. J., Engel, R., Rachen, J. P., & Stanev, T. 2003, Astroparticle Physics, 18, 593

Narayan, R., McClintock, J. E., & Yi, I. 1996, ApJ, 457, 821

Nieppola, E., Tornikoski, M., & Valtaoja, E. 2006, A&A, 445, 441

Nieto Castaño, D., Brill, A., Feng, Q., Humensky, T. B., Kim, B., Miener, T., Mukherjee, R., & Sevilla, J. 2019, in International Cosmic Ray Conference, Vol. 36, 36th International Cosmic Ray Conference (ICRC2019), 752

Nieto Castaño, D., Brill, A., Kim, B., Humensky, T. B., & Consortium, C. 2017, in International Cosmic Ray Conference, Vol. 301, 35th International Cosmic Ray Conference (ICRC2017), 809

Nilsson, K., et al. 2018, A&A, 620, A185

Ojha, R., Carpenter, B., & Valverd, J. 2017a, The Astronomer's Telegram, 10721

Ojha, R., & Valverde, J. 2018, The Astronomer's Telegram, 11419

Ojha, R., Valverde, J., & Van Zyl, P. 2017b, The Astronomer's Telegram, 10987

Padovani, P. 1998, in IAU Symposium, Vol. 179, New Horizons from Multi-Wavelength Sky Surveys, ed. B. J. McLean, D. A. Golombek, J. J. E. Hayes, & H. E. Payne, 257

Padovani, P. 2011, MNRAS, 411, 1547

—. 2016, A&A Rev., 24, 13

Padovani, P., & Giommi, P. 1995, ApJ, 444, 567

Padovani, P., et al. 2017, A&A Rev., 25, 2

Paiano, S., Landoni, M., Falomo, R., Treves, A., Scarpa, R., & Righi, C. 2017, ApJ, 837, 144

Park, N., & VERITAS Collaboration. 2015, in International Cosmic Ray Conference, Vol. 34, 34th International Cosmic Ray Conference (ICRC2015), 771

Petropoulou, M., Dimitrakoudis, S., Padovani, P., Mastichiadis, A., & Resconi, E. 2015, MNRAS, 448, 2412

Pian, E., et al. 1998, ApJ, 492, L17

Piner, B. G., & Edwards, P. G. 2018, ApJ, 853, 68

Planck Collaboration et al. 2016, A&A, 594, A26

Potter, W. J. 2018, MNRAS, 473, 4107

Punch, M., et al. 1992, Nature, 358, 477

Pushkarev, A. B., Kovalev, Y. Y., Lister, M. L., & Savolainen, T. 2017, MNRAS, 468, 4992

Quinn, J., et al. 1996, ApJ, 456, L83

Rees, M. J. 1966, Nature, 211, 468

Richards, J. L., et al. 2011, ApJS, 194, 29

Roache, E., Irvin, R., Perkins, J. S., Harris, K., Falcone, A., Finley, J., & Weeks, T. 2008, in International Cosmic Ray Conference, Vol. 3, International Cosmic Ray Conference, 1397–1400

Roming, P. W. A., et al. 2005, Space Sci. Rev., 120, 95

Rybicki, G. B., & Lightman, A. P. 1986, Radiative Processes in Astrophysics

Salpeter, E. E. 1964, ApJ, 140, 796

Scargle, J. D. 1982, ApJ, 263, 835

Scargle, J. D., Norris, J. P., Jackson, B., & Chiang, J. 2013, ApJ, 764, 167

Schmidt, M. 1963, Nature, 197, 1040

—. 1965, ApJ, 141, 1295

Seyfert, C. K. 1943, ApJ, 97, 28

Shah, Z., Mankuzhiyil, N., Sinha, A., Misra, R., Sahayanathan, S., & Iqbal, N. 2018, Research in Astronomy and Astrophysics, 18, 141

Shapiro, S. S., & Wilk, M. B. 1965, Biometrika, 52, 591

Shields, G. A. 1974, ApJ, 191, 309

Shukla, A., et al. 2018, ApJ, 854, L26

Sinha, A., Sahayanathan, S., Acharya, B. S., Anupama, G. C., Chitnis, V. R., & Singh, B. B. 2017, ApJ, 836, 83

Souffrin, S. 1969, A&A, 1, 414

Takalo, L. O., Nilsson, K., Lindfors, E., Sillanpää, A., Berdyugin, A., & Pasanen, M. 2008, in American Institute of Physics Conference Series, Vol. 1085, American Institute of Physics Conference Series, ed. F. A. Aharonian, W. Hofmann, & F. Rieger, 705–707

Tammi, J., & Duffy, P. 2009, MNRAS, 393, 1063

Tanabashi, M., et al. 2018a, Phys. Rev. D, 98, 030001

—. 2018b, Phys. Rev., D98, 030001

Tavani, M., et al. 2009, A&A, 502, 995

Tavecchio, F., Becerra-Gonzalez, J., Ghisellini, G., Stamerra, A., Bonnoli, G., Foschini, L., & Maraschi, L. 2011, A&A, 534, A86

Tavecchio, F., et al. 2001, ApJ, 554, 725

Teräsranta, H., et al. 1998, A&AS, 132, 305

The Fermi-LAT collaboration. 2019, arXiv e-prints, arXiv:1905.10771

Timmer, J., & Koenig, M. 1995, A&A, 300, 707

Uttley, P., & McHardy, I. M. 2001, MNRAS, 323, L26

Uttley, P., McHardy, I. M., & Papadakis, I. E. 2002, MNRAS, 332, 231

Valverde, J., Horan, D., Bernard, D., Noto, G., Feng, Q., & Mukherjee, R. 2018a, Fermi-LAT Spring Collaboration Meeting 2018, Pisa, Italy

Valverde, J., Horan, D., Bernard, D., Noto, G., & Mukherjee, R. 2018b, International school of Cosmic Ray Astrophysics (ISCRA) 21st Course, Erice, Sicily, Italy

Valverde, J., Horan, D., Feng, Q., & Hervet, O. 2018c, 8th International Fermi Symposium, Baltimore, USA

Valverde, J., Horan, D., Noto, G., & Mukherjee, R. 2017a, Fermi-LAT Spring Collaboration Meeting 2017, CERN, Switzerland

—. 2017b, Fermi Summer School 2017, Delaware, USA

—. 2017c, Blazars and other AGNs LAT Teleconference

—. 2017d, XVI Meeting of Physics, Lima, Peru

Valverde, J., Horan, D., Noto, G., Mukherjee, R., Bernard, D., Fermi-Lat Collaboration, & VERITAS Collaboration. 2017e, in Proceedings of the 7th International Fermi Symposium, held 15-20 October 2017, in Garmisch-Partenkirchen, Germany (IFS2017), 116

Valverde, J., & Ojha, R. 2017a, The Astronomer's Telegram, 10952

—. 2017b, The Astronomer's Telegram, 10951

Valverde, J., Ojha, R., & Buehl, R. 2018d, The Astronomer's Telegram, 11412

Valverde, J., et al. 2020, ApJ, 891, 170

van Putten, M. H. P. M., & Della Valle, M. 2019, MNRAS, 482, L46

Vaughan, S., Edelson, R., Warwick, R. S., & Uttley, P. 2003, MNRAS, 345, 1271

Weekes, T. C., et al. 1989, ApJ, 342, 379

Weidinger, M., & Spanier, F. 2015, A&A, 573, A7

Westfold, K. C. 1959, ApJ, 130, 241

Wilks, S. S. 1938, Ann. Math. Statist., 9, 60

Williams, R. E., & Weymann, R. J. 1968, AJ, 73, 895

Wills, B. J., Netzer, H., & Wills, D. 1985, ApJ, 288, 94

Woltjer, L. 1959, ApJ, 130, 38

—. 1966, ApJ, 146, 597

Woo, J.-H., & Urry, C. M. 2002, ApJ, 579, 530

Yamada, M., Kulsrud, R., & Ji, H. 2010, Rev. Mod. Phys., 82, 603

Zhang, H., Diltz, C., & Böttcher, M. 2016, ApJ, 829, 69

Titre : De nouvelles perspectives sur la nature des blazars à partir d'une décennie d'observations à multi longueurs d'onde: Découverte d'un très grand décalage de la fréquence de crête de l'émission synchrotron, des corrélations de flux optique-gamma à long terme et d'une tendance à la hausse du flux dans le BL Lac 1ES 1215+ 303

Résumé : Cette thèse traite de l'observation, des données, analyses et études multi-longueurs d'onde, focalisées sur les hautes énergies, des noyaux actifs de galaxie, en particulier sur 1ES 1215+303. Le domaine de l'astrophysique gamma de haute et très haute énergie est particulièrement dynamique actuellement, grâce à la pleine exploitation des installations existantes comme *Fermi*-LAT dans l'espace, et VERITAS, H.E.S.S. et MAGIC au sol, et la construction en cours de la prochaine génération de télescopes au sol Cherenkov, CTA (Cherenkov Telescope Array), qui est un effort mondial.

Le premier chapitre fournit un résumé de l'état actuel de l'astrophysique des hautes énergies, en particulier concernant le domaine émergent de l'astrophysique multi-messagers avec la récente détection des ondes gravitationnelles avec, dans un cas, GW 170817, une contrepartie électromagnétique qui lui est associée, ainsi que la première indication d'un signal de neutrino astrophysique coïncidant avec un état d'activité élevé à hautes et très hautes énergies dans un noyau actif de galaxie, TXS 0506+056. Ce travail de doctorat a donc été réalisé dans un contexte plus large d'un champ actuellement très actif, avec de nouvelles fenêtres passionnantes et non électromagnétiques s'ouvrant sur notre Univers.

Le deuxième chapitre donne un aperçu historique de la découverte des noyaux actifs de galaxie et la construction d'un modèle unifié permettant de comprendre les nombreuses manifestations de ce phénomène à partir d'un type commun de moteur, c'est-à-dire un trou noir supermassif donnant lieu à des phénomènes d'accrétion avec une efficacité progressive d'un type de source à l'autre, et, dans certains cas, à des jets relativistes et collimatés. Le chapitre continue avec les principaux processus radiatifs standards supposés être à l'œuvre dans les noyaux actifs de galaxie, avec l'émission synchrotron et sa polarisation, les processus Compton inverse, et les mécanismes d'accélération des particules. Les mouvements relativistes observés dans les radio-galaxies sont abordés également, ainsi que le cas particulier des blazars, une sous-classe de noyaux actifs de galaxie dont le jet est étroitement aligné sur notre ligne de visée, et à laquelle appartient 1ES 1215+303. Le chapitre se termine par une description de l'état actuel de l'astronomie gamma, avec une présentation des derniers catalogues de sources de haute énergie fournies par la collaboration *Fermi*-LAT.

Le troisième chapitre couvre une description des différentes installations qui ont été utilisées pour recueillir les données multi-longueurs d'onde obtenues sur 1ES 1215+303, puis utilisées dans les chapitres restants. L'accent est mis sur les instruments à haute énergie, avec une description des gerbes atmosphériques et leur rayonnement Chérenkov correspondant, qui est utilisé pour détecter les rayons gamma primaires par télescopes atmosphériques Chérenkov d'imagerie au sol tels que VERITAS. Le dernier instrument est ensuite présenté, avec une brève explication du système de déclenchement et de l'étalonnage. Une description détaillée du *Fermi*-LAT et de sa réponse instrumentale est alors donnée; c'est l'instrument principal que j'ai utilisé pour les données présentées dans les chapitres suivants. Enfin, une brève description des instruments et des données obtenues sur cette source à des énergies plus faibles (du domaine des rayons X à la bande radio) est donnée.

Le quatrième chapitre se concentre sur le cadre d'analyse des données *Fermi*-LAT, et l'analyse que j'ai effectuée sur le noyau actif de galaxie 1ES 1215+303, le cœur de mon travail de doctorat, et pourrait servir de guide aux chercheurs intéressés par ce domaine. Je présente les efforts approfondis de validation des méthodes utilisées et les contrôles d'intégrité des résultats effectués. Une description des analyses de niveau supérieur est fournie, comme la sélection des éruptions (flares) en utilisant la méthode Blocs Bayésiens, qui est également brièvement décrite.

Le dernier chapitre principal est consacré au cas de 1ES 1215+303, avec une présentation complète et une étude exhaustive des courbes de lumière multi-longueurs d'onde obtenues avec les différentes installations présentées au chapitre 3, et constitue avec le chapitre 4 ma principale contribution dans le domaine. Il convient de noter les images complémentaires obtenues dans le domaine radio, qui révèle plusieurs nœuds distincts et compacts. Grâce à une surveillance de long terme de cet objet, qui a duré près de 10 ans, les nœuds radio

les plus internes se révèlent être quasi-stationnaires, fournissant une preuve supplémentaire de la classification de 1ES 1215 + 303 comme blazar à pic de fréquence, qui sera débattu plus loin dans le chapitre, grâce à une modélisation de sa distribution d'énergie spectrale. Le chapitre se poursuit par une analyse détaillée de la caractéristiques de cette source avec l'utilisation d'outils avancés tels que les corrélations flux-flux et flux-index, le rapport de dureté, la fonction d'intercorrélation discrète transformée en z (zDCF), une analyse du spectre de puissance et des périodogrammes utilisant plusieurs méthodes statistiques, une sélection minutieuse d'états actifs observés à des énergies élevées et très élevées, et la découverte d'une tendance à long terme à l'augmentation du flux à la fois dans le domaine optique et aux hautes énergies. Ce chapitre présente enfin une modélisation auto-Compton synchrotron de 1ES 1215+303 pour ses états de flare en 2017 et post-flare, révélant un décalage inhabituel et extrême de la fréquence du pic synchrotron lors du flare, remettant en question le schéma global de classification des blazars.

Le manuscrit se termine par des conclusions sur les principaux résultats obtenus à partir de cette étude à long terme, multi-longueurs d'onde sur 1ES 1215+303, et s'ouvre sur la question d'une classification des blazars qui devrait bénéficier d'une prise en compte plus approfondie des différents états d'activité. Des annexes sont fournies pour illustrer des analyses similaires commencées sur les caractéristiques temporelles de trois autres sources, à savoir PKS 1222+216, Ton 599 et 3C 279, d'après les données de *Fermi*-LAT.

Titre : De nouvelles perspectives sur la nature des blazars à partir d'une décennie d'observations à multi longueurs d'onde: Découverte d'un très grand décalage de la fréquence de crête de l'émission synchrotron, des corrélations de flux optique-gamma à long terme et d'une tendance à la hausse du flux dans le BL Lac 1ES 1215+ 303

Mots clés : Galaxies: actives, jets, rayons gamma, blazars.

Résumé : Les blazars sont connus pour leur variabilité sur une large gamme d'échelles de temps à toutes les longueurs d'onde; et leur classification (en quasars radio à spectre plat, BL Lac à basse fréquence crête, intermédiaire ou haute fréquence; FSRQ, LBL, IBL, HBL) est basée sur des caractéristiques spectrales à large bande qui ne considèrent pas la source comme étant, éventuellement, dans différentes états d'activité. Récemment, il a été proposé de classer les blazars en fonction de la cinématique de leurs caractéristiques radio. La plupart des études sur les blazars à rayons gamma TeV se concentrent sur des échelles de temps courtes, en particulier pendant les éruptions, en raison de la rareté des campagnes d'observation ou de l'existence relativement récente de détecteurs spécialisés suffisamment sensibles.

Avec une décennie d'observations du *Fermi*-LAT, VERITAS, je présente une étude approfondie de la variabilité à long terme multi longueurs d'onde du blazar 1ES 1215+303, des rayons gamma à la radio. Cet ensemble de données sans précédent révèle de multiples éruptions de rayons gamma fortes et une augmentation à long terme de la ligne de base des rayons gamma et du flux optique de la source sur une période de dix ans, ce qui se traduit par une corrélation linéaire entre ces deux bandes d'énergie sur cette période. Des comportements HBL typiques sont identifiés dans la morphologie radio de la source. Cependant, des analyses de la distribution d'énergie spectrale à large bande à différents états de flux de la source, révèlent un déplacement extrême de l'énergie de la fréquence de crête de l'émission synchrotron de l'IR aux rayons X mous; indiquant que la source présente les caractéristiques IBL pendant les états de repos et le comportement HBL pendant les états éruptifs. Un modèle synchrotron self-Compton à deux composantes est utilisé pour décrire ce changement spectaculaire.

Un cadre détaillé de l'analyse des données de l'instrument *Fermi*-LAT est fourni et pourrait servir de guide aux chercheurs intéressés par ce domaine. Je présente les efforts approfondis de validation des méthodes utilisées et les contrôles d'intégrité des résultats effectués. Une description des analyses de niveau supérieur est fournie, comme la sélection des éruptions et la recherche d'un comportement plus-dur-quand-plus-lumineux dans les données de *Fermi*-LAT, l'analyse de corrélation croisée et de variabilité à plusieurs longueurs d'onde; la recherche de tendances, log-normalité et variabilité, la caractérisation des éruptions et des distributions spectrales d'énergie, et la recherche d'observations *Fermi*-LAT - VERITAS simultanées. C'est le coeur de ce travail de doctorat.

Les différentes méthodes appliquées et présentées dans ce travail fournissent un panorama complet et détaillé de la nature complexe de ce blazar et peuvent même remettre en question notre système de classification actuel. De plus, ce travail fournit une illustration du type d'analyses à long terme que les futurs instruments d'imagerie atmosphérique, tels que le Cherenkov Telescope Array (CTA), non seulement permettront mais pourraient même améliorer.

Title : New insights on the nature of blazars from a decade of multi-wavelength observations: Discovery of a very large shift of the synchrotron peak frequency, long-term optical-γ-ray flux correlations, and rising flux trend in the BL Lac 1ES 1215+303

Keywords : Galaxies: active, jets, gamma-rays, blazars.

Abstract : Blazars are known for their variability on a wide range of timescales at all wavelengths; and their classification (into flat spectrum radio quasars, low-, intermediate- or high-frequency-peaked BL Lac; FSRQ, LBL, IBL, HBL) is based on broadband spectral characteristics that do not consider the source being at, possibly, different states of activity. Recently, it was proposed that blazars could be classified according to the kinematics of their radio features. Most studies of TeV γ-ray blazars focus on short timescales, especially during flares, due to the scarcity of observational campaigns or due to the relatively young existence of specialized, sensitive enough detectors.

With a decade of observations from the *Fermi*-LAT and VERITAS, I present an extensive study of the long-term multi-wavelength variability of the blazar 1ES 1215+303 from γ-rays to radio. This unprecedented data set reveals multiple strong γ-ray flares and a long-term increase in the γ-ray and optical flux baseline of the source over the ten-year period, which results in a linear correlation between these two energy bands over a decade. Typical HBL behaviors are identified in the radio morphology of the source. However, analyses of the broadband spectral energy distribution at different flux states of the source, unveil an extreme shift in energy of the synchrotron peak frequency from IR to soft X-rays; indicating that the source exhibits IBL characteristics during quiescent states and HBL behavior during high states. A two-component synchrotron self-Compton model is used to describe this dramatic change.

A detailed framework of the analysis of the data from the *Fermi*-LAT instrument is provided, and could serve as a guideline for researchers interested in this field. I present the thorough efforts that were employed in validating the methods used and the sanity checks that were performed on the results obtained. A description of the higher-level analyses are provided, including the flare-selection algorithms, the search for harder-when-brighter behavior in the *Fermi*-LAT data, the multi-wavelength cross-correlation and variability analysis, the search for trends, log-normality and variability, the characterization of flares and of the spectral energy distributions, and the search for simultaneous *Fermi*-LAT - VERITAS observations. These are the heart of this PhD work.

The different methods applied and presented in this work provide a complete and detailed panorama of the intricate nature of this blazar, and possibly even challenge our current classification scheme. Moreover, this work provides an illustration of the type of long-term analyses that future imaging atmospheric instruments, such as the Cherenkov Telescope Array (CTA), will not only allow but potentially improve.